Structure property relations in chalcopyrite based intermediate band solar absorber materials

Dissertation zur Erlangung des akademischen Grades

Doktor der Naturwissenschaften

(Dr. rer. nat.)

vorgelegt von

Julien Marquardt

Eingereicht am Fachbereich Geowissenschaften

der Freien Universität Berlin

Angefertigt am Helmholtz-Zentrum Berlin für Materialien und Energie

Abteilung für Struktur und Dynamik von Energiematerialien

Die Arbeit ist in englischer Sprache verfasst

2018

Erstgutachterin: Prof. Dr. Susan Schorr

Zweitgutachterin: Prof. Dr. Christiane Stephan-Scherb

Datum der Disputation: 20.12.2018

Eidesstattliche Erklärung

Hiermit versichere ich, dass ich die vorliegende Arbeit selbstständig verfasst und keine anderen als die angegebenen Quellen und Hilfsmittel benutzt habe. Alle Ausführungen, die fremden Quellen wörtlich oder sinngemäß entnommen wurden, sind kenntlich gemacht. Die Arbeit war in gleicher oder ähnlicher Form noch nicht Bestandteil einer Studien- oder Prüfungsleistung.

Berlin, den

_____

Unterschrift

Summary

Over the last decades the need of electrical energy increased continuously, whereas the percentage of electric energy from renewable sources became larger in the last years. The demand of an energy supply, which is produced by renewable sources completely, is more important than before. Nowadays, solar cells reach power conversion efficiencies of 46% [1] using multi-junction concentrator cells, which are very complicated and expensive in production. The maximum power conversion efficiency for a single junction solar cell is restricted to ~32% [2], named the Shockley Queisser limit. However, the incorporation of transition metals into the wide gap $CuGaS_2$ chalcopyrite type absorber material was proposed to create an intermediate band, which cause two additional absorption ranges and an increase in power conversion efficiency up to 63% [3, 4]. The aim of this study was to determine the solid solubility limits of several transition metals as well as to study their effect on the chalcopyrite type crystal structure and optoelectronic properties.

All investigated transition metals were successfully incorporated into the chalcopyrite type structure, by solid state reaction synthesis of pure elements. The lowest solid solubility was obtained from chromium and nickel with 0.003(1)mol% CrS and 0.008(1)mol% NiS in $Cu_{0.5}Ga_{0.5}S$, which results in no observable changes in the chalcopyrite type crystal structure. A much higher solid solubility limit was observed for manganese with 0.098(1)mol% MnS in $Cu_{0.5}Ga_{0.5}S$. The pseudo-binary section of $Cu_{0.5}(Fe_xGa_{0.5-x})S$ was earlier reported [5] to have complete solubility, was showing a phase separation at $x_i>0.1$ into an iron rich and iron poor chalcopyrite type phase, respectively. Two different substitution mechanisms were observed from the iron alloyed chalcopyrite type phases. For those with low initial iron contents ($x_i<0.1$), the trend of chemical composition and lattice parameters indicate a coupled substitution (Cu+Ga↔Fe), whereas higher initial iron contents show a unilateral substitution (Ga↔Fe). The substitution of manganese into the chalcopyrite type structure is rather coupled than unilateral as would be necessary for an intermediate band absorber material. Using the average neutron scattering length analysis method, it was observed that manganese is occupying both cationic sites of the chalcopyrite type structure. From these extrinsic defects (Mn_{Ga}, Mn_{Cu}) two optoelectronic active defect states result, located within the band gap of the chalcopyrite type semiconductor, but not corresponding to the proposed intermediate band position. The obtained photoluminescence (PL) spectra was correlated to the predictions given by density functional theory [6]. In addition, correlating the PL spectra with the defect concentration, it can be seen that the dominant PL band at 1.86eV is rather related to the intrinsic Ga_{Cu} cation anti-site defect than anion vacancies.

Based on the obtained anion parameter of the chalcopyrite type phases from X-ray diffraction using the Rietveld method, the effect of copper vacancies on local structural changes was derived and existing calculation models were enhanced to give more precise predictions for overall structural parameter (e.g. tetragonal distortion).

Zusammenfassung

Seit Jahrzehnten steigt der Bedarf an elektrischer Energie kontinuierlich, wobei der Anteil an erneuerbaren Energien in den letzten Jahren stetig zunimmt. Die Forderung nach einer vollständigen Loslösung von fossilen Brennstoffen wird immer größer. Heutzutage erreichen Solarzellen mit mehreren p-n Übergängen einen Wirkungsgrad von 46%. Jedoch sind diese äußerst aufwendig herzustellen und kostspielig. Der maximale Wirkungsgrad, der mit nur einem p-n Übergang erzielt werden kann, beträgt ~32% und ist bekannt als Shockley Queisser Limit. Dieses Limit soll jedoch durch den Einbau von Übergangsmetallen in den Chalkopyrit Strukturtyp Absorber überschritten werden können. Die eingebauten Übergangsmetalle erzeugen dabei ein Zwischenband wodurch zwei zusätzliche Wellenlängenbereiche absorbiert werden können und der Wirkungsgrad bis auf 63% anwachsen kann. Ziel dieser Arbeit ist die Bestimmung der Feststoff-Löslichkeitsgrenzen einiger Übergangsmetalle in $CuGaS_2$ sowie deren Auswirkungen auf die Kristallstruktur und optoelektronischen Eigenschaften.

Alle untersuchten Übergangsmetalle konnten erfolgreich in den Chalkopyrit Strukturtyp Halbleiter mittel Festkörpersynthese von reinen Elementen integriert werden. Dabei ist die Festkörper-Löslichkeit von Chrom und Nickel mit 0.003(1)mol% CrS und 0.008(1)mol% NiS in $Cu_{0.5}Ga_{0.5}S$ am niedrigsten. Aufgrund dieser geringen Löslichkeit sind die Auswirkungen auf die Kristallstruktur vernachlässigbar. Eine weit höhere Festkörper-Löslichkeit ist für Mangan zu beobachten, hier beträgt die Löslichkeit 0.098(1)mol% MnS in $Cu_{0.5}Ga_{0.5}S$. Bei der Mischreihe $Cu_{0.5}(Fe_xGa_{0.5-x})S$ handelt es sich zufolge früherer Arbeiten um eine vollständige Machbarkeit von Eisen und Gallium, allerdings ist für Eisengehalte von $x_i>1$ eine Phasenseperation in eine eisen-reiche und eine eisen-arme Chalkopyritphase zu beobachten. Des Weiteren weisen diese Proben zwei unterschiedliche Substitutionen auf. Anhand der beobachteten Trends der chemischen Zusammensetzung und der Gitterkonstanten ist abzuleiten, dass Proben mit einem niedrigen initialen Eisengehalt ($x_i<1$) einer gekoppelten Substitution (Cu+Ga↔Fe) zuzuordnen sind, während solche mit hohem initialen Eisengehalt ($x_i>1$) eine unilaterale Substitution (Ga↔Fe) aufweisen. Die Substitution von MnS und $Cu_{0.5}Ga_{0.5}S$ ist ausschließlich gekoppelt und nicht unilateral, wie es für die Erzeugung eines Zwischenband-Halbleiters notwendig ist. Mithilfe der Analyse der mittleren Neutronenstreulängen kann eindeutig nachgewiesen werden, dass Mangan auf beiden Kationenplätzen eingebaut wird. Diese extrinsischen Defekte führen zu zwei optoelektronisch aktiven Defektleveln innerhalb der Bandlücke des Chalkopyrite Strukturtyp Halbleiters, welche nicht mit der vorgeschlagenen Position des Zwichenbands übereinstimmen. Das beobachtete Photolumineszenz-Spektrum (PL) konnte mit Berechnungen der Dichtefunktionaltheory korreliert werden. Zusätzlich ist das PL Band bei 1.86eV, eher auf intrinsische Anti-Lagen-Defekte zurückzuführen als auf Anionleerstellen.

Basierend auf den erhobenen strukturellen Daten wurde der Effekt von Kupferleerstellen auf die Struktur gezeigt und bestehende Berechnungen um diesen erweitert.

Table of content

EIDESSTATTLICHE ERKLÄRUNG ..... **I**

SUMMARY ..... **II**

ZUSAMMENFASSUNG ..... **III**

TABLE OF CONTENT ..... **IV**

1. INTRODUCTION **1**

1.1 BASICS OF CHALCOPYRITE TYPE SEMICONDUCTORS 1

1.2 THE CONCEPT OF INTERMEDIATE BAND CHALCOPYRITE TYPE SEMICONDUCTORS 5

1.3 POINT DEFECTS IN INTERMEDIATE BAND CHALCOPYRITE TYPE COMPOUND 7

1.4 SUBSTITUTION OF TRANSITION METALS 8

2. PHASE RELATIONS **10**

2.1 THE CU-GA-S TERNARY SYSTEM 10

2.2 CHROMIUM RELATED BINARY PHASE DIAGRAMS 14

2.3 IRON RELATED BINARY PHASE DIAGRAMS 16

2.4 MANGANESE RELATED BINARY PHASE DIAGRAMS 18

2.5 NICKEL RELATED BINARY PHASE DIAGRAMS 20

2.6 SUMMARY – PHASE DIAGRAMS 22

3. EXPERIMENTAL **24**

3.1 SELECTION OF INITIAL WEIGHT 24

3.2 SYNTHESIS ROUTE 25

3.3 ANALYSIS TECHNIQUES 28

3.3.1 Electron microprobe analysis *28*

3.3.2 X-ray diffraction *29*

3.3.3 Neutron diffraction *29*

3.3.4 The Rietveld method *31*

3.3.5 Average neutron scattering length analysis method *32*

3.3.6 Photoluminescence spectroscopy *34*

3.3.7 Superconducting quantum interference device *35*

3.3.8 Temperature dependent resistivity *36*

3.3.9 ^{57}Fe Mössbauer spectroscopy *37*

4. RESULTS AND DISCUSSION **39**

4.1 CHROMIUM INCORPORATION INTO THE CHALCOPYRITE TYPE PHASE 39

4.1.1 Phase analysis *39*

4.1.2 Structural trends of the chalcopyrite type phase *42*

4.1.3 Cation distribution within the chalcopyrite type phase *43*

4.1.4 Optoelectronic properties of Cr:$CuGaS_2$ *45*

4.1.5 Interim conclusion ... *46*
4.2 NICKEL INCORPORATION INTO THE CHALCOPYRITE TYPE PHASE ... 47
4.2.1 Phase analysis ... *47*
4.2.2 Structural trends of the chalcopyrite type phase ... *51*
4.2.3 Optoelectronic properties of Ni:$CuGaS_2$ ... *52*
4.2.4 Interim conclusion ... *53*
4.3 IRON INCORPORATION INTO THE CHALCOPYRITE TYPE PHASE ... 54
4.3.1 Phase analysis ... *54*
4.3.2 Structural trends of the chalcopyrite type phase ... *57*
4.3.3 Optoelectronic properties of iron alloyed $CuGaS_2$ ... *60*
4.3.4 ^{57}Fe Mössbauer spectroscopy at iron containing $CuGaS_2$ ... *60*
4.3.5 Interim conclusion ... *61*
4.4 MANGANESE INCORPORATION INTO THE CHALCOPYRITE TYPE PHASE ... 62
4.4.1 Phase analysis ... *62*
4.4.2 Structural trends of the chalcopyrite type phase ... *65*
4.4.3 Cation distribution within the chalcopyrite type phase ... *69*
4.4.4 Impact of synthesis temperature on chemical composition and structural trends ... *72*
4.4.5 The 3-3-4 ($Cu_{0.3}Ga_{0.3}Mn_{0.4}S$) phase ... *74*
4.4.6 Calculation of structural parameters regarding copper vacancies ... *78*
4.4.7 Optoelectronic properties of manganese alloyed $CuGaS_2$ ... *88*
4.4.8 Magnetic properties of manganese containing $CuGaS_2$ ... *92*
4.4.9 Temperature dependent resistivity of manganese alloyed $CuGaS_2$ ... *93*
4.4.10 Interim conclusion ... *96*
5. CONCLUSION ... **97**
6. OUTLOOK ... **101**
REFERENCES ... **i**
LIST OF FIGURES ... **ix**
LIST OF TABLES ... **xvi**
ACKNOWLEDGMENT ... **xvii**
APPENDIX ... **xix**

1. Introduction

The focus of this work is a systematic study of the solubility limits of certain transition metals into the chalcopyrite type $CuGaS_2$. The key aspects are the material synthesis and characterization by means of chemical composition and crystal structure. Second major focus is the evolution of the structural parameters regarding the fraction of the incorporated transition metal as well as the effect on the general chemical composition. Based on this, the substitution behavior can be derived for each transition metal which was proposed to be unilateral substitution of gallium by the transition metal. Furthermore, the optoelectronic properties are investigated using photoluminescence spectroscopy in order to detect the intermediate band which was proposed to occur as a result of the incorporation of transition metals into the chalcopyrite type structure [7].
The main goal would be the detection of the intermediate band within the chalcopyrite type band structure which could lead to a solar cell material with a solar conversion efficiency above the Shockley-Queisser limit. Furthermore, these kinds of solar cell material would be easier and cheaper to produce than others solar cell techniques e.g. the tandem solar cells.
Some results of this work are part of scientific publications.

1.1 Basics of chalcopyrite type semiconductors

Semiconductors based on the chalcopyrite type structure have been investigated for more than 40 years. One of the first reported record power conversation efficiency of $CuInSe_2$ solar cells was 12% in 1975 [8]. In the meanwhile several breakthroughs, i.e. the introduction of gallium pushed the efficiency up to 22.6% of $Cu(In,Ga)Se_2$ solar cells [9]. The latest rapid increase was possible due to the application of alkali elements either as precursor or as post deposition treatment. The general chemical composition of chalcopyrite type semiconductors is $Cu(Ga,In)(S,Se)_2$. The advantages of the chalcopyrite type compound semiconductor are the direct band gap, the high absorption coefficient and the usage of only non-/low-toxic elements. But there is also a disadvantage, in order to produce high efficiency cells indium is necessary. Indium is rare and is also used in modern monitors and television screens. Nonetheless, due to the high absorption coefficient in the order of $10^5 cm^{-1}$ [10], the thickness of the absorber layer can be reduced up to >1µm thin films. This has a side benefit; very thin films can be fabricated even on flexible substrates to cover any kind of surface. In a direct band gap semiconductor, the conduction band minima and the valence band maxima are located at the same high-symmetry line, thus they have the same wave vector. This means, photons with energies higher than the band gap energy can be absorbed directly. In the case of an indirect band gap, the conduction band minima and valence band maxima are shifted against each other. In order to absorb a photon its

momentum needs to change which results in a significant decrease in light absorption. Furthermore, the direct band gap of the chalcopyrite type semiconductor can easily be adapted to its application. By changing the gallium to indium ratio as well as the sulfur to selenium ratio the band gap can be adjusted in a region of almost 1.4eV from 1.05eV to 2.43eV [11, 12]. However, for technical reasons scientists renounce sulfur for the fabrication of thin film solar cells. Already within this much more simplified system the band gap fits to the maximum of the Shockley-Queisser limit [2] shown in Figure 1.

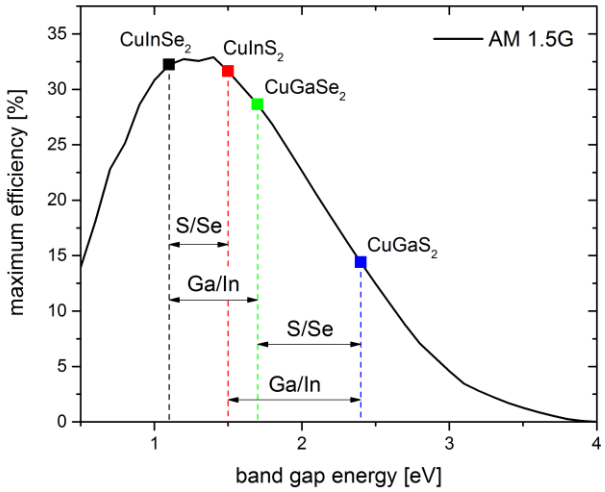

Figure 1 - Maximum power conversation efficiency for solar cell operating at ambient conditions illuminated with the AM 1.5G spectral irradiance (ASTM 173-03; AM1.5: 1.5 atmosphere thickness) as function of the band gap energy, adapted from the data of Rühle [13]. Arrows indicate the variability of the band gap due to chemical changes.

These semiconductors crystallize in the chalcopyrite type structure (space group $I\bar{4}2d$). The name comes from the eponymous natural mineral chalcopyrite ($CuFeS_2$), named in 1725 by Johann Friedrich Henckel. In 1932 Pauling and Brockway [14] published first the crystal structure of $CuFeS_2$. More than 20 years later Hahn et al. [15] reported about other compounds that crystallize in the chalcopyrite type structure (e.g. $CuGaS_2$). The chalcopyrite structure is derived from the diamond type structure ($F\,4_1/d\,\bar{3}\,2/m$) and sphalerite type structure ($F\bar{4}3m$). The diamond type structure is a face centered cubic monoatomic crystal structure consisting of group IV elements. In order to generate the sphalerite type structure, the group IV element is replaced by group II and VI elements, respectively. The next step is an ordered replacement of the group II element by group I and III elements. As a consequence, the unit cell is doubled in $\vec{c}$ direction. All structures deriving from the diamond type structure are part of the so called adamantine family [16], the structural evolution is shown in Figure 2.

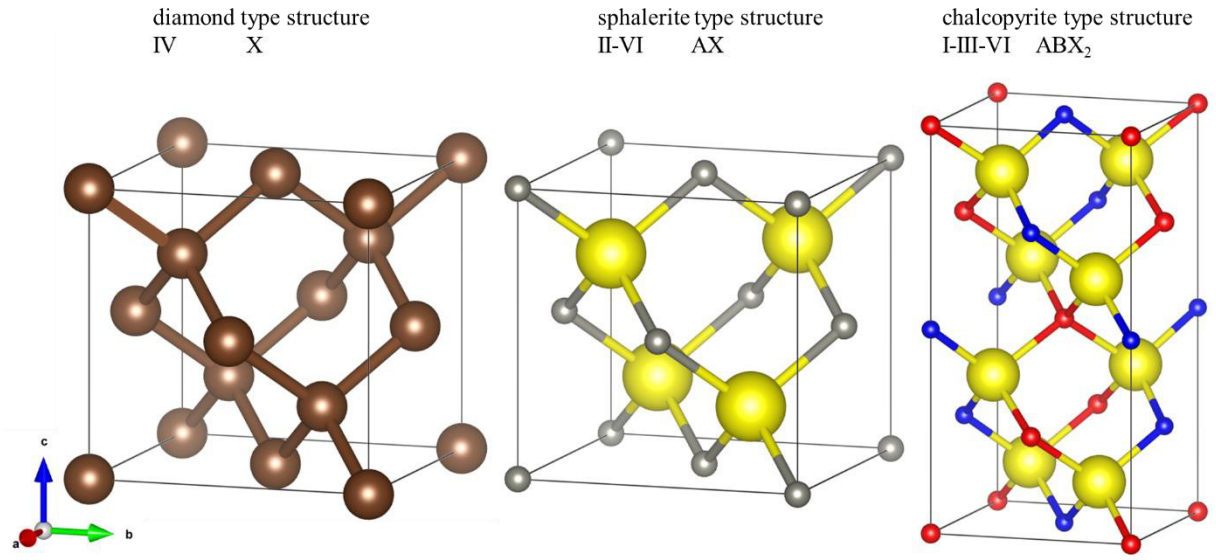

Figure 2 - Schematic progress in structural evolution from the diamond to chalcopyrite type structure adapted from Schorr [17]. Roman numbers indicate the valence state of the cations and anions. The anion are big spheres (brown-carbon, yellow-sulfur) and the cations are represented as small spheres (grey-zinc, blue-gallium and red-copper). The size of the spheres refers to their crystal radius in the structure taken from Shannon [18].

The structural derivation from the sphalerite to the chalcopyrite type structure results in an important and material specific parameter. This parameter is called tetragonal deformation η and gives the deviation of the chalcopyrite type structure to a sphalerite structure ($\eta = \left|1 - {}^{c}/_{2a}\right|$). The sphalerite structure accrues if the lattice parameter *c* is exactly two times lattice parameter *a* (η=0) [17]. In this case the X-ray diffraction pattern becomes very similar to the sphalerite diffraction pattern and a structural determination is only possible with very small Bragg peaks (e.g. 101). If $\eta \neq 0$, a peak splitting due to the deviation from the sphalerite structure is observed. For example, the 220 sphalerite peak splits up into the 204 and 220 chalcopyrite peaks, whereby it is possible to determine the shape (height to width ratio) of the tetragonal unit cell by comparing the position of these Bragg peaks. If the smaller 220 Bragg peak appears at lower 2θ than the 204 Bragg peak, the tetragonal cell is clinched and vice versa the tetragonal unit cell is elongated.

In the chalcopyrite type structure, the group I element is occupying the 4a Wyckoff position (0, 0, 0), the group III element is occupying the 4b Wyckoff position (0, 0, 0.5) and the anion is located on 8d Wyckoff position (*x*, 0.25, 0.125) [15]. The *x* coordinate of the anion is not fixed by symmetry, it varies with the chemical composition of the chalcopyrite type material. In literature the anion position *x* is called anion parameter *x*, but also tetragonal distortion *u*. The tetragonal distortion *u* is defined as the deviation of the anion position *x* from its ideal position ($u = |0.25 - x|$). The impact on the diffraction pattern are relatively small. A determination is only possible by a proper Rietveld refinement. In addition to the involved elements, the anion position is affected by the actual cation distribution including intrinsic anti-site defects, vacancies, interstitials and extrinsic defects. The anion parameter *x* is the most important structural parameter of the chalcopyrite type structure, since the anion position directly influences the band gap energy of these semiconductor materials (Figure 3). In

the solid solution $Cu(In,Ga)S_2$, starting from the $CuGaS_2$ endmember, the substitution of indium for gallium increases the average radius of the 4b site, resulting in a decrease of the anion parameter *x*. This decrease of the anion parameter *x* leads to a decrease of the energy band gap of the chalcopyrite type semiconductor.

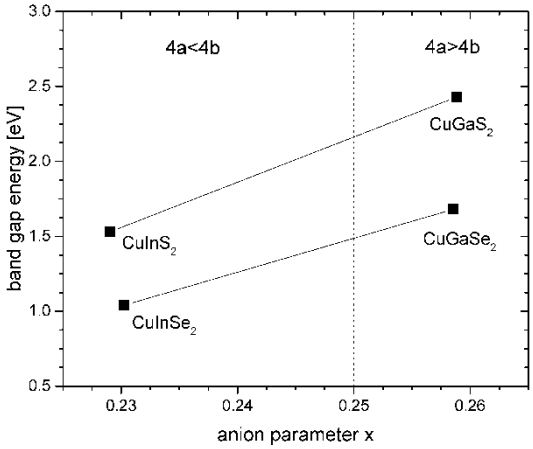

Figure 3 - Correlation between the mean radii of the cation sites 4a (R4a) and 4b (R4b) ratio and the anion parameter x as function of the bandgap energy. The anion parameter x was calculated by the formalism of Jaffe and Zunger [19]. The band gap energies of the chalcopyrite type compound semiconductors were taken from literature [12, 20, 21]. The solid lines indicate the solid solution of $Cu(In,Ga)S_2$ and $Cu(In,Ga)Se_2$ chalcopyrite type compound semiconductor.

The calculated band structure of the chalcopyrite type $CuGaS_2$ is shown in Figure 4. The upper valence bands corresponds to the bonding and anti-bonding of hybridized of Cu-3d and S-3p states [22]. The lower bands are formed by Ga-S bonding states [22]. Whereas the conduction band is made by the bonding and anti-bonding of hybridized of Ga-4s and S-3p states [23]. The direct band to band transition takes place at the high symmetry line Γ.

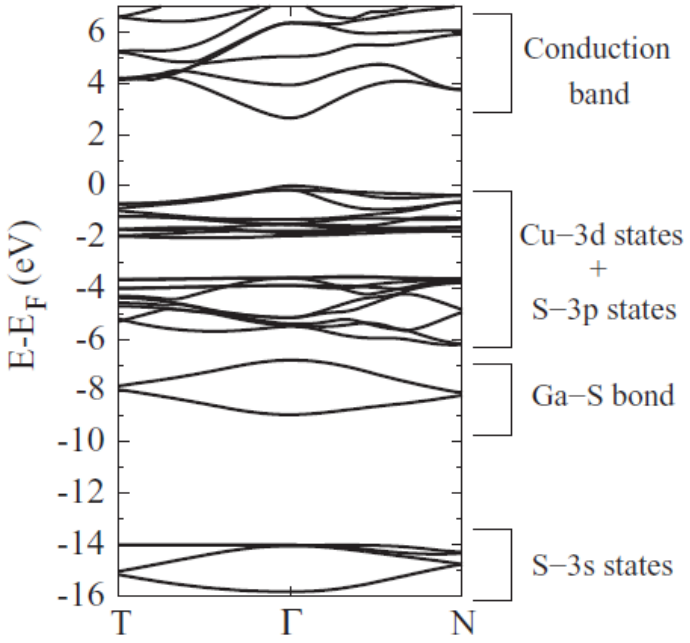

Figure 4 - Band structure of $CuGaS_2$ using scCOHSEX + G_0W_0 taken from Aguilera et. al [22].

1.2 The concept of intermediate band chalcopyrite type semiconductors

Nowadays, $Cu(In,Ga)(S,Se)_2$ solar cells gain a power conversion efficiency of almost 23%. However, a maximum power conversion efficiency of 32% is given by the Shockley-Queisser limit [2] shown in Figure 1. One year before Shockley and Queisser published their work regarding the efficiency limit of solar cells, Wolf published a paper with the title: "Limitations and possibilities for improvement of photovoltaic solar energy converters: Part I: Considerations for earth's surface operation." [24]. This paper summarizes the factors which lead to the limitation of the solar energy conversion performance. Additional to that, factors as losses due to reflection on the surface, incomplete absorption, utilization of only a part of the photon energy for the creation of electron-hole pairs, are discussed [24]. The same paper describes possibilities to minimize these losses, to reach the theoretically limit of a single p-n junction solar cell, as well as new methods to even overcome the theoretically limit are suggested. The new methods were “The Multi-Layer Solar Cell” mentioned by Jackson [25], “Graded Energy Gap Solar Cells” mentioned by Kroemer [26] and “The Multitransition Solar Cell” mentioned by Reynolds and Czyzak [27].

In a multitransition solar cell introduced trap levels were proposed to generate additional transitions, besides the main transition from valence to conduction band. With this approach photons with energies below the band gap energy can be absorbed, resulting in two additional absorption ranges (Figure 5) and in a significant increase in solar conversion efficiency. For solar cells with a single trap level a limit conversion efficiency of 50% and more than 60% using two trap levels were proposed [24]. In 2006 Palacios et al. [28] performed DFT calculations for a transition metal alloyed chalcopyrite type semiconductor. The presence of an intermediate band due to the substitution of 25% gallium atoms by titanium atoms is shown. The concept of intermediate band absorber materials was couched. Due to the incorporation of transition metals on the 4b cation site of the chalcopyrite type structure an intermediate band appears [29]. More recent calculations show, that the intermediate band is still separated at a transition metal concentration of 6.25% [23].

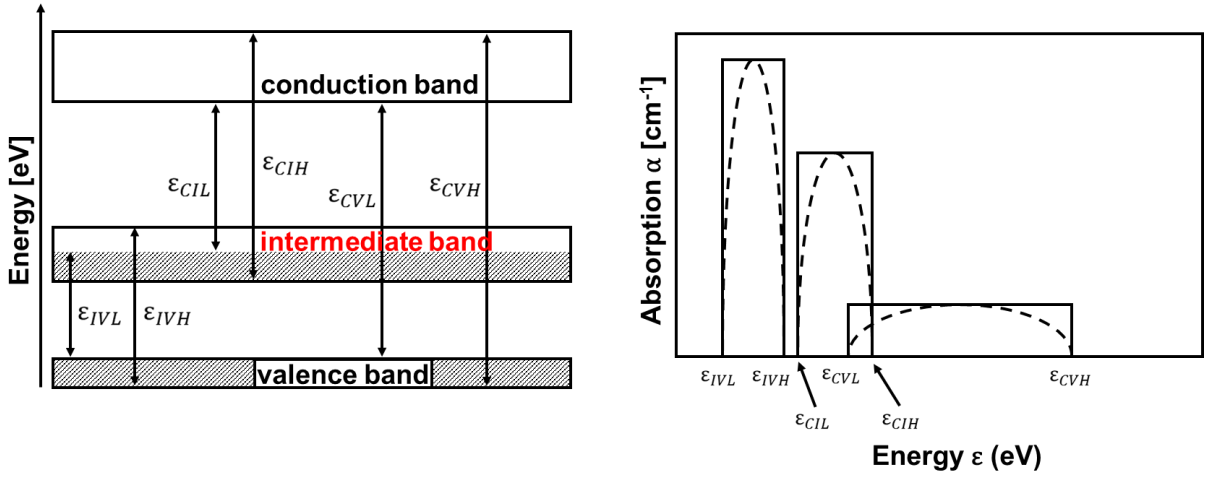

Figure 5 - Band diagram showing the transitions corresponding to absorption thresholds and bounds (left). Absorption bands associated with the electronic band structure of the IB semiconductor (right). Dashed lines represent qualitatively the real absorption coefficients. Squared shapes represent the simplified absorption coefficients [30].

The maximum potential efficiency of 46.77% appears at 2.41eV with the intermediate band located at 0.92eV [7]. With a band gab of 2.43eV [12], $CuGaS_2$ seems to be the best host compound fitting the necessary band gap of all compounds within the $Cu(In,Ga)(S,Se)_2$ solid solution. In a $CuGaS_2$ chalcopyrite type host the most promising transition metals are titanium and iron, but also chromium [7]. These transition metals are proposed to induce the intermediate band close to the optimal position of 0.92eV, as shown in Figure 6.

However, the solubility of chromium as well as titanium was calculated to be rather low [31]. The reason might be the preference of both trivalent metals for octahedral rather than tetrahedral coordination. Iron is very promising due to the similarity in cationic radius. Nevertheless, first intermediate band solar cells containing iron did not show the desired effect [32].

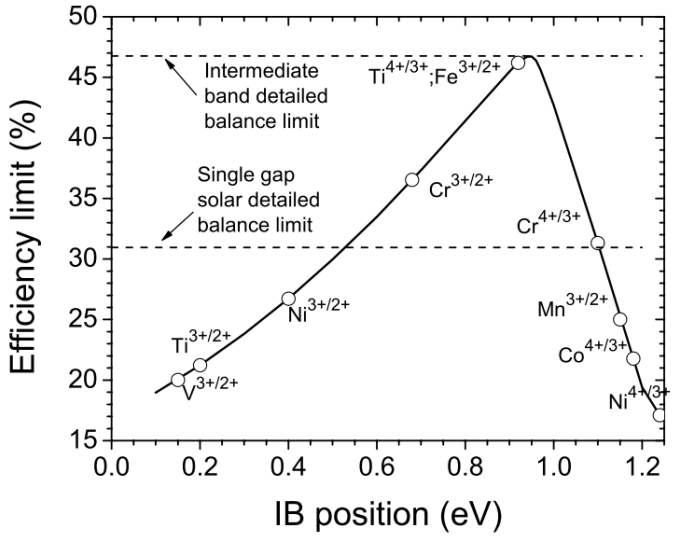

Figure 6 - Limiting efficiency at one sun of a solar cell with the bandgap of CuGaS2. The transition metals that could lead to the intermediate band located at the indicated position are shown as hollow dots [33].

1.3 Point defects in intermediate band chalcopyrite type compound

The $CuGaS_2$ chalcopyrite type compound has a specific number of intrinsic defects that makes this material interesting as a solar absorber material. These defects act as natural doping and cause a p-type conductivity of the material [34]. Responsible for the p-type conductivity are copper vacancies (V_{Cu}) and copper on gallium (Cu_{Ga}) anti-site defects [34]. All intrinsic defects possible are listed in Table I, giving an overview of their defect formation energy. Regarding the defect formation energies, the most probable intrinsic defects are Ga_{Cu}^{2+} and $Cu_{Ga}^{\square}$ anti-site defects as well as $V_{Cu}^{\square}$ or V_{Cu}^{-}. However, due to the similar atomic radii of copper and gallium, a certain amount of disorder can be assumed any times. Disorder is defined as a replacement of a certain amount of gallium on the copper site and the same amount of copper on the gallium site.

Table I - Defect formation energies, ΔG_D, for intrinsic defects in $CuGaS_2$, from Bailey et al. [34].

Vacancies	ΔG_D (eV)	Substitutions	ΔG_D (eV)
$V_{Cu}^{\square}$	1.82	$Ga_{Cu}^{\square}$	2.60
V_{Cu}^{-}	1.83	Ga_{Cu}^{+}	1.61
$V_{Ga}^{\square}$	4.52	Ga_{Cu}^{2+}	0.40
V_{Ga}^{-}	4.69	$Cu_{Ga}^{\square}$	1.85
V_{Ga}^{2-}	5.58	Cu_{Ga}^{-}	2.34
V_{Ga}^{3-}	7.14	Cu_{Ga}^{2-}	3.57
$V_S^{\square}$	2.35		
V_S^{+}	2.96		
V_S^{2+}	2.38		

The incorporation of transition metals leads to the formation of extrinsic defects. However, calculated defect formation energies for extrinsic defects in $CuGaS_2$ are only available for one of the proposed transition metals. The formation energies of a manganese defect in $CuGaS_2$ are $\Delta E(Mn_{Ga})$=0.43eV and $\Delta E(Mn_{Cu})$=0.80eV [35]. As consequence, manganese is supposed to be preferentially incorporated at the cation site 4b.

1.4 Substitution of transition metals

The incorporation of transition metals in the $CuGaS_2$ chalcopyrite type compound leads to a systematic change in chemical composition. The general substitution behavior can by derived from these trends. In the first step, the substitution behavior can be divided into unilateral and coupled. The coupled substitution refers to the replacement of copper and gallium by a transition metal. This keeps the copper to gallium ratio (Cu/Ga) constant and increases the copper to gallium plus transition metal ratio (Cu/(Ga+TM)) with increasing transition metal content, as shown in Figure 7.

The unilateral substitution can be divided into a replacement of either copper or gallium by a transition metal. With a unilateral substitution of gallium, the Cu/Ga ratio is supposed to increase, while the Cu/(Ga+TM) ratio is constant with increasing amount of transition metals. In the case of a unilateral substitution of copper, the Cu/Ga ratio and the Cu/(Ga+TM) ratio decrease.

The actual substitution depends on the charge of the incorporated transition metal ion. Oddly charged ions are supposed to result in a unilateral substitution of copper (univalent) or gallium (trivalent), while even charged ions are supposed to result in a coupled substitution. Combinations are possible and will be considered if required. Another very important ratio is the cation to anion ratio or metal to sulfur ratio (M/S). From this ratio, the concentration of vacancies or interstitials can be derived. In addition, the charge of the incorporated transition metal ion can be concluded by the substitution behavior.

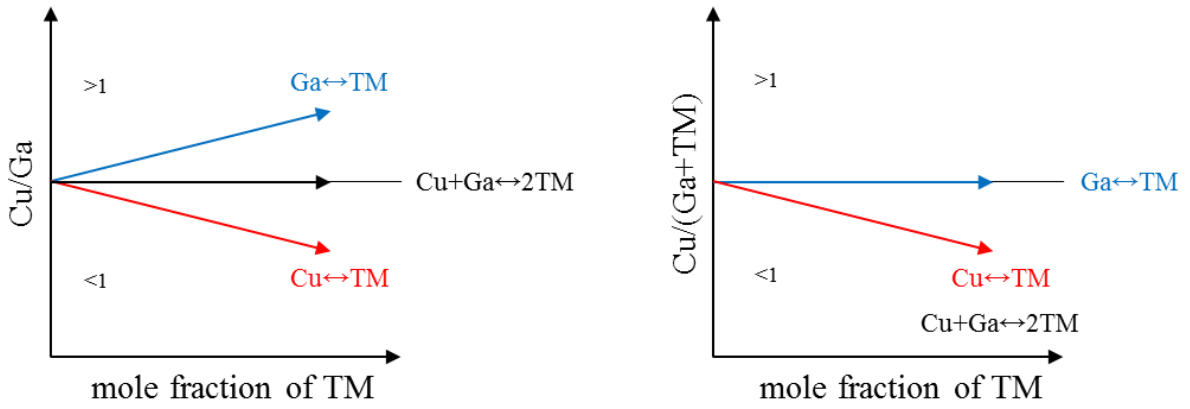

Figure 7 - Evolution of the Cu/Ga ratio (left) and the Cu/(Ga+TM) ratio (right) resulting from its specific substitution as function of the transition metal (TM) content. The black arrow refers to a coupled substitution, whereas the blue and red refer to a unilateral substitution of the transition metal with copper (red) or gallium (blue).

The substitution of copper by divalent or trivalent transition metal ions ($2Cu^{+}\leftrightarrow TM^{2+}$, $3Cu^{+}\leftrightarrow TM^{3+}$) leads to a decrease in the M/S ratio, as shown in Figure 8 and also leads to the formation of vacancies. When gallium is substituted by divalent transition metal ions ($Ga^{3+}\leftrightarrow TM^{2+}$), the M/S ratio decreases and interstitials occur. However, if gallium is substituted by trivalent transition metal ions ($Ga^{3+}\leftrightarrow TM^{3+}$), the M/S ratio remains constant and no vacancies or interstitials occur.

With a coupled substitution of copper and gallium by divalent transition metal ions ($Cu^{+}+Ga^{3+}\leftrightarrow TM^{2+}$) the M/S ratio remains constant and there are neither vacancies nor interstitials. If the substituting transition metal is trivalent ($Cu^{+}+Ga^{3+}\leftrightarrow TM^{3+}$), the M/S ratio decreases and vacancies are formed.

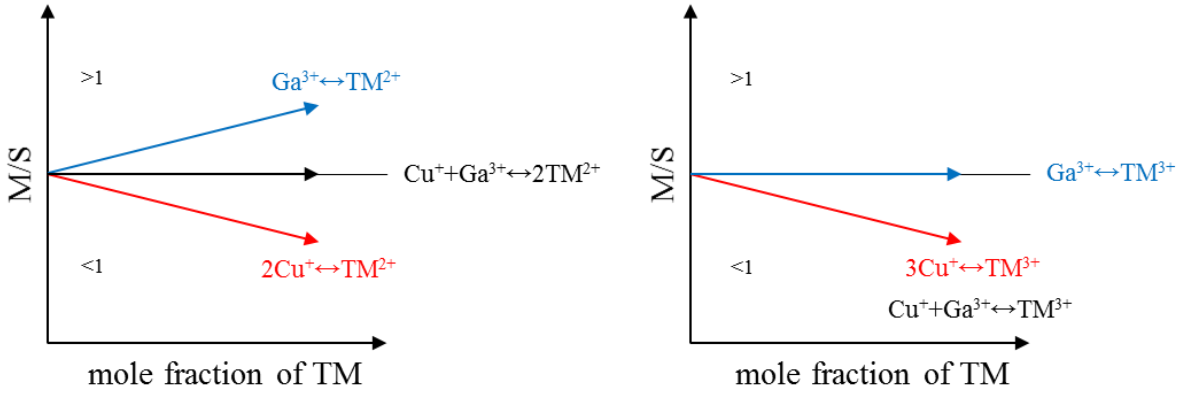

Figure 8 - Evolution of the M/S ratio resulting from its specific substitution as function of the transition metal (TM) content with respect to the charge of the transition metal (divalent- left; trivalent-right). The black arrow refers to a coupled substitution, whereas the blue and red refer to a unilateral substitution of the transition metal with copper (red) or gallium (blue).

Univalent as well as ions with a charge of more than 3+ were not considered because all transition metals investigated are supposed to be either di- or trivalent.

Table II - Sulfide Crystal Radii from Shannon [36]; LS-low spin; HS-high spin.

ion	coordination number	crystal radius [Å]
Cu^{+}	IV	0.635
Ga^{3+}	IV	0.580
Cr^{2+}	VI	0.90
Cr^{3+}	VI	0.705
Cr^{4+}	VI	0.64
Fe^{2+}	IV	0.66
Fe^{3+}	IV	0.555
Mn^{2+}	IV	0.725
Mn^{3+}	VI	0.770
Mn^{4+}	VI	0.62
Ni^{2+}	IV	0.53
Ni^{3+}	VI LS	0.66
	VI HS	0.70
Ni^{4+}	VI LS	0.56

2. Phase relations

In order to successfully synthesize pure chalcopyrite type phase powder samples, a fundamental knowledge of phase relations is necessary. By adjusting the synthesis conditions several secondary phases can be avoided, e.g. changing the maximum synthesis temperature. Furthermore, the knowledge concerning stabile secondary phases is helpful to analyze multiphase powder samples.
This chapter will show all binary phase diagrams needed for this study. The maximum synthesis temperature is in the region of 900°C to 950°C with an error of less than 5°C.

2.1 The Cu-Ga-S ternary system

The stability region of the chalcopyrite type phase, within the copper-gallium-sulfur phase diagram, is comparatively small to other ternary phases (Figure 9). In general, the stability region is stretched by three extrema with the shape of a boomerang. Extrema I is the lower edge, with a maximal copper content of ~25.3mol% and a minimal sulfur content of ~49.5mol%. The maximal gallium content in the chalcopyrite compound is reached at ~26.6mol% in the second extrema (II) and a copper content of ~22.4mol%. The remaining extrema (III) represents the composition with the maximum sulfur content of ~54.7mol% and the minimum gallium content of ~22.4mol%. Summarized, the chemical composition of the chalcopyrite type phase can have a copper content of 22.4-25.3mol%, a gallium content of 22.4-26.6mol% and a sulfur content of 49.5-54.7mol%. Based on the phase diagram possible intrinsic defects can be assumed from the chemical composition of the chalcopyrite type phase. In the direction of extrema I probable defects are sulfur vacancies, gallium interstitials and copper on gallium anti-sites. The major defect towards the direction of extrema II and III are V_{Cu}. In addition to vacancies, anti-site defects are formed, Ga_{Cu} for extrema II and Cu_{Ga} for extrema III.
Besides several binary phases within this phase diagram, two ternary phases are reported [37, 38]. On the one hand the $CuGa_5S_8$ phase which crystallizes in zinc blende type structure [38, 39] and on the other hand the $CuGa_3S_5$ phase which crystallizes in a different cubic structure [37]. These two phases are commonly known as ordered vacancy compounds (OVC) or ordered defect compounds (ODC). Recent results show, the $CuGa_3S_5$ as well as the $CuGa_5S_8$ phase crystallize in the stannite type structure [40, 41]. However, a record in the Inorganic Crystal Structure Database (ICSD) is still not available.

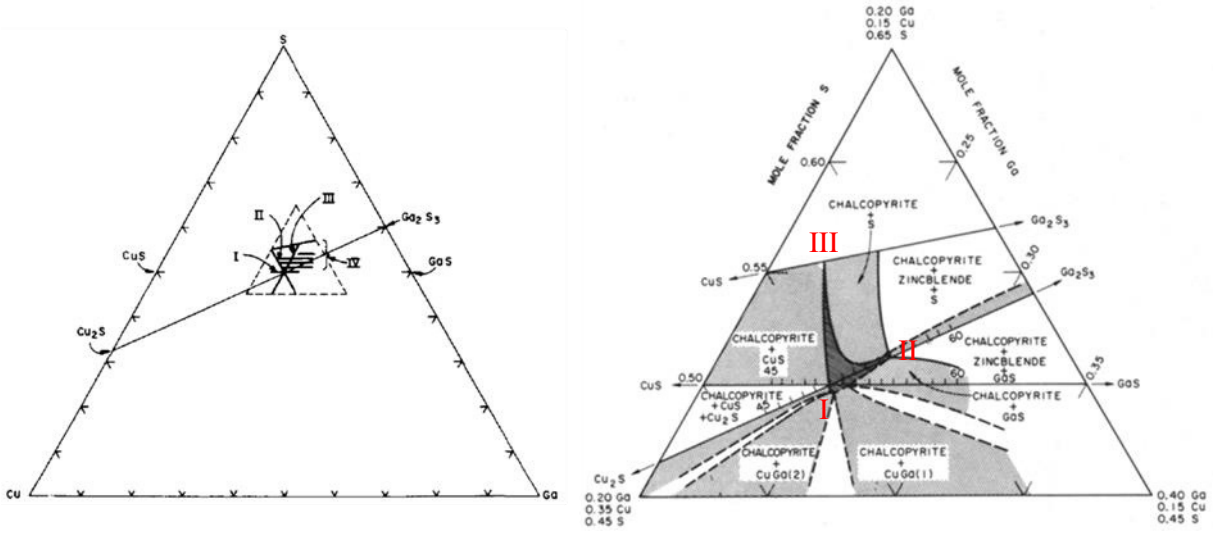

Figure 9 - Schematic illustration of locations of the ternary isopleths examined by DTA and Guinier diffraction in the ternary phase field surrounding copper gallium sulfide (left). Ternary phase fields around copper gallium sulfide as determined in this investigation at room temperature by Guinier x-ray diffraction (right). Chalcopyrite phase denoted by cross-hatched area [39].

Cu-S

The Copper-Sulfur phase diagram (Figure 10) is characterized by liquid phase separation. Considering the maximum synthesis temperature of 950°C, a liquid phase can exclusively be observed at the sulfur rich side which is separated into two liquid phases. While cooling the system, Digenite (Cu_9S_5) will occur at 813°C in a monotectic reaction. Digenite (Dg) crystallizes in the trigonal system (space group $R\bar{3}m$) [42] or cubic system (space group $Fm\bar{3}m$), its sulfur content can vary from ~32.9at% to 36.6at%. At 507°C a peritectic reaction of digenite and liquid take place where Covellite is formed. Covellite has the chemical formula CuS, crystallizes in the hexagonal space group $P6_3/mmc$ and can be very easily detected by the characteristic blue color in reflected-light microscopy.

On the copper rich side, the first reaction to point out takes place at 435°C. The solid copper and Digenite react to βCh (Chalcocite) with a stoichiometric composition of Cu_2S. Reported are a monoclinic $P2_1/c$ and a hexagonal $P6_3/mmc$ structure [43], whereas the monoclinic type is stable at temperatures below 103.5°C. In addition to the phases mentioned before, two more phases occur due to peritectoid or eutectoid reactions at temperatures below 100°C. Djurleite ($Cu_{31}S_{16}$) can occur in different orthorhombic structures (space groups $Pmnm$, $P2nm$, $Pmn2$), whereas Anilite ($Cu_{1.75}S$) crystallizes exclusively in the orthorhombic structure (space group $Pnma$).

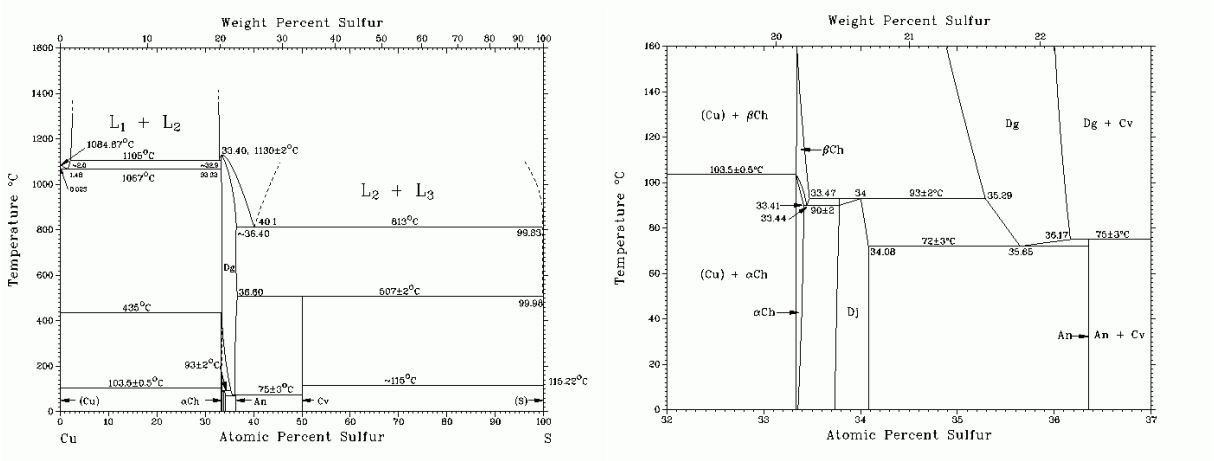

Figure 10 - Binary phase diagram of copper and sulfur with the phases Dg-Digenite, Ch-Chalcocite, An-Anilite, Cv-Covellite (left) [44]. Detail view into the copper - sulfur binary phase diagram within the sulfur range of 32-37at% (right) [44].

Ga-S

The gallium-sulfur system was already investigated in the 1930s, but some phases within this system are still not completely discovered. Phases like αGa_4S_5 and βGa_4S_5 were observed by several groups, but crystallographic information were not reported. The transition of βGa_4S_5 to αGa_4S_5 is supposed to take place at 900°C. Ga_2S_3 is the phase with the highest gallium content, three different modifications are shown in Figure 11 (left). At a temperature of 1020°C the wurzite type structure of γGa_2S_3 (space group $P6_3mc$) [45] changes into a monoclinic wurzite superlattice structure [46] which can either have space group $B11b$ [47] or $C1c1$ [48]. The monoclinic βGa_2S_3 transforms to the sphalerite type αGa_2S_3 (space group $F\bar{4}3m$) at 550-600°C.

Besides the pure gallium the last phase to consider is the hexagonal GaS (space group $P6_3/mmc$) [49] which is solid below temperatures of 1015°C. However, in the phase diagram one additional phase can be observed, but the Ga_2S phase can only be synthesized by sublimation [50].

Cu-Ga

The Cu-Ga phase diagram (Figure 11 (right)) is one of the most important diagrams for synthesizing chalcopyrite type $CuGaS_2$ from pure elements because of the large number of intermetallic compounds and alloys. The elements are forming intermetallic compounds very easily that become very resistant against sulfurization. From low gallium to high gallium content, the first phase is the fcc copper (space group $Fm\bar{3}m$) with a maximum of 20.6at% gallium at the peritectoid temperature of 620°C [51]. Pure copper is solid below temperatures of 1084°C and the melting temperature decreases with increasing gallium content [52]. In general, it can be seen, that an increase in gallium causes a decrease in melting temperature of the binary phases. The second phase is an intermetallic compound labeled as β (space group $Im\bar{3}m$), in which the gallium content varies between 19.3-27.5at% at temperatures between 915–616°C [53]. The maximum gallium content of the β phase is related to a peritectoid temperature of 836°C. By cooling down the β phase below 620°C, a peritectoid reaction can be observed. The solid copper and β phase form the hexagonal ζ phase (space group *P6₃/mmc*). At 616°C the β phase reacts at the eutecticum to the ζ phase and the cubic γ phase (space group $P\bar{4}3m$). The ζ phases show only narrow chemical variation with gallium contents between 20.4-22.5at%. At a temperature of 322°C a transition from ζ to ζ' phase is suggested but not observed [54]. The γ phase (space group $P\bar{4}3m$) shows several temperature dependent phase transitions which have no impact on the crystallographic structure. The transitions are only related to an increase in vacancy concentration [55]. However, the four different γ phase modifications can have a broad chemical variability from 29.5-42.7at% Ga below temperatures of 836°C. The last intermetallic compound is the only stoichiometric compound in this phase diagram. $CuGa_2$ (υ) crystallizes at 254°C in a peritectic reaction of the liquid and γ_3 - modification within the tetragonal system (space group *P4/mmm*) [56], with an approximate homogeneity range of 64.6-66.67at% Ga. Finally, at the high gallium content of the binary phase diagram is gallium itself. Gallium crystallizes in the orthorhombic system (space group Cmca) and shows only very little or no solid solubility of copper [53].

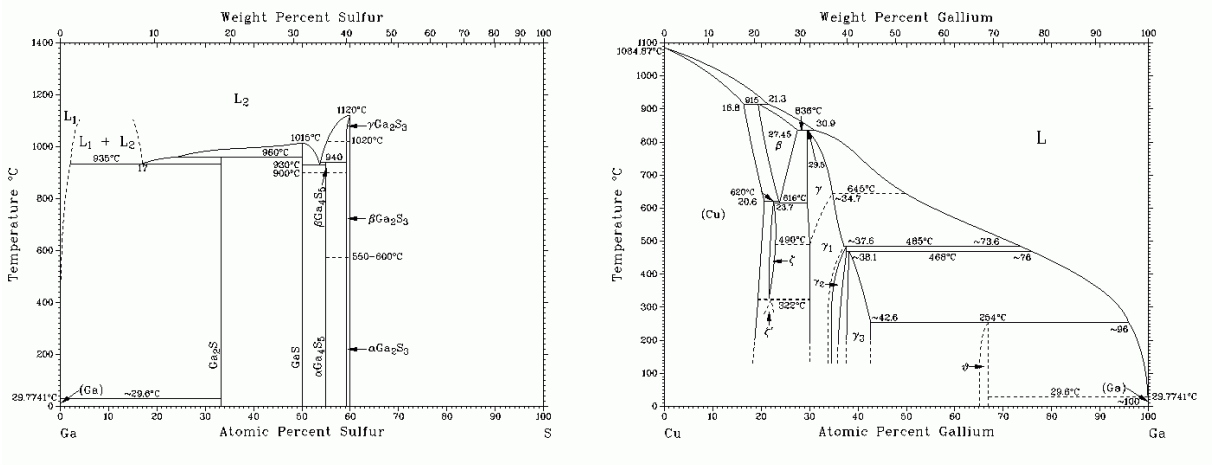

Figure 11 - Binary phase diagram of gallium and sulfur(left) [57]. Binary phase diagram of copper and gallium (right) [58].

2.2 Chromium related binary phase diagrams

Chromium crystallizes in the cubic space group $Im\bar{3}m$ [59]. Because of its high melting temperature of 1550°C it has to be considered as one of the secondary phases. In that case the further preparation needs to be done very carefully due to the high mechanical hardness of chromium.

Cr-S

The most conspicuous characteristic of this phase diagram is the liquid phase separation at very high temperatures. At temperatures above 1600°C three different liquid phases are reported and shown in Figure 12 (left). The second characteristic is the dense agglomeration of phases in the region of 49-62at% Cr. The most common phases in this binary phase diagram are the monoclinic $Cr_{1.03}S$ (C12/c1) [60], the NiAs structure type (space group *P63/mmc*) CrS and Cr_2S_3 [61, 62]. Cr_2S_3 can also occur as a rhombohedral modification [62]. Minor phases are the trigonal Cr_7S_8 (space group $P\bar{3}m1$) and Cr_5S_6 (space group $P\bar{3}1c$) [60]. All phases have a very narrow chemical variability except for CrS in its stability region between 1565°C and ~300°C. Within this area the chromium content can vary from 50at% to 59at%. Further phases are Cr_2S_5, Cr_5S_8 and Cr_3S_4, but the Cr_3S_4 phase is supposed to decompose below 1200°C. The Cr_5S_8 phase was only found by Sleight et al. [63], who used a synthesis temperature of 1200°C and 89kbar pressure. During decomposition of a Cr-S alloy the Cr_2S_5 compound can be observed between temperatures from 70°C to 300°C, depending on the external pressure [64].

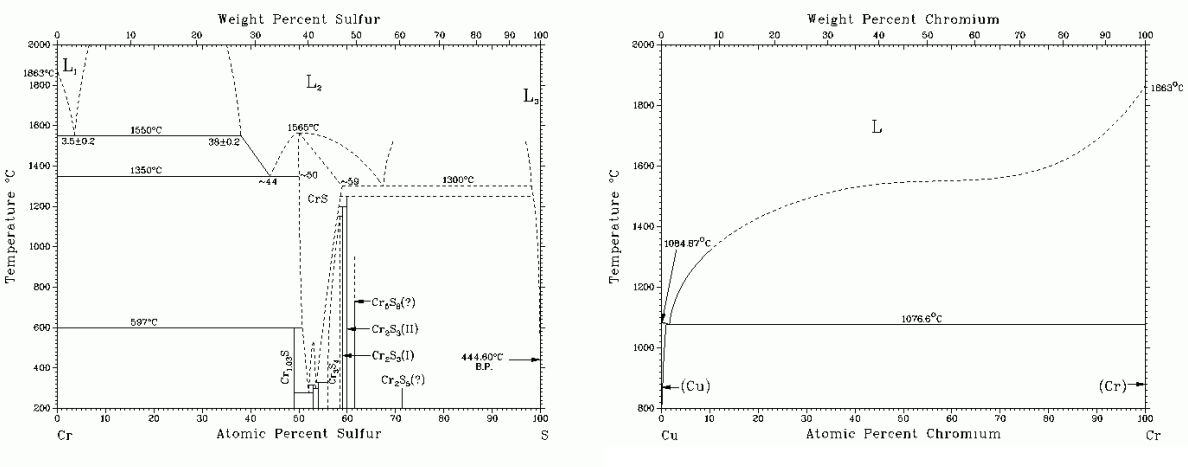

Figure 12 - Binary phase diagram of chromium and sulfur (left) [65]. Binary phase diagram of chromium and copper (right) [66].

Cr-Cu

The binary diagram of chromium and copper (Figure 12 (right)) is very simple. There are just the two endmembers as solid phases, copper with a maximum chromium solubility of 0.89at% at 1076.6°C and chromium with a negligible solubility of copper [66].

Cr-Ga

Besides the endmembers, four intermetallic phases can be observed within this binary phase diagram, shown in Figure 13. Chromium can be alloyed by gallium up to 16at% at 1620°C, vice versa the alloying is negligible. Starting from low gallium mole fraction the first phase is Cr_3Ga which crystallizes in the cubic space group $Pm\bar{3}n$ [67]. This phase is stabile up to a temperature of 1620°C as indicated by the phase diagram, but Bornand and Feschotte [68] reported a phase transition at 1100°C without mentioning the characteristic of this transition. CrGa is formed by a peritectic reaction at 879°C and crystallizes in trigonal space group $R\bar{3}m$ [69]. Gourdon et al. [69] reported the stability of CrGa against moisture and air of several month.
The gallium rich phases are Cr_5Ga_6 and $CrGa_4$. However, in literature three more intermetallic phases were reported [70-73] which are not described in this phase diagram. The first phase is the monoclinic Cr_3Ga_4 (space group *C2/m*) [70] which shows the same chemical composition as Cr_5Ga_6. About this phase no crystallographic information could be found. Very similar in terms of chemical composition to $CrGa_4$ shown in Figure 13 is $Cr_{1.25}Ga_{3.75}$. Both phases crystallize in space group $Im\bar{3}m$ [71, 72]. The third phase, $CrGa_3$, crystallizes in the cubic space group $Im\bar{3}m$ [73] as well.

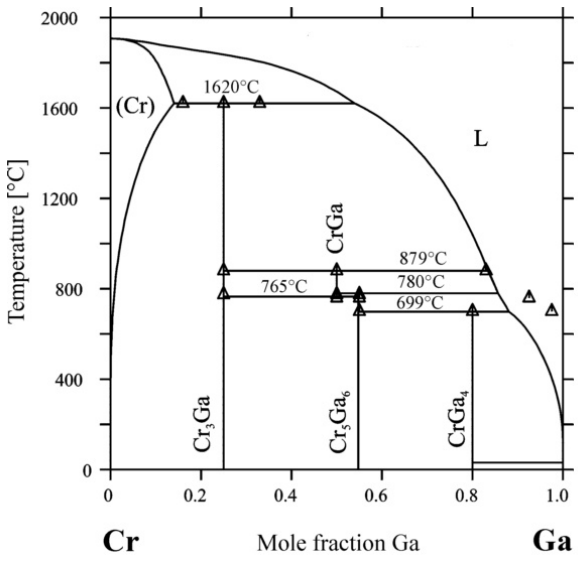

Figure 13 - Calculated binary phase diagram of chromium and gallium from Gröbner et al. [74] based on experimental data from Bornand and Feschotte [68].

2.3 Iron related binary phase diagrams

There are three polymorphs of iron documented, all crystallize in the cubic crystal system. The high-temperature δFe is stable within a temperature region from 1538°C to 1394°C. Decreasing the temperature leads to a structure change from bcc (body-centered cubic) to fcc (face-centered cubic). The new phase is called austenitic iron (γFe), with the space group $Fm\bar{3}m$. At 912°C the structure transforms back to bcc ferric iron (αFe). The α and δ iron crystallizes in space group $Im\bar{3}m$. [75]

Fe-S

The binary phase diagram can be divided into two groups. The first with 50-55at% iron represents the pyrrhotine group (FeS) and the second with 33.3at% iron represents the polymorphs Pyrite and Marcasite (FeS_2). The pyrrhotine group has the general chemical composition $Fe_{1-x}S$ and is characterized by subtraction defects (iron vacancies). Depending on temperature and pressure different structures are reported [76]. If the high temperature phase γFeS has an iron to sulfur ratio of 1 (no iron vacancies) it crystallizes in the hexagonal space group $P\bar{6}2c$ [77]. The stoichiometric phase is called Troilite which is stable in the temperature range between 1188°C and 315°C. Below this temperature, in the field of βFeS and αFeS, several structural modifications from monoclinic to hexagonal can occur [78].

The second group in this binary diagram is related to the chemical composition FeS_2. Pyrite is the high temperature (≤743°C) polymorph that crystallizes in the cubic space group $Pa\bar{3}$. By heating this phase higher than 570°C it transforms into Pyrrhotine [79]. The low temperature phase is called Marcasite which crystallizes in the orthorhombic space group *Pnnm* [78]. Marcasite is less stable than Pyrite, it decomposes after some years. By heating above 400°C a transformation to Pyrite takes place [79].

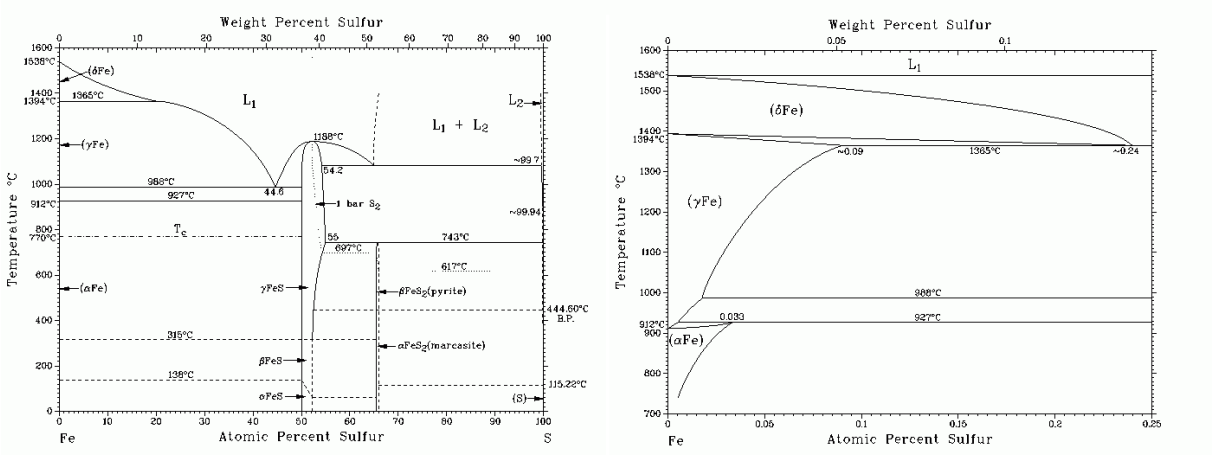

Figure 14 - Binary phase diagram of iron and sulfur (left) [80]. Detail view into the iron - sulfur binary phase diagram within the sulfur range of 0-0.25at% (right) [80].

Fe-Cu

In this binary diagram only the endmembers but no binary phases occur. As mentioned before, iron will exclusively occur as αFe, considering the synthesis process. The iron phase can be alloyed by 1.9at% Cu at the eutectic temperature of 850°C. The iron in copper content can be up to 4.6at% at a temperature of 1096°C. At the maximum synthesis temperature, the maximum solubility of iron in copper should be around 2at% Fe.

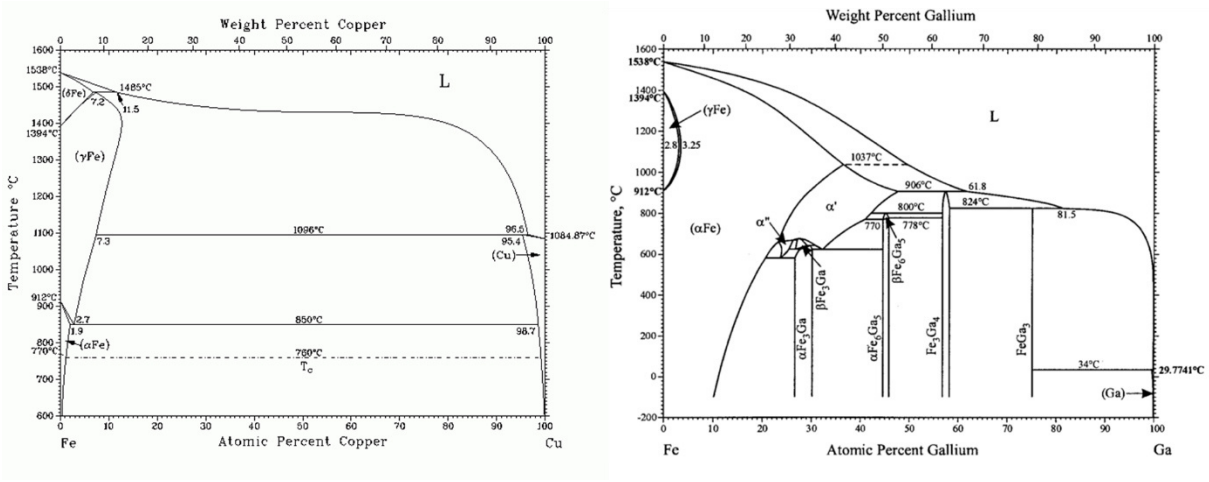

Figure 15 - Binary phase diagram of iron and copper (left) [81]. Binary phase diagram of iron and gallium (right) [82].

Fe-Ga

The intermetallic compounds in the Fe-Ga phase diagram are Fe_3Ga (α, β), Fe_6Ga_5 (α, β), Fe_3Ga_4 and $FeGa_3$ (Figure 15 (right)). The stability region of the hexagonal βFe_3Ga (space group *P6/3mmc*) [83] includes only 61°C, from 680°C to 619°C. At lower temperature the cubic αFe_3Ga (space group $Pm\bar{3}m$) [84] is stable. The scenario is similar for Fe_6Ga_5, but the stability range of βFe_6Ga_5 is even smaller (≤30°C). Below 770°C the trigonal βFe_6Ga_5 (space group $R\bar{3}mH$), in literature named as $Fe_{14}Ga_{12}$ [71], transforms to the monoclinic αFe_6Ga_5 (space group *C12/m1*) [85]. For the intermetallic compound Fe_3Ga_4 also two polymorphs were suggested by Köster and Gödecke [86], a monoclinic and a tetragonal. But only the monoclinic phase (space group *C12/m1*) [70] was confirmed by others and can be found in the database.

Besides the intermetallic compounds αFe can occur. The αFe phase can be alloyed by up to 20at% Ga. By incorporating more gallium into the αFe lattice, the αFe structure transforms to ordered α' and α'' [87]. The α phases are supposed to disappear while cooling. Literature reports α' to crystallize in space group $Pm\bar{3}m$ and α'' in space group $Pnma$ [80]. Kubaschewski [80] proposed a third α phase, which was not approved by other authors.

2.4 Manganese related binary phase diagrams

Manganese has four allotropes, all of cubic symmetry [88]. Below 727°C, αMn is stable. At higher temperatures, the $I\bar{4}3m$ αMn transforms to a $P432$ βMn which will transform to a $Fm\bar{3}m$ γMn at 1100°C. The last structural change takes place at 1138°C, when the $Im\bar{3}m$ δMn becomes stable. The melting temperature of manganese is at 1246°C [89].

Mn-S

In the binary phase diagram of manganese and sulfur only two phases are reported as stable, αMn and αMnS, both are solid at the maximum synthesis temperature of 950°C. The manganese mono-sulfide crystallizes in space group $Fm\bar{3}m$ [90]. MnS_2 crystallizes in space group $Pa\bar{3}$ [91] and is unstable with respect to αMnS and sulfur gas at 1bar [92], it can be synthesized only hydrothermally [93].

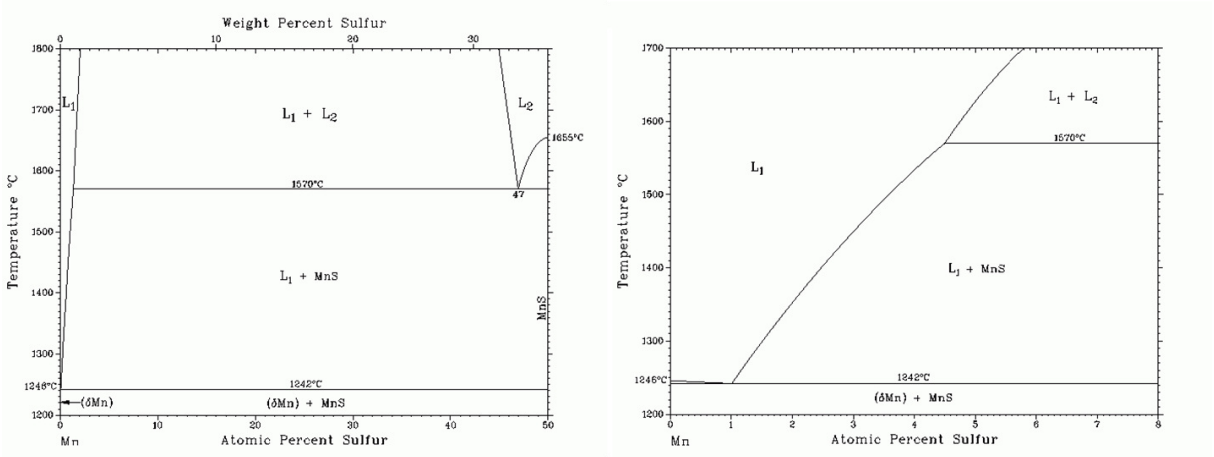

Figure 16 - Binary phase diagram of manganese and sulfur (left) [89]. Detail view into the manganese - sulfur binary phase diagram within the sulfur range of 0-8at% (right) [89].

Mn-Cu

Manganese and copper show full solubility (Cu, γMn) (Figure 17). Depending on the Cu/Mn ratio the solid mixture segregates between 1100°C and almost 450°C. While cooling, the Cu-Mn alloy becomes depleted in manganese and either the βMn type structure or αMn type structure is formed depending on the Cu/Mn ratio. However, below 707°C the βMn type structure is transformed into the αMn type structure. Two intermetallic phases (Cu_5Mn and Cu_3Mn) have been reported, but the crystal structure of both compounds is unknown [65].

Mn-Ga

The manganese-gallium phase diagram is very complex. In total 13 different phases are visualized in Figure 17 (right), whereas Meissner et al. [94] reported 16 different phases. Combining the binary diagrams from Lu [95] and Meissner [94], 15 phases remain, including gallium as well as four manganese modifications. Gallium shows almost no incorporation of manganese, whereas the manganese phases can be alloyed with more than 40at% gallium (δMn). This alloy is only stable at temperatures of more than 715°C, below it segregates to the λ and γ phases. The βMn can incorporate 8-19at% Ga which stabilizes the structure in so far as the phase becomes stable down to ambient conditions. The αMn is stable as well and can be alloyed by approximately 2at% Ga. The first phase not mentioned by Lu [95] is the $MnGa_6$ phase which is supposed to occur below 340°C. The crystal structure determination was incomplete, it crystallizes either in space group Ccc2 or Cccm [94].
Furthermore, some of those phases, e.g. the ω phase, is reported to crystallize in two different crystal systems, depending on their chemical composition. The slightly gallium depleted $MnGa_{4.96}$ crystallizes in the tetragonal system (space group $P4/mnc$) and the more gallium depleted $MnGa_{4.83}$ crystallizes in the triclinic system ($P\bar{1}$). The stoichiometric compound $MnGa_4$ (ϕ phase) crystallizes in the cubic space group $Im\bar{3}m$ [96]. Below 480°C the χ phase (Mn_2Ga_5) is stable. It has to be pointed out, that the chemical composition of those phases (ω, χ) is slightly different compared to those from Figure 17 (right). In the chemical region between 40-50at% Mn two phases are reported, the high temperature λ phase which crystallizes in space group ($R3m$) [73] and the low temperature η phase. The η phase can be divided into two phases, Mn_3Ga_5 and Mn_5Ga_7. For both compounds the crystal structure could not be identified yet [65]. A much higher chemical variety than all mentioned phases before can be observed from the γ phases, in total 55-100at% Mn. The γ_1 phase crystallizes just as the γMn in space group $Fm\bar{3}m$, which is not shown in the diagram due to the very small thermal stability range of 38°C. The γ_2 phase crystallizes in space group $I4/mmm$, the γ_3 phase and the ε phase crystallize in space group $P4/mmm$ [65].

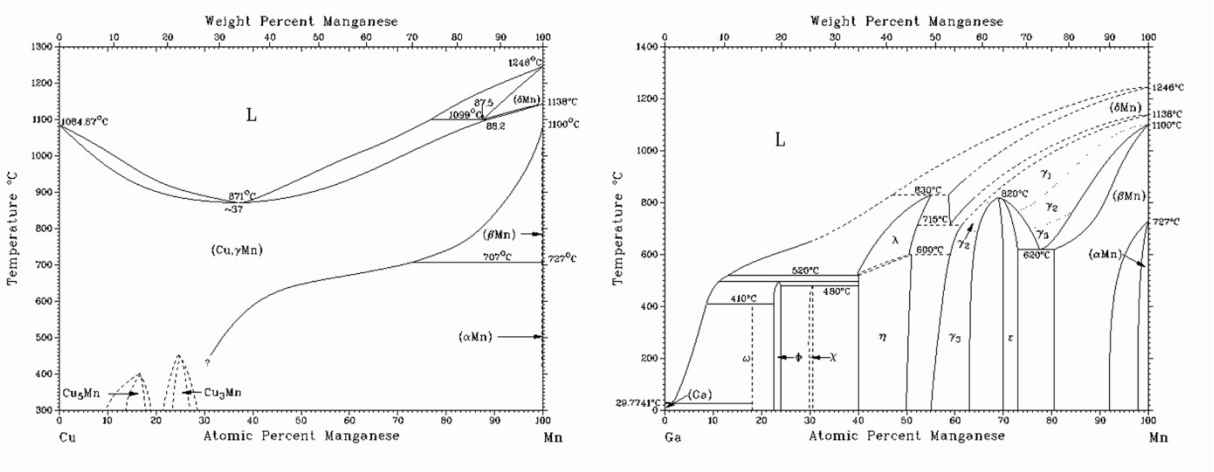

Figure 17 - Binary phase diagram of manganese and copper (left) [94]. Binary phase diagram of manganese and gallium (right) [95].

2.5 Nickel related binary phase diagrams

Nickel is one of the elements which do not have polymorphs. Below 1455°C it starts to crystalize in the cubic space group $Fm\bar{3}m$ [97].

Ni-S

Besides the endmembers, five phases need to be considered. The β phase reacts at temperatures below 600°C either to nickel and Ni_3S_2 or Ni_3S_2 and Ni_7S_6 depending on the chemical composition. Ni_7S_6 reacts at around 400°C to Ni_3S_2 and the cubic Ni_9S_8 (space group $I\bar{4}2d$) [98]. The Ni_3S_2 compound crystallizes in space group $R32$ and is known as Heazlewoodite [99]. The δ phase, named Nickelin (NiS), reacts at temperatures below 350-300°C to Millerite (NiS) and Polydymite (Ni_3S_4). Millerite crystallizes in space group $R\bar{3}m$ [100] and Ni_3S_4 in space group $Fd\bar{3}m$ [101].

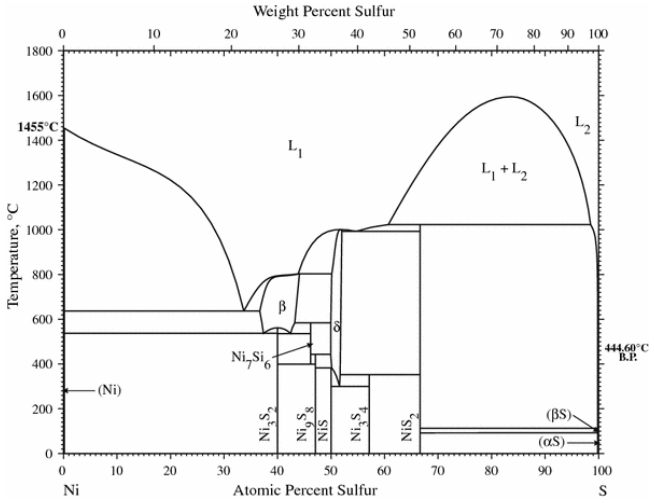

Figure 18 - Binary phase diagram of nickel and sulfur [102].

Ni-Cu

A full miscibility of nickel and copper is only existing at temperatures above 354.5°C. Below this temperature, a phase segregation takes place. The temperature for the phase segregation depends on the chemical composition of the solid alloy.

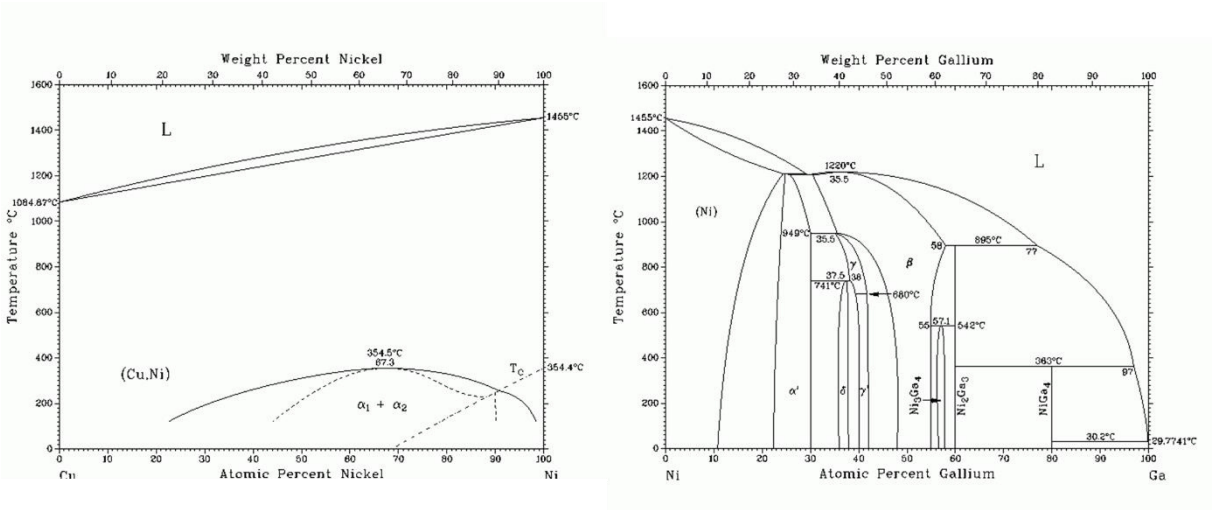

Figure 19 - Binary phase diagram of nickel and copper (left) [103]. Binary phase diagram of nickel and gallium (right) [104].

Ni-Ga

Nickel can be alloyed with almost 18at% Ga at maximum synthesis temperature (950°C). Gallium, on the other hand, shows no incorporation of nickel into the structure. The melting temperatures follows a similar trend than all melting temperatures of other binary diagrams with gallium, with increasing gallium content decreasing melting temperatures are observed. Phases which can be synthesized by solid state reaction are the α′, β and γ phase. In contrast to the γ phase, the α′ and β phase (space group $Fm\bar{3}m$) can be preserved during synthesis. At 741°C γ reacts (peritectoid) with the α′ phase to the monoclinic δ phase (space group $Cmmm$) [65] or undergoes a phase transition at 680°C to γ′. The γ′ phase is supposed to crystallize in a NiAs superstructure [105]. Besides these phases, three more phases need to be mentioned: Ni_3Ga_4, Ni_2Ga_3 and $NiGa_4$. All crystallize due to peritectic reactions, Ni_2Ga_3 (space group $P\bar{3}m1$) at 895°C and Ni_3Ga_4 (space group $Ia3d$) at 542°C. $NiGa_4$ (space group $I\bar{4}3m$) is formed at 363°C during the reaction of Ni_2Ga_3 with the liquid phase [104].

2.6 Summary – phase diagrams

Besides the three elemental phases copper, gallium and sulfur, 9 further phases can occur during synthesis within the ternary Cu-Ga-S phase diagram. The most of them are displayed in the Cu-S binary phase diagram. These phases are Djurleite ($Cu_{31}S_{16}$), Anilite (Cu_7S_6), Chalcocite (Cu_2S), Covellite (CuS) and Digenite (Cu_9S_5). Two more phases each need to be considered from the other two binary phase diagrams of the main chalcopyrite type compound, Ga_2S_3 and GaS as well as the γ and υ Cu-Ga intermetallic compound.

By introducing chromium six more phases can occur, including elemental chromium. Two chromium sulfides (CrS, Cr_2S_3) and three Cr-Ga intermetallic compounds (Cr_3Ga, $CrGa_3$, $CrGa_4$) which can be synthesized with respect to the synthesis conditions.

The number of additional phases due to the introduction of iron is the same as for chromium. The αFe is the only elemental iron polymorph which need to be considered. From the Fe-S binary phase diagram only Pyrrhotine ($Fe_{1-x}S$) occurs. From the Fe-Ga binary phase diagram four intermetallic compounds (αFe_3Ga, αFe_6Ga_5, Fe_3Ga_4, $FeGa_3$) can occur.

The same number of additional phases need to be considered due to the introduction of manganese. Three manganese polymorphs can occur in total, elemental αMn, βMn which can be stabilized by gallium alloying as well as γMn which can be stabilized by copper alloying. αMnS is the only sulfide phase which can occur with respect to the synthesis conditions as well as two intermetallic compounds (ε, γ_3 Mn-Ga).

The most binary phases, that need to be considered as secondary phases, can occur due to an introduction of nickel, in total 14. Elemental nickel, which can be alloyed with copper additionally, five nickel sulfides and seven Ni-Ga intermetallic (α´, γ´, δ, β, Ni_3Ga_4, Ni_2Ga_3, $NiGa_2$) can occur. The nickel sulfides are Heazlewoodite (Ni_3S_2), Millerite (NiS), Polydymite (Ni_3S_4), Vaesite (NiS_2) and Ni_9S_8 that need to be considered.

In total seven elemental and 37 binaries can occur in the powder samples as secondary phases, consisting of 18 intermetallic compounds, three alloys and 16 sulfides.

Table III - Overview of all possible phases according to the relevant binary phase diagrams and the Cu-Ga-S ternary phase diagram discussed in this chapter.

copper	gallium	sulfur	
I	III	VI	elemental
I-III	I-VI	III-VI	
~2:1 1:2	31:16 2:1 9:5 7:6 1:1	2:3 1:1	binary
	I-III-VI		
	1:1:2 1:3:5 1:5:8		ternary

copper	gallium	sulfur	
Cr-I	Cr-III	Cr-VI	
	3:1 1:3 1:4	1:1 2:3	+ chromium
Fe-I	Fe-III	Fe-VI	
	3:1 6:5 3:4 1:3	1:1-1.1	+ iron α
Mn-I	Mn-III	Mn-VI	
	3:2 5:2	1:1	+ manganese α, β, γ
Ni-I	Ni-III	Ni-VI	
	3:1 5:3 3:2 1:1 3:4 2:3 1:4	3:2 9:8 1:1 3:4 1:2	+ nickel

3. Experimental

The chapter is concerned with the synthesis of the powder samples as well as the prior selection of the initial composition to guarantee reproducibility.

3.1 Selection of initial weight

The main focus of this work is the determination of the practical solubility limits of certain transition metals into the $CuGaS_2$ chalcopyrite type structure. For some elements there were already calculations such as chromium and titanium [31] or experimental data on similar compounds [106]. According to this, powder samples from the pseudo-binary section of the ternary $CuGaS_2$ chalcopyrite and the binary metal sulfide (chromium Cr_2S_3, manganese MnS and nickel NiS) were synthesized.
The second substitution series refers the proposed substitution for an intermediate band absorber material. Theoretical calculation predict the intermediate band due to the replacement of some gallium atoms by transition metals [23]. Those samples were synthesized along the pseudo-binary section of $CuGaS_2$ and $CuTMS_2$. The most promising candidate, based on first experiments, is manganese. In addition, iron was promising due to the natural existents of $CuFeS_2$. An overview of the studied systems as well as the corresponding chemical equations are listed in Table IV.

Table IV - Overview of studied systems and their corresponding pseudo-binary section. Y indicates the area of variation or as a first approximation the transition metal content within the pseudo-binary section.

transition metal	pseudo-binary section	y
Cr^{3+}	$3(CuGaS_2)_{1-y} - 2(Cr_2S_3)_y$	0.02-0.2
Mn^{2+}	$(CuGaS_2)_{1-y} - 2(Mn^{II}S)_y$	0.01-0.25
Ni^{2+}	$(CuGaS_2)_{1-y} - 2(Ni^{II}S)_y$	0.05-0.2
$Mn^{2+/4+}$	$(CuGaS_2)_{1-y} - \left("CuMn^{\Sigma III}S_2"\right)_y$	0.02-0.5
Fe^{3+}	$(CuGaS_2)_{1-y} - (CuFe^{III}S_2)_y$	0.05-0.7

3.2 Synthesis route

Powder samples studied in this work were synthesized by solid state reaction of pure elements in evacuated and sealed silica tubes. The used elements had a purity of at least 99.99%. The synthesis route for chalcopyrite powder samples was adapted from Schorr et al. [107]. At first the initial weight for every single element was calculated according to their explicit chemical composition. Afterwards the elements were weighted with an accuracy of ± 0.0005g, placed in a pyrolytic graphite boat and inserted in a quartz glass tube. A quartz glass plug was used to close the tubes. Further, the tube was connected to a vacuum pump. To keep the reaction volume equal for all samples, the plug was regularly positioned in the same distance from the bottom of the tube. With a vacuum pump the tube was evacuated to a pressure of $3*10^{-5}$mbar and sealed with a H_2/O_2 flame. Thereafter the ampules were placed in a tubular furnace and slowly heated up to a maximum synthesis temperature with intermediate temperature steps. The first synthesis step heating treatment is illustrated in Figure 20 (a). If the first synthesis step was successful, the ampule was cracked and the reacted sample was ground in an agate mortar. Samples with chromium were ground in a tungsten carbide mortar with a much higher Mohs hardness than an agate mortar. In order to guarantee a complete sulfurization of the metal pieces, 0.1g excess sulfur was added to each sample. Afterwards, the powder samples were pressed into pellets. The pellets were transferred into pyrolytic graphite boats, placed in quartz glass tubes, evacuated and sealed as in the step before. Within the homogenization heat treatment, the sample can be heated faster than in the first synthesis step and without intermediate steps as illustrated in Figure 20 (b). The homogenization was repeated a second time, but without adding additional sulfur. Subsequent to the complete synthesis procedure the pellets were ground to powder and could be further examined. During this study various synthesis temperatures were tested to minimize the amount of secondary phases, in detail only the third and fourth temperature step were modified. The exact experimental details of each sample series are listed in Table V.

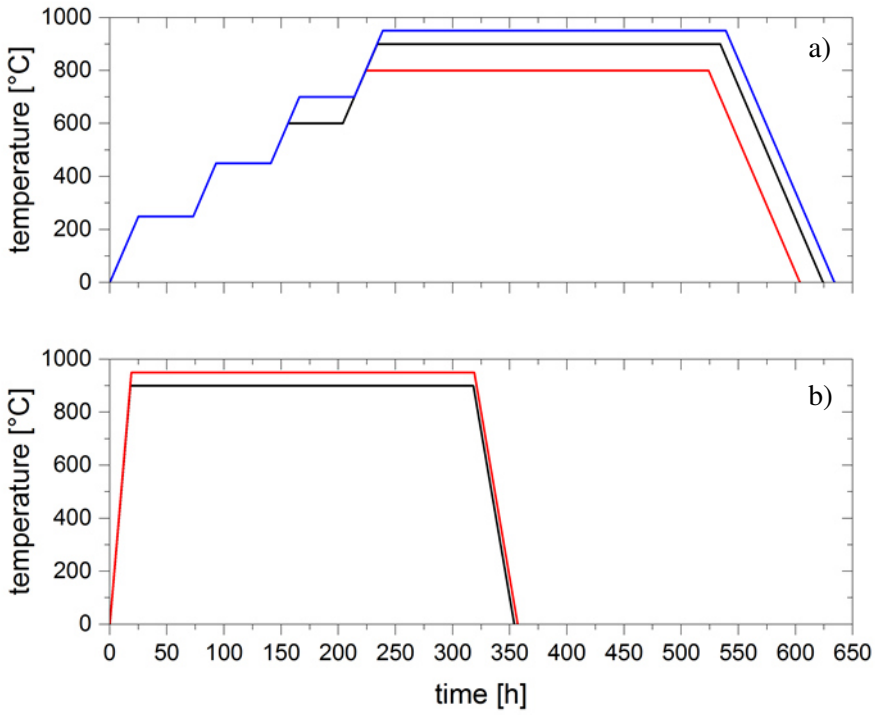

Figure 20 - Schematic temperature profiles of the first synthesis step (a) and the homogenization step (b). The different color code does not represent specific sample series, it is only a matter of visualization.

Table V - Detailed overview of experimental series and their synthesis temperature profile.

system	sample description	1st synthesis temp. [°C]	homogenization temp. [°C]
Chp - Cr_2S_3	Cr-I-I	600/900	900
	Cr-I-II	700/950	950
Chp - MnS	Mn-I-I	600/900	900
	Mn-I-II	700/800	900
	Mn-I-III	700/950	950
	Mn-334	I-600 II-700/950	950
Chp - NiS	Ni	700/900	950
Chp - "$CuMnS_2$"	Mn-X-I	600/900	900
	Mn-X-II	700/950	950
Chp - $CuFeS_2$	Fe	700/950	950

Figure 21 is showing photographs of a sample within the different synthesis stages, starting from the weighted elements (a), after first synthesis (b), after first homogenization (c) and final sample before grinding (d).

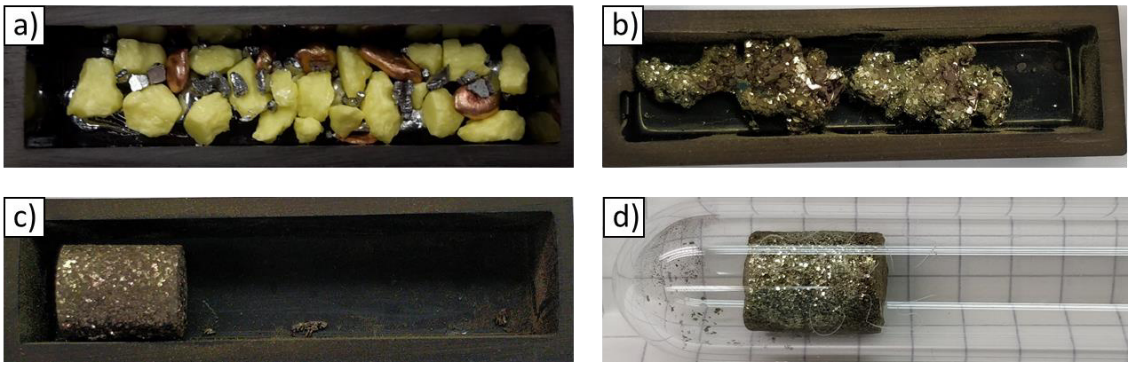

Figure 21 - Photographs of a sample from the iron series during preparation, a) weighted elements before first reaction, b) after first reaction, c) after first homogenization and d) final pellet before grinding.

3.3 Analysis techniques

The chapter is concerned with used analysis techniques to investigate the powder samples, especially referring the measurement conditions and details, respectively to guarantee reproducibility.

3.3.1 Electron microprobe analysis

In order to correlate the structural parameters of the compounds to each other, a determination of the exact chemical composition is mandatory. Therefore, the sample composition was ascertained by wavelength dispersive X-ray (WDX) spectroscopy using a JEOL-JXA 8200 electron probe micro analyzer (EPMA). In an electron microprobe an electron beam, exited by a tungsten wire, hits the sample were the contained elements emit characteristic X-rays amongst others [108]. These characteristic X-rays were diffracted by a crystal, with a specific lattice distance which is placed at the position on the Rowland Circle were Bragg´s law is fulfilled regarding the probed characteristic X-rays wavelength and a detector collects the signal [108]. Five spectrometers, with one or two crystals, are placed around the sample stage to measure at maximum five different elements at the same time. Elemental standards for copper, chromium, nickel, iron and manganese as well as GaAs and CuFeS were used to calibrate the WDX system. 25 lines of each ten points were positioned on grains of the supposed chalcopyrite typ phase at two different regions of the sample. With a total number of 500 points per sample the statistic is sufficient to give reasonable chemical composition of the probed material. In addition to that, measurements on secondary phases were performed with less statistics compared to the chalcopyrite type phase.

A special sample preparation is necessary in order to perform a proper WDX analysis. Therefore, a small amount of ~0.1g was embedded in epoxy and mechanically sanded and polished to obtain a very smooth surface, which is necessarily needed for reliable data.

The acquired data was averaged and normalized to the chalcopyrite type formula or rather to a sum of one sulfur per formula from atomic percent.

To normalize the chemical composition of the secondary phases, a phase with similar chemical ratios must first be found in the phase diagrams or literature and then the chemical composition is normalized to this specific formula.

3.3.2 X-ray diffraction

Powder X-ray diffraction (XRD) was performed in order to determine the lattice parameters of the chalcopyrite type phase and to obtain structural trends due to the incorporation of different transition metals. The method is based on Bragg´s law [109],

$$n\lambda = 2 * d_{hkl} * \sin\theta \quad (4)$$

with n as the order of reflection, λ as wavelength, d_{hkl} as distance between specific lattice planes and θ as diffraction angle. The incoming radiation hits the sample, with a certain angle θ and gets diffracted at the electron shells. In case of a constructive interference ($n \in \mathbb{N}$) a Bragg peak can be observed and the lattice plane spacing can be calculated. The received diffraction pattern is phase specific, the peak positions and the intensity of the peaks are given by the crystallographic structure [110]. The samples, except for iron containing samples were measured using a Panalytical MPD operating with copper radiation and a PIXcel line detector. Iron containing samples were measured using a Panalytical Empyrean operating with copper radiation and an energy dispersive PIXcel line detector to cut off possible fluorescence effects of the iron. The measurements were performed in Bragg Brentano geometry, were the X-ray source and the detector move towards each other with the same speed. In order to improve statistics, a sample rotation was applied to the sample holder.

3.3.3 Neutron diffraction

In contrast to X-rays, neutron radiation interacts with the nucleus of the element. The scattering factor does not depend on the atomic number rather arbitrary, as shown in Figure 22. Using neutron diffraction (ND) it is possible to distinguish isoelectronic elements, e.g. copper and gallium which have the same scattering power for X-rays and cannot be distinguished by XRD [110]. Furthermore, the attenuation coefficient of the elements is much smaller for neutron radiation than for X-rays [110]. Resulting from that, samples can be measured in transmission, whereby the potential effect of a preferred orientation is minimized.

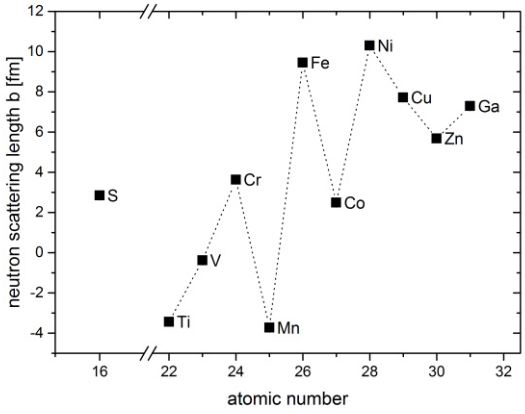

Figure 22 - Neutron scattering length b of relevant elements as function of atomic number after [111].

Neutron experiments were performed at the Fine Resolution Powder Diffractometer E9 (FIREPOD) [112] at Berlin Research Reactor II (BERII), a schematic drawing is shown in Figure 23. The neutrons from the reactor passes through an evacuated flight tube and hits a 19 Germanium composite plates with reflecting planes which is used as monochromator [112]. Depending on its orientation, a wavelength of λ=1.3084(2)Å from Ge(711), λ=1.7982(1)Å from Ge(511) and λ=2.8172(2)Å from Ge(311) can be chosen [112], λ=1.7982(1)Å was used in this case. The powder samples were placed in cylindrical vanadium containers with a diameter of 6mm and mounted on a room temperature sample changer. The measurement time for this kind of material is 4.5h reaching a maximum intensity of the main Bragg peak of at least $8x10^3$ counts.

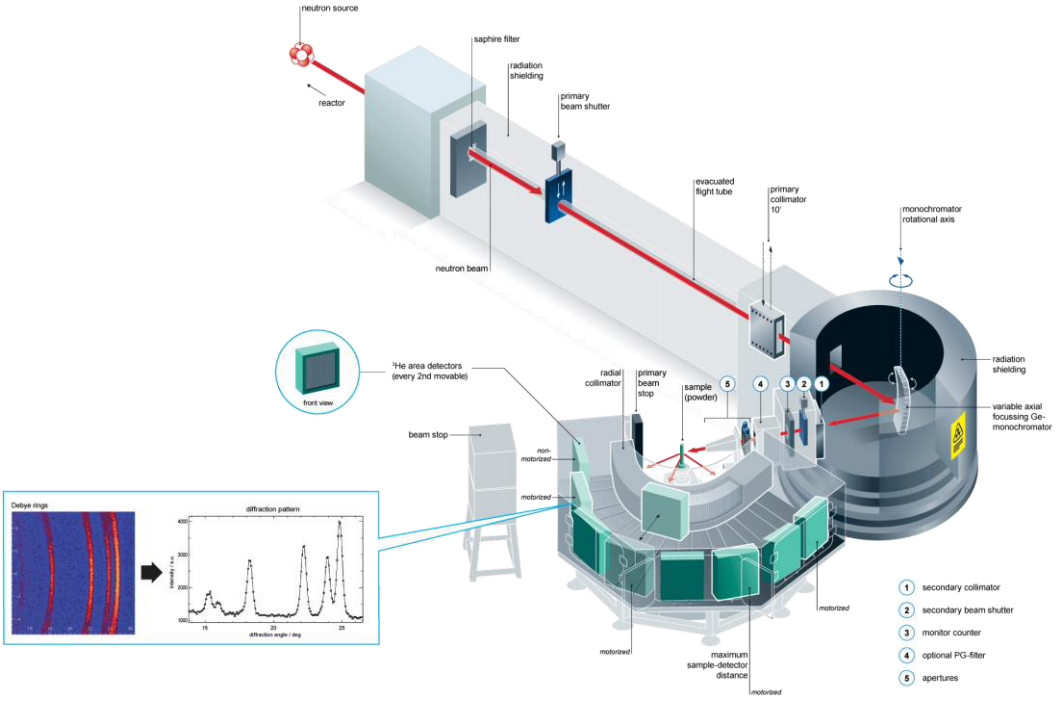

Figure 23 - Schematic drawing of E9 [112].

3.3.4 The Rietveld method

The Rietveld method is an empirical calculation to fit a simulated to an observed diffraction pattern based on the least square approach [113-115]. A given structure is adjusted in a way that the resulting pattern has a smaller deviation from the observed pattern than the calculation step before. In case of multi-phased samples, one structure per phase has to be adapted. The calculations were executed using the FullProf Suite 3.0 [116]. As peak-shape function the Thompson-Cox-Hastings pseudo-Voigt function convoluted with axial divergence asymmetry was chosen [117]. This formalism is used to calculate the shares of Gaussian and Lorentzian peak broadening. These two effects are formulated by the Caglioti function to calculate the full width at half maximum (FWHM) [118].
The peak broadening can have several reasons, which cause either a Gaussian (H_G) or Lorentzian (H_L) type of broadening. The Gaussian type of peak broadening is defined by:

$$H_G^2 = \left(U + (1-\xi)^2 D_{ST}^2(\alpha_D)\right)\tan^2\theta + V\tan\theta + W + \frac{I_G}{\cos^2\theta}$$

whereas the Lorentzian type of peak broadening is defined by:

$$H_L = \left(X + \xi D_{ST}(\alpha_D)\right)\tan\theta + \frac{[Y + (\alpha_Z)]}{\cos\theta}. \qquad (6)$$

The parameters V and W are exclusively attributed to a broadening caused by the instrument, notice that other parameters as well are influenced by the instrument. In order to include these values, all refinements were carried out using an instrumental resolution function. This function includes the instrumental broadening determined by the Rietveld refinement of a standard material, here lanthanum hexa-boride (LaB_6). The remaining parameters of the profile function can be either strain (U, α_D, X) or size (Y, I_G, α_Z) related. Depending on the strain model used, the functions $D_{ST}(\alpha_D)$ and $F(\alpha_Z)$ have different expressions. The Lorentzian contribution to strain is limited using the parameter ξ.
In order to guarantee comparable results, the order of the refined parameter was equal for all samples:

1. global parameters (scale factor, zero shift)
2. lattice parameters and background
3. profile parameter U and Y
4. anion parameter x
5. preferred orientation
6. temperature factor B_{ov}.

For Rietveld refinement of neutron diffraction data, the procedure was similar to that used for X-ray diffraction data. In addition, the temperature factors were refined for each position, as well as site occupancy factors:

1. global parameters (scale factor, zero shift)
2. lattice parameters and background
3. profile parameter U and Y
4. anion parameter x
5. temperature factor B_{iso} for 8d
6. site occupancy factors for 4a and 4b
7. temperature factor B_{iso} for 4a and 4b.

Usually, parameters that are once refined were also refined in the following refinement steps. However, often it is necessary to alternately refine parameters e.g. the temperature factors and the occupancy factors to avoid errors. For further details see the guideline of the Rietveld method by McCusker et al. [119].

3.3.5 Average neutron scattering length analysis method

The method of the average neutron scattering length analysis [120] is a mathematical approach of gaining the distribution of atoms in the crystal structure. Based on this, the defect concentration of all considered defects can be calculated. In order to apply this method, good quality neutron diffraction data is necessary and a proper Rietveld refinement has to be carried out. Using the Rietveld refinement, the site occupancy factors of the Wyckoff positions were determined. Those site occupancies refer to a distinct neutron scattering length. Deviations from the neutron scattering length of a certain position can occur due to vacancies as well as incorporation of other elements (e.g. anti-site defects) [120]. If a position is considered to be occupied by one element only (with a neutron scattering length of b_x) but actually occupied by a different element (with a neutron scattering length of b_y) or rather empty (V_a), the average neutron scattering length of this site $\bar{b}_a$ changes [120]. This correlation is given by equation (1):

$$\bar{b}_a = N_x * b_x + N_y * b_y. \quad (1)$$

with N_x, N_y referring to the fraction of the element on the regarded site [120]. By the Rietveld method using the FullProf Software [116] an site occupancy factor (SOF) is calculated from the powder pattern and used in equation (2):

$$\bar{b}_a^{exp} = SOF_a * b_x. \quad (2)$$

The measured average neutron scattering length $\bar{b}_a^{exp}$ is compared to the calculated average neutron scattering length $\bar{b}_a^{cal}$ which is simulated from the chemical composition [120]. Therefore, a precise chemical composition of the compound as well as a good knowledge of the possible defects is needed. On this basis the elements were distributed until the simultaneously calculated average neutron scattering length fits the measured average neutron scattering length. The chalcopyrite structure has two cation positions, 4a and 4b. In case of $CuGaS_2$, copper is supposed to occupy 4a and gallium 4b. Additionally, transition metals are incorporated and have to be distributed in equation (3) and (4):

$$\bar{b}_{4a}^{cal} = N_{Cu} * b_{Cu} + N_{Ga} * b_{Ga} + N_{TM} * b_{TM} \quad (3)$$

$$\bar{b}_{4b}^{cal} = N_{Cu} * b_{Cu} + N_{Ga} * b_{Ga} + N_{TM} * b_{TM}. \quad (4)$$

For the chalcopyrite structure only vacant 4a positions and no anion interstitials or anion anti-site defects (S_{4a} or S_{4b}) are considered based on the defect formation energies. Thus, the amount of vacancies is directly given by the chemical composition. If equation (5) becomes negative, cation interstitials need to be considered.

$$N_{V_{4a}} = N_{anion} - N_{cation} \quad (5)$$

The number of defects per cm^3 can be calculated by multiplying the fraction of the element on the regarded site with the multiplicity of the Wyckoff position, divided by the unit cell volume

$$V_{4a} = \frac{(4 * N_{V_{4a}})}{cell\ volume} \quad (6)$$

The values for the neutron scattering length of all elements and certain isotopes can be found in literature [111].

3.3.6 Photoluminescence spectroscopy

To address the optoelectronic properties photoluminescence spectroscopy was performed. It is a very powerful tool for probing the band structure of semiconductor materials. Therefore, a laser with a short wavelength points on the sample, which can be powders, thin films or crystals [121]. Thereby, electrons from the valence band are excited to the conduction band [121]. The electrons recombine to lower energy states in the valence band which results in the emittance of light, as shown in Figure 24 [121]. The emitted light has a certain wavelength, depending on the energy release which can be recorded by a detector [121].

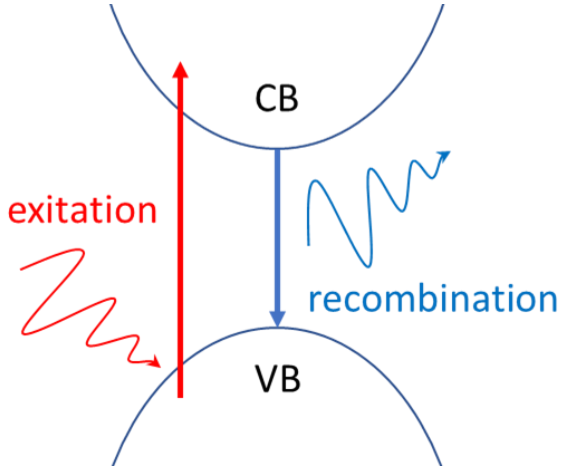

Figure 24 - Schematic representation of the excitation and relaxation processes of photoluminescence.

During recombination, the electrons can also be trapped into levels between valence band and conduction band [121]. Those levels are related to electronic active defects produced by structural defects, for example intrinsic and extrinsic point defect [121]. In case of chalcopyrite semiconductor materials, anti-site defects with copper occupying gallium positions and vice versa as well as interstitials and vacancies are possible. According to defect formation energies, gallium on copper anti-sites as well as copper vacancies are the common defects [34]. However, sulfur vacancies and copper on gallium anti sites are also typical whereas gallium vacancies are very unlikely. By incorporating transition elements additional extrinsic defects are created which can also be tracked by photoluminescence measurements. Those were performed using a 409nm laser at room temperature. In order to cover the whole range necessary for the $CuGaS_2$ bandgap and possible defect bands the laser light needed to be adjusted and two different detectors were used. At first step the laser light was reduced to 433nm to cover the range from 2.90eV to 1.59eV, at second 550nm were used with a range of 2.29eV to 1.38eV. The last step using the CCD camera the laser light was reduced to 700nm which covers a range of 1.80eV to 1.19eV. Afterwards the detector was changed to an InGaAs detector to record low energy signals of 1.55eV to 0.76eV using a wavelength of 800nm. Afterwards all single measurements were merged to receive a spectrum covering the whole range from 0.8eV to 2.6eV.

3.3.7 Superconducting quantum interference device

A superconducting quantum interference device (SQUID) is a magnetometer which is able to detect very small magnetic fields of up to 5aT [122]. It consists of a superconducting loop discontinued by an electronic isolating material, shown in Figure 25 [123]. Applying a direct current on the superconducting loop, enables pairs of bound electrons to tunnel through the isolating material [124]. This effect is known as Josephson Effect [125]. Therefore, the isolating material of the so-called Josephson junction has to be very thin in order to allow the Cooper-pairs to path through [124]. The occurring magnetic field is dependent on the current, while the magnetic flux is dependent of the fluxon [124]. Shunt resistors are placed around the Josephson junctions to prevent hysteretic behavior of the superconducting loop [124].

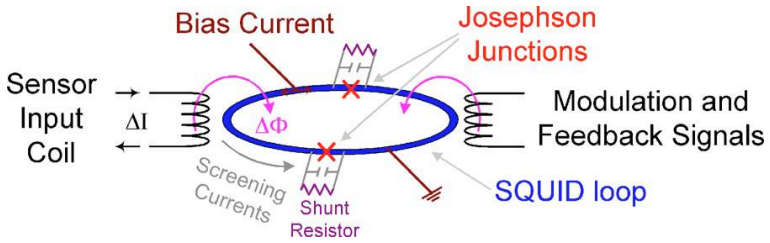

Figure 25 – Dual junction (dc) SQUID loop. The capacitor represents the self-capacitance of the junction [123].

Changing the external magnetic field influences the magnetic flux and leads to a change in the voltage of the loop, which can be measured [124]. The magnetic flux can also be influenced by placing a sample into the magnetic field [124]. Measurements were carried out using a Magnetic Properties Measurement System VSM (Quantum Design) with a maximum magnetic field of 7T in a temperature range from 1.9-1100K. Magnetic field depending measurements (hysteresis loops) were carried out at 5K, 10K and 16K in which the external magnetic field was varied between +50kOe and -50kOe (or +10kOe and -10kOe). In order to measure in a temperature depending mode, the sample was at first cooled to 5K and secondly heated up to 380K. During heating a magnetic field of 200Oe was applied and the change in magnetic flux was measured. This was performed in two different ways, on the one hand with zero field cooling (ZFC), were the magnetic field was applied after reaching the minimum temperature and on the other hand with field cooling (FC), were the magnetic field is already applied while cooling.

3.3.8 Temperature dependent resistivity

The temperature dependent resistivity was measured using the Van-der-Pauw method [126] in a temperature range of 80-300 K. The synthesized powders were pressed in thin pellets, four contacts were made by silver paste and the contacts were connected, as shown in Figure 26, to perform the measurements. In a basic resistivity measurement, the current is measured between the contacts connected with the red wire and the voltage between the contacts connected with the blue wire. The Resistance is given by:

$$R_{rb} = \frac{U_b}{I_r}. \tag{7}$$

However, in order to increase accuracy, the measurements were executed according to the reciprocity theorem. This means, the resistance of Equation (7) is equal to the resistance of the reciprocal case, if the current is measured at blue wire and voltage at red wire [127]. According this, the resistivity can be calculated by:

$$\rho = \frac{\pi d}{\ln 2} * \frac{R_{rb} + R_{br}}{2} * f. \tag{8}$$

With *d* representing the sample thickness and *f* representing a correction factor which is related to the ratio of the calculated resistances R_{rb}/R_{br} [127]. The calculated resistivity needs to be further transformed in order to determine the dominant conductivity mechanism. Three different conductivities are usually considered, nearest-neighbor hopping (NNH), Mott type of variable range hopping (VRH) and Shklovskii-Efros type of VRH [128]. Shklovskii-Efros type of VRH can be excluded, this conductivity mechanism becomes dominant at temperatures below 10K and is usually observed only from single crystals [128]. Further, intergrain tunneling can be excluded, because it is related to grain boundaries that are not present in powders. The Mott VRH conductivity is defined by:

$$\log \sigma \sim T^{-1/4} \tag{9}$$

and NNH conductivity is defined by:

$$\log \sigma \sim T^{-1}. \tag{10}$$

From the linear behavior of equation (9) and equation (10) the width of the acceptor band, the acceptor concentration, the localization radii of holes and the density of the localized states at the fermi level can be calculated [128].

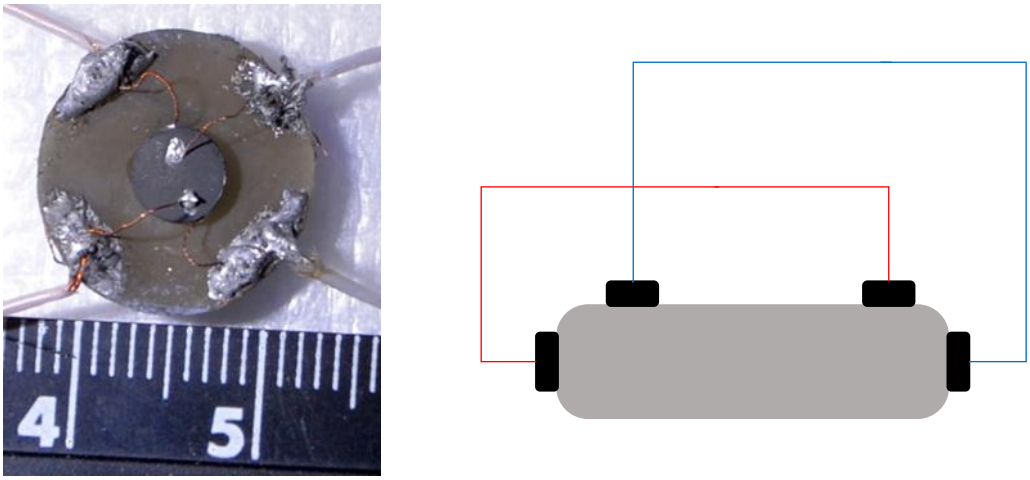

Figure 26 - The actual (left) and the schematic (right) experimental assembly of the temperature dependent resistivity measurements.

In addition to that, the hot probe method, which is addressed to the thermopower, was used to determine the type of conductivity, either n or p. Therefore, the sample was heated up to 50°C. The heat produced charge carriers can be measured by a voltmeter.

3.3.9 ^{57}Fe Mössbauer spectroscopy

In order to quantify the Fe^{2+}/Fe^{3+} ratio, Mössbauer spectroscopy was performed. This spectroscopic method uses the Mössbauer effect, which is a recoilless emission and absorption of gamma radiation by atomic nuclei [129]. This process is only recoilless if the emitting or absorbing atom is bond in a solid [129]. Further, this method is only applicable to ^{57}Fe isotope with the quantum number $I \neq 0$. A second effect, which plays an important role, is the Doppler effect induced by continuous periodic movement of the γ-source (-v 0 +v) [129]. As a consequence, the Mössbauer spectrum is detected twice, laterally reversed respectively. Three interdependencies can be observed at first the chemical isomer shift δ, which is the divergence of the mirror plane from v = 0 [129]. It dependents on the probed element, as well as on the oxidation state (in case of iron, Fe^{3+} it has a lower shift than Fe^{2+} [130]). In addition, an energy level splitting can be detected due to either quadrupole or magnetic splitting [129]. The quadrupole splitting refers to the interaction of the nucleus and the peripheral electric field gradient (EFG), whereas the magnetic splitting refers to the interaction of the nucleus and surrounding magnetic field [129]. In total six iron corresponding peaks are observed, two due to quadrupole and four due to magnetic splitting [130].

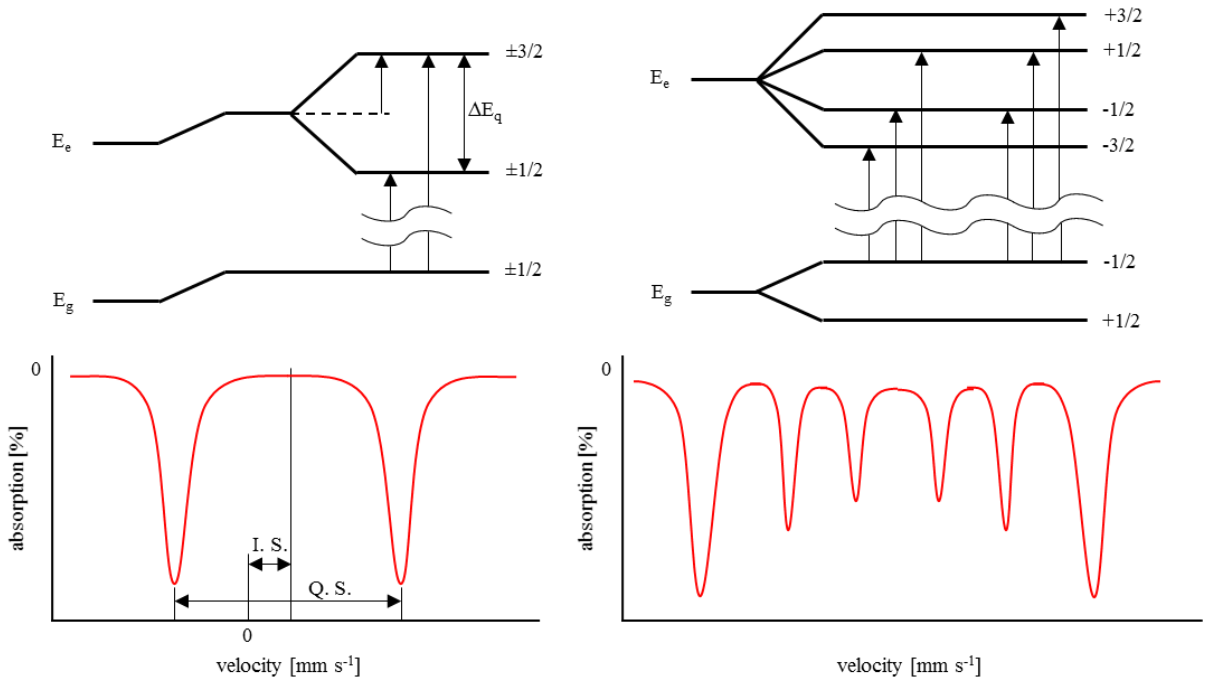

Figure 27 - Origin of quadrupole splitting (Q. S.) (left), the magnitude is given by ΔEq as well as the source of magnetic splitting (I. S. isomer shift) (right); modified from Herber [131].

The ^{57}Fe Mössbauer spectroscopy was performed using a multichannel analyzer linked with an electromechanical movement system at room temperature. A 57Co/Rh 50 mCi source was used operating with a radiation of 40keV. Two spectra were obtained simultaneous which were merged for data evaluation.

4. Results and discussion

4.1 Chromium incorporation into the chalcopyrite type phase

4.1.1 Phase analysis

The chromium alloyed chalcopyrite type samples were synthesized along the pseudo-binary section of chalcopyrite type $CuGaS_2$ and the binary CrS_2 $\left[3(CuGaS_2)_{1-y} - 2(Cr_2S_3)_y\right]$. In total nine samples were prepared and analyzed. The first set consists of five samples which were synthesized at lower temperatures (600°C/950°C) with substitution range varying from y=0.02-0.2 (y=0.02; 0.04; 0.06; 0.08; 0.1; 0.2). For the second set of samples, the synthesis temperature was increased to 700°C/950°C in order to improve the synthesis and the substitution range was narrowed (y=0.02-0.05; Δy=0.01). All samples showed a multi-phase composition, as shown in a backscattered electrons (BSE) micrograph in Figure 28. Each sample contained three phases which were fist analyzed using the energy dispersive X-ray (EDX) system of the electron microprobe. The "dark" phase has a high content of Cr and S, but also certain amounts of gallium and copper. The "medium gray" phase was supposed to be the chalcopyrite type phase, with equal amounts of gallium and copper and the double amount of sulfur. The "light gray" phase contained only copper and gallium.

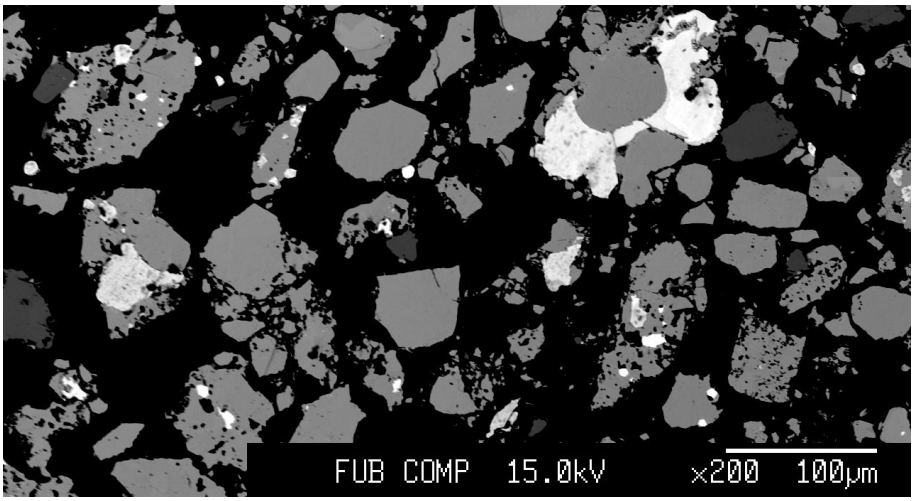

Figure 28 - BSE micrograph of chromium doped chalcopyrite sample, dark gray grains: Cr-spinel, medium gray: chalcopyrite, light gray: γ CuGa phase.

WDX results showed a very limited incorporation of chromium into the chalcopyrite type phase independent of the synthesis temperature, visualized in Figure 29. The maximum solubility is 0.003(1)mol% CrS in the chalcopyrite type phase. The reason for this very limited solubility is the trivalent chromium itself. Usually, Cr^{3+} is coordinated by six atoms (octahedral), but in the case of the chalcopyrite type structure all atoms are coordinated by four atoms (tetrahedral). Cr^{2+} and Cr^{4+} were not considered here, because Cr^{2+} (0.9Å) is too large for being incorporated and Cr^{4+} occurs exclusively in an octahedral coordination (see Table II). Very little is known about the ionic radius of

three valent chromium in the tetrahedral coordination yet. However, a ternary compound where gallium is completely exchanged by chromium is reported. This phase crystallizes in space group $R3m$ [132]. This compound was not detected in any samples discussed here. Instead of being incorporated, the chromium forms a spinel type phase, with the chemical composition $Cu_{0.5}Ga_{0.5}Cr_2S_4$ and space group $Fd\bar{3}m$ [133]. X-ray diffraction experiments have confirmed the existence of the Al_2MgO_4-spinel type phase. With a maximum volume fraction of 5%, effects on the whole composition are rather small and the copper to gallium ratio is unaffected additionally. Another secondary phase has a larger impact on the synthesis. The γ Cu-Ga compound is present in seven of nine samples. From WDX spectroscopy, two different species can be distinguished. On the one hand, γ_3 with 60at% copper and 40at% gallium and on the other hand γ_1 with 65at% copper and 35at% gallium. The crystallization of this copper rich intermetallic phase leads to a copper depletion and a gallium enrichment of the whole system, respectively. This needs to be covered by gallium remnants or a crystallization of gallium rich intermetallic phases or gallium sulfides. $CuGa_2$ (υ) was found in diffraction patterns of several samples as well as in the microprobe analysis. Both intermetallic compounds are easy to detect using XRD, due to their high scattering power. Whereas, gallium sulfides have very low X-ray scattering power which makes a detection less than 5% impossible. However, the presence of a small percentage of gallium sulfides (Ga_2S_3 or GaS) is plausible but not proven. They could not be found in the microprobe or clearly identified by XRD.

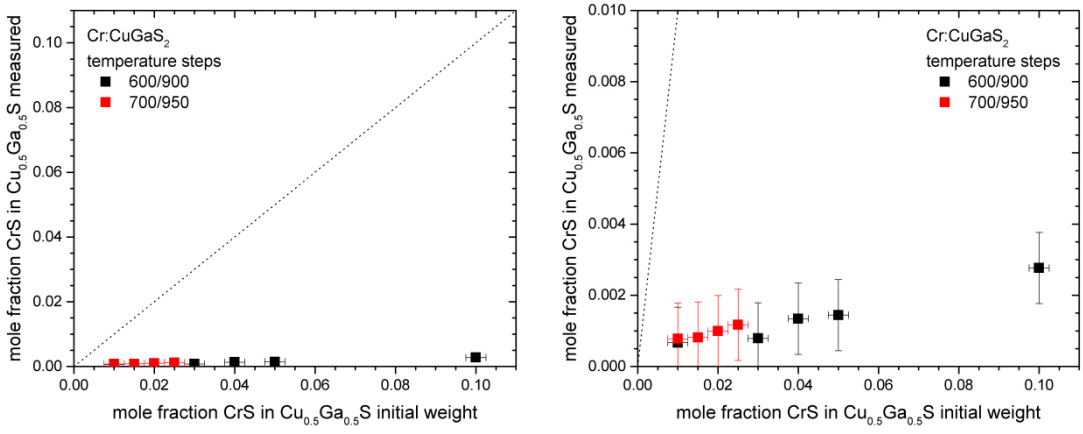

Figure 29 - Initial vs. measured chromium mole fraction within the chalcopyrite type phase (left), zoomed-in area (right).

The amount of the secondary phases depends on the amount of chromium, as visualized in Figure 31. With increasing chromium content, the Cr-spinel volume fraction increases as well, while a decrease in γ Cu-Ga and $CuGa_2$ can be observed. An increase in synthesis temperature results in an increase of intermetallic phases. Furthermore, a higher synthesis temperature leads to more off-stoichiometric chalcopyrite type phases, which are slightly copper rich. In contrast a lower temperature leads to slightly copper depleted, less off-stoichiometric chalcopyrite type phases (Figure 30).

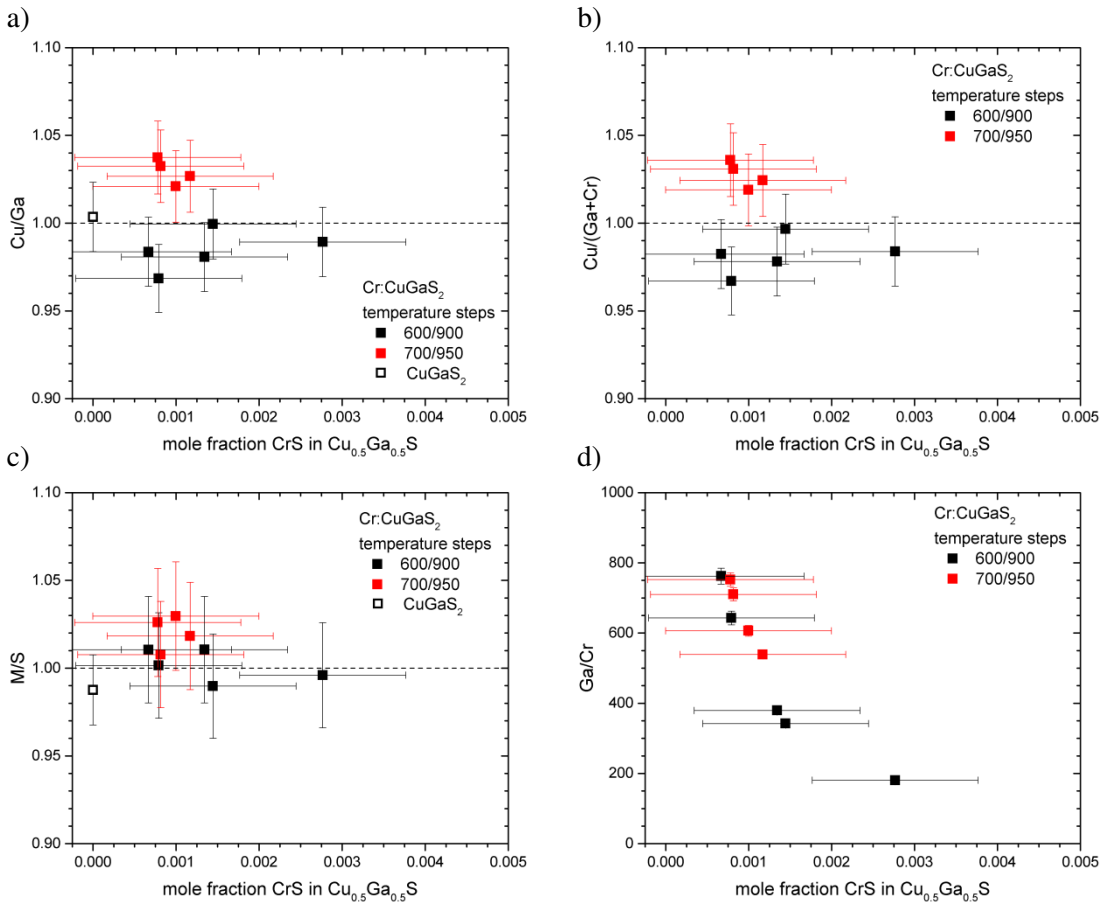

Figure 30 - Copper to gallium ratio (a), copper to trivalent cations ratio (b), cation to anion ratio (c) and gallium to chromium ratio (d) as a function of the chromium molar fraction within the chalcopyrite type phase.

In this context off-stoichiometry is defined as the deviation of the M/S ratio from its ideal value 1. Lower values are a hint for the existence of cation vacancies, whereas higher values are a hint for cation interstitials or anion vacancies. Cation vacancies are rather vacancies of the 4a position (V_{Cu}) than vacancies of the 4b position (V_{Ga}) because of their lower defect formation energy. In $CuGaS_2$ the defect formation energy of V_{Cu} is much lower than V_{Ga} (V_{Cu}=1.83eV, V_{Ga}=4.52eV) [34]. Anion vacancies are also possible, the defect formation energy for V_S is 2.35eV. However, sulfur is always present in excess, so the formation might be implausible. Formation energies regarding interstitial atoms within the structure were not reported, but considering the atomic radii of the cations, gallium interstitials are more likely.

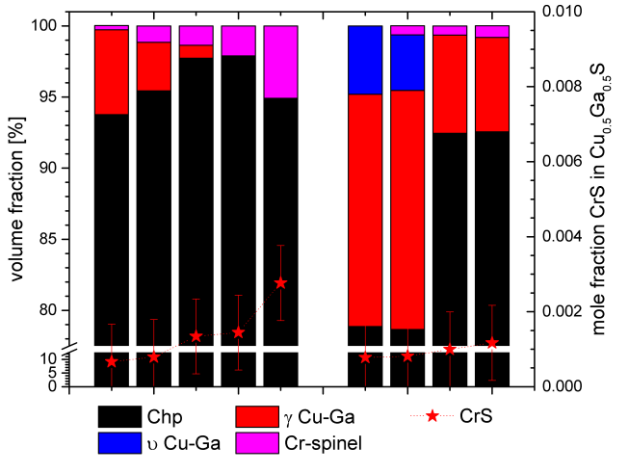

Figure 31 - Volume fraction of the phases and the corresponding chromium content of the chalcopyrite type phase. On the left-hand side, low temperature and on the right-hand side, high temperature synthesis.

It needs to be mentioned that the phases, shown in Figure 31, were found in the electron microprobe analysis and clearly identified by XRD. Some samples contain phases which were not included, because of their limited volume fraction. As mentioned before, samples containing γ Cu-Ga, must have a gallium rich phase which unfortunately could not always be detected.

4.1.2 Structural trends of the chalcopyrite type phase

The solubility of chromium into the chalcopyrite type structure is very small, whereby the impact on the crystal structure is expected to be very small as well. In Figure 32 (left) the lattice parameters of the chalcopyrite type phase are plotted as a function of the chromium content. The changes in lattice parameter *a* and *c/2* due to the incorporation of chromium are within the experimental error, as expected. The same applies to the tetragonal deformation η.

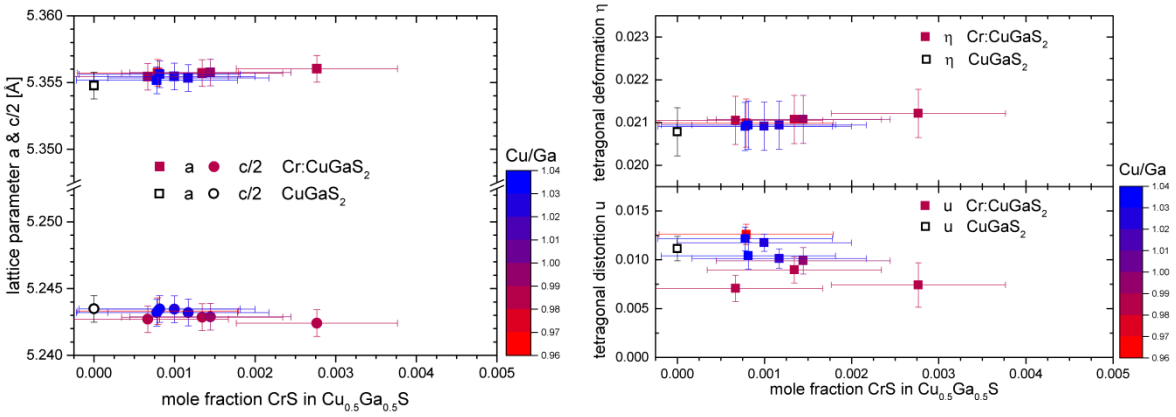

Figure 32 - Lattice parameter a and c/2 of the chalcopyrite type phase as function of the chromium molar fraction and color coded according their copper to gallium ratio (left). Tetragonal deformation and distortion of the chalcopyrite type phase as function of the chromium molar fraction and color coded according their copper to gallium ratio (right).

The interpretation of changes of the tetragonal distortion *u* is very challenging. The anion position is sensitive to smallest changes of the site occupation of the doping elements but also to disorder effects. Due to the similar atomic radii of copper and gallium, a certain amount of disorder needs to be considered. Reasons for the changes of the tetragonal distortion *u* can be differences in off-stoichiometry, amount of anti-site defects as well as the incorporation of chromium.

4.1.3 Cation distribution within the chalcopyrite type phase

Only the chromium containing samples from the low temperature series were analyzed using neutron diffraction. Due to the limited amount of chromium incorporated into the chalcopyrite type structure, the effect on the average neutron scattering length is negligible, despite the large difference in neutron scattering length of the elements. The neutron scattering length of chromium is 3.635fm, whereas the neutron scattering lengths of copper (7.718fm) and gallium (7.228fm) are very similar. In the starting model which was used for the Rietveld refinement, the main cations copper and gallium are placed on their specific position respectively and chromium was placed only on 4b. Vacancies as mentioned before occur exclusively on 4a. The model considers anti-site defects only if necessary, for example if the copper fraction is larger than the available site. Figure 33 (left) shows the experimental average neutron scattering lengths (b^{exp}) in comparison to the calculated average neutron scattering length (b^{cal}). In two cases the model does not fit the experimental data which can be interpreted by anti-site defects. The corresponding cation distribution is shown in Figure 33 (right). Interstitials are visualized only, if the fraction of the 4b site is larger than 100%.

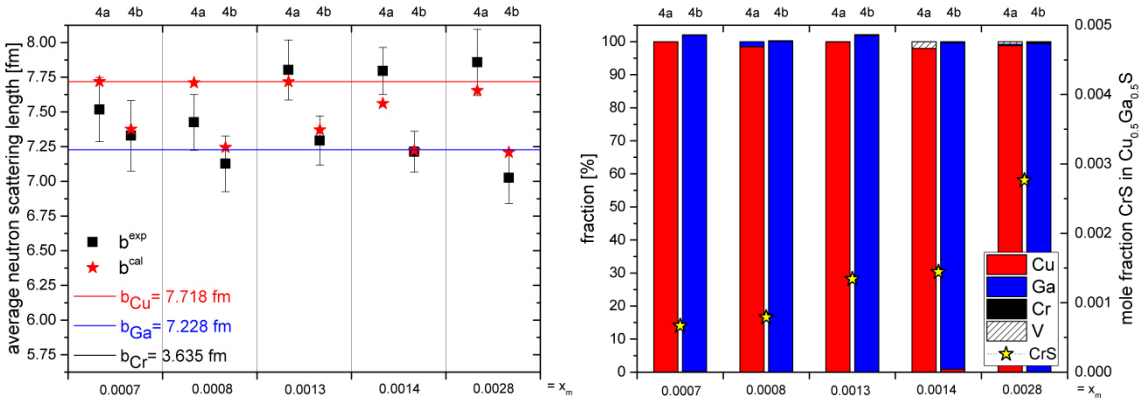

Figure 33 - Comparison of the measured and calculated average neutron scattering length (ANSL) (left). Red line marks the NSL of copper, the blue line of gallium. Resulting cationic distribution and corresponding chromium molar fraction (right); x_m refers to the chromium molar fraction within the chalcopyrite type phase.

The defect concentration was calculated on the basis of the cation distribution. The majority of the chalcopyrite type phases, shown in Figure 34, do either have copper vacancies or gallium interstitials as main defects. The chalcopyrite type phases with the highest chromium content show vacancies and those with lower chromium content show interstitials. Unfortunately, no general trend could be observed, thus the presence of vacancies or interstitials cannot be correlated with the amount of chromium incorporated into the chalcopyrite type structure.

Minor defects are mainly Cu_{Ga} or Ga_{Cu} anti site defects. Due to the model used for the distribution of the elements, the Cr_{Ga} defects increase with increasing chromium content. Nonetheless, the general defect concentration is very low. The small chromium fraction within the chalcopyrite type phase does not allows to determine, which site is preferred by chromium.

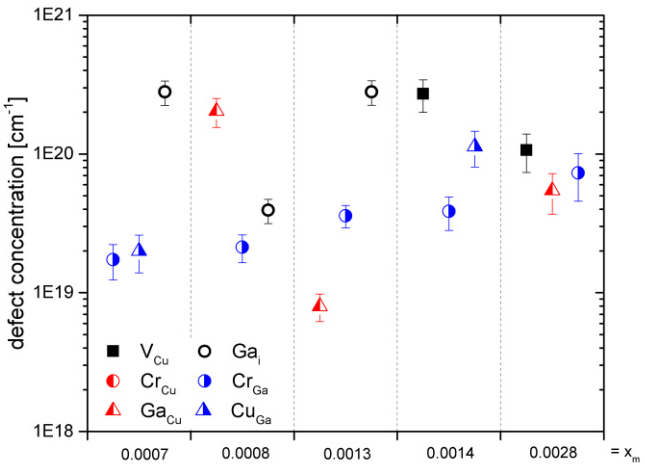

Figure 34 - Defect concentration calculated from cation distribution of the chalcopyrite type phase regarding the measured chromium content (x_m).

4.1.4 Optoelectronic properties of Cr:$CuGaS_2$

From the chromium alloyed chalcopyrite type sample series only two samples were studied by PL spectroscopy. The selected samples showed a higher chromium content compared to other samples. Two different behaviors were observed, which are shown in Figure 35. The chalcopyrite type phase with 0.0014(10)mol% CrS shows a weak PL band at 1.2eV. Additional peaks are interpreted to be background. In contrast to that, the chalcopyrite type phase with 0.0028(10)mol% CrS shows one intense PL band at 1.4eV. This peak was observed from $CuGaS_2$ in this study and before by several authors [134-136]. Ooe et al. [134] related this peak to a defect level caused by copper vacancies. This is in agreement with the results of the cation distribution from the neutron diffraction experiments, where V_{Cu} were observed in both samples. In defiance of the highest chromium content, this chalcopyrite type phase shows the same PL characteristic as $CuGaS_2$. However, the chalcopyrite type phase with lower chromium content shows a PL characteristic that was not observed before. In literature the PL spectrum usually covers a range from 1.4eV to 2.8eV, thus a band at 1.2eV could not be observed. The proposed position of the intermediate band due to chromium incorporation is located at 1.35eV for $Cr^{4+/3+}$ or 2.3eV for $Cr^{3+/2+}$ from valence band maximum [7]. An intermediate band located at 1.35eV might be more probable than at 2.3eV. However, the proposed intermediate band positions could not explain a PL band at the observed position. If the position of the intermediate band is a bit shifted compared to the calculated 1.35eV it might be possible, that this is the proposed defect level. A second solution for the small deviation can be explained by the widening of the bandgap due to the incorporation of chromium [29]. Summarizing both explanations, this might be most likely. Nevertheless, further PL experiments as well as complimentary techniques are necessary in order to determine the bandgap of this material.

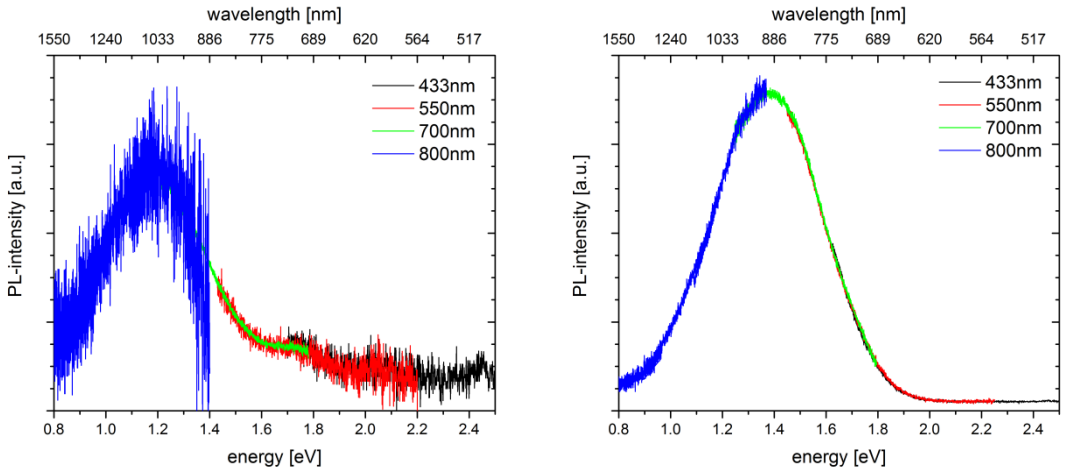

Figure 35 - PL spectra of chromium containing chalcopyrite type phases, with 0.0014(10)mol% CrS (left) and 0.0028(10)mol% CrS (right) in $Cu_{0.5}Ga_{0.5}S$.

4.1.5 Interim conclusion

The incorporation of chromium into the chalcopyrite type $CuGaS_2$ is very limited with a maximum CrS molar fraction of 0.003(1). Chromium rather forms a spinel type phase ($Cu_{0.5}Ga_{0.5}Cr_2S_4$) because of the preference of an octahedral than tetrahedral coordination. Other secondary phases are γ and υ Cu-Ga intermetallic compounds. An increase of the initial chromium content results on the one hand in an increasing amount of the chromium spinel and on the other hand in a decreasing amount of the intermetallic compounds. The composition of the doped ternary phase shows an explicit temperature dependency. The chalcopyrite type phases synthesized at high temperatures are copper rich and more off-stoichiometric, whereas those synthesized at low temperatures are copper poor and less off-stoichiometric. However, no impact of the incorporated chromium on the crystal structure could be observed due to the almost negligible solubility of chromium. For the same reason, a site preference of chromium could not be obtained.

Table VI - Overview of the observed secondary phases within the Cr:$CuGaS_2$ experiments as well as their commonness; the max. volume fraction of the phases was determined by Rietveld refinement of XRD data.

observed secondary phases	max. volume fraction [%]	present in _ of 9
γ Cu-Ga	16.81(16)	7
υ Cu-Ga	4.81(10)	2
Cr-Spinel $Cu_{0.5}Ga_{0.5}Cr_2S_4$	5.09(7)	8

4.2 Nickel incorporation into the chalcopyrite type phase

4.2.1 Phase analysis

The solubility limits of nickel in the chalcopyrite type structure of $CuGaS_2$, either theoretical or practical, were not reported so far. Nickel is preferentially in oxidation state 2+ in which it can be in a tetrahedral coordination, but it can also occur in oxidation state 3+, where the tetrahedral coordination is rather unlikely. The crystal radius (0.53Å) is smaller than this of gallium (0.580Å) and copper (0.635Å) [36]. For the synthesis of nickel containing chalcopyrite type $CuGaS_2$, the coupled substitution was assumed in order to stay charge balanced. Four samples along the pseudo-binary section of $CuGaS_2$ and NiS $\left[(CuGaS_2)_{1-y} - 2(NiS)_y\right]$ within a substitution range from y=0.05-0.2 (Δy=0.05 steps) were synthesized. The temperatures for this synthesis were adapted, in the first synthesis step the third temperature was 700°C and the final temperature was 900°C. For homogenization the temperature was increased to 950°C in order to get rid of secondary phases, which were macroscopically observed. The BSE image of all samples is similar, a micrograph is shown in Figure 36 as example.

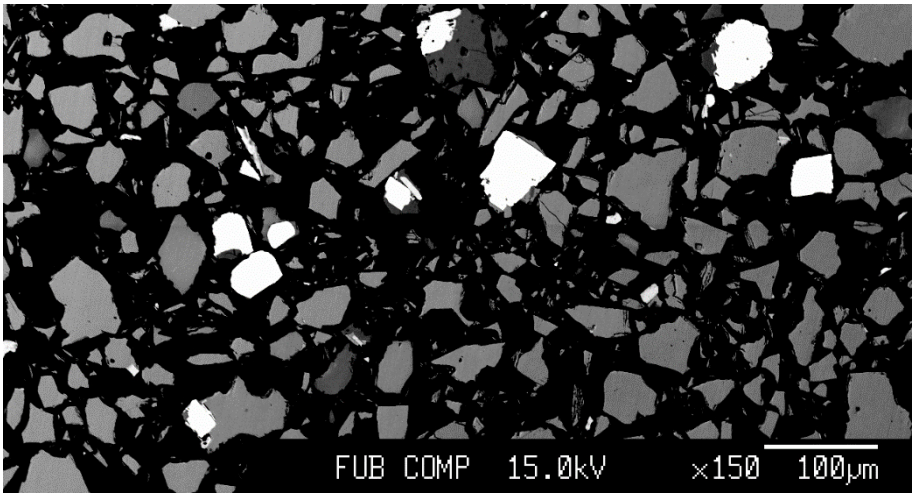

Figure 36 - BSE micrograph of chromium doped chalcopyrite sample, dark gray grains: Nickeline, medium gray: chalcopyrite, light gray: α´ Ni-Ga phase.

The observations from WDX analysis of the nickel alloyed chalcopyrite type phases are comparable to those of the chromium study, there the transition metal also form rather secondary phases than is incorporated into the chalcopyrite compound. Secondary phases observed are Nickeline (NiS), Heazlewoodite (Ni_3S_2) and α´ Ni-Ga with almost 10at% copper and 70at% nickel. In comparison to chromium study, the maximum solubility of nickel into the chalcopyrite type phase (0.008(1)mol%) is almost three times higher than chromium. However, the limited solubility of nickel into the chalcopyrite type $CuGaS_2$ does not have a significant impact on the chemical composition or on the structural properties.

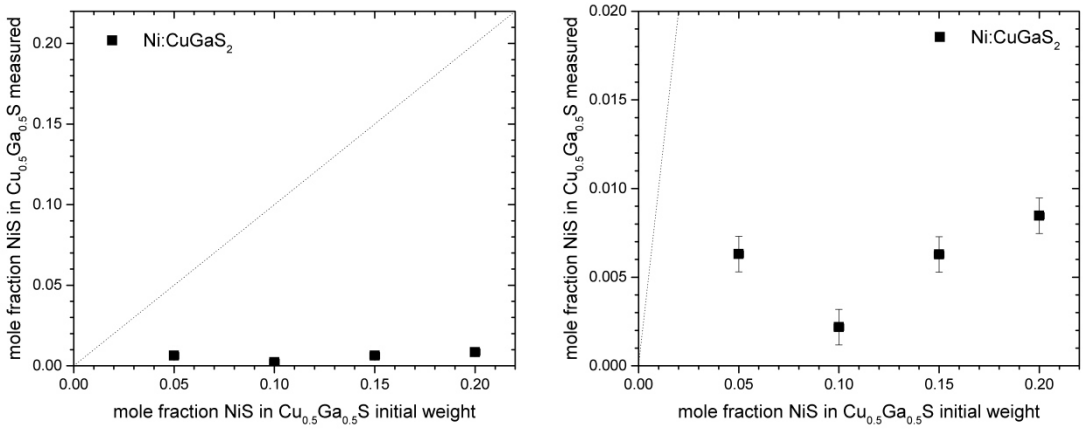

Figure 37 - Initial vs. measured nickel mole fraction within the chalcopyrite type phase (left), zoomed-in area (right).

Due to the incorporation of nickel into the chalcopyrite type structure of $CuGaS_2$, a weak decreasing trend in the Cu/Ga ratio is visible, as shown in Figure 38 (a). A slightly more pronounced trend can be observed in the Cu/(Ga+Ni). This can be either a coupled substitution or a unilateral substitution of copper and nickel. In case of a coupled substitution, the Cu/Ga ratio stays constant, thus the incorporation of nickel seems to be a unilateral substitution of copper and nickel. This would lead to a visible trend in the M/S ratio. The substitution of univalent copper by divalent nickel causes vacancies in order to stay charge balanced. The M/S ratio needs to decrease with nickel content, which was not observed (Figure 38 (c)). A certain amount of vacancies is present, but without a trend referring to the incorporated nickel. Since the experimental error of the M/S ratio is considerably large a unilateral substitution of copper and nickel is highly probable. However, the interpreted trends are very weak or within the errors of the measured points, which does not allow a clear statement about the actual substitution behavior.

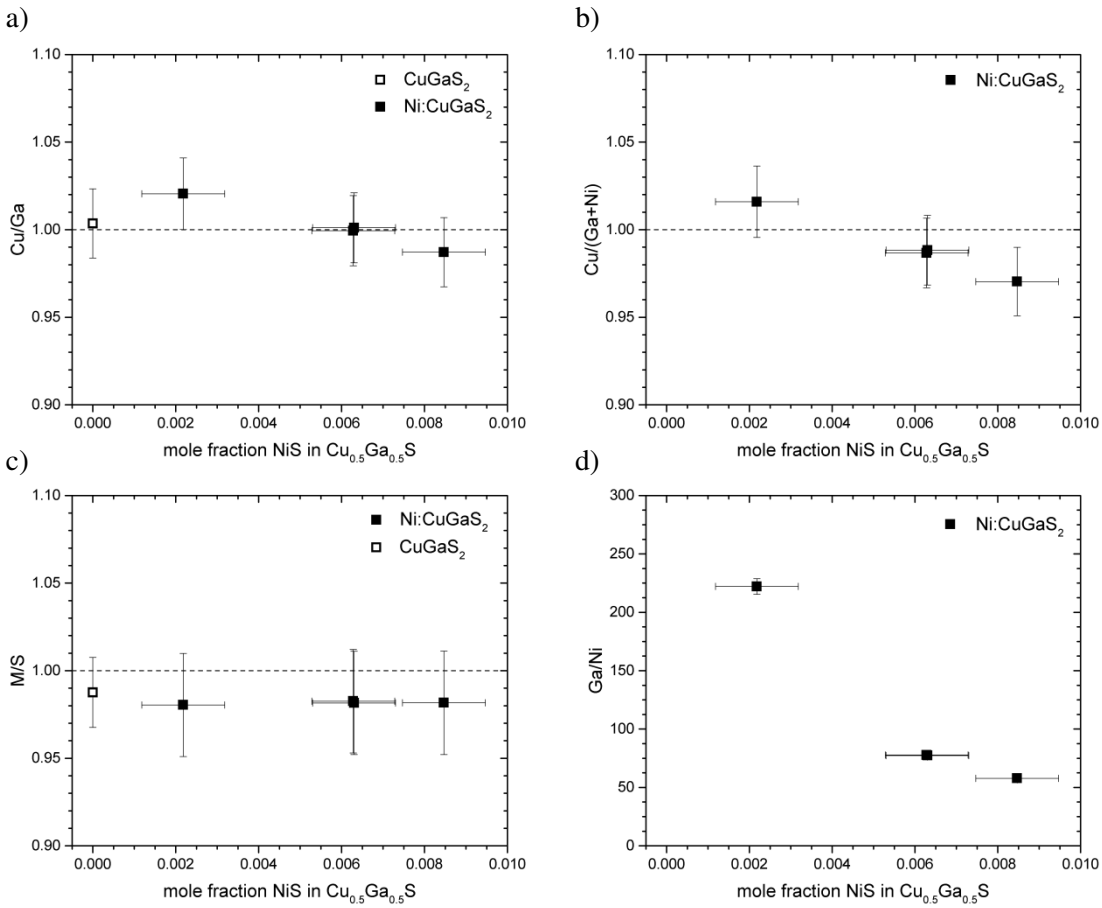

Figure 38 - Copper to gallium ratio (a), copper to trivalent cations ratio (b), cation to anion ratio (c) and gallium to nickel ratio (d) as a function of the nickel molar fraction within the chalcopyrite type phase.

The volume fraction of secondary phases mentioned before are displayed in Figure 39. Here the volume fraction is shown as a function of the initial mole fraction of nickel. The metastable Nickeline which crystallizes in the NiAs (Nickeline) type structure (space group $P6_3/mmc$) was found in two of the four samples, with a maximum volume fraction of almost 18%. Millerite, the stable polymorph was not observed. The fcc α´ Ni-Ga phase is only present in one powder sample with a volume fraction of 7%. The third secondary phase found by WDX spectroscopy is Heazlewoodite. If only a small amount of Heazlewoodite is present, its observation is not easy because the main peak overlaps with the 200 reflex of the chalcopyrite type phase, as shown in Figure 40. The second intense reflex is solely, but it has only one ninth of intensity compared to the main peak. Nevertheless, it is present in all of the samples. The volume fraction of Heazlewoodite within the powder samples varies between 0.65vol% and 2vol%.

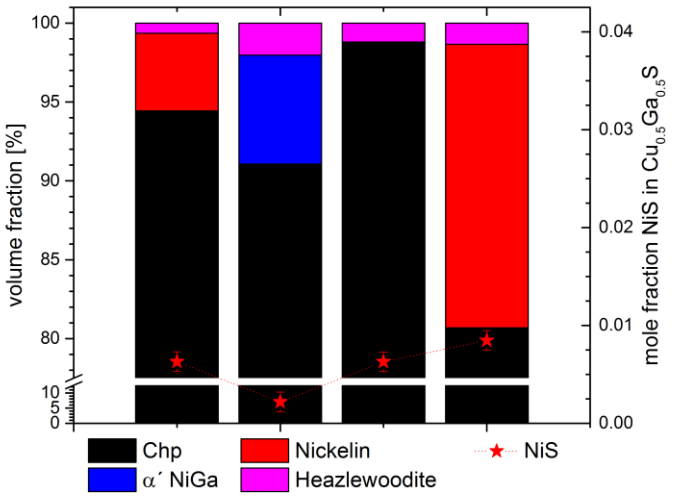

Figure 39 - Volume fraction of the phases and the corresponding nickel content of the chalcopyrite type phase.

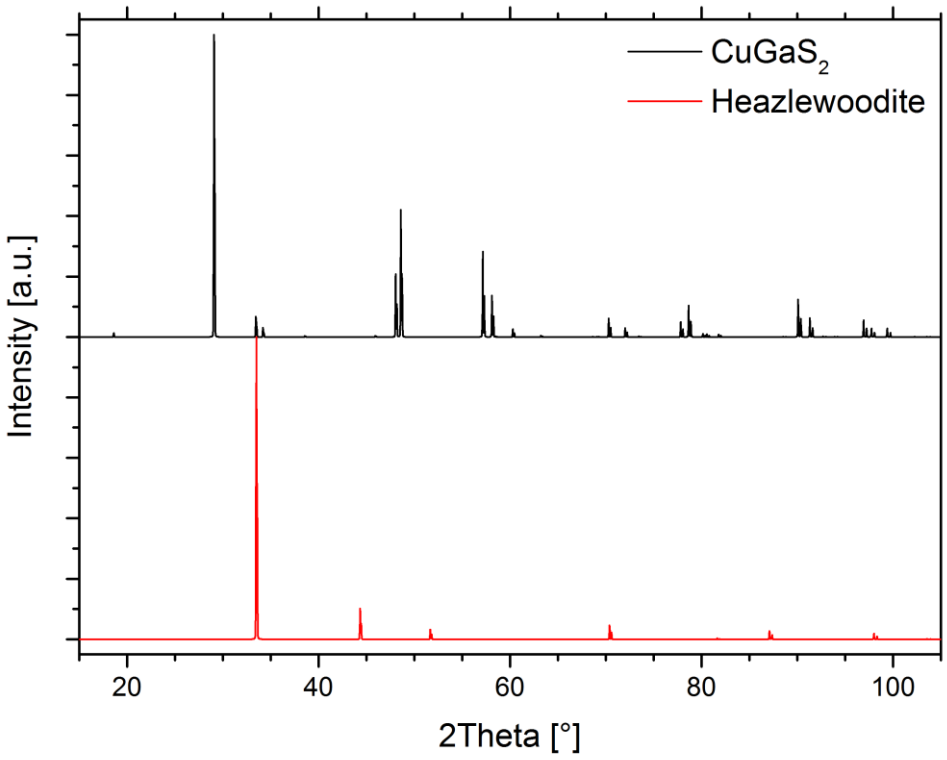

Figure 40 - Simulated X-ray diffraction pattern of the $CuGaS_2$ chalcopyrite type phase and Heazlewoodite (Ni_3S_2).

4.2.2 Structural trends of the chalcopyrite type phase

The nickel incorporation into the chalcopyrite type $CuGaS_2$ is expected to result in a decrease of the lattice parameters of the chalcopyrite type phase, due to the smaller atomic radius of nickel. However, the maximum solid solubility is very limited, which is similar compared to the solubility of chromium. Figure 41 (left) shows the lattice parameters of the chalcopyrite type phase as a function of the nickel molar fraction where no increase or decrease was observed. The lattice parameter *a* and *c/2* stay constant which results in a constant tetragonal deformation η. The lattice constants and the tetragonal deformation are similar to those of $CuGaS_2$. Two chalcopyrite type phases show a much smaller tetragonal distortion than $CuGaS_2$ which can be explained by intrinsic anti-site defects. The formation of intrinsic anti-site defects results in an adjustment of the cation to anion bond length of both sites which leads to a decrease of the tetragonal distortion. The two remaining chalcopyrite type phases show an equal tetragonal distortion compared to $CuGaS_2$.

In general, the tetragonal distortion *u* is increasing while incorporating more nickel into the chalcopyrite type lattice, which is in agreement with the expected trend from an incorporation of nickel on the gallium position. In case of an incorporation on the copper site, the average site radius of the 4a position decreases which results in a decrease in tetragonal distortion *u*. The observed trend is far too steep, considering the small size difference of gallium and nickel. The increase in tetragonal distortion *u* could be enhanced by a simultaneous decrease in the concentration of intrinsic anti-site defects with increasing nickel content. According to the decreasing Cu/Ga ratio, a decrease of Cu_{Ga} anti-site defects is quite probable.

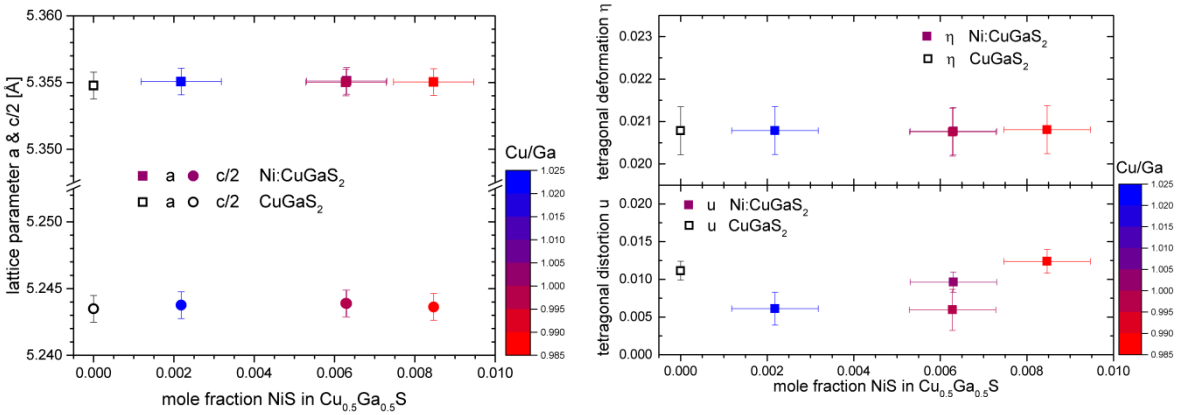

Figure 41 - Lattice parameter a and c/2 of the chalcopyrite type phase as function of the nickel molar fraction and color coded according their copper to gallium ratio (left). Tetragonal deformation and distortion of the chalcopyrite type phase as function of the nickel molar fraction and color coded according their copper to gallium ratio (right).

4.2.3 Optoelectronic properties of Ni:$CuGaS_2$

The nickel containing chalcopyrite type phases were analyzed by PL spectroscopy. The spectra, shown in Figure 42, covers the range from 1.5eV to 2.0eV, where PL intensity was observed. For further interpretation, the chalcopyrite type phases were divided into two groups. The first group is represented by the red and blue graph in Figure 42, were the PL characteristic is an intense peak at 1.75eV, whereas the second group is represented by the black and magenta graphs. The second group shows only a weak PL band which is shifted towards higher energies. The slightly different observations cannot be explained with chemical or structural fluctuations. Even the two chalcopyrite type phases containing 0.006mol% (x_m) NiS, which are chemically and structurally similar, show a difference in PL characteristic. However, all chalcopyrite type phases show the same PL characteristic despite the small differences which are caused by fluctuations in band gap and position of defect state. A PL band at ~1.8eV is well known, even in $CuGaS_2$. Massé [137] interpreted this as defect level referring sulfur vacancies, which vanish after annealing in sulfur atmosphere. This interpretation is in contradiction to the results obtained from this chalcopyrite type phases. During the first synthesis step the sulfur content was raised by 10% excess additionally. Furthermore, in the first homogenization step additional 0.1g were added to the powder sample, assuming that the chalcopyrite type phase is sulfur saturated. The measured chemical composition is showing no hint at sulfur deficit, since the M/S ratio is always slightly below 1. Interpretations of this PL band are further discussed in chapter 4.4.7 (Manganese – optoelectronic properties).

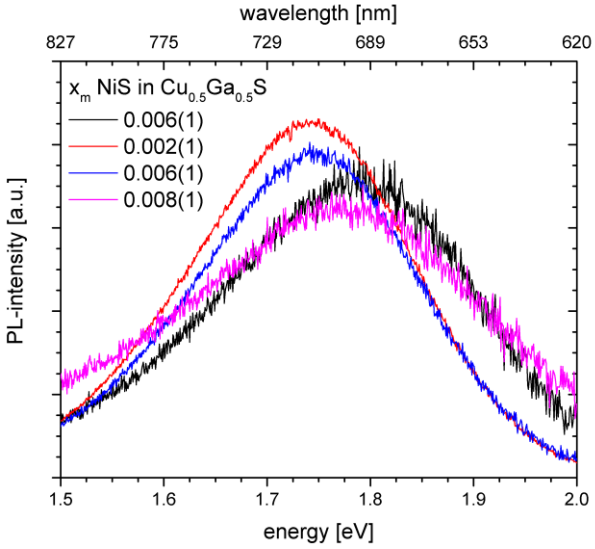

Figure 42 - 550nm PL spectra of nickel containing chalcopyrite type phases as function of NiS mole fraction (x_m) in $Cu_{0.5}Ga_{0.5}S$.

4.2.4 Interim conclusion

The incorporation of nickel in chalcopyrite type $CuGaS_2$ is comparable to that of chromium. Nickel is more likely to be incorporated into secondary phases than into the chalcopyrite type lattice. The maximum solubility is 0.008(1)mol% NiS, which is twice the maximum solubility of chromium. The increase in nickel content leads to a continuous decrease in Cu/Ga and Cu/(Ga+Ni) ratio. The ratio of M/S shows no deviation caused by the incorporation of nickel. On this basis, a substitution of copper and nickel can be assumed. However, the limited solubility does not lead to a change in lattice constants, but a clear trend in tetragonal distortion *u*. The tetragonal distortion *u* increases with increasing nickel content which can be interpreted as the incorporation of nickel on gallium site. In addition, the increasing trend is likely reinforced by a decrease in Cu_{Ga} anti-site defect concentration with increasing nickel content which is assumed by the Cu/Ga ratio. The nickel-doped chalcopyrite type samples show only a PL band at ~1.8eV which is not related to the incorporation of nickel. This band is more likely related to Ga_{Cu} anti-site defects which are discussed in a following chapter (4.4.5).

Table VII - Overview of the observed secondary phases within the Ni:$CuGaS_2$ experiments as well as their commonness; the max. volume fraction of the phases was determined by Rietveld refinement of XRD data.

observed secondary phases	max. volume fraction [%]	present in _ of 4 powder samples
Nickelin NiS	17.97(46)	2
α´ Ni-Ga	6.91(15)	1
Heazlewoodite Ni_3S_2	2.03(9)	4

4.3 Iron incorporation into the chalcopyrite type phase

4.3.1 Phase analysis

Regarding the natural existing mineral Chalcopyrite ($CuFeS_2$) the synthesis of powder samples within the solid solution of the iron endmember and the gallium endmember was mandatory. The exchange mechanism is supposed to be unilateral, with one Fe^{3+} substituting one Ga^{3+}. Thus, the initial weight chosen was $Cu_{0.5}(Ga_{0.5-x}Fe_x)S$, to compare it to the incorporation experiments of the other transition metals as well as the high temperature (700°C/950°C) profile. The iron alloyed chalcopyrite type $CuGaS_2$ sample series – in all 12 samples – was synthesized in two sample sets. In the first incorporation experiments the initial iron molar fraction x_i is between 0.025 and 0.1 (Δx_i=0.025). Within this set the powder samples consist of one chalcopyrite type phase and small amounts of secondary phases (γ Cu-Ga, bornite, Cu-Ga-Fe compounds). In the second experimental set x_i was increased to 0.125-0.35 (Δx_i=0.025 [x_i<0.25] and Δx_i=0.05 [x_i>0.25]). Within this second sample set, no secondary phases were observed, but two different chalcopyrite type phases. Figure 43 shows two micrographs of two different samples from different sample sets. The left figure shows the chalcopyrite type phase in gray and the intermetallic compounds in white, with an approximate volume fraction of 5%. In the right figure, a complex intergrowth of two phases can be seen. These two phases are both chalcopyrite type phases. The contrast in the picture results from the different chemical composition. All samples of the second sample series show this phase segregation and the chemical homogeneity of both phases decreases with increasing initial iron content. Due to inhomogeneity, samples with an initial $x_i \geq 0.25$ will not be discussed.

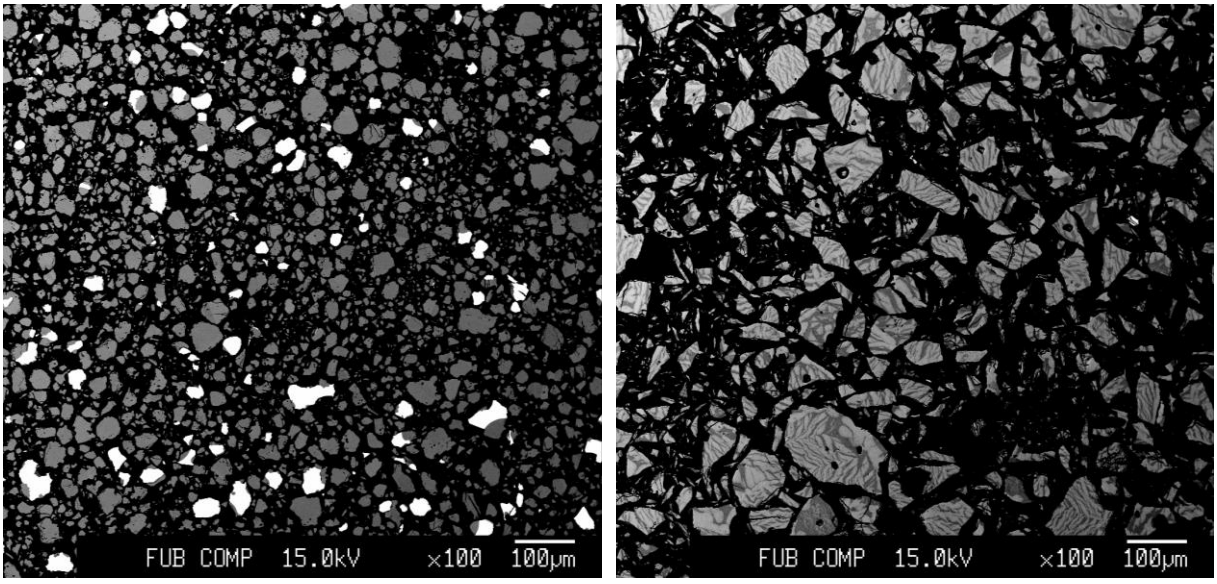

Figure 43 - BSE micrograph of iron alloyed chalcopyrite samples, gray grains: chalcopyrite type phase, white grains: intermetallic compounds (left); bright grains: low iron content, dark grains: high iron content (right).

The samples from the first experimental set follow the pseudo-binary section perfectly, with a very small amount of secondary phases observed. Whereas, the samples from the second experimental set split up, forming two chalcopyrite type phases. From linear balancing, the volume fraction of the chalcopyrite type phases can be assumed. The closer the measured composition plots to the line, the higher the volume fraction. Considering this correlation, the chalcopyrite type phase with the low iron content has a higher volume fraction than the chalcopyrite type phase with the high iron content. Within this two-phase region, an increase of the measured iron molar fraction with increasing initial iron molar fraction can be observed. However, the observed trend is less steep than the trend referring to the pseudo-binary section (Figure 44, dotted line). That means, with increasing initial iron content, the amount of the iron rich chalcopyrite type phase increases, while the amount of the iron poor chalcopyrite type phase decreases.

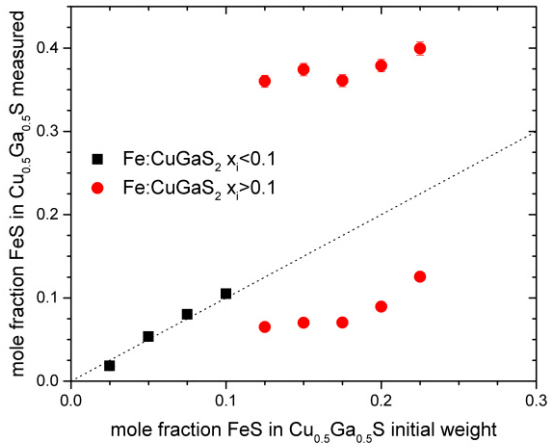

Figure 44 - Initial vs. measured iron mole fraction within the chalcopyrite type phase.

The chemical composition of the chalcopyrite type phases of both sample sets show some similarities, but also some distinctions. In Figure 45 (d) the Ga/Fe ratio is plotted as a function of the iron content. All chalcopyrite type phases show a trend in Ga/Fe ratio which is comparable to a decay function. No clear trend is observed from the change in M/S ratio. The chalcopyrite type phases of the first set plot slightly above 1 and their increasing trend with increasing iron content plots within the errors. The same can be observed from the chalcopyrite type phases of the second experimental set, but the M/S ratio is almost 1. Only the two chalcopyrite type phases with the highest iron content are an exception, the M/S ratio is slightly above 1. These two chalcopyrite type phases are more similar to those from the first experimental set. Values above 1 have their origin mainly from the overestimation of the charge of an element. In this case, a certain amount of the incorporated iron is divalent which enhances the formation of interstitials in order to ensure charge balance.

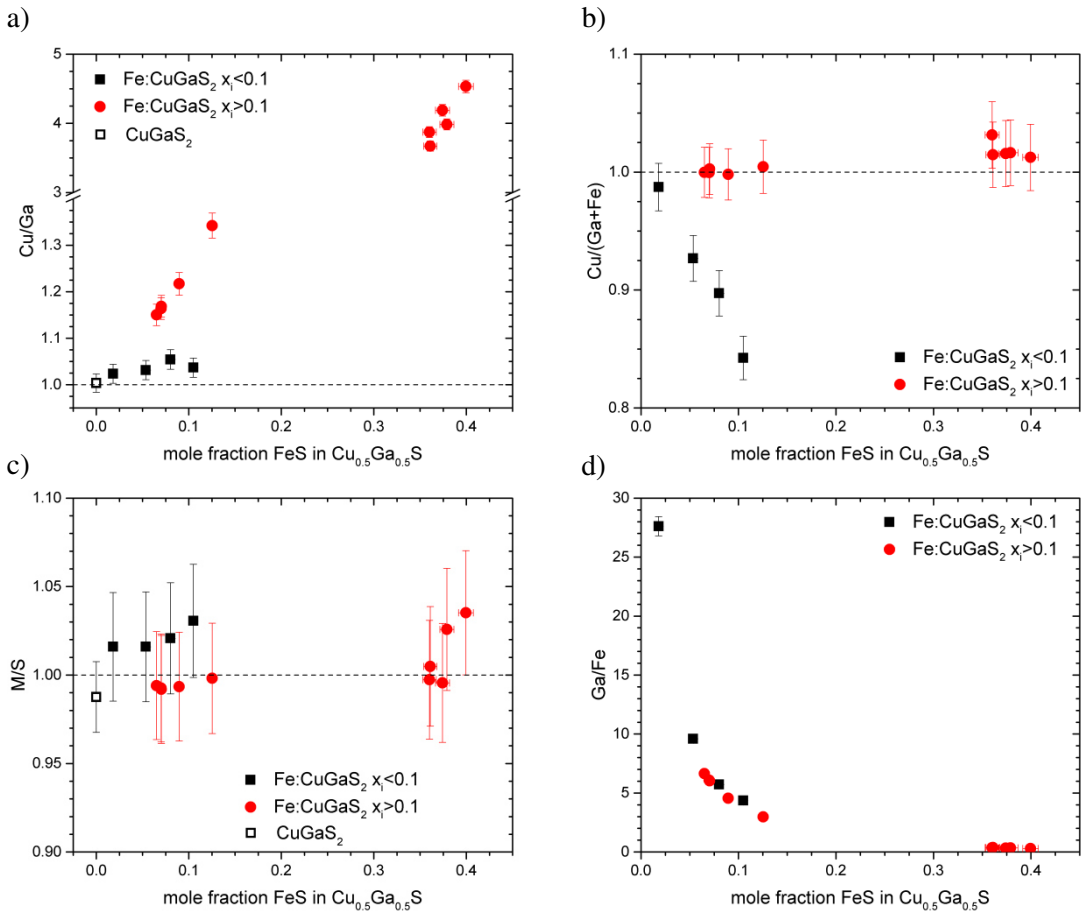

Figure 45 - Copper to gallium ratio (a), copper to trivalent cations ratio (b), cation to anion ratio (c) and gallium to iron ratio (d) as a function of the iron molar fraction within the chalcopyrite type phase.

Based on the trends from Ga/Fe and M/S ratio the general substitution mechanism cannot be assumed. Therefore, the correlation of the trends from the Cu/Ga ratio and the Cu/(Ga+Fe) ratio are necessary. However, it needs to be considered, that all iron ions are supposed to be trivalent which is not mandatory. The Cu/Ga ratio of the chalcopyrite type phases of the first experimental set – one chalcopyrite type phase – is slightly above 1 with a steady trend, which means with increasing iron content copper and gallium are substituted in the same amount. Whereas, the chalcopyrite type phases from the second sample set – two chalcopyrite type phases – show a significant increasing trend, which means a gallium depletion due to the incorporation of iron. However, the trends observed from the Cu/(Ga+Fe) ratio are reverse to those of Cu/Ga. The Cu/(Ga+Fe) ratio of the chalcopyrite type phases of the second sample set is constant, which means the amount of incorporated iron is equal to the depletion of gallium. The chalcopyrite type phases of the first experimental set are showing a significant decrease in Cu/(Ga+Fe) ratio, with the constant Cu/Ga ratio, a coupled substitution ($Cu^{+} + Ga^{3+} \leftrightarrow 2Fe^{2+}$) can be concluded. In contrast to this, the increasing copper to gallium ratio and the constant Cu/(III) ratio of the chalcopyrite type phases of the second set, can be concluded as unilateral substitution of gallium and iron.

However, a statement regarding the solid solubility of iron into the $CuGaS_2$ chalcopyrite type phase or a potential miscibility gaps cannot be made. The observed phase separation is rather related to the synthesis, due to the close proximity of the used synthesis temperature. The melting temperature of $CuFeS_2$ is 950°C, which is used as maximum synthesis temperature. However, the melting temperature of the initial composition is assumed to be much higher. Indeed, the temperature in furnaces vary within a certain error, but phase melting can be excluded. There is no reliable explanation of the observed phase separation. Nonetheless, a real phase separation caused by an miscibility gap is doubtful and was not observed by DiGiuseppe et al. [5]. Perhaps, a further homogenization step could solve the problem of phase separation.

4.3.2 Structural trends of the chalcopyrite type phase

The pseudo-binary section of the $CuGaS_2$ and $CuFeS_2$ is supposed to be a complete solubility [5, 138]. By following Vegard´s law, the lattice parameters are assumed to decrease with increasing iron content. DiGuiseppe et al. [5] showed that lattice parameter *a* attends to Vegard´s law, whereas lattice parameter *c* increases to a maximum at x_m=0.1-0.15 ($Cu_{0.5}Ga_{0.5-x}Fe_xS$) and decreases afterwards. This is in agreement with the observation from the chalcopyrite type phases of the second sample set (x_i>0.1), visualized as triangles in Figure 46. Lattice parameter *a* is following Vegard´s law and lattice parameter *c* is increasing. However, it needs to be mentioned, that in case of the presence of two chalcopyrite type phases only the chalcopyrite type phase with the low iron content will be discussed in this part. A proper structural analysis of the chalcopyrite type phase with high iron amounts is prone to errors due to the overlapping of the Bragg peaks. The chalcopyrite type phases from the first sample set (x_i<0.1) discount Vegard´s law in any case. Lattice parameter *a* and *c/2* increase with increasing iron content. Considering the ionic radii of the involved ions, this is a hint for the incorporation of the divalent iron instead of the trivalent. The trivalent iron with an atomic radius of 0.555 Å is smaller than copper and gallium, but the divalent iron (0.66 Å) is larger than copper and gallium. The incorporation of divalent iron will result in an increasing trend in lattice parameters, whereas the incorporation of trivalent iron will result in a decrease. This assumption is in good agreement with the conclusion from the chemical composition of the chalcopyrite type phases. The chalcopyrite type phases of the first experimental set (x_i<0.1) show a trend in chemical composition which is concluded to be caused by a coupled substitution. Here, the incorporation of divalent iron is favorable which results in a significant increase in lattice parameters.

The lattice parameter *a* of the chalcopyrite type phases of the second experimental set (x_i>0.1) is following Vegard´s law strictly, which can be correlated with the assumed substitution mechanism from chemical evolution. However, the increase in lattice parameter *c* is not understood yet.

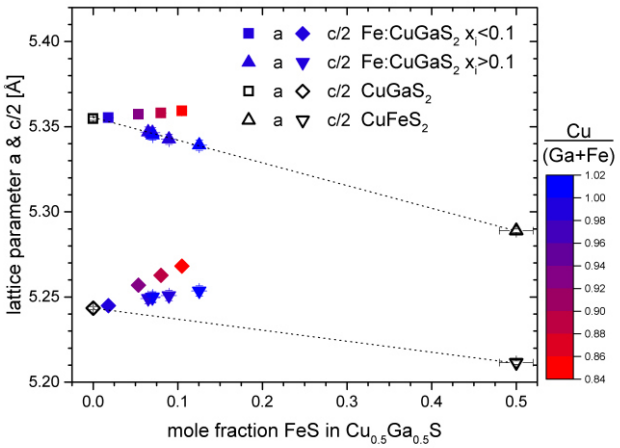

Figure 46 - Lattice parameter a and c/2 as a function of the measured iron content of the chalcopyrite type phase and Cu/(Ga+Fe) ratio. The dotted lines refer to the evolution of the lattice parameters regarding Vegard´s law.

Along the pseudo-binary section, the tetragonal deformation η is supposed to decrease slightly because of the slightly smaller atomic radius of Fe^{3+}, compared to gallium. However, the observed decrease is substantially larger than expected from Vegard´s law, which results from the massive increase of lattice parameter *c* with increasing iron content. The maximum expansion in the $\vec{c}$ direction is expected to be in the region of x_m=0.1-0.15. For higher x_m, lattice parameter *c* decreases. The decrease of the lattice parameters *a* and *c/2* becomes similar, which results in no change in tetragonal deformation η for phases with x_m>0.2. Furthermore, the tetragonal deformation η of both sample sets is following the same trend, despite the different trends observed from the lattice parameters. From this it is assumed, the actual substitution mechanism does not affect the tetragonal deformation η, which decreases independently with increasing iron content.

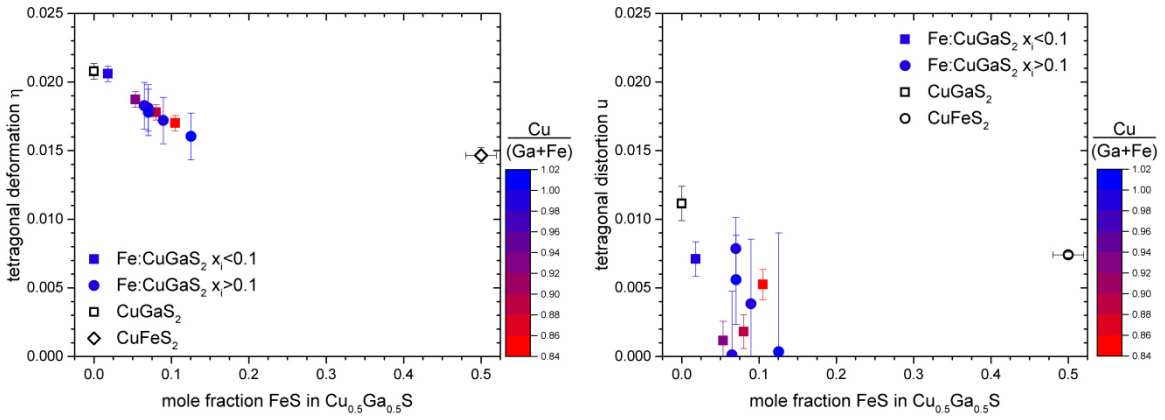

Figure 47 - Tetragonal deformation (left) and tetragonal distortion (right) as a function of the measured iron content of the chalcopyrite type phase and Cu/(Ga+Fe) ratio.

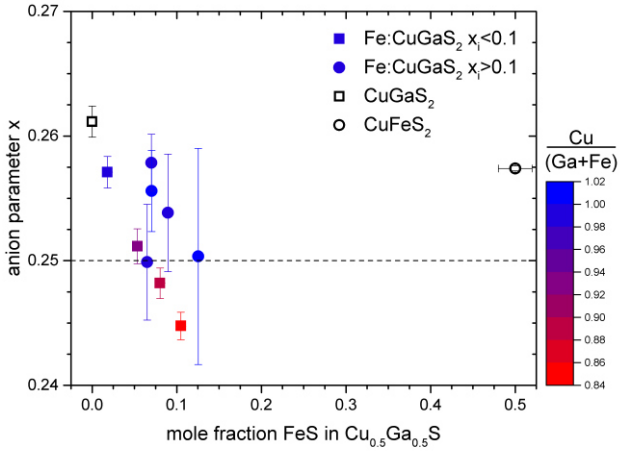

Figure 48 – Anion parameter x as function of the measured iron content of the chalcopyrite type phase, color-coded regarding the Cu/(Ga+Fe) ratio.

The tetragonal distortion *u* is very sensitive to changes of the chemical composition and cation distribution, which are essentially affected by the substitution mechanism. In this particulate case it is necessary to discuss the anion parameter *x* rather than the tetragonal distortion *u*, since the tetragonal distortion *u* is the deviation from the ideal anion position, whereas the anion parameter *x* is the position of the anion within the unit cell. For the chalcopyrite type phase from the first experimental set (x_i<0.1) the anion parameter *x* decreases in a linear trend. The increasing iron content shifts the anion into the direction of the 4a site which results in a decreasing anion parameter *x*. At iron content of x_m=0.05 the cation 4a site and 4b site are almost equal in size. For higher x_m the 4b site is larger than the 4a site. Based on this, the chemical evolution of those chalcopyrite type phases is assumed to be a coupled substitution ($Cu^+ + Ga^{3+} \leftrightarrow 2Fe^{2+}$) which is furthermore encouraged by increasing trends of the lattice parameters. By considering these observations with those of the anion parameter the incorporation of divalent iron occupying the 4b position can be concluded.

A different behavior is obtained from the second experimental set (x_i>0.1) were the tetragonal distortion *u* varies between zero and 0.008(2) without clear trend. From chemical evolution a unilateral substitution was concluded. However, the increase of lattice parameter *c* cannot be explained by an incorporation of trivalent iron only. The incorporation of a certain amount of divalent iron might be the reason for the increase of lattice parameter *c*. The decrease in tetragonal distortion *u* could be explained by a certain amount of disorder, which is in particular, Ga_{Cu} and Cu_{Ga}.

4.3.3 Optoelectronic properties of iron alloyed $CuGaS_2$

The optoelectronic properties of iron alloyed chalcopyrite type materials were already probed before. Marsen et al. [32] showed the positive effect on the optoelectronic properties by transmittance, reflectance and absorption, due to the incorporation of iron into the chalcopyrite type structure. Results concerning photoluminescence experiments were not published. Five iron containing chalcopyrite type phases of this work were investigated in terms of optoelectronic properties, using photoluminescence spectroscopy. Within the range from 0.8eV to 2.6eV no PL intensity was observed. The incorporation of iron seems to produce too many defects, which results in rather metal like than semiconductor optoelectronic properties.

4.3.4 ^{57}Fe Mössbauer spectroscopy at iron containing $CuGaS_2$

The ^{57}Fe Mössbauer spectroscopy is applicable on the ^{57}Fe isotope exclusively. The ^{57}Fe isotope has the ability to cause recoilless absorption and emission of gamma radiation due to its quantum number $I \neq 0$. The abundance of ^{57}Fe of the total iron is only 2.119% [139]. The samples examined already contain a very small amount of iron, which is furthermore decreasing the number of Mössbauer active nuclei by the abundance of the ^{57}Fe isotope. In addition, the containing copper massively absorbs the radiation. The measurements could not be used and the incorporation of Fe^{2+} could not be proven.

4.3.5 Interim conclusion

The solubility of iron and gallium into the chalcopyrite type $Cu(Ga,Fe)S_2$ is supposed to be complete [5, 138]. However, in the substitution experiments with an initial substitution parameter of >0.1 a phase separation was observed which cannot be interpreted as a miscibility gap. This is more a result of the sample synthesis, as all samples containing one chalcopyrite type phase are synthesized in a first experimental set (x_i<0.1), while those containing two chalcopyrite type phases were synthesized in a second experimental set (x_i>0.1). This is supported by the different substitution behavior of the two studies. The chalcopyrite type phases of the first experimental set (x_i<0.1) show a constant Cu/Ga ratio and a decreasing Cu/(Ga+Fe) ratio with increasing iron content, indicating a coupled substitution ($2Fe^{2+} \rightarrow Cu^{+}+Ga^{3+}$). This results in the preferred incorporation of the larger divalent iron, which is in good agreement with the observed increasing lattice parameters. The chalcopyrite type phases of the second experimental set (x_i>0.1) shows an increasing Cu/Ga ratio and a constant Cu/(Ga+Fe) ratio with increasing iron content which was concluded as unilateral substitution of gallium and iron. This in turn is in good agreement with the trends resulting from the lattice parameters. However, the chalcopyrite type phases from both studies do not strictly follow Vegard´s law, which in turn indicates an incorporation of divalent iron. No activity was observed from PL spectroscopy. Unfortunately, ^{57}Fe Mössbauer spectroscopy could not be evaluable because of the high amount of copper and the very low amount of ^{57}Fe.

Table VIII - Overview of the observed secondary phases from iron alloyed $CuGaS_2$ as well as their commonness; the max. volume fraction of the phases was determined by Rietveld refinement of XRD data.

observed secondary phases	max. volume fraction [%]	present in _ of 9 powder samples
γ Cu-Ga	4.31(7)	1

4.4 Manganese incorporation into the chalcopyrite type phase

4.4.1 Phase analysis

The incorporation of manganese into the chalcopyrite type structure of $CuGaS_2$ was studied in six sample series. The total number of samples is 32. The sample series are divided into two different sets. Set (1) is following the pseudo-binary section of $Cu_{0.5}(Ga_{0.5-x}Mn_x)S$ (unilateral substitution) which was supposed to form an intermediate band within the forbidden gap and set (2) is following pseudo-binary section of $(Cu_{0.5}Ga_{0.5}S)_{1-x}(MnS)_x$ (coupled substitution). In addition, different synthesis routes were tested to improve the synthesis and to evaluate the influence of the synthesis temperature. These effects are discussed in the following chapter (4.4.4).

Most of the synthesized powder samples are multiphase, comparable to the BSE micrograph shown in Figure 49 (left), only two samples are single phase. The three different phases can easily be distinguished by their massive contrast in chemical composition in the BSE micrographs (Figure 49 (left)). The chalcopyrite type phase shows a medium atomic mass (light grey), the darker grains correspond to a lighter atomic mass, which belongs to MnS or Digenite. The immense contrast of the white phase to the grey phases is attributed to the lack of sulfur in these phases. These bright phases consist exclusively of metals. Three different metallic phases were determined from the combination of wavelength-dispersive X-ray spectroscopy and X-ray diffraction. The first metallic phase refers to the fcc copper, which contains only small amounts of gallium and even smaller amounts of manganese. The second metallic phase, which is only present in absence of the fcc copper phase, is determined as γ phase (Cu-Ga). This intermetallic compound generally shows a chemical composition of Cu_2Ga, which also contains small amounts of manganese. The enrichment of gallium during the crystallization of a copper-rich alloy or intermetallic compound produces the third metallic compound. This compound has a chemical composition of $CuGa_2$. The occurrence of some secondary phases is specific to the intended substitution series. Samples with initial weight following the unilateral substitution show all described secondary phases, whereas in those following the coupled substitution only γ Cu-Ga and MnS occur. A second difference between the two substitution routs also applies to secondary phases. The intended substitution mechanisms influence the amount of secondary phases. Samples from the unilateral substitution show a secondary phase fraction of up to 36%, while the coupled substitution shows only up to 7%.

It should be noted that the total manganese, initial and measured, is calculated as divalent (MnS), regardless of its intentional substitution mechanism.

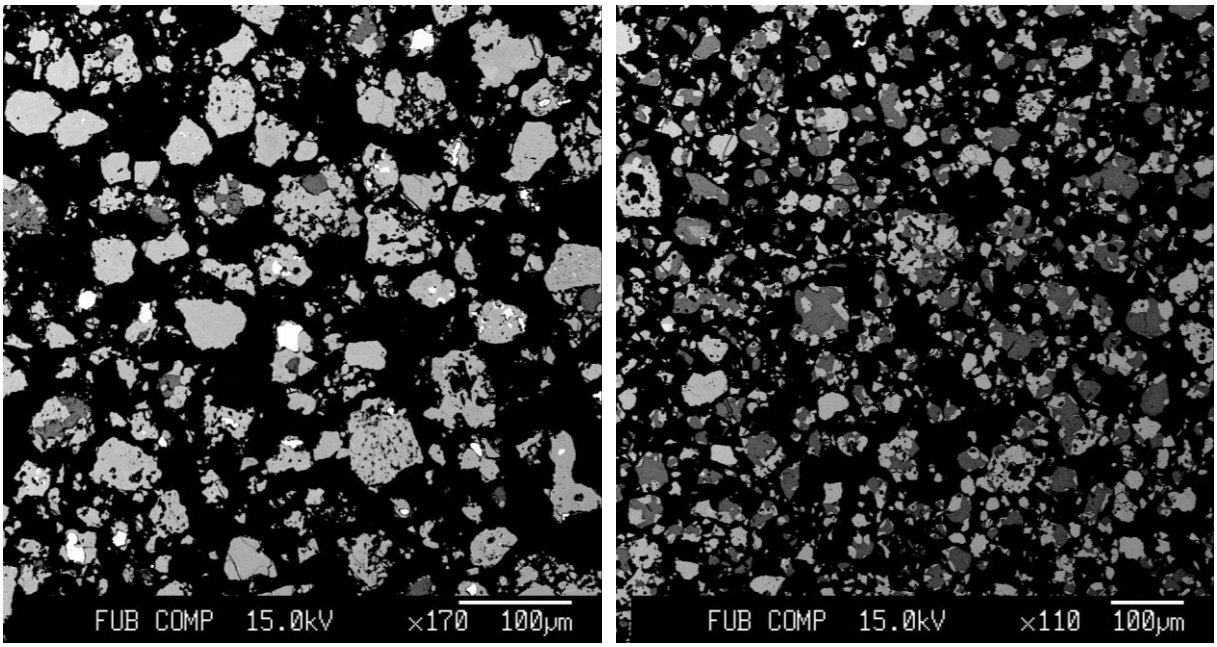

Figure 49 - BSE micrograph of manganese alloyed chalcopyrite samples, light gray grains: chalcopyrite type phase, dark gray grains: manganese sulfide, white grains: intermetallic compounds (left); light gray grains chalcopyrite type phase, dark grains: 3-3-4 Cu-Ga-Mn-sulfide phase (right).

Manganese shows a good incorporation into the $CuGaS_2$ chalcopyrite type compound. The maximum solubility of MnS into $Cu_{0.5}Ga_{0.5}S$ is 0.098(2)mol%. This value is similar to the observations from manganese incorporation in $CuInS_2$ and $CuInSe_2$ by Herkelrath [106]. At a molar fraction of x>0.1 a phase separation appears as shown in Figure 50 (right). In addition to a chalcopyrite type phase, a phase with the chemical composition $Cu_{0.3}Ga_{0.3}Mn_{0.4}S$ occurs. This 3-3-4 phase was found in several powder samples, as shown in Figure 50 (left). In the range of 0.1<x<0.4 no further phases were observed; this region was interpreted as miscibility gap.

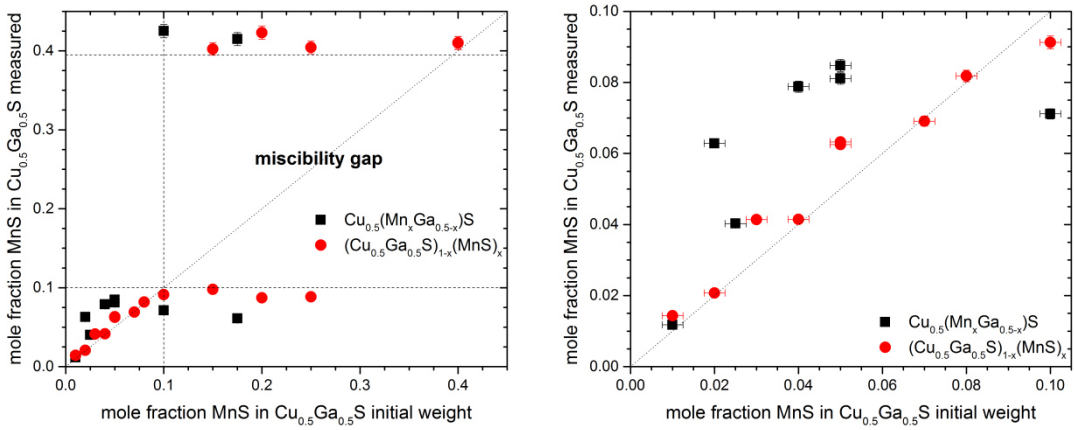

Figure 50 - Initial vs. measured manganese mole fraction within the chalcopyrite type phase (left) and zoomed-in area with manganese mole fraction below the miscibility gap (right).

The differences of the intended substitution route within the solubility range is very pronounced (Figure 50 (right)). The deviations of the measured manganese content (x_m) from the initial manganese content (x_i) is very small for the chalcopyrite type phases following the coupled substitution, whereas for the chalcopyrite type phases following the unilateral substitution, the deviation is much larger. This results from the manganese enrichment of the chalcopyrite type phase due to the occurrence of high amounts of manganese poor metal compounds. It can be assumed that the actual substitution mechanism is rather coupled than unilateral. This is supported by the Cu/(Ga+Mn) ratio, shown in Figure 51 (b). In case of the deliberately unilateral substitution, gallium is replaced by manganese and this ratio remains constant while the manganese incorporation is increased. But the observed trend of the two intentional substitutions is the same. In general, manganese replaces both, copper and gallium, in equal quantities. The Cu/Ga ratio shows that it is not a unilateral substitution of gallium and manganese that would show a decreasing trend. The ratio of copper to gallium varies without any significant trend.

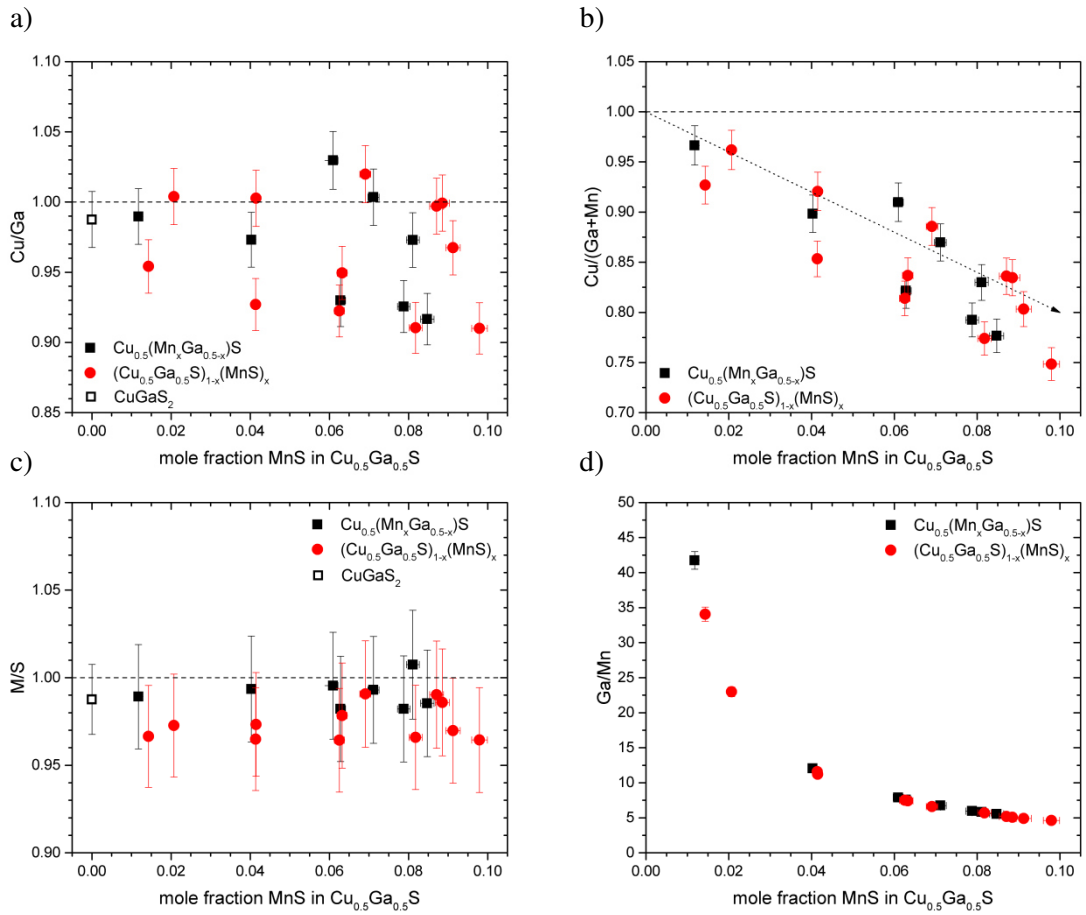

Figure 51 - Copper to gallium ratio (a), copper to gallium plus manganese cations ratio (b), cation to anion ratio (c) and gallium to manganese ratio (d) as a function of the manganese molar fraction within the chalcopyrite type phase.

Almost all synthesized chalcopyrite type phases show a M/S ratio of slightly below 1, although despite the relatively large errors it can be assumed that all chalcopyrite type phases are slightly metal depleted (M/S<1). Therefore, the presence of copper vacancies can be expected. Additionally, the chalcopyrite type phases following the coupled substitution show slightly lower M/S ratios than the chalcopyrite type phases following the unilateral substitution. However, the increasing manganese molar fraction incorporated into the chalcopyrite type phase does not lead to a trend in the M/S ratio. This also supports the theory of a coupled substitution mechanism, as otherwise the M/S ratio must be increased or decreased depending on the charge of the manganese ions.

4.4.2 Structural trends of the chalcopyrite type phase

The incorporation of manganese into the chalcopyrite structure is clearly visible in the structural trends of the chalcopyrite type phases. Due to the larger atomic radius of manganese, compared to gallium and copper, the lattice parameter *a* and *c* increase with increasing manganese content. In addition to the incorporated manganese content, the lattice parameters are influenced by the actual Cu/Ga ratio and the M/S ratio (shown in Figure 52), the lattice parameter *c* is much more sensitive to changes in the chemical composition than lattice parameter *a*. The figure shows *c/2*, but even there the deviation is much more pronounced than for *a*. Both, the Cu/Ga and the M/S ratio, influence the lattice parameters in the same way. In general, an increase of copper vacancies and a higher gallium content lead to a decrease in the lattice parameters. In the case of vacancies, a decrease in the lattice parameters is obvious. In the case of the Cu/Ga<1, the unit cell shrinks due to the smaller atomic radius of gallium in comparison to the atomic radius of copper. Whereas, if Cu/Ga>1, the amount of incorporated copper is higher than that of gallium, resulting in an increase in lattice parameters.

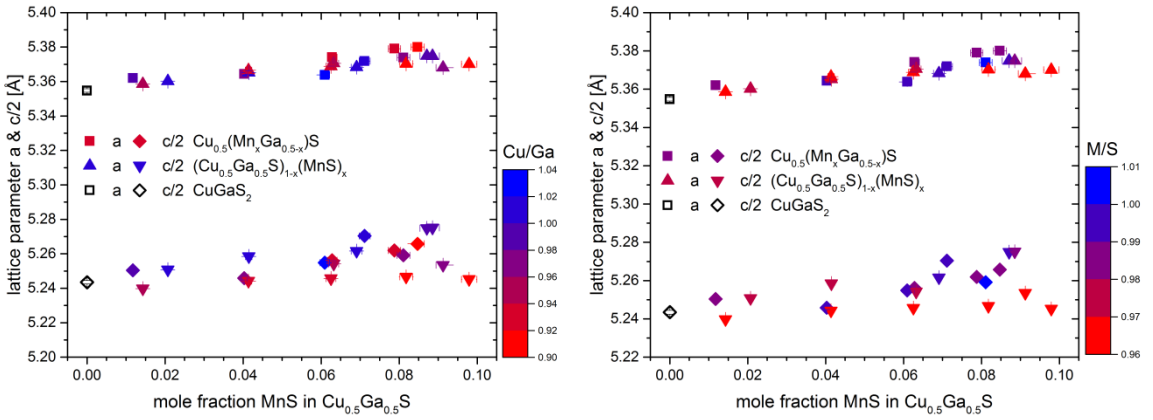

Figure 52 - Lattice parameter of chalcopyrite type phase as function of the containing MnS mole fraction, color-coded regarding their copper to gallium ratio (left) and their cation to anion ration (right).

However, the general increasing trend of *a* and *c/2* is very similar, resulting in a constant *c/2a* ratio. The absolute changes of the tetragonal deformation η are comparatively small. Nevertheless, the tetragonal deformation *η* varies with increasing manganese concentration, but no general trend can be observed. The variation is induced by differences in the manganese distribution on the two cation sites and the Cu/Ga ratio. As previously assumed, a low Cu/Ga ratio leads to a decrease in the lattice parameters, which is more pronounced for lattice parameter *c*. This results an increase of the tetragonal deformation *η*, since *c* shrinks more than *a*. The opposite is the case with a high Cu/Ga ratio. Due to the higher copper concentration, the lattice parameter *c* increases more strongly than the lattice parameter *a* which leads to a decrease in tetragonal deformation *η*. The influence of the vacancy concentration on the tetragonal deformation *η* is not as clear as that of the Cu/Ga ratio. However, it can be assumed that the situation is similar. A high vacancy concentration leads to a stronger decrease of the lattice parameter *c* than *a*, whereby the tetragonal deformation increases.

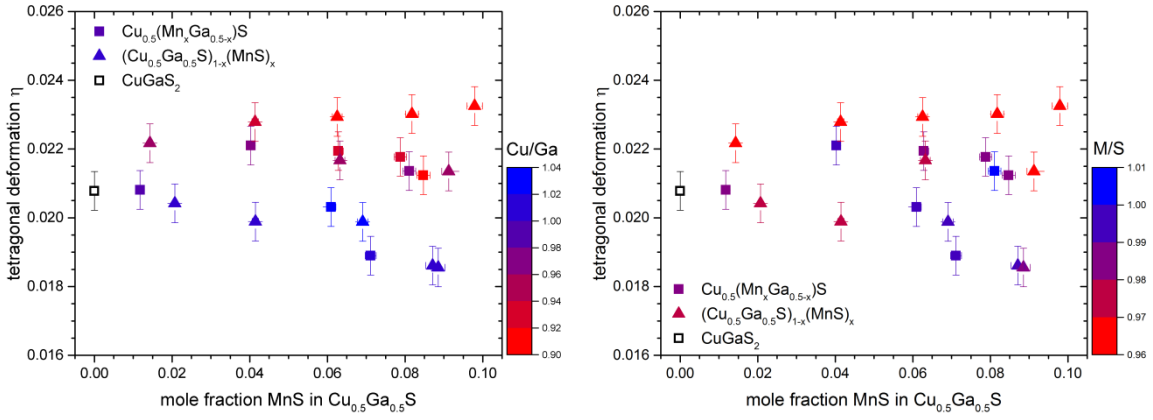

Figure 53 - Tetragonal deformation η of chalcopyrite type phase as function of the containing MnS mole fraction, color-coded regarding their copper to gallium ratio (left) and their cation to anion ration (right).

The Cu/Ga ratio has a lasting effect on the lattice parameters which cannot be explained exclusively by Ga_{Cu} and Cu_{Ga} anti-sites. In a copper-poor chalcopyrite type phase manganese is supposed to occupy primarily the 4a site. While in a copper-rich chalcopyrite type phase manganese preferably occupies the 4b site [140]. This site preference of manganese, which is forced by the Cu/Ga ratio, results in the observed trends of tetragonal distortion *u*. The trends from tetragonal distortion *u* (shown in Figure 54) show a clear dependence on the Cu/Ga ratio. In a copper-poor chalcopyrite type phase manganese preferentially occupies the 4a site. This in turn leads to an enlargement of this site and an increase in tetragonal distortion *u*. In copper-rich chalcopyrite type phases the inverse behavior can be observed. Manganese prefers to occupy the 4b site which is enlarged and the tetragonal distortion decreases. This behavior was already observed from the tetragonal deformation. However, the tetragonal distortion is much more sensitive to changes in cation distribution than the tetragonal deformation. For the tetragonal distortion, a further dependence on the vacancy concentration is observed. A high vacancy concentration leads to a preferred manganese incorporation on 4a site, while at low concentration, manganese preferentially occupies 4b.

Accordingly, two different extrema can be observed. (1) A copper-poor chalcopyrite type phase with a high concentration of vacancies in which the tetragonal deformation is increasing with increasing manganese content. (2) A chalcopyrite type phase which is copper-rich (Cu/Ga>1) with a M/S ratio slightly below 1, showing a low vacancy concentration and a decreasing trend with increasing manganese content.

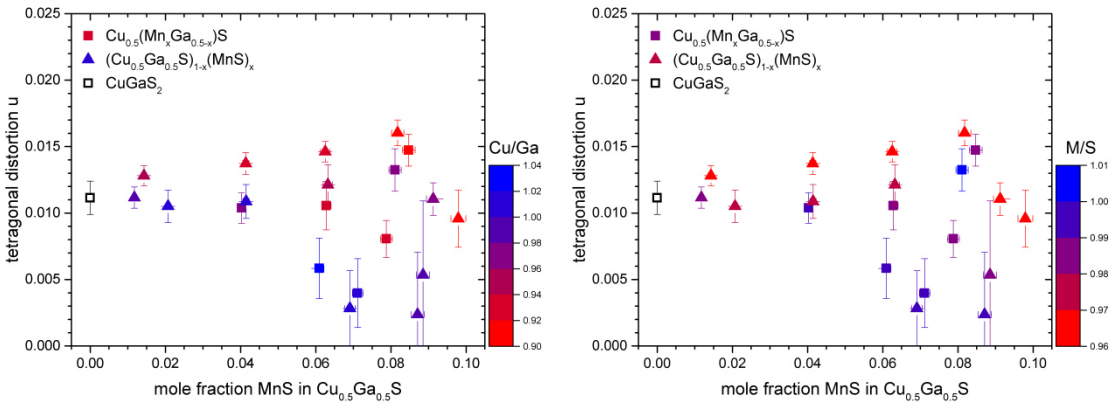

Figure 54 - Tetragonal distortion u of chalcopyrite type phase as function of the containing MnS mole fraction, color-coded regarding their copper to gallium ratio (left) and their cation to anion ration (right).

The role of the Cu/Ga ratio can be further demonstrated by comparing the experimental structural parameters with the expected structural evolution, taking into account Vegard´s law [141]. To establish this correlation, the structural parameters of the endmembers $CuGaS_2$, $MnGaS_2$ and $CuMnS_2$ (listed in Table IX) were calculated by the formalism of Jaffe and Zunger [19], particularly explained in chapter 4.4.6 using the atomic radii of Shannon [36]. The lattice parameter *a* increases in both cases, but the lattice parameter *c* only increases when manganese substitutes gallium. When manganese substitutes copper, the lattice parameter *c* remains constant. Derived from this, the tetragonal deformation η increases with copper-manganese substitution and decreases with gallium-manganese substitution. The evolution of the tetragonal distortion *u* is similar to that of the tetragonal deformation η. If Cu/Ga<1 the tetragonal distortion *u* is increased, whereas if Cu/Ga>1 the tetragonal distortion *u* is decreased.

Table IX - Calculated structural parameters of the endmembers using the routine from Jaffe and Zunger [19], (-) is marking actually negative values.

endmember	*a* [Å]	*c* [Å]	η	*u*
$CuGaS_2$	5.359	10.531	0.0175	0.008
$MnGaS_2$	5.507	10.531	0.0439	0.022
$CuMnS_2$	5.441	11.201	0.0294 (-)	0.014 (-)

The trend lines, shown in Figure 55, are permanently shifted against the experimental data. If this offset is neglected, the deviations of the lattice parameter *a* with respect the evolution due to Vegard´s law cannot be explained exclusively by changes in the Cu/Ga ration. In contrast to the lattice parameter *a*, the lattice parameter *c*, the tetragonal deformation and the tetragonal distortion show a traceable dependence on the Cu/Ga ratio. A low Cu/Ga ratio leads to a preferred manganese incorporation on the 4a site, the experimental values rather follow the trend according to Vegard´s law between $CuGaS_2$ and $MnGaS_2$. At high Cu/Ga ratios the opposite can be observed. The offset and the large deviations of the calculated structural parameters with respect to the experimental values result from the calculation itself, which does not consider copper vacancies, for example.

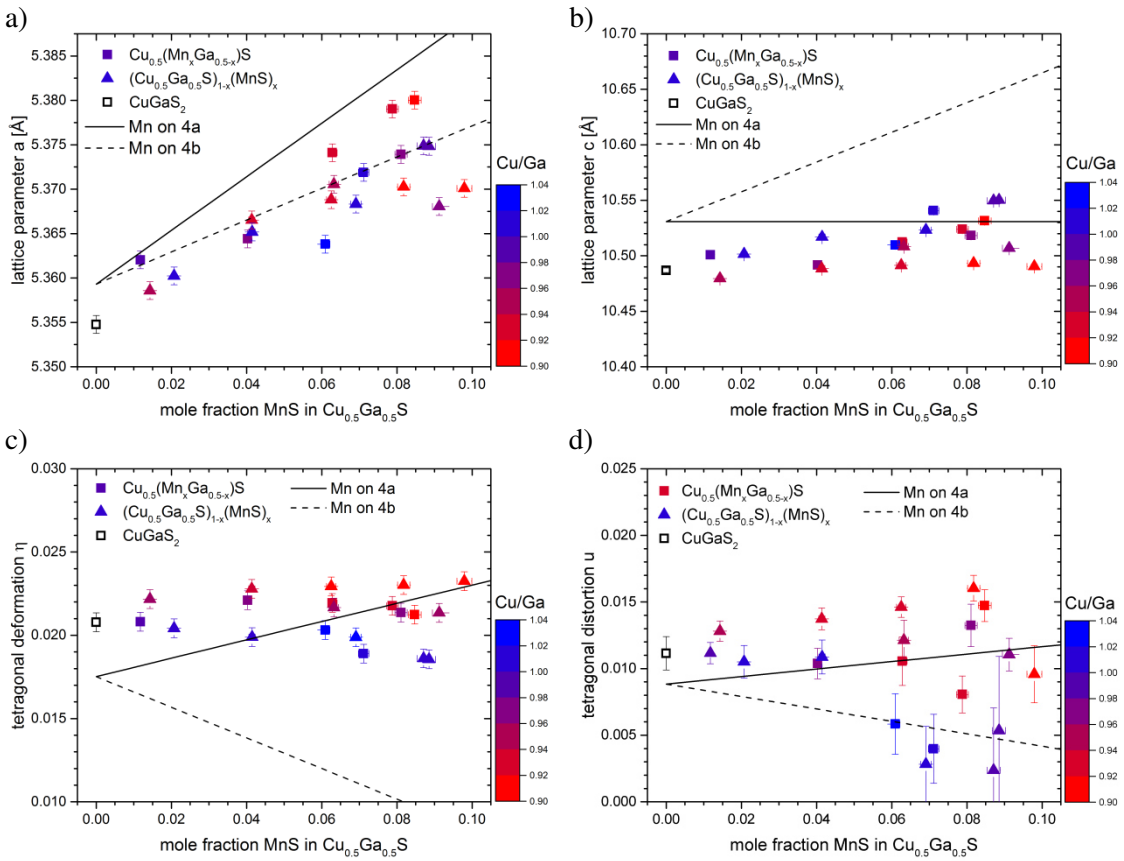

Figure 55 - Structural parameters obtained by XRD, color-coded regarding the measured copper to gallium ratio, compared to the structural evolution considering Vegard´s law as a function of the MnS molar fraction (lines); lattice parameter a (a); lattice parameter c (b); tetragonal deformation η (c); tetragonal distortion u (d).

All observed data points plot between two extremes, but due to the neglect of copper vacancies within the calculation most of the observed data point are not represented by the calculated trends. The possibility of deriving the distribution of manganese within the chalcopyrite type structure depending on the chemical composition is not fulfilled. Further interpretations of the structural parameters that refer to the local structure will be discussed in a following chapter (4.4.6).

4.4.3 Cation distribution within the chalcopyrite type phase

The cation distribution was determined by applying the average neutron scattering length analysis method using the site occupancy factors from Rietveld refinement of neutron diffraction data. As first-order approximation, manganese was distributed on the two cation positions 4a and 4b in such a way that the depletion of copper on 4a and gallium on 4b was compensated. This model considers vacancies as intrinsic defect and is marked with blue triangles in the figure (w/o anti-site defects). At the copper site vacancies ($V_{Cu}^{\square}$) are expected to occur due to a significantly lower defect formation energy than at the gallium site ($V_{Ga}^{\square}$) [34]. In the second-order approximation, the cations are distributed taking anti-site defects into account in order to match the experimental data. In literature V_{Cu}^{-} and Ga_{Cu}^{2+} defects are described as the dominant intrinsic defects of chalcopyrite type $CuGaS_2$ [34]. However, uncharged copper vacancies and copper on gallium anti-site defects are reported as well. The V_{Cu} and Ga_{Cu} defects are the reason for the p-type conductivity in $CuGaS_2$ chalcopyrite type semiconductors [34]. To limit the possibilities, the defect with the highest formation energy of the considerable intrinsic defects (copper on gallium) was restricted to a minimum. If the first-order approximation average neutron scattering length matches the experimental values, no anti-site defects were introduced. If this is not the case, anti-site defects have been introduced. The distribution of cations to model the actual distribution is an iterative process. If the average neutron scattering length of position 4a is higher than the experimental value, the amount of manganese and/or gallium must be increased. This forces a certain amount of copper to the 4b position. If the average neutron scattering length is lower as the observed value, the manganese content must be reduced and the gallium content on 4a site increased. This leads to a decrease in the gallium content and an increase in manganese content on 4b site. The same procedure applies to the average neutron scattering length of the 4b site, whereby the first-order approximation always serves as starting point.

The obtained average neutron scattering length of the cation sites from the chalcopyrite type phases that were synthesized following the unilateral substitution and the corresponding modeled average neutron scattering length are shown in Figure 56. The cation distribution according to the second-order approximation is displayed directly next to the average neutron scattering length. It is shown that the first-order approximation is only suitable for one of the four chalcopyrite type phases (x_m=0.079). To represent the measured average neutron scattering length of two chalcopyrite type phases with a lower manganese incorporation (x_m=0.012 and x_m=0.0063), copper on gallium anti-sites are required. Whereas to represent those of the chalcopyrite type phases with a higher manganese content (x_m=0.085) gallium on copper anti-sites are required. However, the chalcopyrite type phase with x_m=0.079 was slightly improved by the introduction of 1% Ga_{Cu} anti-sites.

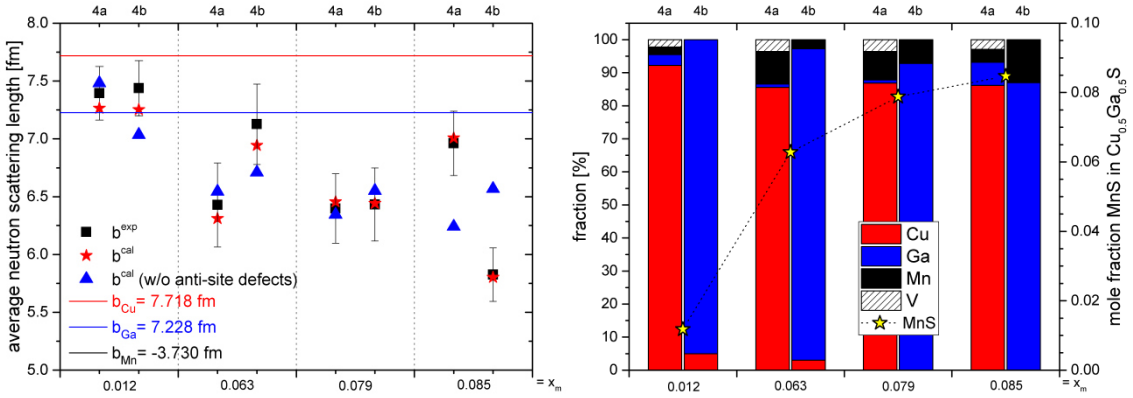

Figure 56 - Average neutron scattering length (left) and corresponding cation distribution (right) of chalcopyrite type phases from unilateral substitution; x_m refers to the manganese molar fraction within the chalcopyrite type phase.

General trends can be derived from the cation distribution of the unilateral substitution series. The amount of Cu_{Ga} decreases and the amount of Mn_{Ga} increases with increasing manganese content. These trends can also be observed in the chalcopyrite type phases of the coupled substitution series (shown in Figure 57). In addition, the amount of Mn_{Cu} also increases as the manganese content increases. The fraction of V_{Cu} within a substitution series is constant despite increasing manganese incorporation. The general vacancy concentration in the chalcopyrite type phases following the coupled substitution is somewhat higher than of the unilateral substitution.

The main difference between the two substitution series is the total amount of intrinsic anti-site defects. While the first-order approximation is only suitable for 25% of the chalcopyrite type phases of the unilateral substitution, it is completely sufficient for 75% of the chalcopyrite type phases of the coupled substitution. Exclusively the chalcopyrite type phase with x_m=0.082 required Ga_{Cu} anti-site defects. Nonetheless, small amounts of Cu_{Ga} anti-site defects are present in all phases.

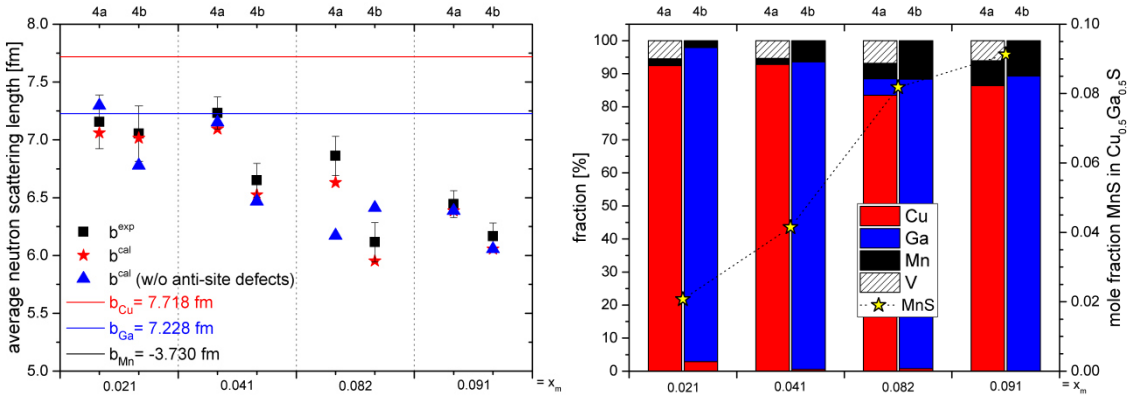

Figure 57 - Average neutron scattering length (left) and corresponding cation distribution (right) of chalcopyrite type phases from coupled substitution; x_m refers to the manganese molar fraction within the chalcopyrite type phase.

The defect concentration results from the cation distribution of the second-order approximation (Figure 58). The concentration of defects ranges from $7x10^{19}cm^{-3}$ to $2x10^{21}cm^{-3}$. A defect concentration of $7x10^{19}cm^{-3}$ refers to a site fraction of 0.5% and a defect concentration of $2x10^{21}cm^{-3}$ refers to a site fraction of 15%.

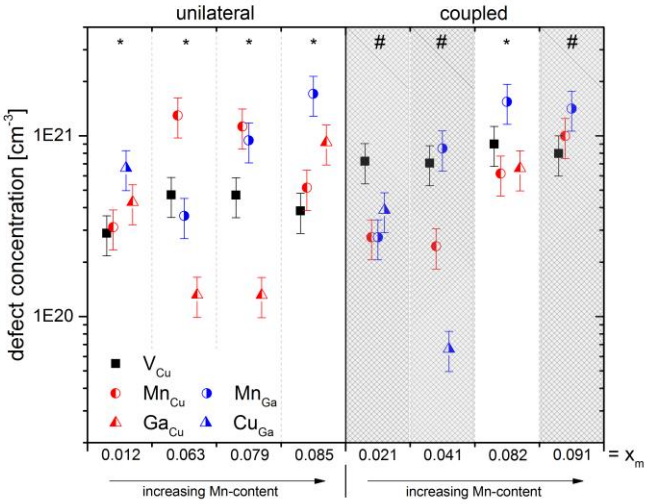

Figure 58 - Defect concentration calculated from cation distribution, x_m refers to the manganese molar fraction within the chalcopyrite type phase. (*) marks samples which show one PL band, (#) marks samples with two PL band.

The dominant intrinsic defects are copper vacancies and Ga_{Cu} anti-sites, for chalcopyrite type phases marked with *. The chalcopyrite type phases marked with # do not show Ga_{Cu}, but only Cu_{Ga} anti-sites and V_{Cu} as dominant intrinsic defects. These two different types result each in specific optoelectronic properties, which will be discussed in a separate chapter (4.4.7).

In this study no site preference of manganese is observed from the average neutron scattering length analysis as proposed by Picozzi et al. [35]. Based on defect formation energies, manganese was proposed to substitute rather gallium than copper [35]. The site preference, proposed by Zhao and Zunger [140], could not be clearly determined from the chalcopyrite type phases examined. Therefore, a study would be necessary were the experimental focus is more on the Cu/Ga ratio. However, this would not reflect the observed substitution mechanism (coupled), which was always assumed to be unilateral by the theoreticians.

4.4.4 Impact of synthesis temperature on chemical composition and structural trends

The influence of the synthesis temperature is very important, as the phase formation is essentially influenced. At a higher or lower synthesis temperature, specific secondary phases can be avoided, but these are mainly influenced by the initial chemical composition. For this reason, the intentional substitution series must be discussed separately. The experimental approach following the unilateral substitution consists of two experimental sets, one synthesized at low and a second at high temperatures. In the low temperature synthesis (600°C /900°C), γ (Cu-Ga), υ (Cu-Ga) and MnS are present, whereas in the high temperature synthesis (700°C /950°C) only metallic copper (alloyed with gallium and manganese) and digenite are present. In the coupled substitution series, the phase content is independent of synthesis temperature. However, a general assumption about the phase content from the synthesis temperature is not possible, which is why this would have to be investigated in particular. The influence of synthesis temperature on the chemical composition of the chalcopyrite type phase is shown in Figure 59 and Figure 60. In the unilateral sample series, a higher synthesis temperature forms chalcopyrite type phases which are less copper-poor or even copper-rich and more stoichiometric (M/S≈1) compared to low temperature synthesis. The same applies to the coupled substitution sample series, when comparing 600°C /900°C and 700°C /800°C. Furthermore, it can be assumed that chemical changes are caused by the final temperature of the first synthesis and not by an increase in temperature of the intermediate step. For the high temperature sample series (700°C /950°C), however, no trend can be observed. The differences in Cu/(Ga+Mn) can be explained by the differences in Cu/Ga ratio.

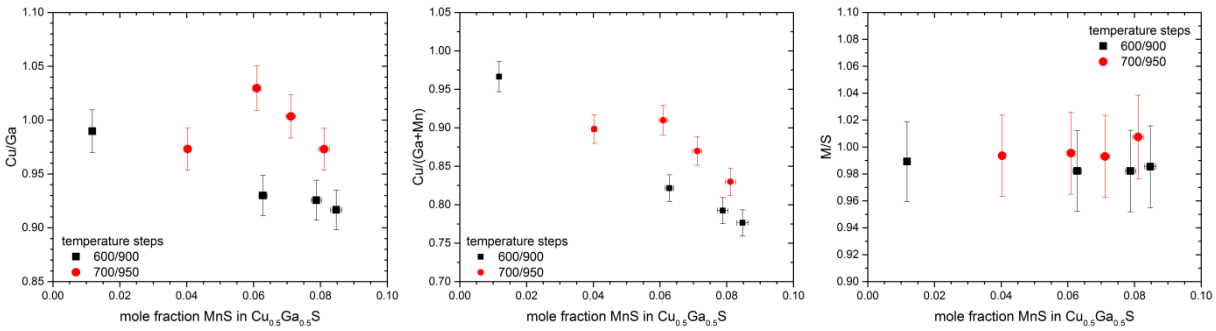

Figure 59 - Effect of synthesis temperature on the Cu/Ga ratio (left), the Cu/(Ga+Mn) ratio (middle) and the M/S ratio (right) of chalcopyrite type phases from unilateral substitution series.

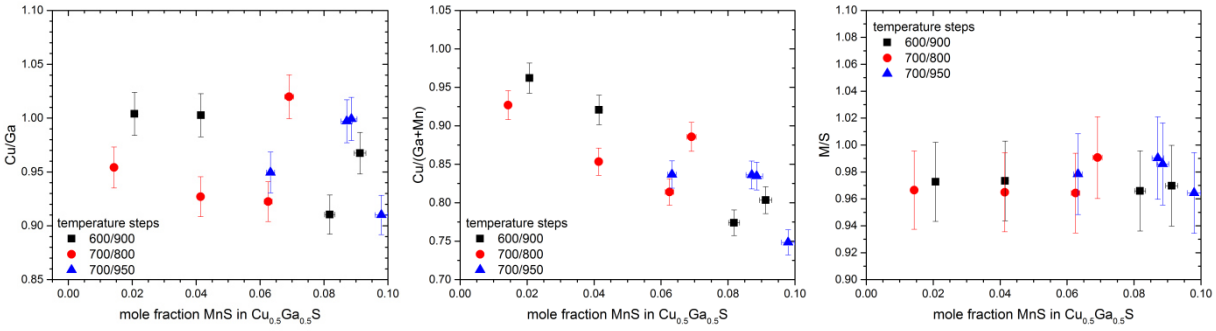

Figure 60 - Temperature dependency of the Cu/Ga ratio (left), the Cu/(Ga+Mn) ratio (middle) and the M/S ratio (right) of chalcopyrite type phases from coupled substitution series.

The effect on structural parameter results from the chemical composition. At high synthesis temperatures, the chalcopyrite type phase is approximately stoichiometric, while at low synthesis temperatures, the chalcopyrite type phase is copper poor, resulting in a higher copper vacancy concentration. This results in larger tetragonal deformation η and tetragonal distortion u for samples synthesized at lower final temperatures. This can be observed at least for the chalcopyrite type phases from the coupled substitution series (Figure 62).

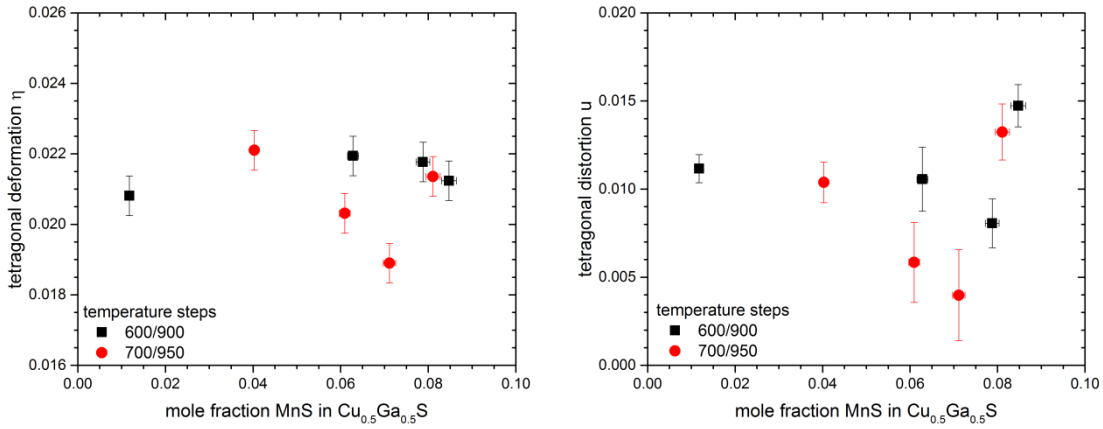

Figure 61 - Effect of synthesis temperature on tetragonal deformation η (left) and tetragonal distortion u (right) of chalcopyrite type phases from unilateral substitution series.

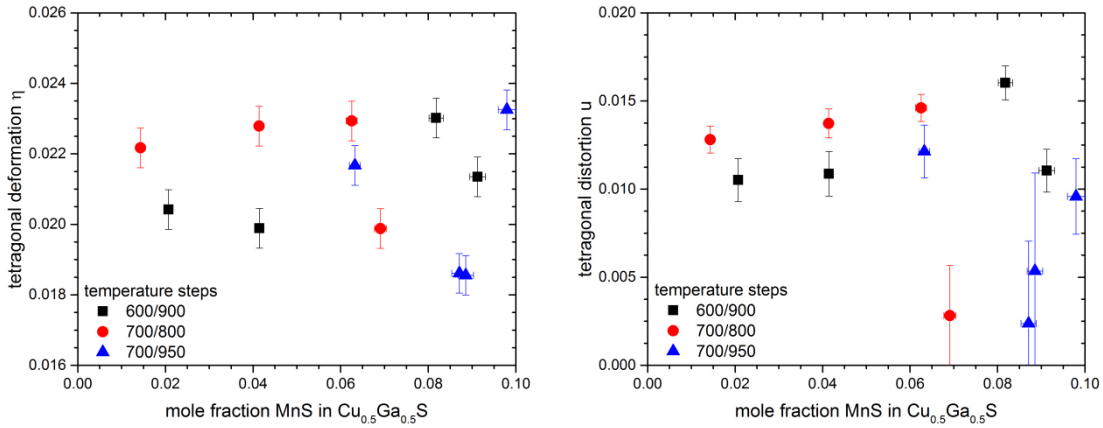

Figure 62 - Temperature dependency of tetragonal deformation η (left) and tetragonal distortion u (right) of chalcopyrite type phases from coupled substitution series.

It can be concluded that both the phase content and the chemical composition are influenced by the synthesis temperature and that the chemical composition in turn influences the structural parameters. However, the temperature programs developed in this work are still not optimally suited for the synthesis of these samples and would have to be optimized further.

4.4.5 The 3-3-4 ($Cu_{0.3}Ga_{0.3}Mn_{0.4}S$) phase

In several manganese containing samples, a phase was observed by WDX which corresponds approximately to a chemical composition $Cu_{0.3}Ga_{0.3}Mn_{0.4}S$. The WDX measurements of this phase show a certain variation, but no indication of inhomogeneity or phase separation by drastically changes in chemical composition. Nevertheless, the 3-3-4 phase was not observed by X-ray diffraction. Therefore, two powder samples with this chemical composition were synthesized and analyzed like all other samples. The BSE micrographs (Figure 63) show a slightly inhomogeneous, but single-phase sample. In addition, the WDX analysis confirms the initially weighted chemical composition, as shown in Figure 64. However, the X-ray diffraction pattern shows two phases (Figure 65), one chalcopyrite type phase and one phase with a NaCl type structure which is assumed to be MnS. The refined lattice parameters of the chalcopyrite type phase allow the conclusion that the manganese incorporation is rather low. Compared to $CuGaS_2$, the lattice parameter *a* is increased by 0.005Å, while lattice parameter *c* is reduced by 0.014Å. In view of this, the 3-3-4 phase is not a real phase, but an intergrowth of two phases. A possible scenario for the formation might be a solid-state phase separation during cooling. This phase separation leads to a very fine layered structure of $CuGaS_2$ and MnS. The intergrowth is so fine that the electron beam of the microprobe hits both areas equally and the analysis always delivers similar results.

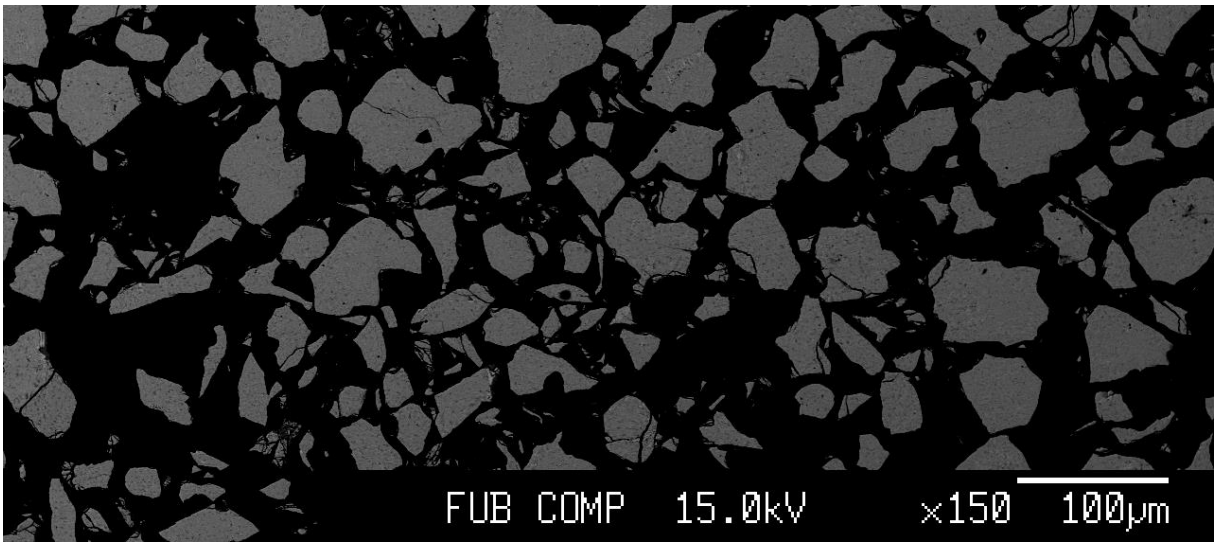

Figure 63 - BSE micrograph of the expected 3-3-4 phase.

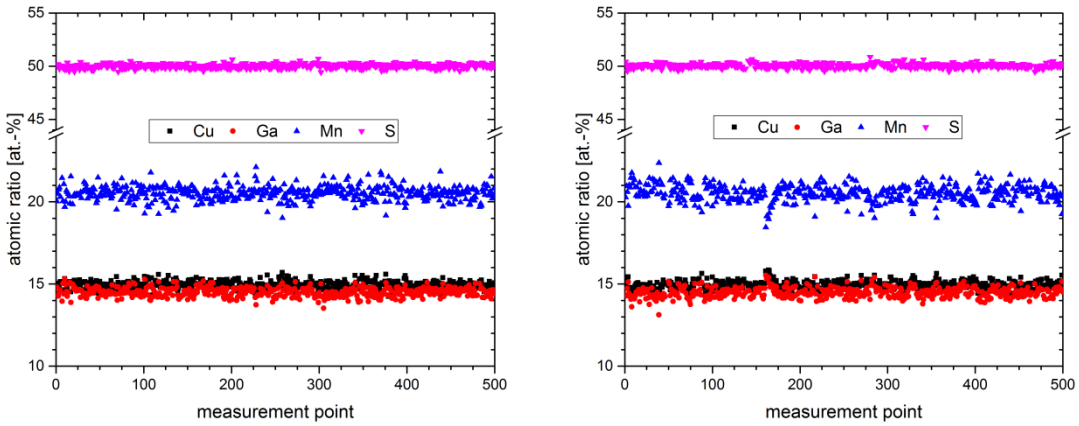

Figure 64 - Measured atomic ratio of both 3-3-4 samples, left - I, right - II.

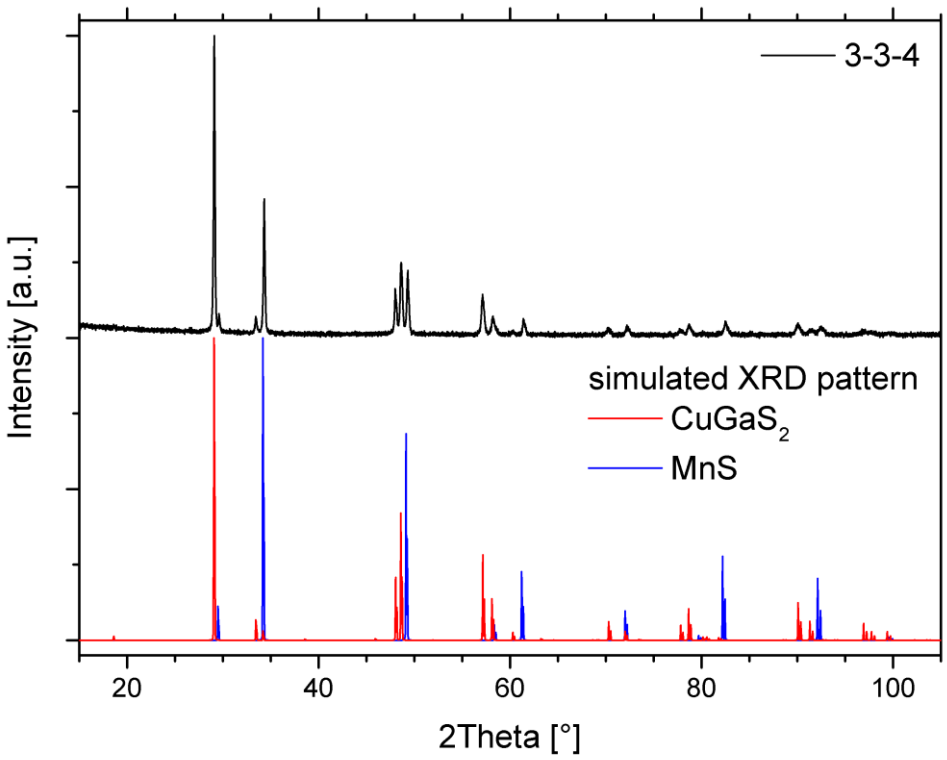

Figure 65 - Obtained XRD pattern of the 3-3-4(I) sample and simulated XRD pattern of chalcopyrite type $CuGaS_2$ and MnS.

Similar observations were made within the pseudo-binary sections of $CuInS_2$ and $CuInSe_2$ with MnS. Figure 66 is showing the intergrowth of $CuInS_2$ and MnS observed from transition electron microscopy and Figure 67 the intergrowth of $CuInSe_2$ and MnS. Both figures show a very fine intergrowth of a chalcopyrite type phase with manganese sulfide. At high temperatures the solubility of gallium and copper in the cubic αMnS phase as well as the solubility of manganese into the chalcopyrite type phase is much higher. Similar observations have been found in literature in the MnS-$CuInS_2$ system [142]. During cooling, the solubility decreases and the phases begin to separate. The solid-state phase separation also results in a twinning structure as shown in the marked areas in Figure 66, where the selected area diffraction (SAD) image was captured [106].

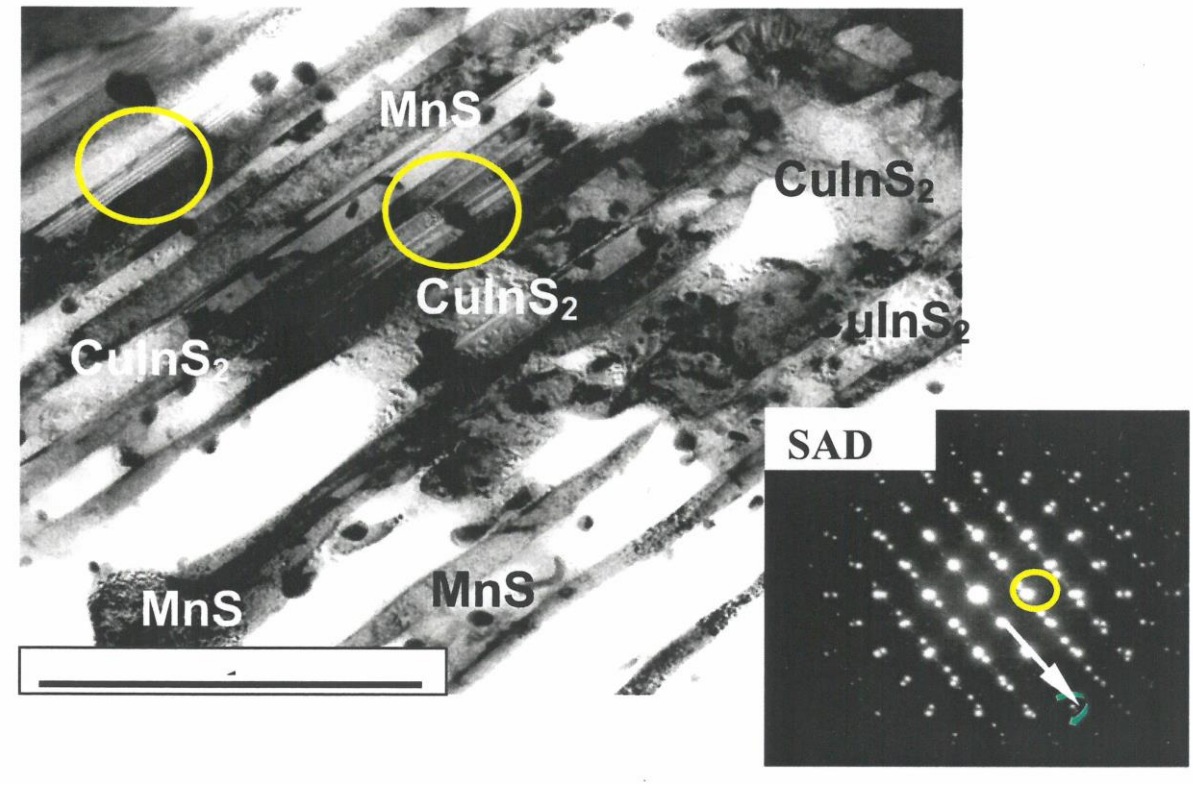

Figure 66 - TEM bright field image with corresponding electron diffraction pattern taken from Herkelrath [106].

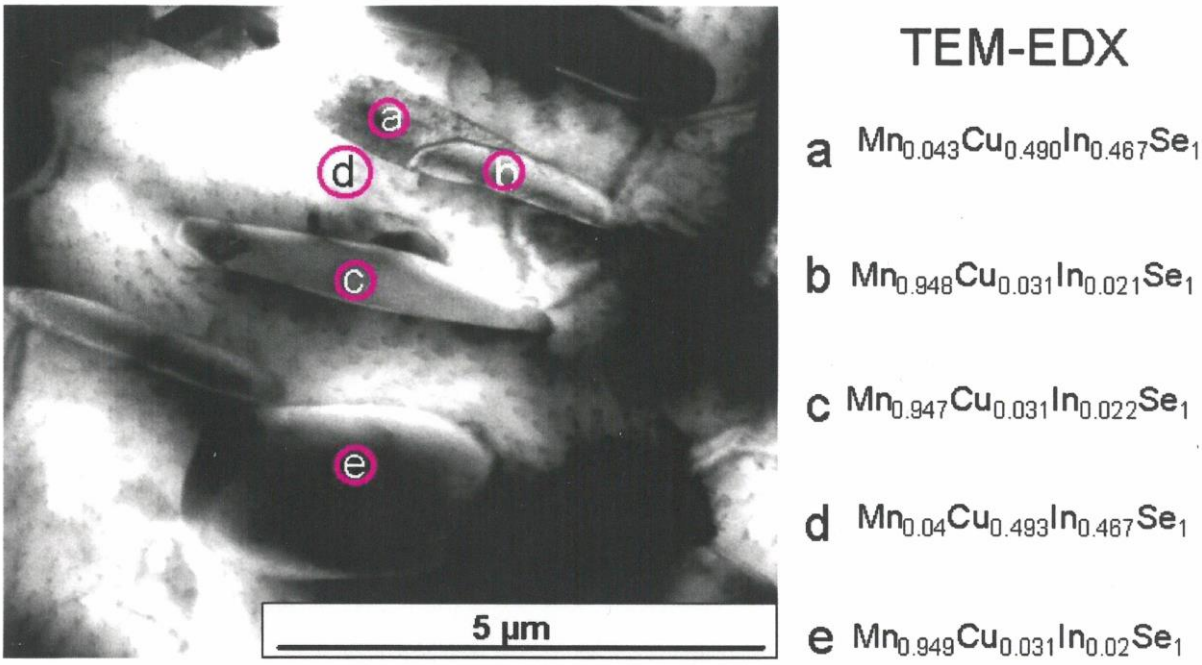

Figure 67 - TEM bright field image with corresponding EDX analysis of the marked phases taken from Herkelrath [106].

The exsolution behaviors, shown in Figure 66, can be explained by a comparison with the solid solution of $CuGaS_2$ and ZnS. At temperature above 250°C a zinc blende type (Cu, Ga, Zn)S solid solution with a partial occupation of copper and gallium on zinc sites is formed [143]. During slow cooling, diffusive segregation occurs, the Cu and Ga atoms diffuse to collection sites, where they form independent lamellae of gallite ($CuGaS_2$) with S in a now Cu and Ga free host crystal of zinc blende (ZnS) [143]. This phenomenon is called exsolution pseudomorphosis [143]. Manganese sulfide can also crystallize in the sphalerite type structure which is as well as the wurtzite modification of MnS metastable [144, 145]. Thus, the sphalerite type MnS would transform into the rock salt type MnS starting at a temperature of 200°C [144, 145] during the annealing process. The opposite was observed in the solid solution of the selenium endmembers. The binary manganese selenide forms small lenses within a chalcopyrite type matrix. However, the reason why the sulfur solid solution shows a different exsolution behavior than the selenium solid solution is unclear up to now.
In order to observe a (Cu, Ga, Mn)S solid solution in a sphalerite type structure, further experiments, especially with very rapid cooling (quenching), would be necessary.
Unfortunately, there is no 3-3-4 phase in the solid solution of $CuGaS_2$ and MnS.

4.4.6 Calculation of structural parameters regarding copper vacancies

The tetragonal distortion plays a subordinate role in the characterization of chalcopyrite type absorber materials, despite the large influence on the band gap. In literature several names are used to describe the position of the anion, e.g. anion parameter or anion displacement. Most of these parameters refer to the anion position itself, while the tetragonal distortion u describes the deviation from the ideal position. The ideal case is when the cation site 4a and 4b are of the same size. For chalcopyrite type phases, these positions are usually unequal in size. This in turn results in a displacement of the anion towards the smaller site (Figure 68). This changes the bandgap for $CuInSe_2$, E_g=1.4eV at x=0.25 and E_g=0.6eV at x=0.20 [19]. The same behavior was also calculated for $CuAlS_2$, E_g=1.5eV at x=0.25 and E_g=2.4eV at x=0.30 [19]. If the anion is moved in the direction of the trivalent cation, the bandgap increases. This fundamental correlation is shown in Figure 69 together with a comparison of the calculated and experimental values for the anion parameter x from the examples given above.

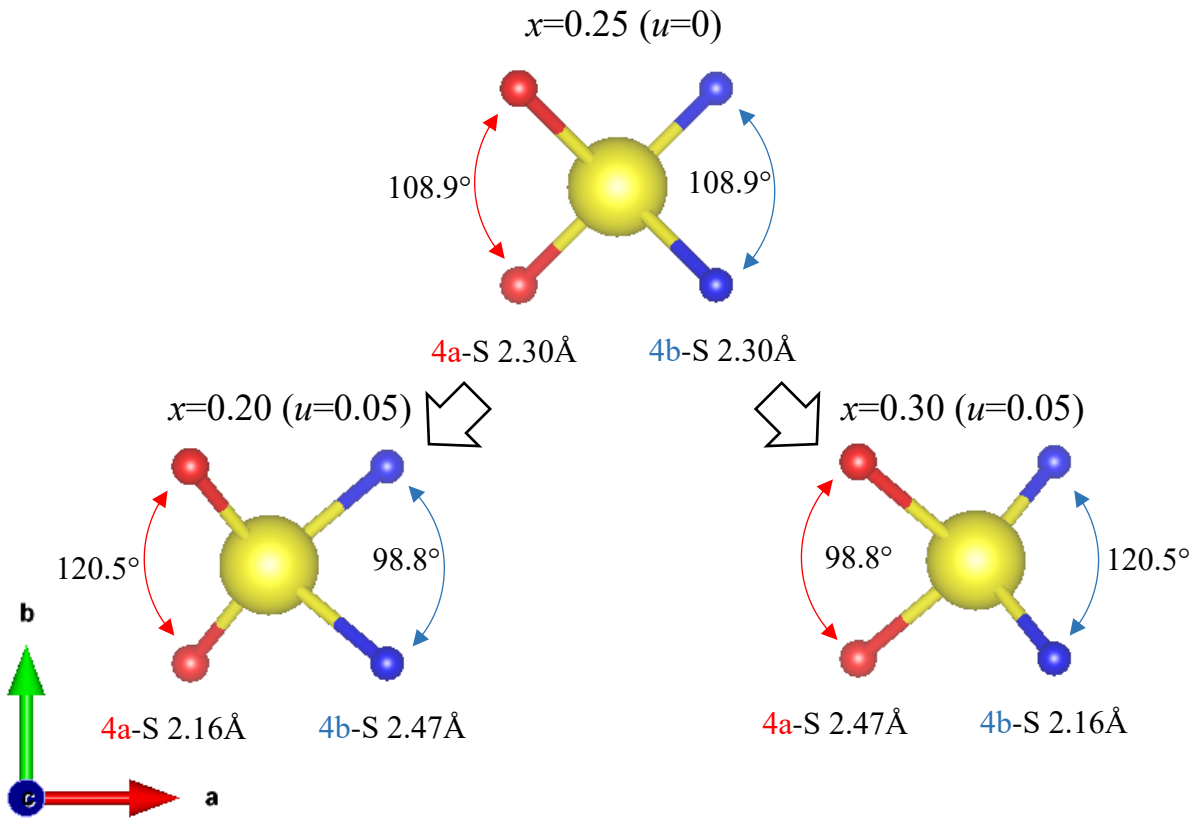

Figure 68 - Detailed view on a $Cu_{0.5}Ga_{0.5}S$ tetrahedron from the chalcopyrite type structure with the bond length of the cation site 4a and 4b to the sulfur anion, as well as the 4a-S-4a and 4b-S-4b bond angles with respect to the anion parameter x.

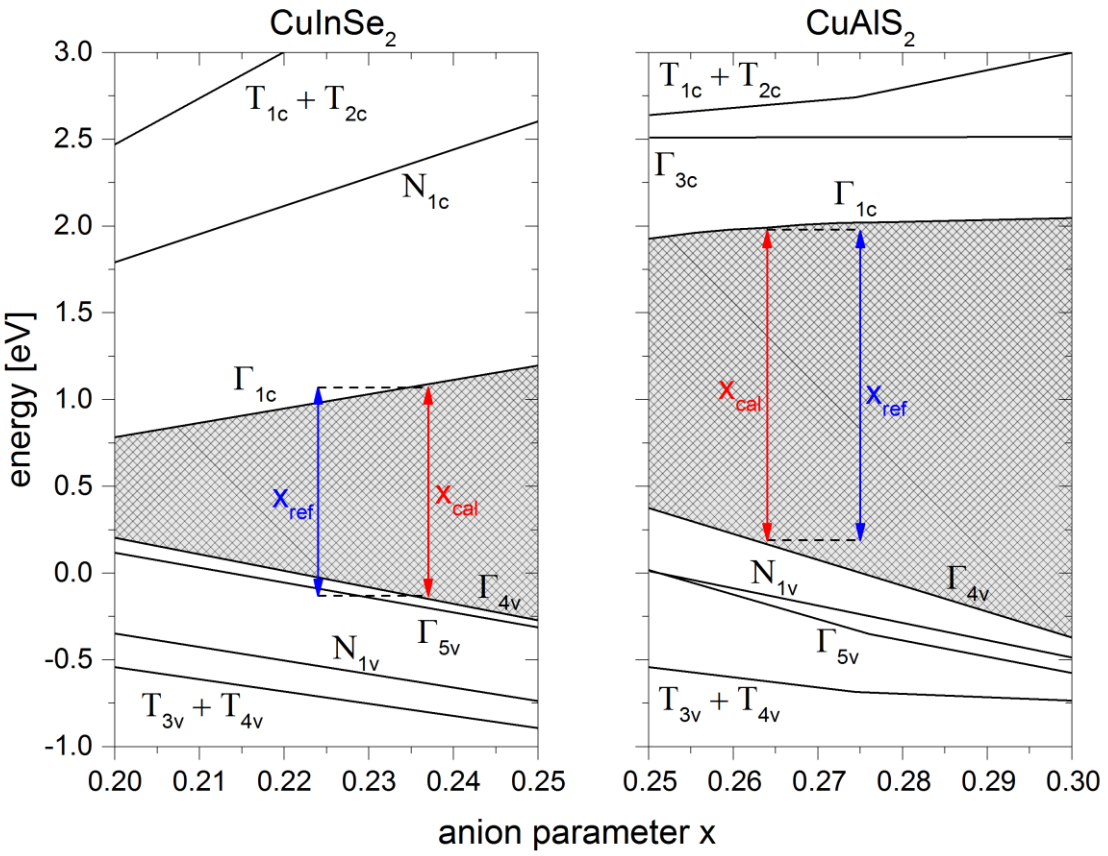

Figure 69 - Variation of band energies at high-symmetry points of $CuInSe_2$ (left) and $CuAlS_2$ (right) with anion parameter x after Jaffe and Zunger [19]. Shaded areas denote the direct band gap; arrows mark the calculated [19] (red) and experimental [146] (blue) values.

The anion parameter *x* is in first approximation dependent on the ratio of the mean radii of the cation sites 4a (R_{4a}) and 4b (R_{4b}) (see Figure 3) according to Jaffe and Zunger [19]. Jaffe and Zunger [19] published a method for calculating the anion position based on the bond length of the cations to the anion. In the first step, a bond mismatch parameter α (Equation (11)) and a mean-square bond β (Equation (12)) are calculated. These are calculated from the bond length or the atomic radii which gives the opportunity of modeling the cation distribution within the chalcopyrite type structure.

$$\alpha = R_{AC}^2 - R_{BC}^2 = (r_A + r_C)^2 - (r_B + r_C)^2 \quad (11)$$

$$\beta = R_{AC}^2 + R_{BC}^2 = (r_A + r_C)^2 + (r_B + r_C)^2 \quad (12)$$

These two parameters are related to calculate the dimensions of the unit cell. The resulting a^2 (Equation (13)), refers to the area of the base surface, which is further used to calculate η^2 (the cubic tetragonal deformation, Equation (14)).

$$a^2 = \frac{12\alpha^2}{2\beta + \alpha - [(2\beta + \alpha)^2 - 18\alpha^2]^{1/2}} \quad (13)$$

$$\eta^2 = \frac{8(\beta - \alpha)}{3a^2} \quad (14)$$

From this, u can be calculated by the relation proposed from Abrahams and Bernstein [147], which implies a constant bond angle at the 4b site:

$$u = u_{tet}(\eta) = \frac{1}{2} - \frac{1}{4}(2\eta^2 - 1)^{1/2}. \quad (15)$$

In this case u means the anion displacement parameter, which can easily be converted to the absolute tetragonal distortion *u*:

$$tetragonal\ distortion\ u = |0.25 - x|. \quad (16)$$

Using the cation radii from Shannon [36] (Cu^+ 0.635Å, Ga^{3+} 0.580Å, S^{2-} 1.70Å) the calculated tetragonal distortion of $CuGaS_2$ is *u*=0.0088. The comparison of this value with those from the literature leads to a large discrepancy. The tetragonal distortion in literature varies from *u*=0 [15] to *u*=0.025 [146].

Table X - Compilation of experimentally obtained anion parameter x and tetragonal distortion u.

anion parameter *x*	tetragonal distortion *u*	reference
0.25	0	[15]
0.2539(4)	0.0039(4)	[147]
0.272(5)	0.022(5)	[148]
0.275(5)	0.025(5)	[146]

The tetragonal distortion of $CuGaS_2$ obtained in this study is *u*=0.011 and only slightly above the calculated value. In general, the calculated tetragonal distortion is slightly underestimated in comparison to the observed data, shown in chapter 4.4.2. The reason for this are copper vacancies which are not taken into account in the calculation. This raises the question about the effect of a vacancy and how can it be considered in the calculation. However, the anion must be shifted in the direction of the trivalent cation position. As a first approximation, the radius and the fraction of vacancy can simply be added to the calculation of the bond mismatch parameter α and a mean-square bond β. Using this approximation, the vacancy would require a size of 1.7Å, which is much too large. Taking one step back to the observed and reported average cation radii allows the conclusion that not only the 4a site must increase, but also the 4b site must decrease. The observed average radius of the 4a site is 0.003Å larger than the radius of Cu^+ and the average radius of the 4b site is 0.011Å smaller than the radius of Ga^{3+}. The error of the obtained radii is 0.004Å, respectively. But how do vacancies

affect the local structure? Figure 70 is showing a schematic representation of the environment of a vacancy with three different anion parameters. In the case of a vacancy, four sulfur atoms which are normally separated by a copper atom, are neighbors. As a result, they repel each other and are pushed in the direction of the trivalent atoms. The distance between gallium to sulfur shrinks. Overall, one copper vacancy influences the position of four sulfur atoms. This shift leads to a shortening of eight sulfur to gallium bonds and the expansion of four copper to sulfur bonds. This means that at a copper vacancy concentration of 1%, 4% of the 4a sites are enlarged and 8% of the 4b sites are narrowed.

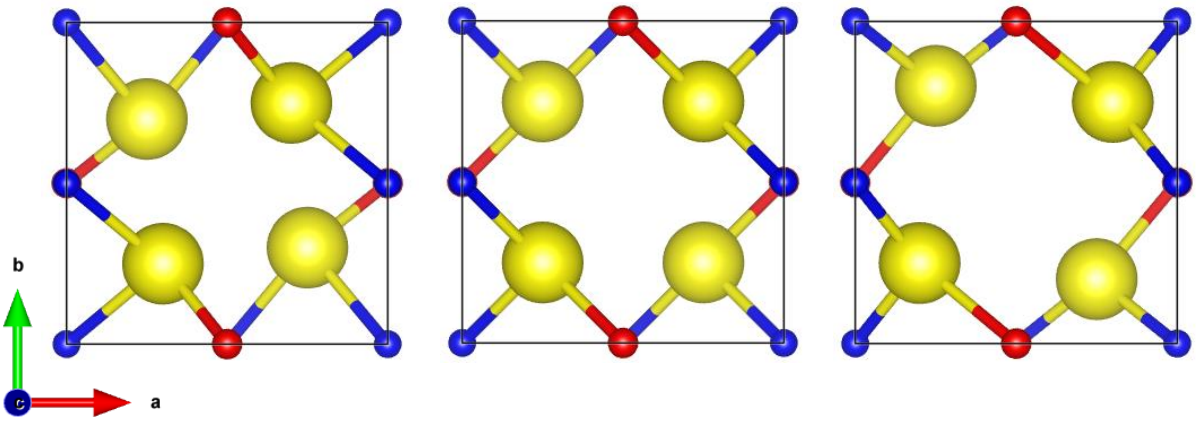

Figure 70 - Chalcopyrite type structure around a copper vacancy with an anion position of x=0.2 (left), x=0.25 (middle) and x=0.3 (right) parallel to the c-axis.

This relationship can be easily integrated into the calculation of the average radii of the 4a and 4b sites. Each cation fraction *x*, which occupies 4a or 4b, is multiplied by the atomic radius. To maintain symmetry, the enlarged copper radius affected by the copper vacancy must be the same size as the vacancy itself. Another limitation is, manganese atoms are not placed on a site that is affected by the copper vacancy. Disorder or anti-site defects can be considered to calculate the tetragonal deformation based on the cation distribution gained, e.g. from neutron experiment, but for a general model they were neglected. However, the anti-site atoms are also not placed on a site that is affected by the copper vacancy. In particular, only Cu^{+} on 4a site and Ga^{3+} on 4b site are placed in copper vacancy affected tetrahedral site. The site radii are calculated as followed:

$$r_A = r_{4a} = r_{Cu} * \left(x_{Cu} - \left(4x_{V_{Cu}}\right)\right) + r_{CuL} * \left(4x_{V_{Cu}}\right) + r_{V_{Cu}} * x_{V_{Cu}} + r_{Ga} * x_{Ga} + r_{Mn} * x_{Mn} \quad (18)$$

$$\rightarrow\ r_A = r_{Cu} * \left(x_{Cu} - \left(4x_{V_{Cu}}\right)\right) + r_{V_{Cu}} * \left(5x_{V_{Cu}}\right) + r_{Ga} * x_{Ga} + r_{Mn} * x_{Mn}$$

$$r_B = r_{4a} = r_{Ga} * (x_{Ga} - 8x_V) + r_{GaS} * (8x_V) + r_{Cu} * x_{Cu} + r_{Mn} * x_{Mn}. \quad (19)$$

The enlargement and the narrowing of the sites was iteratively determined to be 5% of the cation site radius, respectively. This results in a size of 0.667Å for the enlarged copper radius (r_{CuL}) as well as

the copper vacancy radius (r_V) and 0.551Å for the narrowed gallium radius (r_{GaS}). From the corrected average radii of the 4a and 4b sites the tetragonal distortion *u* can be calculated as before. To compare the calculated values with experimental values, the evolution of average radii of the 4a and 4b sites with increasing manganese content is compared with measured data (see Figure 71). Without vacancies, the average radius R_{4a} is always underestimated by the calculation, while the average radius R_{4b} is overestimated. The inclusion of copper vacancies into the calculation results in a very good agreement with the experimental data. The observed tetragonal distortion *u* that are still not represented by advanced calculation plot within these calculated values are most probably affected by a certain amount of disorder.

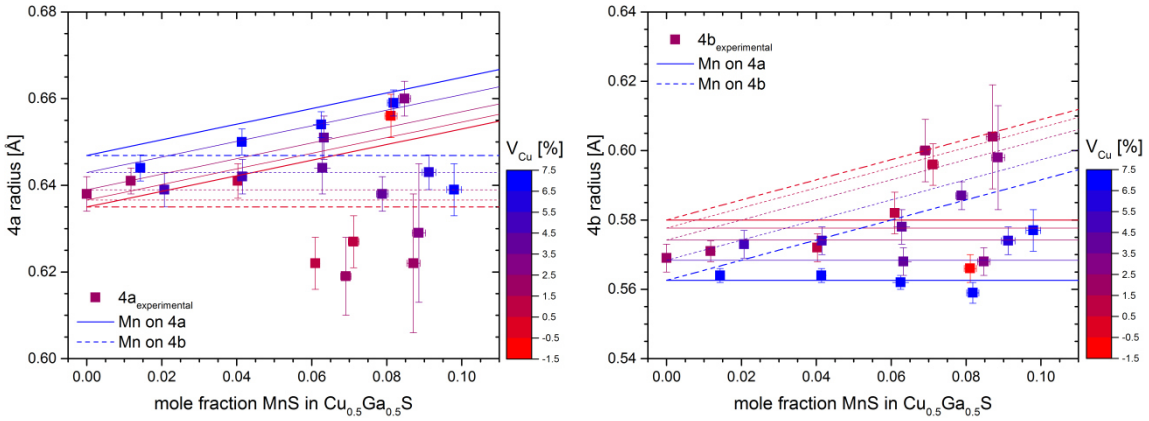

Figure 71 - Observed cation site radii (4a-left, 4b-right) as function of the manganese molar fraction, color-coded regarding the calculated vacancy concentration from chemical composition. As comparison with the simulated evolution due to the incorporation of manganese on 4a or 4b color-coded regarding the calculated vacancy concentration. The two extrema of 0% and 7.5% copper vacancies are displayed in thicker lines.

The effect of vacancies on the tetragonal distortion *u* is not negligible, as shown in Figure 72. Even if the calculated average radii R_{4a} and R_{4b} do not correspond to all measured data, the calculated tetragonal distortion corresponds to the observed tetragonal distortion *u*. But, as shown in Figure 71, the deviation from the calculated values indicates a certain amount of anti-site defects. These would reduce the average radius R_{4a} and increase the average radius R_{4b}, resulting in a decrease of the tetragonal distortion *u*.

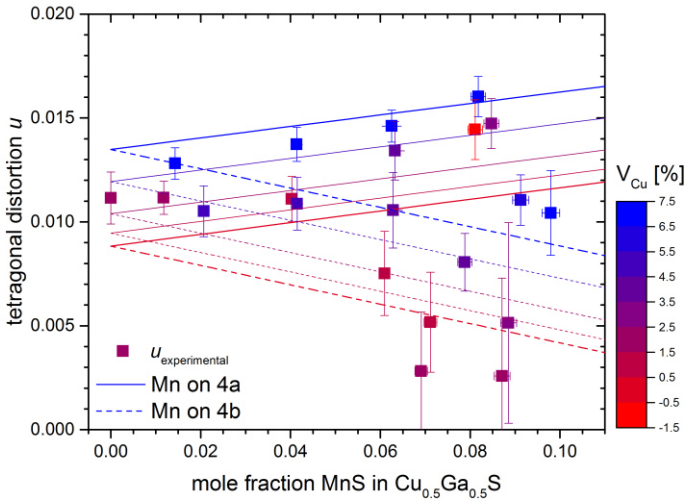

Figure 72 - Observed tetragonal distortion as function of the manganese mole fraction, color-coded regarding the calculated vacancy concentration from chemical composition. As comparison with the simulated evolution due to the incorporation of manganese on 4a or 4b color-coded regarding the calculated vacancy concentration. The two extrema of 0% and 7.5% copper vacancies are displayed in thicker lines.

The restrictions listed above (e.g. no Mn^{2+} within V_{Cu} affected tetrahedron) serve as simplifications and to maintain symmetry. Really considered, the anion is probably shifted in all three directions with different amount. The anion displacement therefore takes place in all directions and not exclusively in $\vec{a}$. However, the main shift will take place in the direction of the trivalent cations, as shown in Figure 71. The observed average radius of the 4a site of $CuGaS_2$ corresponds to the calculated value, without taking vacancies into account. Whereas, the observed average radius of the 4b site does not correspond to the calculated values and vacancies must be considered (see Figure 71). It can be assumed that the anion displacement is locally comparable to that of the kesterite type structure, where the tetrahedron is formed by two cations of equal size and two larger cations, which in turn differ in size. The anion position of this structure is defined as 8g (x,y,z). This results in a different anion displacement in all three directions.

The evolution of the lattice parameters according to Vegard´s law taking into account the copper vacancies, gives an indication of a local lowering of the symmetry, as shown in Figure 73. The lattice parameter *a* is supposed to increase as the concentration of copper vacancy increases, which is not consistent with the experimental data. The experimental data points are arbitrary scattered rather than following a trend caused by copper vacancies. Better conformity can be observed by the lattice parameter *c*, which decreases with increasing copper vacancy concentration. However, the absolute changes are twice as high as the experimental values. The resulting tetragonal deformation η can represent all measured data point and some data points are clearly affected by the vacancies, but the effect of the copper vacancies is overestimated as for the lattice parameters *a* and *c* (Figure 74).

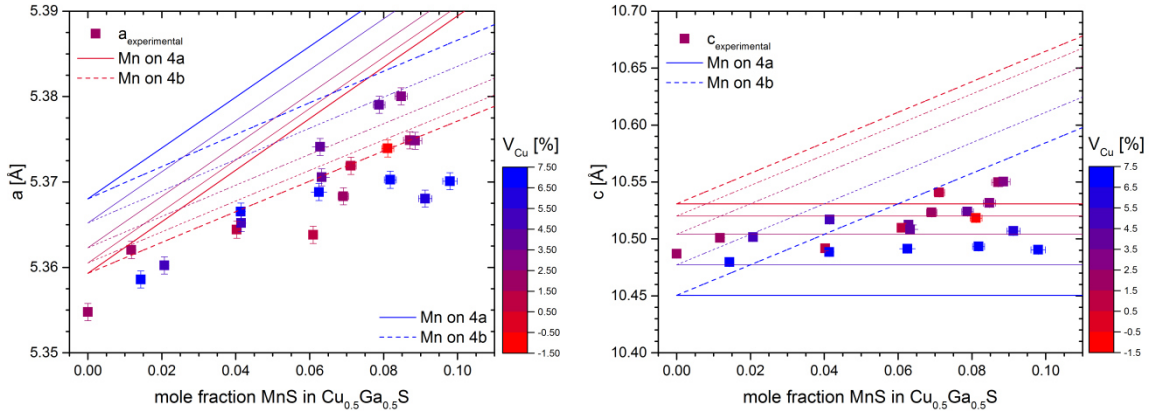

Figure 73 - Observed lattice constants a (left) and c (right) as function of the manganese molar fraction, color-coded regarding the calculated vacancy concentration from chemical composition. As comparison with the simulated evolution due to the incorporation of manganese on 4a or 4b color-coded regarding the calculated vacancy concentration. The two extrema of 0% and 7.5% copper vacancies are displayed in thicker lines.

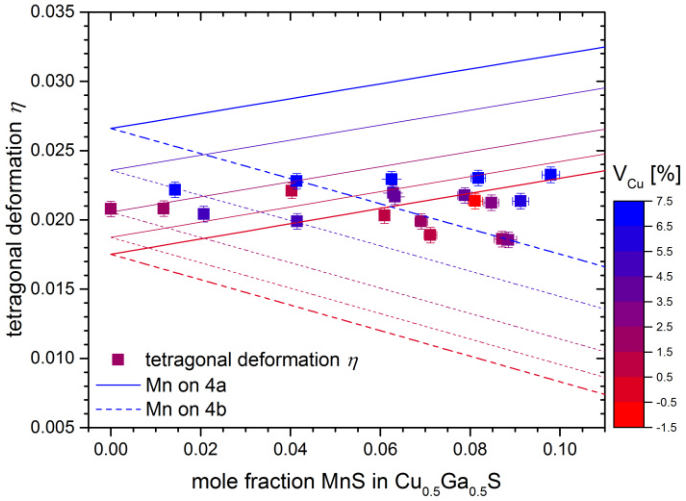

Figure 74 - Tetragonal deformation as function of the manganese molar fraction, color-coded regarding the calculated vacancy concentration from chemical composition. As comparison with the simulated evolution due to the incorporation of manganese on 4a or 4b color-coded regarding the calculated vacancy concentration. The two extrema of 0% and 7.5% copper vacancies are displayed in thicker lines.

From those observations it can be concluded that copper vacancies have no impact on the lattice parameter *a*, but the lattice parameter *c* decreases with increasing vacancy concentration. This can also be seen from a detailed view on the crystal structure in Figure 75. The copper atom at the central site (0.5, 0.5, 0.5) is missing, thus represents a copper vacancy. The surrounding sulfur atoms are drawn in the direction of the remaining three cations. The lattice parameter *c* decreases and the lattice parameter *a* remains unaffected.

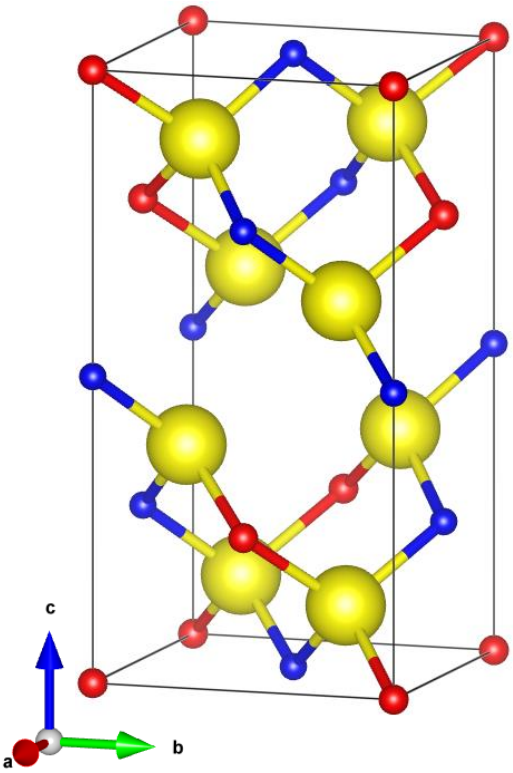

Figure 75 - $CuGaS_2$ chalcopyrite type structure with one copper vacancy (0.5, 0.5, 0.5). The anion are big spheres (yellow-sulfur) and the cations are represented as small spheres, (red-copper, and blue-gallium). The size of the spheres refers to their crystal radius in the structure taken from Shannon [18].

Applying the advanced calculation on the obtained cation distribution of the chalcopyrite type phases from the average neutron scattering length analysis of the neutron diffraction data (chapter 4.4.3), the average cation radii of the 4a and 4b site as well as the tetragonal distortion *u* can be calculated considering copper vacancies. Furthermore, these calculated structural parameters can be compared with the structural parameters observed from Rietveld refinement of X-ray diffraction data. As shown in Figure 76, the calculated average cation radii of the 4a and 4b site can represent 75% of the observed values. However, the 25% which could not be represent, show much too high values for the average cation radius of the 4a site and much too low values for the average cation radius of the 4b site. These radii are probably discordant values resulting from the Rietveld refinement of X-ray or neutron diffraction data.

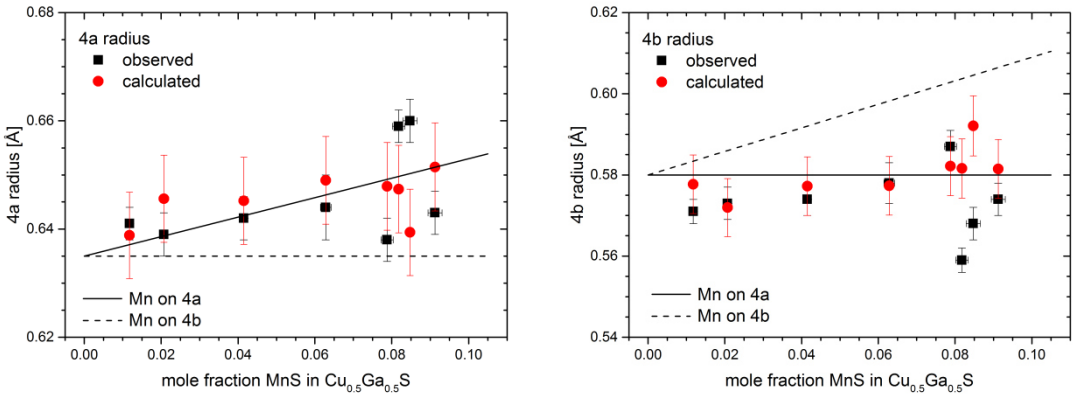

Figure 76 - Comparison of observed and calculated average cation radii of the 4a (left) and 4b (right) site. The lines refer to the trends following Vegard´s law of manganese occupying exclusively the 4a (solid) or 4b (dashed) site, without consideration of copper vacancies.

The same applies to the comparison of the calculated and observed tetragonal distortion *u*. 75% of the observed data can be represented by the calculated values, even those that were too high to be represented by the calculation without considering copper vacancies.

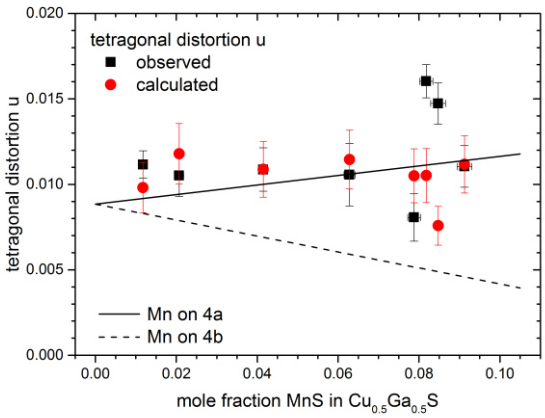

Figure 77 - Comparison of observed and calculated tetragonal distortion u. The lines refer to the trends following Vegard´s law of manganese occupying exclusively the 4a (solid) or 4b (dashed) site, without consideration of copper vacancies.

As mentioned before, the actual anion displacement is rather comparable to that of the kesterite type structure.

However, the locally lowered symmetry cannot be visualized with the methods used (XRD, ND) because the differences in the diffraction pattern are very small and the amount of this locally modified structure is also small. To determine the actual size of a vacancy and the actual anion displacement due to copper vacancies, further analysis with more sensitive techniques are required (e.g. XANES). However, this model is sufficient to calculate the cation site radii and tetragonal distortion with respect to vacancies. To calculate the lattice parameters, the entire formalism must be revised.

4.4.7 Optoelectronic properties of manganese alloyed $CuGaS_2$

The optoelectronic properties of the chalcopyrite type phases which were analyzed also in terms of neutron powder diffraction were investigated using photoluminescence (PL) spectroscopy. Two different photoluminescence spectra were observed, which differ from the spectra of $CuGaS_2$ (see Figure 78). The spectra of $CuGaS_2$ shows two PL bands. The first at ~2.35eV which can be interpreted as PL band, which refers to the transition from the conduction band minimum (CBM) to the valence band maximum (VBM) or band gap energy. The second PL band at ~1.49eV, which is very broad and intense compared to high energy band (~2.35eV), is supposed to be associated with copper vacancies [134]. These two bands were not observed in manganese alloyed chalcopyrite type phases. As already mentioned (see chapter 4.4.3), the chalcopyrite type phases containing manganese can be divided into two groups. One group which is showing only one PL band, and a second group which is showing two PL bands. The PL band – in case of one band – is located at ~1.86eV and appeared in five of eight measurements. This PL band was already observed in measurements of nickel alloyed chalcopyrite type phases of this work (chapter 4.2.3) and by other authors [137, 149] and was interpreted to be associated with sulfur vacancies [137]. As mentioned in the chapter of the optoelectronic properties of nickel containing chalcopyrite type phases, the association to sulfur vacancies is rather doubtful. In the first synthesis step, all samples were synthesized with 10% excess sulfur and annealed with additional 0.1g sulfur. A much more likely explanation for this PL band could be due to anti-site defects. Those showing one PL band have a significant amount of Ga_{Cu} anti-site defects. Whereas those showing two PL bands do not have Ga_{Cu} anti-site defects. These chalcopyrite type phases, as shown in Figure 58, have either no or only Cu_{Ga}. This seems to be the only difference between these two types of chalcopyrite type phases and the reason why this peak is induced by Ga_{Cu} anti-site defects. This theory is supported by literature, here it is assumed that this band is rather "related to an abundance of Ga in the lattice" [150].

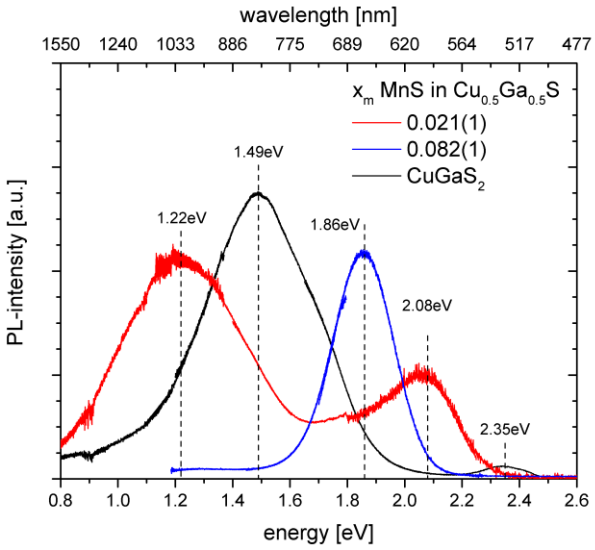

Figure 78 - Comparison of PL spectra of $CuGaS_2$ and two Mn containing $CuGaS_2$ phases from the two different groups (and #).*

The position of the 1.86eV band is quite stable in position and shape, as shown in Figure 79. The small deviations can have several causes, e.g. uncertainties from the measurement, etc.

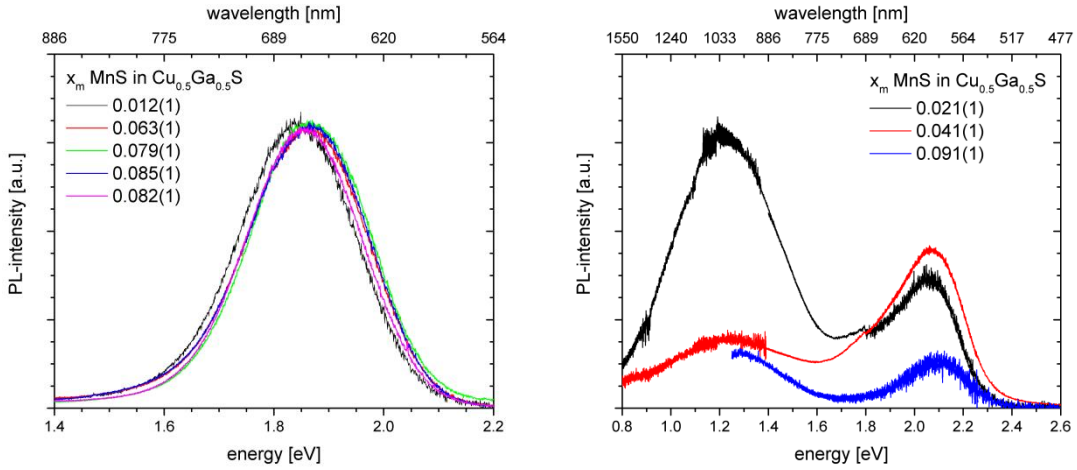

Figure 79 - PL spectra of the chalcopyrite type phases which show only on PL band (left), PL spectra of the chalcopyrite type phases which show two PL bands (right).

The PL spectra with two bands, also shown in Figure 79, were observe in only a minority of manganese alloyed chalcopyrite type phases and in none of the other experimental series (Fe, Ni, Cr) exanimated. The high energy band at about 2.08eV has already been observed before. In literature, this band is referred to the incorporation of manganese into the $CuGaS_2$ chalcopyrite type structure in general [151, 152] or to a donor-acceptor transition between V_{Cu} and Ga_{Cu} [153]. Theoretically, manganese is supposed to occupy only the 4b site, but not the 4a site. Electron paramagnetic resonance (EPR) studies on single crystals have shown the presence of manganese on the 4b site but not on the 4a site [154]. However, the position of the measured PL band does not correspond to the

proposed position of the intermediate band to be created by manganese incorporation [7]. The intermediate band position induced by manganese on gallium defects is proposed to be 1.15eV above VBM [7]. The proposed IB position [7] is very close to the position of the second PL band at 1.22eV. It should be noted that this PL band has never been observed before. The reason for this information leak is the experimental configuration used in previous work. Usually, a CCD camera is used where low energies cannot be detected. An InGaS detector is required to measure energies lower than 1.4eV. As a result, no literature is available for comparison with the observed spectra below 1.4eV. The first interpretation could be that the high energy PL band at 2.08eV refers to the donor-acceptor transition, while the low energy band at 1.22eV is the intermediate band. However, this interpretation neglects the presence of Mn_{Cu} which were observed by applying the average neutron scattering length analysis to obtained site occupancy factors from Rietveld refinement of the neutron diffraction data.

However, the observed spectra can also be correlated with calculations of the band diagram resulting from manganese incorporation at both cation sites [6]. The proposed band diagram (see Figure 80), shows two defect levels within the band gap of $CuGaS_2$, one corresponding to Mn_{Cu} and another one corresponding to Mn_{Ga}. The Mn_{Cu} defect is proposed to have a position of 1.3eV below the CBM, while the Mn_{Ga} has a position of 0.35eV above VBM [6]. With a band gap energy of 2.43eV [12], four transitions are generally possible within the energy range used. From the highest to the lowest energy, the first would be the band-to-band transition of 2.43eV, the second transition from the CBM to the level of Mn_{Ga}, the third transition from the CBM to the level of Mn_{Cu} and the fourth transition from the level of Mn_{Cu} to the level of Mn_{Ga}. Whether the level is visible in the PL spectra depends on the charge of the defect, which in turn depends on the position of the Fermi level. Both defects become negative when the Fermi energy is near the CBM [140]. In this case, Mn_{Cu} and Mn_{Ga} cannot provide holes for the recombination with the exited electron. The resulting PL spectra would exclusively show a band-to-band transition which is not consistent with the observed spectra. If the Fermi level is near the VBM, the Mn_{Ga} defect becomes neutral, while Mn_{Cu} is positive [140]. Both defects now provide holes as recombination centers and become visible in the investigated energy range. The theoretical PL spectra would show three bands, the first refers to the band-to-band transition (2.43eV) and two bands referring to the transition from CBM to the defect states (2.08eV and 1.30eV). This is in very good agreement with the PL spectra observed, despite the small deviations of the low energy band at 1.30eV which was observed at 1.22eV. The two observed PL bands cannot be related to MnS because of its band gap energy of 3.02eV [155] and these two PL bands were even observed from the two single-phase samples. Based on this, the schematic band diagram of Zhao and Zunger [6] can be enhanced by the probable Fermi energy position and the resulting charge of the defects.

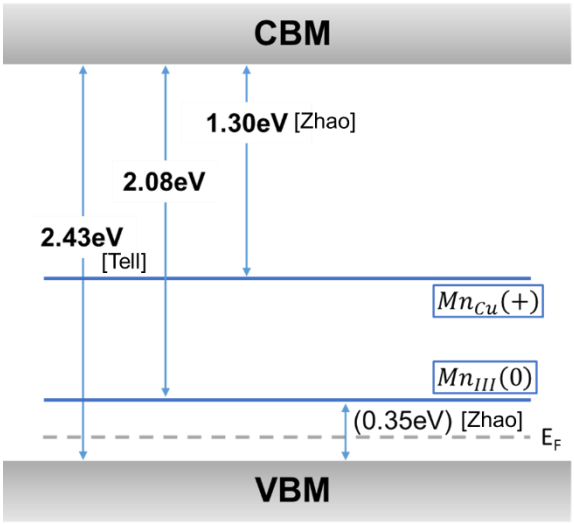

Figure 80 - Schematic drawing of the band diagram with defect levels resulting from the incorporation of manganese adapted from Zhao and Zunger [6]. The bandgap energy of 2.43eV was taken from Tell [12].

The spectra, shown in Figure 79 (right), shows a variation in intensity of the two bands. With the model, that one peak is induced by Mn_{Cu} and the other by Mn_{Ga}, the temptation is high to correlate the ratio of the intensities with the actual cation distribution. However, this correlation cannot be established because not every Mn_{Cu} or Mn_{Ga} induces an active PL defect. Some of the defects can also be deactivated by forming defect pairs. Furthermore, the defect concentration obtained from the average neutron scattering length analysis method is much higher than the expected charge carrier concentrations. These are usually orders of magnitude lower than the defect concentrations obtained [156].

In general, the formation of defect complexes, especially $2V_{Cu}^{-} + Ga_{Cu}^{2+}$, is more favorable than the formation of single defects due to a lower defect formation energy [34]. Neglecting defect formation energies and conclusions from above, six defect complexes are possible:

1. $2V_{Cu}^{-} + Ga_{Cu}^{2+}$
2. $V_{Cu}^{-} + Mn_{Cu}^{+}$
3. $Ga_{Cu}^{2+} + 2Mn_{Ga}^{-}$
4. $Cu_{Ga}^{2-} + 2\ Mn_{Cu}^{+}$
5. $Ga_{Cu}^{2+} + Cu_{Ga}^{2+}$
6. $Mn_{Cu}^{+} + Mn_{Ga}^{-}$

The defect complexes 3 and 6 do not agree with the conclusions based on the observed PL spectra, since the Mn_{Ga} defect is neutral due to the position of the Fermi level. The defect complexes 4 and 5 are very doubtful about the much lower defect formation energy of a neutral $Cu_{Ga}^{\square}$ anti-site defect compare to the charged defects [34]. Based on this, two defect complexes must be taken into account. Unfortunately, no charge carrier concentrations were measured, so that calculations about the share of defect complexes were omitted.

The main reason for the absence of the PL band from manganese related defects in samples with a PL band at 1.8eV is still unclear.

4.4.8 Magnetic properties of manganese containing $CuGaS_2$

For the analysis of the magnetic behavior of materials, it is essential to have phase pure samples or multi-phase samples in which the secondary phases do not incorporate magnetically active elements. In this case, only two single phase samples could be synthesized. Only those were analyzed by the SQUID (Superconducting QUantum Interface Device), since all secondary phases in the multi-phase samples contain manganese.

The field-dependent mass magnetization (Figure 81) becomes linear at higher temperatures. At lower temperatures, a typical s-shaped curve is observed. A linear dependence is typical for paramagnetic, while an s-formed curve is typical for ferromagnetic or superparamagnetic behavior. The magnetization of the chalcopyrite type phase increases with decreasing temperature and increasing manganese content. However, the hysteresis loops show no remnant magnetization at all measured temperatures. This can be interpreted as the absence of a magnetic ordering phenomenon. The same conclusion can be drawn by comparing the reciprocal susceptibility of field cooling (FC) and zero field cooling (ZFC). The ZFC curves (Figure 82 (left)) and the FC curves (Figure 82 (right)) are identical for the same chalcopyrite type phase. This is a completely different observations than for manganese alloyed $CuInS_2$ from literature [107, 157].

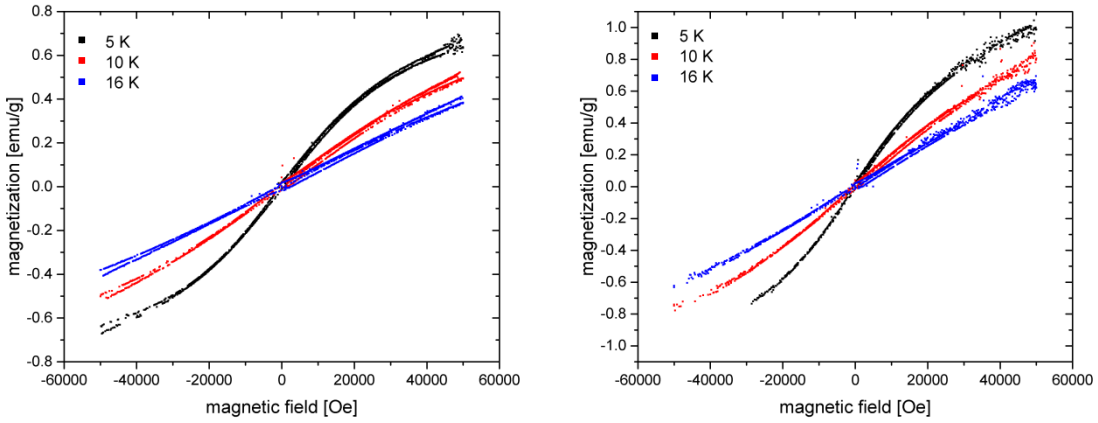

Figure 81 - Magnetization of manganese containing $CuGaS_2$ (x_m=0.021 (left), x_m=0.041 (right)) as a function of the magnetic field cycled between +60 kOe and -60 kOe at different temperatures.

By showing the inverse susceptibility as a function of temperature, the Curie-Weiss temperature Θ can be determined. According to Curie-Weiss law $\chi \sim C/(T+\Theta)$, the Curie-Weiss temperature results from the intercept of the linear part of the temperature dependent inverse magnetic susceptibility with the x

axis. If Θ is greater than zero, the net interaction between the moments is ferromagnetic and if Θ is less than zero, the net interaction between the moments is antiferromagnetic [158]. The chalcopyrite type phase containing a molar fraction of x_m=0.021 MnS has a Curie-Weiss temperature Θ of -387(2)K in FC and -390(2)K in ZFC. A Curie-Weiss temperature Θ of -496(2)K in FC and ZFC was obtained for the chalcopyrite type phase containing a molar fraction of x_m=0.041 MnS. An increase in manganese molar fraction leads to a decrease in Curie-Weiss temperature, which corresponds to the literature [159]. The difference between the Curie-Weiss temperature of FC and ZFC results from the uncertainties of the linear fit and is not related to the magnetic order.

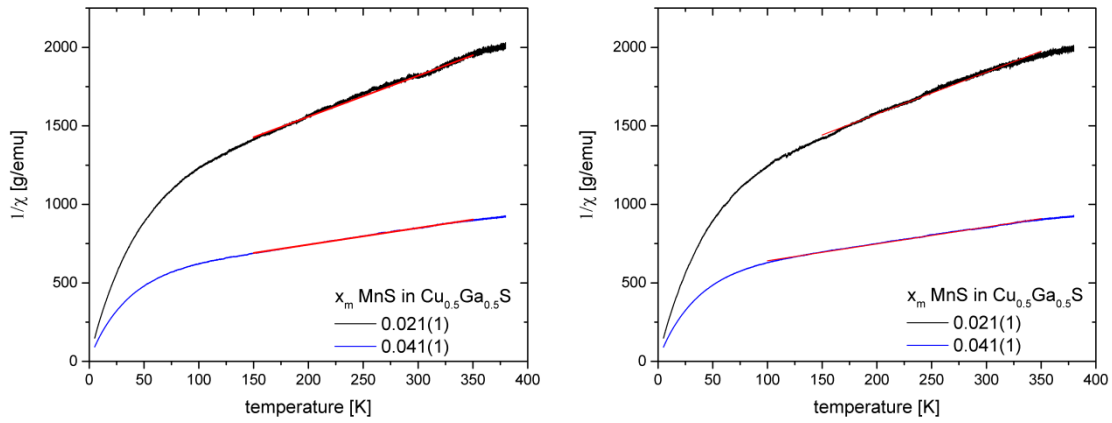

Figure 82 - Inverse magnetic susceptibility as a function of temperature, with zero field cooling (ZFC) (left) and with field cooling (FC) (right). The red lines are linear fit of the data denoting the region of the Curie-Weiss law.

In case of an antiferromagnetic material, however, the reciprocal susceptibility would show a different behavior. The observed behavior is therefore paramagnetic. An antiferromagnetic part could be present, but this would be between 5K and the observed Curie-Weiss temperatures.

4.4.9 Temperature dependent resistivity of manganese alloyed $CuGaS_2$

For the analysis of the temperature dependent resistivity of materials, it is essential to have single-phase samples. In this work, only two single phase samples could be synthesized with a x_m=0.021 and x_m=0.041 in $(Cu_{0.5}Ga_{0.5}S)_{1-x}MnS_x$. Only these two samples were analyzed by the hot probe method.
The hot probe method, addressed to the thermopower measurements, exhibited the p-type conductivity in both chalcopyrite type phases at room temperature.
The temperature dependencies of resistivity for the two analyzed chalcopyrite type phases are presented in the Figure 83 (left). Here the activated character of the temperature dependent resistivity is evident in the whole temperature range. The resistivity value of the chalcopyrite type phase containing a molar fraction of x_m=0.041 MnS is slightly higher than this with molar fraction of

x_m=0.021 MnS at any temperatures. However, the behavior of the dependencies is quite similar in both chalcopyrite type phases. Here the saturation of the resistivity at low temperatures (<120K) is rather connected with the instrumental limits than with real effect of the chalcopyrite type phase. The comparison of the resistivity values with previously published data of $CuGaS_2$ single and poly crystals [160-162] yields the significantly higher resistivity in the chalcopyrite type phases of this work. The only comparable data were found for the as-grown poly crystals (Ref. [161]).

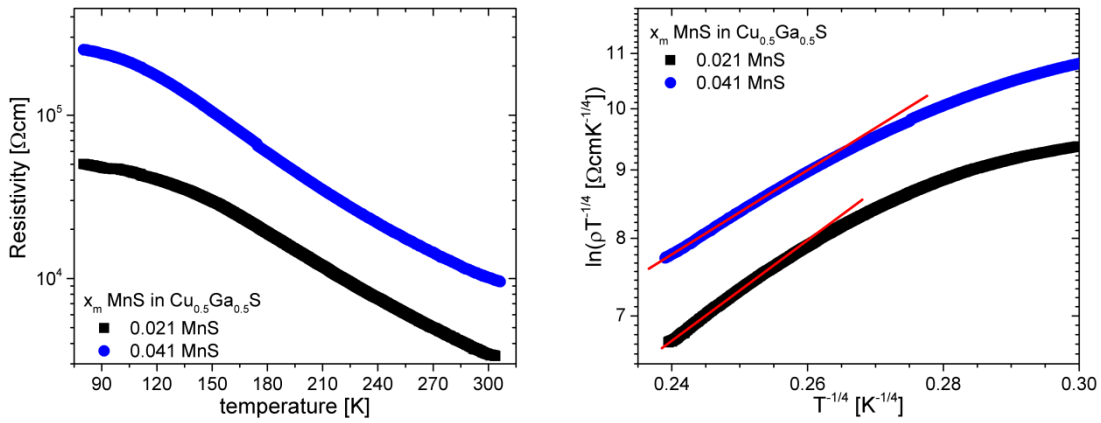

Figure 83 - Temperature dependence of resistivity of pure manganese doped chalcopyrite type phases (left). The plots of $ln(\rho T^{-1/4})$ vs. $T^{-1/4}$ for the investigated samples (right). The red lines are linear fit of the data denoting the region with Mott VRH conductivity.

Subsequent analysis of the temperature dependent resistivity was performed taking into account the high concentration of intrinsic and extrinsic defects and relatively deep position of the corresponding energy levels in the chalcopyrite type semiconductor band gap. Such conditions are favorable for the appearance of a hopping conductivity mechanism [163, 164]. A similar mechanism was previously observed in the $CuGaS_2$ single crystals [162], as well as in the familiar quaternary compounds, like Cu_2ZnSnS_4 [165, 166], Cu_2ZnGeS_4 [167], $Cu_2ZnGeSe_4$ [168], $Cu_2ZnSiSe_4$ [169] or their solid solutions [128, 170]. To determine the specific mechanisms of conductivity in the manganese alloyed chalcopyrite type $CuGaS_2$, the resistivity spectra were represented in different coordinates as it was proposed in [163, 164] and performed in [128, 165-170]. As result a Mott type of variable range hopping (Mott VRH) was observed in a wide temperature range (~210–295K). In the framework of Mott VRH model the values of characteristic temperature (T_{04}=1.03×10^{7}K for x_m=0.021 and 1.35×10^{7}K for x_m=0.041) and the semi width of the acceptor band (W=154meV for x_m=0.021 and 186meV for x_m=0.041) were determined [163-168]. These values were found to be slightly higher for the chalcopyrite type phase containing a molar fraction of x_m=0.041 MnS, which is related to the higher impurity concentration [164]. In the framework of rectangular approximation of the density of states in the impurity level the values of relative acceptor concentration (N/N_c=0.22 for x_m=0.021 and 0.21 for x_m=0.041) and relative localization radius (a/a_0=1.28 for x_m=0.021 and 1.27 for x_m=0.04) were also estimated [128, 165-170]. Here, N and a are the acceptor concentration and localization

radius, respectively, while N_c and a_0 are the critical acceptor concentration for the metal insulator transition (MIT) and localization radius far from the MIT, respectively [164]. In spite of a difference in the T_{04} and W values for the analyzed samples, the values of relative acceptor concentration and localization radius are almost similar, which means the similar proximity of the chalcopyrite type phases to the MIT. Although, the values of chalcopyrite type phases are quite far from the MIT, which leads to the observed relatively high values of T_{04} and W. This is quite different from the results observed in $CuGaS_2$ single crystals [162], where the Mott VRH was found at much lower temperatures (< 10 K) and the value of defect band width is also significantly lower (~ 0.5 meV). These differences could be explained first of all by the important influence of the Mn incorporation in chalcopyrite type phase and further by the amount of the intrinsic defects which results in a widening of the defect band additionally.

Table XI - Overview of all parameters obtained from temperature dependent resistivity measurements of the two manganese containing chalcopyrite type phases $(Cu_{0.5}Ga_{0.5}S)_{1-x}Mn_xS_x$

	x_m=0.021	x_m=0.041
Mott VRH model characteristic temperature T_{04} [K]	1.03×10^7	1.35×10^7
semi width of the acceptor band W [meV]	154	186
relative acceptor concentration N/N_c	0.22	0.21
relative localization radius a/a_c	1.28	1.27

4.4.10 Interim conclusion

The $CuGaS_2$ chalcopyrite type compound can be alloyed with a maximum of 0.098(2)mol% MnS. The observed substitution behavior is rather coupled ($Cu^{+}+Ga^{3+}\rightarrow 2Mn^{2+}$) than unilateral (Ga→Mn) as wanted. With higher manganese content, a miscibility gap was achieved and a new phase with the chemical composition $Cu_{0.3}Ga_{0.3}Mn_{0.4}S$ occurs. However, the mentioned 3-3-4 phase is not a real phase but rather a fine intergrowth of $CuGaS_2$ and MnS, comparable to exsolution lamella in (Cu,Ga,Zn)S solid solution [143]. The incorporation of manganese into the chalcopyrite type structure leads to an increase in lattice parameters. A general site preference of manganese cannot be assumed from the lattice parameters. However, the site preference of manganese within each specific chalcopyrite type phase can be assumed from the lattice parameter *a* which is not as strong affected be the Cu/Ga ratio as the lattice parameter *c*. The Cu/Ga ratio has also an effect on the manganese distribution. In copper-poor manganese containing $CuGaS_2$, manganese preferably occupies the 4a site and in gallium-poor manganese containing $CuGaS_2$, manganese preferably occupies the 4b site. This is also consistent with the trends according to Vegard´s law based on the calculated structural parameters of the three endmembers. Unfortunately, this site preference could not be observed from the cation distribution obtained by the average neutron scattering length analysis. Furthermore, the incorporation of manganese leads to the occurrence of two defect states within the band gap. A high energy PL band at 2.08eV which refers to a transition from the CBM to the defect level corresponding to Mn_{Ga}. As well as a low energy PL band at 1.22eV which refers to a transition from the CBM to the defect level induced by Mn_{Cu}. The presence of a PL band at 1.86eV is attributed to intrinsic anti-site defects. This band can be obtained in case of an adequate concentration of Ga_{Cu} anti-site defects. Two of samples are single-phase and could be investigated in terms of magnetic properties and temperature dependent resistivity. In magnetic measurements, the manganese alloyed chalcopyrite type phases showed a clearly paramagnetic behavior without remnant magnetization. The total magnetization increases with increasing manganese content, while the Curie-Weiss temperature decreases. A Mott type of variable range hopping was observed from temperature dependent resistivity measurements. Both the resistivity and the semi width of the acceptor band increase with increasing manganese content.

Table XII - Overview of the observed secondary phases from manganese alloyed $CuGaS_2$; the max. volume fraction of the phases was determined by Rietveld refinement of XRD data.

observed secondary phases	max. volume fraction [%]	present in _ of 23 powder samples
γ Cu-Ga	33.94(22)	13
υ Cu-Ga	3.78(62)	4
Digenite Cu_9S_5	1.03(12)	1
Cu	2.57(15)	1
MnS	37.09(50)	11

5. Conclusion

- **Chemical composition of the transition metal alloyed chalcopyrite type phases**

All transition metals investigated were successfully incorporated into the chalcopyrite type structure of $CuGaS_2$. Chromium and nickel show a very limited solid solubility of 0.003(1)mol% CrS and 0.008(1)mol% NiS into $Cu_{0.5}Ga_{0.5}S$. Chromium and nickel form secondary phases rather than being incorporated into the chalcopyrite type structure. Nickel forms Nickeline (NiS) and/or Heazlewoodite (Ni_3S_2) and chromium forms an Al_2MgO_4-spinel type phase with the chemical composition $Cu_{0.5}Ga_{0.5}Cr_2S_4$. Resulting from this, the increasing amount of nickel or chromium leads to an increase of the volume fraction of these secondary phases. From the chromium containing chalcopyrite type phases, no trends can be observed from the evolution of the chemical composition with increasing chromium content. This is caused by the very limited solubility of chromium into $CuGaS_2$. From the nickel containing chalcopyrite type phases clear trends in chemical composition can be observed. With increasing nickel content, the Cu/Ga ratio and the Cu/(Ga+Ni) ratio increase, whereas the M/S ratio remains constant as for the incorporation of all transition metals into $CuGaS_2$.
Despite the complete solubility of $CuFeS_2$ and $CuGaS_2$, the actual substitution differs from the expected one. Two different substitution behaviors can be observed, related to the initial iron content. On the one hand, iron is mainly substituting gallium (unilateral) if $x_i>0.1$ in $Cu_{0.5}(Fe_xGa_{0.5-x})S$ and on the other hand, iron is substituting both cations (coupled) if $x_i<0.1$. The substitution behavior can be derived from the changes in chemical composition with increasing the amount of iron into $CuGaS_2$. The unilateral substitution ($Ga^{3+}\rightarrow Fe^{3+}$) is characterized by an increase in Cu/Ga ratio and a constant Cu/(Ga+Fe) ratio with increasing molar fraction of iron in $CuGaS_2$. Whereas the coupled substitution ($Cu^{+}+Ga^{3+}\rightarrow 2Fe^{2+}$) is characterized by a constant Cu/Ga ratio and a decreasing Cu/(Ga+Fe) ratio with increasing iron content.
The incorporation of manganese differs from the proposed behavior which would be necessary for generating an intermediate band. The substitution of manganese into the chalcopyrite type structure of $CuGaS_2$ is coupled ($Cu^{+}+Ga^{3+}\rightarrow 2Mn^{2+}$) rather than unilateral (Ga→Mn), regardless of the initial chemical composition which is derived from the evolution of the chemical composition of the chalcopyrite type phase. With increasing manganese molar fraction, the Cu/(Ga+Mn) ratio decreases while the Cu/Ga ratio and the M/S ratio remain constant. The maximum solubility of manganese is 0.098(2)mol% in $CuGaS_2$, which is enough to provide adequate amounts of defects for the intermediate band. For samples with an initial manganese content above this limit, a 3-3-4 phase ($Cu_{0.3}Ga_{0.3}Mn_{0.4}S$) from WDX analysis is observed. However, the 3-3-4 phase is rather a fine intergrowth of $CuGaS_2$ and MnS, comparable to the exsolution lamella in (Cu,Ga,Zn)S solid solution [143].

- **Structural trends of the transition metal alloyed chalcopyrite type phases**

From a structural point of view, the incorporation of iron was supposed to result in a decrease in lattice parameters according to Vegard´s law. From the lattice parameters two different trends were observed which were interpreted to result from two different substitution mechanisms. In the unilateral substitution regime (x_i>0.1), the lattice parameter *a* is following Vegard´s law, while the lattice parameter *c* increases with increasing iron content. However, this behavior was already reported in literature [5]. In the coupled substitution regime (x_i<0.1), both lattice parameters increase, since the incorporated iron ions are more divalent than trivalent in view of the evolution of the chemical composition.

The structural evolution of the manganese-alloyed chalcopyrite type phases generally shows an increase of the lattice parameters *a* and *c* with increasing manganese content. However, the structural parameters are influenced by the chemical composition, in particular by the Cu/Ga ratio and the M/S ratio. The Cu/Ga ratio is further affecting the site preference of manganese, as proposed [140]. Manganese is preferably incorporated on the copper site if the composition is copper depleted and on the gallium site if gallium depleted which can be observed from the lattice parameters. However, a definite site preference for manganese on one of the cation sites was not observed by the average neutron scattering length analysis.

The structural parameters calculated by the formalism of Jaffe and Zunger [19] do not match the determined values, since vacancies are neglected in the calculation. It is assumed that one copper vacancy leads to a shift in the position of four sulfur atoms, this in turn influences 12 cation to anion bonds. Based on the observed chemical and structural information, the local copper-sulfur bond length is calculated to increase by 0.032Å and the gallium to sulfur bond length to decrease by 0.029Å as a result of a copper vacancy. The average cation radii of 4a and 4b site calculated by using the advanced calculation considering copper vacancies represent 75% of the obtained values from Rietveld refinement of XRD data. This results furthermore in a much better agreement for the tetragonal distortion *u* of the calculated and observed values.

The incorporation of nickel and chromium into $CuGaS_2$ does not show any effect on the chalcopyrite type structure due to the limited solubility of both transition metals into $CuGaS_2$.

- **Optoelectronic properties of the transition metal alloyed chalcopyrite type phases**

The optoelectronic properties investigated by photoluminescence spectroscopy differ with regard to the substituted transition metal. Chromium substituted chalcopyrite type $CuGaS_2$ show either a PL band at 1.2eV or 1.4eV which is concluded to result from the same defect present in $CuGaS_2$. In $CuGaS_2$ the PL band at 1.4eV was associated to copper vacancies [134], the slight positional shift results probably from changes in the band gap.

The incorporation of nickel into the chalcopyrite type $CuGaS_2$ also does not lead to any additional PL bands which can be related to Ni_{Ga} or Ni_{Cu}. The nickel containing chalcopyrite type phases show a PL band at 1.8eV which was previously associated with sulfur vacancies [137]. Due to a sufficient excess of sulfur during sample synthesis, this interpretation is rather doubtful.

However, a PL band at 1.8eV was also observed in the majority of the manganese alloyed Chalcopyrite type phases, but additional bands were obtained which can be related to manganese defects. Comparing the defect concentration, the difference is the presence or absence of Ga_{Cu} anti-site defects. Those chalcopyrite type phases showing a PL band at 1.8eV have a high concentration of Ga_{Cu}, while those showing no band at this position do not have Ga_{Cu} according to the average neutron scattering length analysis. On this basis, it is concluded that these are Ga_{Cu} anti-site defects that produce a recombination center which result in this PL band. However, the minority of the manganese alloyed chalcopyrite type phases shows two PL bands that are related to manganese incorporation on the specific cation site as proposed [6]. The PL band at 1.22eV represents Mn_{Cu} and the PL at 2.08eV represents Mn_{Ga}. Furthermore, the position of the fermi level was assumed based on the observed PL spectra referring calculations of Zhao and Zunger [6]. None of the transition metal substituted chalcopyrite type phases showed a PL band representing a transition from the conduction band minimum to the valence band maximum.

The incorporation of iron into the chalcopyrite type $CuGaS_2$ results in no photoluminescence signal at all.

- **Magnetic properties of the transition metal alloyed chalcopyrite type phases**

Two single-phase samples, containing a molar fraction of x_m=0.021 and x_m=0.041 MnS in $Cu_{0.5}Ga_{0.5}S$, could be synthesized. These were investigated in terms of magnetic properties using the Superconducting QUantum Interface Device. In magnetic measurements, the chalcopyrite type phases show a paramagnetic behavior without remnant magnetization. The total magnetization increases with increasing manganese content while decreasing Curie-Weiss temperature. The Curie-Weiss temperature for the chalcopyrite type phase with a manganese content of x_m=0.021 was calculated to be -387(2)K in FC and -390(2)K in ZFC, respectively. Whereas for the chalcopyrite type phase with a manganese content of x_m=0.041 the Curie-Weiss temperature decreases to -496(2)K in FC and ZFC.

- **Temperature dependent resistivity of the transition metal alloyed chalcopyrite type phases**

The two single-phases samples containing a molar fraction of x_m=0.021 and x_m=0.041 MnS in $Cu_{0.5}Ga_{0.5}S$ were analyzed by the hotprobe method to address the temperature dependent resistivity. A Mott type of variable range hopping was obtained with Mott VRH model characteristic temperatures T_{04} of 1.03×10^7 for x_m=0.021 and 1.35×107 for x_m=0.041. The semi width of the acceptor band W is increasing as T04 with increasing molar fraction of manganese in $CuGaS_2$, from 154meV for x_m=0.021 to 186meV for x_m=0.041. The relative acceptor concentration and the relative localization radius remain constant, despite the increasing manganese molar fraction.

The incorporation of transition metals into the chalcopyrite type structure of $CuGaS_2$ could be shown, but only the incorporation of manganese shows additional features in the optoelectronic properties. It remains unclear whether the defects caused by incorporation form an intermediate band or merely defects states within the band gap.

6. Outlook

The next step would be to transfer the knowledge about the maximum solid solubility of the transition metals into the $CuGaS_2$ compound to the growth of thin film absorbers for solar cell applications. Manganese seems to be the most promising candidate for further investigations because of its high solid solubility and the optoelectronic active defects that are caused by manganese incorporation. The investigation of thin film solar cells can clarify whether these two observed PL bands act as real bands or merely as defect states. This could be the only way to prove the concept of the intermediate band solar absorber. In addition, the growth of thin film absorbers by co-evaporation prevents the formation of alloys. Another important question could be whether it is possible to adjust the growth process to prevent the formation of intrinsic anti-site defects. It may also be interesting to know whether the process conditions influence the site preference of the incorporated manganese.

However, the synthesis as a thin film absorber also leads to new problems, but also to investigation possibilities. Thin films often show a chemical gradient, both laterally and medially which must be analyzed by Glow Discharge Optical Emission Spectroscopy (GDOES), for example. A chemical gradient also leads to strain within the grains which can be determined by a proper strain analysis. In addition, external quantum efficiencies and other parameters, such as the open-circuit voltage and the short-circuit current, can be measured to validate the influence of manganese incorporation on the performance of a solar cell.

Furthermore, the influence of the incorporated transition metals on the bandgap is unclear. In order to quantify this effect, absorption measurements should be carried out.

References

[1] I. Fraunhofer, "New world record for solar cell efficiency at 46% French-German cooperation confirms competitive advantage of European photovoltaic industry," *Press release,* vol. 26, 2014.

[2] W. Shockley and H. J. Queisser, "Detailed balance limit of efficiency of p-n junction solar cells," *Journal of applied physics,* vol. 32, pp. 510-519, 1961.

[3] A. Luque and A. Martí, "Increasing the Efficiency of Ideal Solar Cells by Photon Induced Transitions at Intermediate Levels," *Phys Rev Lett,* vol. 78, pp. 5014-517, 1997.

[4] A. Luque, A. Martí, E. Antolín, and C. Tablero, "Intermediate bands versus levels in non-radiative recombination," *Physica B: Condensed Matter,* vol. 382, pp. 320-327, 2006.

[5] M. DiGiuseppe, J. Steger, A. Wold, and E. Kostiner, "Preparation and Characterization of the System $CuGa_{1-x}Fe_xS_2$," *Inorganic Chemistry,* vol. 13, pp. 1828-1831, 1974.

[6] Y.-J. Zhao and A. Zunger, "Electronic structure and ferromagnetism of Mn-substituted $CuAlS_2$, $CuGaS_2$, $CuInS_2$, $CuGaSe_2$, and $CuGaTe_2$," *Physical Review B,* vol. 69, p. 104422, 2004.

[7] A. Martí, D. F. Marrón, and A. Luque, "Evaluation of the efficiency potential of intermediate band solar cells based on thin-film chalcopyrite materials," *Journal of Applied Physics,* vol. 103, p. 073706, 2008.

[8] J. Shay, S. Wagner, and H. Kasper, "Efficient $CuInSe_2$/CdS solar cells," *Applied Physics Letters,* vol. 27, pp. 89-90, 1975.

[9] P. Jackson, R. Wuerz, D. Hariskos, E. Lotter, W. Witte, and M. Powalla, "Effects of heavy alkali elements in $Cu(In,Ga)Se_2$ solar cells with efficiencies up to 22.6%," *physica status solidi (RRL) - Rapid Research Letters,* vol. 10, pp. 583-586, 2016.

[10] A. Rockett and R. W. Birkmire, "$CuInSe_2$ for photovoltaic applications," *Journal of Applied Physics,* vol. 70, pp. R81-R97, 1991.

[11] S. Siebentritt, "Wide gap chalcopyrite: material properties and solar cells," *Thin Solid Films,* vol. 403-404, pp. 1-8, 2002.

[12] B. Tell, J. L. Shay, and H. M. Kasper, "Electrical Properties, Optical Properties, and Band Structure of $CuGaS_2$and $CuInS_2$," *Physical Review B,* vol. 4, pp. 2463-2471, 1971.

[13] S. Rühle, "Tabulated values of the Shockley–Queisser limit for single junction solar cells," *Solar Energy,* vol. 130, pp. 139-147, 2016/06/01/ 2016.

[14] L. Pauling and L. Brockway, "The crystal structure of chalcopyrite $CuFeS_2$," *Zeitschrift für Kristallographie-Crystalline Materials,* vol. 82, pp. 188-194, 1932.

[15] H. Hahn, G. Frank, W. Klingler, A. D. Meyer, and G. Störger, "Untersuchungen über ternäre Chalkogenide. V. Über einige ternäre Chalkogenide mit Chalkopyritstruktur," *Zeitschrift für anorganische und allgemeine Chemie,* vol. 271, pp. 153-170, 1953.

[16] B. Pamplin, "The adamantine family of compounds," *Progress in Crystal Growth and Characterization,* vol. 3, pp. 179-192, 1980.

[17] S. Schorr, "Structural aspects of adamantine like multinary chalcogenides," *Thin Solid Films,* vol. 515, pp. 5985-5991, 2007.

[18] R. D. Shannon, "Reised Effective Ionic Radii and Systematic Studies of Interatomic Distances in Halides and Chalcogenides," *Acta Crystallographica,* pp. 751-767, 1976.

[19] J. E. Jaffe and A. Zunger, "Theory of the band-gap anomaly inABC_2chalcopyrite semiconductors," *Physical Review B,* vol. 29, pp. 1882-1906, 1984.

[20] J. Shay, B. Tell, H. Kasper, and L. Schiavone, "p− d Hybridization of the Valence Bands of I-III-VI 2 Compounds," *Physical Review B,* vol. 5, p. 5003, 1972.

[21] J. Shay, B. Tell, H. Kasper, and L. Schiavone, "Electronic Structure of $AgInSe_2$ and $CuInSe_2$," *Physical Review B,* vol. 7, p. 4485, 1973.

[22] I. Aguilera, J. Vidal, P. Wahnón, L. Reining, and S. Botti, "First-principles study of the band structure and optical absorption of $CuGaS_2$," *Physical Review B,* vol. 84, p. 085145, 2011.

[23] M. Han, X. Zhang, and Z. Zeng, "The investigation of transition metal doped $CuGaS_2$ for promising intermediate band materials," *RSC Adv.,* vol. 4, pp. 62380-62386, 2014.

[24] M. Wolf, "Limitations and possibilities for improvement of photovoltaic solar energy converters: Part I: Considerations for earth's surface operation," *Proceedings of the IRE,* vol. 48, pp. 1246-1263, 1960.

[25] E. Jackson, "Areas for improvement of the semiconductor solar energy converter," in *Transactions of the Conference on the Use of Solar Energy*, 1955, pp. 122-126.

[26] H. Kroemer, "Theory of a wide-gap emitter for transistors," *Proceedings of the IRE,* vol. 45, pp. 1535-1537, 1957.

[27] D. Reynolds and S. Czyzak, "Mechanism for photovoltaic and photoconductivity effects in activated CdS crystals," *Physical Review,* vol. 96, p. 1705, 1954.

[28] P. Palacios, K. Sánchez, J. C. Conesa, and P. Wahnón, "First principles calculation of isolated intermediate bands formation in a transition metal-doped chalcopyrite-type semiconductor," *physica status solidi (a),* vol. 203, pp. 1395-1401, 2006.

[29] P. Palacios, K. Sánchez, J. C. Conesa, J. J. Fernández, and P. Wahnón, "Theoretical modelling of intermediate band solar cell materials based on metal-doped chalcopyrite compounds," *Thin Solid Films,* vol. 515, pp. 6280-6284, 2007.

[30] A. Luque and A. Martí, "A Metallic Intermediate Band High Efficiency Solar Cell," *Progress In Photovoltaics: Research and Applications,* vol. 9, pp. 73-86, 2001.

[31] P. Palacios, I. Aguilera, P. Wahnón, and J. C. Conesa, "Thermodynamics of the Formation of Ti- and Cr-doped $CuGaS_2$ Intermediate-band Photovoltaic Materials," *The Journal of Physical Chemistry C,* vol. 112, pp. 9525-9529, 2008.

[32] B. Marsen, S. Klemz, T. Unold, and H.-W. Schock, "Investigation of the Sub-Bandgap Photoresponse in $CuGaS_2$: Fe for Intermediate Band Solar Cells," *Progress in Photovoltaics: Research and Applications,* vol. 20, pp. 625-629, 2012.

[33] A. Martí, E. Antolín, P. G. Linares, E. Cánovas, D. F. Marrón, C. Tablero*, et al.*, "IB-Power: Intermediate Band Materials and Solar Cells for Photovoltaics with high efficiency and reduced cost," *Photovoltaic Specialists Conference (PVSC),* vol. 34, 2009.

[34] C. L. Bailey, L. Liborio, G. Mallia, S. Tomić, and N. M. Harrison, "Defect physics of$CuGaS_2$," *Physical Review B,* vol. 81, 2010.

[35] S. Picozzi, Y.-J. Zhao, A. J. Freeman, and B. Delley, "Mn-doped $CuGaS_2$ chalcopyrites: An ab initio study of ferromagnetic semiconductors," *Physical Review B,* vol. 66, 2002.

[36] R. D. Shannon, "Bond distances in sulfides and a preliminary table of sulfide crystal radii," in *Industrial Chemistry Library*. vol. 2, ed: Elsevier, 1981, pp. 53-70.

[37] K. Tsubaki and K. Sugiyama, "Phase Equilibria in the Cu-Ga-S-Sn System," *Journal of Electronic Materials,* vol. 12, pp. 43-59, 1983.

[38] E. Belova, V. Koshkin, and L. Palatnik, "Study of the structure and optical properties of $CuGaS_2$-Ga_2S_3 alloys," *Inorganic Materials (Translation of Izvestiya Akademii Nauk SSSR, Neorganicheskie Materialy),* vol. 3, pp. 543-548, 1967.

[39] M. Kokta, J. R. Carruthers, M. Grasso, H. M. Kasper, and B. Tell, "Ternary phase relations in the vicinity of the chalcopyrite copper gallium sulfide," *Journal of Electronic Materials,* vol. 5, pp. 69-89, 1976.

[40] T. Maeda, Y. Yu, Q. Chen, K. Ueda, and T. Wada, "Crystallographic and optical properties and band diagrams of $CuGaS_2$ and $CuGa_5S_8$ phases in Cu-poor Cu_2S–Ga_2S_3 pseudo-binary system," *Japanese Journal of Applied Physics,* vol. 56, p. 04CS12, 2017.

[41] K. Ueda, T. Maeda, and T. Wada, "Crystallographic and optical properties of $CuGa_3S_5$, $CuGa_3Se_5$ and $CuIn_3(S,Se)_5$ and $CuGa_3(S,Se)_5$ systems," *Thin Solid Films,* vol. 633, pp. 23-30, 2017/07/01/ 2017.

[42] S. Kashida and K. Yamamoto, "An X-ray study of the incommensurate structure in digenite ($Cu_{1.8}S$)," *Journal of Physics: Condensed Matter,* vol. 3, p. 6559, 1991.

[43] H. T. Evans, "The crystal structures of low chalcocite and djurleite," *Zeitschrift für Kristallographie-Crystalline Materials,* vol. 150, pp. 299-320, 1979.

[44] D. J. Chakrabarti and D. E. Laughlin, "The Cu-S (Copper-Sulfur) System," *Bulletin of Alloy Phase Diagrams,* vol. 4, pp. 254-271, 1983.

[45] H. Hahn and W. Klingler, "Über die Kristallstrukturen von Ga_2S_3, Ga_2Se_3 und Ga_2Te_3," *Zeitschrift für anorganische Chemie,* vol. 259, pp. 135-142, 1949.

[46] H. Hahn and G. Frank, "Zur Struktur des Ga_2S_3," *Zeitschrift für anorganische und allgemeine Chemie,* vol. 278, pp. 333-339, 1955.

[47] G. Collin, J. Flahaut, M. Guittard, and A.-M. Loireau-Lozach, "Preparation et structure de Ga_2S_3 α type wurtzite lacunaire," *Materials Research Bulletin,* vol. 11, pp. 285-292, 1976.

[48] C. Jones, J. Bryan, K. Kirschbaum, and J. Edwards, "Refinement of the crystal structure of digallium trisulfide, Ga_2S_3," *Zeitschrift für Kristallographie-New Crystal Structures,* vol. 216, pp. 349-350, 2001.

[49] A. Kuhn, A. Chevy, and R. Chevalier, "Refinement of the 2H GaS β-type," *Acta Crystallographica Section B: Structural Crystallography and Crystal Chemistry,* vol. 32, pp. 983-984, 1976.

[50] W. Klemm and H. U. v. Vogel, "Messungen an Gallium- und Indium-Verbindungen. X. Über die Chalkogenide von Gallium und Indium," *Zeitschrift für anorganische und allgemeine Chemie,* vol. 219, pp. 45-64, 1934.

[51] E. Owen and V. Rowlands, "Solubility of certain elements in copper and in silver," *J INST MET,* vol. 66, pp. 361-378, 1940.

[52] W. Hume-Rothery, G. W. Mabbott, and K. C. Evans, "The freezing points, melting points, and solid solubility limits of the alloys of silver, and copper with the elements of the B sub-groups," *Philosophical Transactions of the Royal Society of London. Series A, Containing Papers of a Mathematical or Physical Character,* pp. 1-97, 1934.

[53] F. Weibke, "Das Zustandsdiagramm des Systems Kupfer-Gallium," *Zeitschrift fur anorganische und allgemeine Chemie,* vol. 220, pp. 293-311, 1934.

[54] Y. Zhang, J.-B. Li, J. Liang, Q. Zhang, B. Sun, Y. Xiao*, et al.*, "Subsolidus phase relations of the Cu–Ga–N system," *Journal of alloys and compounds,* vol. 438, pp. 158-164, 2007.

[55] O. Tikhomirova, M. Pikunov, I. Marchukova, I. Tochenova, and I. Izotova, "An investigation of structural transformation during the solidification of copper-gallium alloys," *Materials Science,* vol. 5, pp. 355-358, 1972.

[56] M. El-Boragy and K. Schubert, "Crystal Structure of $CuGa_2$," *Z. Metallkunde,* vol. 63, pp. 53-53, 1972.

[57] P. G. Rustamov, B. N. Mardakhaev, and M. G. Safarov, *Inorganic materials,* vol. 3, pp. 429-433, 1967.

[58] P. Subramanian and D. Laughlin, "Cu-Ga (Copper-Gallium)," *Binary Alloy Phase Diagrams,* pp. 1410-1412, 1994.

[59] M. Straumanis and C. Weng, "The absorption and refraction corrections and the lattice constant of chromium," *Am. Mineral,* vol. 41, pp. 437-448, 1956.

[60] F. Jellinek, "The structures of the chromium sulphides," *Acta Crystallographica,* vol. 10, pp. 620-628, 1957.

[61] S. Vaidya, C. Karunakaran, and R. Krishnan, "X-ray diffraction study of NiS and CrS at high-pressures," vol. 14, ed: Council Scientific Industrial Research Publ & Info Directorate, New Delhi 110012, India, 1976, pp. 600-601.

[62] M. Widenmeyer, E. Meissner, A. Senyshyn, and R. Niewa, "On the formation mechanism of chromium nitrides: An in situ study," *Zeitschrift für anorganische und allgemeine Chemie,* vol. 640, pp. 2801-2808, 2014.

[63] A. W. Sleight and T. A. Bither, "Chromium chalcogenides prepared at high pressure and the crystal growth of chromium sesquisulfide," *Inorganic Chemistry,* vol. 8, pp. 566-569, 1969.

[64] A. Noel, J. Tudo, and G. Tridot, "Sur l´existence d´une nouvelle phase dans le système chrome-soufre : le polysulfure de chrome Cr_2S_5," *Comptes Rendus Hebdomadaires des Seances de l'Academie des Sciences, Serie C,* vol. 264, pp. 443-445, 1967.

[65] T. B. Massalski and J. Murray, "Binary phase diagrams," *ASM International,* p. 1096, 1990.

[66] D. J. Chakrabarti and D. E. Laughlin, "The Cr-Cu (Chromium-Copper) system," *Bulletin of Alloy Phase Diagrams,* vol. 5, pp. 59-68, February 01 1984.

[67] K. Girgis, "Crystallographic studies on ternary superconductors of the A15 type: $V_{3-x}Me_xGa$ (Me = Ti, Cr, Mn, Fe, Co, Ni)," *Journal of the Less Common Metals,* vol. 65, pp. 1-12, 1979/05/01/ 1979.

[68] J.-D. Bornand and P. Feschotte, "The Binary Cr-Ga System," *J. Less-Common Metals,* vol. 29, pp. 81-91, 1972.

[69] O. Gourdon, S. L. Bud'ko, D. Williams, and G. J. Miller, "Crystallographic, Electronic, and Magnetic Studies of ζ2-GaM (M= Cr, Mn or Fe): Trends in Itinerant Magnetism," *Inorganic chemistry,* vol. 43, pp. 3210-3218, 2004.

[70] M. Philippe, B. Malaman, B. Roques, A. Courtois, and J. Protas, "Structures cristallines des phases Fe_3Ga_4 et Cr_3Ga_4," *Acta Crystallographica Section B: Structural Crystallography and Crystal Chemistry,* vol. 31, pp. 477-482, 1975.

[71] H.-G. Meissner and K. Schubert, "Zum Aufbau einiger zu T5-Ga homologer und quasihomologer Systme. 2. Die Systeme Chrom-Gallium, Mangan-Gallium und Eisen-Gallium sowie einige Bemerkungen zum Aufbau der Systeme Vanadium-Antimon und Vanadium-Arsen," *Zeitschrift fur Metallkunde,* vol. 56, pp. 523-&, 1965.

[72] P. Y. Lyutyi, Y. O. Tokaichuk, and A. O. Fedorchuk, "Ternary Cr–Ga–Si system at 870 K," *Materials Science,* vol. 46, p. 486, March 16 2011.

[73] K. Schubert, T. R. Anantharaman, H. O. K. Ata, H. G. Meissner, M. Pötzschke, W. Rossteutscher*, et al.*, "Einige strukturelle Ergebnisse an metallischen Phasen (6)," *Naturwissenschaften,* vol. 47, pp. 512-512, January 01 1960.

[74] J. Gröbner, R. Wenzel, G. G. Fischer, and R. Schmid-Fetzer, "Thermodynamic Calculation of the Binary M-Ga and Investigation of Ternary M-Ga-N Phase Equilibria (M = Ni, Co, Pd, Cr)," *Journal of Phase Equilibria,* vol. 20, pp. 615-625, 1999.

[75] Z. Basinski, W. Hume-Rothery, and A. Sutton, "The lattice expansion of iron," in *Proceedings of the Royal Society of London A: Mathematical, Physical and Engineering Sciences*, 1955, pp. 459-467.

[76] M. Okrusch and S. Matthes, *Mineralogie: eine Einführung in die spezielle Mineralogie, Petrologie und Lagerstättenkunde*: Springer-Verlag, 2013.

[77] W. A. Deer, R. A. Howie, and J. Zussman, *An introduction to the rock-forming minerals* vol. 2: Longman Scientific & Technical Hong Kong, 1992.

[78] H. King and C. Prewitt, "High-pressure and high-temperature polymorphism of iron sulfide (FeS)," *Acta Crystallographica Section B: Structural Crystallography and Crystal Chemistry,* vol. 38, pp. 1877-1887, 1982.

[79] H. J. Rösler, "Lehrbuch der Mineralogie. 4. durchgesehene und erweiterte Auflage," ed: Deutscher Verlag für Grundstoffindustrie (VEB), Leipzig, 1979.

[80] O. Kubaschewski, *Iron—Binary phase diagrams*: Springer Science & Business Media, 2013.

[81] L. Swartzendruber, "Cu-Fe (copper-iron)," *Phase Diagrams for Binary Alloys,* 1996.

[82] H. Okamoto, "Fe-Ga (iron-gallium)," *Journal of Phase Equilibria and Diffusion,* vol. 25, pp. 100-100, February 01 2004.

[83] J.-J. B. Couderg, J.; Fagot, M., " Étude de la structure ordonée de l'alliage Fe_3Ga," *Comptes Rendus Hebdomadaires des Seances de l'Academie des Sciences, Serie B,* vol. 272, pp. 781-784, 1971.

[84] K. Schubert, S. Bhan, W. Burkhardt, R. Gohle, H. Meissner, M. Pötzschke*, et al.*, "Einige strukturelle Ergebnisse an metallischen Phasen (5)," *Naturwissenschaften,* vol. 47, pp. 303-303, 1960.

[85] B. Malaman, M. Phillippe, B. Roques, A. Courtois, and J. Protas, "Structures cristallines des phases Fe_6Ge_5 et Fe_6Ga_5," *Acta Crystallographica Section B: Structural Crystallography and Crystal Chemistry,* vol. 30, pp. 2081-2087, 1974.

[86] W. Köster and T. Gödecke, *Z. Metallkunde,* vol. 68, pp. 661-666, 1977.

[87] O. Ikeda, R. Kainuma, I. Ohnuma, K. Fukamichi, and K. Ishida, "Phase equilibria and stability of ordered bcc phases in the Fe-rich portion of the Fe–Ga system," *Journal of Alloys and Compounds,* vol. 347, pp. 198-205, 2002.

[88] D. A. Young, *Phase Diagrams of the Elements*: Lawrence Livermore Laboratory, 1975.

[89] H. Okamoto, "Mn-S (Manganese-Sulfur)," *Journal of Phase Equilibria and Diffusion,* vol. 32, pp. 78-78, 2010.

[90] H. Ott, "Die Strukturen von MnO, MnS, AgF, NiS, SnI_4, $SrCl_2$, BaF_2, Praezisionsmessungen einiger Alkalihalogenide.," *Zeitschrift fuer Kristallographie, Kristallgeometrie, Kristallphysik, Kristallchemie,* vol. 63, pp. 222 - 230, 1926.

[91] T. Chattopadhyay, H. von Schnering, R. Stansfield, and G. McIntyre, "X-ray and neutron diffraction study of the crystal structure of MnS_2," *Z Kristallogr,* vol. 199, pp. 13-24, 1992.

[92] S. Furuseth and A. Kjekshus, "On the properties of a-MnS and MnS_2," *Acta Chem. Scand,* vol. 19, 1965.

[93] W. Blitz and F. Wiechmann, "Beiträge zur systematischen Verwandtschaftslehre. 68. Zum System Mangan/Schwefel: Abbau und Synthese des Hauerits (MnS_2)," *Zeitschrift für anorganische und allgemeine Chemie,* vol. 228, pp. 268-274, 1936.

[94] H. G. Meissner, K. Schubert, and T. R. Anantharaman, "The constitution and structure of manganese-gallium alloys," *Proceedings of the Indian Academy of Sciences - Section A,* vol. 61, pp. 340-367, June 01 1965.

[95] X.-S. Lu, J.-K. Liang, T.-J. Shi, and M.-Q. Zhou, "A X-ray Investigation of the Manganese-Gallium System," *Acta Physica Sinica,* vol. 29, p. 469, 2005-07-29 1980.

[96] M. Tillard and C. Belin, "Investigation in the Ga-rich side of the Mn–Ga system: Synthesis and crystal structure of $MnGa_4$ and $MnGa_{5-x}$ (x∼ 0.15)," *Intermetallics,* vol. 29, pp. 147-154, 2012.

[97] J. Rouquette, J. Haines, G. Fraysse, A. Al-Zein, V. Bornand, M. Pintard*, et al.*, "High-pressure structural and vibrational study of $PbZr_{0.40}Ti_{0.60}O_3$," *Inorganic chemistry,* vol. 47, pp. 9898-9904, 2008.

[98] S. Merlino and E. Makovicky, "OD (order-disorder) character of the crystal structure of godlevskite Ni_9S_8," *European Journal of Mineralogy,* vol. 21, pp. 863-869, 2009.

[99] M. Fleet, "The crystal structure of heazlewoodite, and metallic bonds in sulfide minerals," *American Mineralogist,* vol. 62, pp. 341-345, 1977.

[100] J. Grice and R. Ferguson, "Crystal structure refinement of millerite (beta-NiS)," *The Canadian Mineralogist,* vol. 12, pp. 248-252, 1974.

[101] Y. Kesler, S. Smirnov, K. Pokholok, and B. Viting, "Peculiarities of the Electronic Structure of Co, Ni-Thiospinel," *Inorganic materials,* vol. 27, pp. 977-980, 1991.

[102] H. Okamoto, "Ni-S (Nickel-Sulfur)," *Journal of Phase Equilibria and Diffusion,* vol. 30, pp. 123-123, February 01 2009.

[103] P. Nash, "Phase diagrams of binary nickel alloys," *ASM International(USA), 1991,* p. 394, 1991.

[104] H. Okamoto, "Ga-Ni (Gallium-Nickel)," *Journal of Phase Equilibria and Diffusion,* vol. 29, pp. 296-296, June 01 2008.

[105] W. Michel, "Magnetische Untersuchungen an intermediären Phasen von Ni und Co mit drei- und vierwertigen B-Metallen," *Annalen der Physik,* vol. 466, pp. 321-353, 1963.

[106] S. Herkelrath, "Struckturelle Charakterisierung von $CuMn_{1-x}In_xX_2$ und $Mn_{2x}(CuIn)_{1-x}X_2$ (X=S,Se)," Diploma, Insitut für Mineralogie, Kristallographie und Materialwissenschaft, Universität Leipzig, 2005.

[107] S. Schorr, R. Höhne, G. Wagner, V. Riede, and W. Kockelmann, "Investigation of the solid solution series $2(MnX)–CuInX_2$ (X=S, Se)," *Journal of Physics and Chemistry of Solids,* vol. 66, pp. 1966-1969, 2005.

[108] S. J. B. Reed, *Electron microprobe analysis and scanning electron microscopy in geology*: Cambridge University Press, 2005.

[109] W. H. Bragg and W. L. Bragg, "The reflection of X-rays by crystals," *Proc. R. Soc. Lond. A,* vol. 88, pp. 428-438, 1913.

[110] L. Spieß, G. Teichert, R. Schwarzer, H. Behnken, and C. Genzel, *Moderne röntgenbeugung: röntgendiffraktometrie für materialwissenschaftler, physiker und chemiker*: Springer-Verlag, 2009.

[111] V. F. Sears, "Neutron scattering lengths and cross sections," *Neutron news,* vol. 3, pp. 26-37, 1992.

[112] A. Franz and A. Hoser, "E9: The Fine Resolution Powder Diffractometer (FIREPOD) at BER II," *Journal of large-scale research facilities JLSRF,* vol. 3, 2017.

[113] H. Rietveld, "A profile refinement method for nuclear and magnetic structures," *Journal of Applied Crystallography,* vol. 2, pp. 65-71, 1969.

[114] H. Rietveld, "Line profiles of neutron powder-diffraction peaks for structure refinement," *Acta Crystallographica,* vol. 22, pp. 151-152, 1967.

[115] R. Young, "The Rietveld Method, International Union of Crystallography Monographs on Crystal and Oxford Science Publications," ed: Oxford, UK, 1995.

[116] J. Rodriguez-Carvajal, "FULLPROF version 3.0. 0," *Laboratorie Leon Brillouin, CEA-CNRS,* 2003.

[117] L. Finger, D. Cox, and A. Jephcoat, "A correction for powder diffraction peak asymmetry due to axial divergence," *Journal of Applied Crystallography,* vol. 27, pp. 892-900, 1994.
[118] G. Caglioti, A. t. Paoletti, and F. Ricci, "Choice of collimators for a crystal spectrometer for neutron diffraction," *Nuclear Instruments,* vol. 3, pp. 223-228, 1958.
[119] L. McCusker, R. Von Dreele, D. Cox, D. Louër, and P. Scardi, "Rietveld refinement guidelines," *Journal of Applied Crystallography,* vol. 32, pp. 36-50, 1999.
[120] G. J. Kearley and V. K. Peterson, *Neutron applications in materials for energy*: Springer, 2015.
[121] S. Perkowitz, *Optical characterization of semiconductors: infrared, Raman, and photoluminescence spectroscopy* vol. 14: Elsevier, 2012.
[122] S. K. Ran, "Gravity probe B: Exploring Einstein's universe with gyroscopes," *NASA.,* p. 26, 2004.
[123] R. L. Fagaly, "Superconducting quantum interference device instruments and applications," *Review of Scientific Instruments,* vol. 77, p. 101101, 2006.
[124] J. Clarke, "Principles and applications of SQUIDs," *Proceedings of the IEEE,* vol. 77, pp. 1208-1223, 1989.
[125] P. W. Anderson and J. M. Rowell, "Probable observation of the Josephson superconducting tunneling effect," *Physical Review Letters,* vol. 10, p. 230, 1963.
[126] A. Ramadan, R. Gould, and A. Ashour, "On the Van der Pauw method of resistivity measurements," *Thin Solid Films,* vol. 239, pp. 272-275, 1994.
[127] L. Van der Pauw, "A method of measuring specific resistivity and Hall effect of discs of arbitrary shape," *Philips research reports,* vol. 13, pp. 1-9, 1958.
[128] E. Lähderanta, E. Hajdeu-Chicarosh, M. Shakhov, M. Guc, I. Bodnar, E. Arushanov*, et al.*, "Hopping magnetotransport of the band-gap tuning $Cu_2Zn(Sn_xGe_{1-x})$ Se_4 crystals," *Journal of Physics: Condensed Matter,* vol. 28, p. 455801, 2016.
[129] L. May, *An introduction to Mössbauer spectroscopy*: Springer Science & Business Media, 2012.
[130] L. R. Walker, G. K. Wertheim, and V. Jaccarino, "Interpretation of the Fe 57 isomer shift," *Physical Review Letters,* vol. 6, p. 98, 1961.
[131] R. H. Herber, "Introduction to Mossbauer spectroscopy," *Journal of Chemical Education,* vol. 42, p. 180, 1965/04/01 1965.
[132] P. F. Bongers, C. F. van Bruggen, K. J., W. P. F. A. M. Omloo, G. A. Wiegers, and F. Jellinek, "Structures and Magnetic Properties of some Metal (I) Chormium (III) Sulfides and Selenides," *Journal of Physics and Chemistry of Solids,* vol. 29, pp. 977-984, 1968.
[133] C. Wilkinson, B. M. Knapp, and J. B. Forsyth, "The magnetic structure of $Cu_{0.5}Ga_{0.5}Cr_2S_4$," *Journal of Physics C: Solid State Physics,* vol. 9, pp. 4021-4033, 1976.
[134] A. Ooe, S. Iida, M. Yagi, H. Kawaguchi, and T. Inagaki, *Proc. 7th Int. Conf. Ternary and Multinary Compounds, Snowmass,* 1986.
[135] M. Yagi, T. Terasako, N. Tsuboi, and S. Iida, "Deep Region Emissions of $CuGaS_2$ Crystals," *Japanese Journal of Applied Physics,* vol. 32, p. 618, 1993.
[136] S. Iida, Y. Oguro, H. Honda, and S. Suzuki, "Photolumeniscence of $CuGaS_2$ and Heterostructure Formation with Sputtered ZnS," *IL NUOVO CIMENTO,* vol. 2D, pp. 1933-1938, 1982.
[137] G. Massé, "Luminescence of $CuGaS_2$," *Journal of Applied Physics,* vol. 58, pp. 930-935, 1985.
[138] A.-M. Lamarche, J. C. Woolley, M. Quintero, and J. Ruiz, "T(z) Phase Diagram for $CuGa_{1-z}Fe_zS_2$ Alloys," *Physica status solidi (a),* vol. 126, pp. 109-113, 1991.
[139] K. Rosman and P. Taylor, "Report of the IUPAC subcommittee for isotopic abundance mea surements," *Pure Appl. Chem,* vol. 71, pp. 1593-1607, 1999.
[140] Y.-J. Zhao and A. Zunger, "Site preference for Mn substitution in spintronic$CuM^{III}X_2{}^{VI}$chalcopyrite semiconductors," *Physical Review B,* vol. 69, 2004.
[141] L. Vegard, "Die Konstitution der Mischkristalle und die Raumfüllung der Atome," *Zeitschrift für Physik,* vol. 5, pp. 17-26, January 01 1921.
[142] C. Sombuthawee, S. B. Bonsall, and F. A. Hummel, "Phase equilibria in the systems ZnS□MnS, ZnS□$CuInS_2$, and MnS□$CuInS_2$," *Journal of Solid State Chemistry,* vol. 25, pp. 391-399, 1978/08/01/ 1978.

[143] H. Strunz, *Pseudomorphosen: der derzeitige Kenntnisstand: Versuch einer Klassifizierung*, 1982.

[144] L. Corliss, N. Elliott, and J. Hastings, "Magnetic structures of the polymorphic forms of manganous sulfide," *Physical Review,* vol. 104, p. 924, 1956.

[145] F. Mehmed and H. Haraldsen, "Magnetochemische Untersuchungen. XXVIII. Das magnetische Verhalten der allotropen Modifikationen des Mangan (II)-Sulfids," *Zeitschrift für anorganische und allgemeine Chemie,* vol. 235, pp. 193-200, 1938.

[146] H. Spiess, U. Haeberlen, G. Brandt, A. Räuber, and J. Schneider, "Nuclear magnetic resonance in IB–III–VI2 semiconductors," *physica status solidi (b),* vol. 62, pp. 183-192, 1974.

[147] S. Abrahams and J. Bernstein, "Piezoelectric nonlinear optic $CuGaS_2$ and $CuInS_2$ crystal structure: Sublattice distortion in $A^{I}B^{III}C^{VI2}$ and $A^{II}B^{IV}C^{V2}$ type chalcopyrites," *The Journal of Chemical Physics,* vol. 59, pp. 5415-5422, 1973.

[148] J. Schneider, A. Räuber, and G. Brandt, "ESR-analysis of the chalcopyrite structure: $CuGaS_2$: Fe^{3+}," *Journal of Physics and Chemistry of Solids,* vol. 34, pp. 443-450, 1973.

[149] S. Eom, S. Kim, H. Ahn, and Y. Yu, "A Study of Photoluminescence and Raman Scattering in $CuGaS_2$:Cd," *physica status solidi (b),* vol. 223, pp. 319-323, 2001.

[150] J. R. Botha, M. S. Branch, P. R. Berndt, A. W. R. Leitch, and J. Weber, "Defect chemistry in $CuGaS_2$ thin films: A photoluminescence study," *Thin Solid Films,* vol. 515, pp. 6246-6251, 2007/05/31/ 2007.

[151] P. Prabukanthan and R. Dhanasekaran, "Influence of Mn doping on $CuGaS_2$ single crystals grown by CVT method and their characterization," *Journal of Physics D: Applied Physics,* vol. 41, p. 115102, 2008.

[152] K. Sato, M. Morita, S. Okamoto, S. Morita, T. Kambara, K. I. Gondaira*, et al.*, "Red photoluminescence spectrum of $CuAlS_2$: Mn," *Progress in Crystal Growth and Characterization,* vol. 10, pp. 311-320, 1984/08/15/ 1984.

[153] J.-H. Kim, B.-Y. Kim, and H. Yang, "Synthesis of Mn-doped $CuGaS_2$ quantum dots and their application as single downconverters for high-color rendering solid-state lighting devices," *Optical Materials Express,* vol. 8, pp. 221-230, 2018/02/01 2018.

[154] P. Prabukanthan and G. Harichandran, "Single Crystal Electron Paramagnetic Resonance (EPR) Study of Mn2+ Ions in $CuGaS_2$," *International Journal of Innovative Reasearch in Science & Engineering,* vol. 2, pp. 696-700, 2014.

[155] C. D. Lokhand, A. Ennaoui, P. S. Patil, M. Giersig, M. Muller, K. Diesner*, et al.*, "Process and characterisation of chemical bath deposited manganese sulphide (MnS) thin films," *Thin Solid Films,* vol. 330, pp. 70-75, 1998.

[156] W.-J. Jeong and G.-C. Park, "Structural and electrical properties of $CuGaS_2$ thin films by electron beam evaporation," *Solar energy materials and solar cells,* vol. 75, pp. 93-100, 2003.

[157] S. Schorr, R. Hoehne, D. Spemann, T. Doering, and B. V. Korzun, "Magnetic properties investigations of Mn substituted ABX_2chalcopyrites," *physica status solidi (a),* vol. 203, pp. 2783-2787, 2006.

[158] M. McElfresh, *Fundamentals of Mgnetism and Magnetic Measurments - Featuring Quantum Design´s Magnetic Property Measurement System*. Purdue University: Quantum Design, 1994.

[159] N. Tsujii, H. Kitazawa, and G. Kido, "Electric and Magnetic Properties of Mn- and Fe-Doped $CuInS_2$ Compounds," *Physica status solidi (a),* vol. 189, pp. 951–954, 2002.

[160] B. Tell and H. M. Kasper, "Electrical properties of $CuGaS_2$," *Journal of Applied Physics,* vol. 44, pp. 4988-4990, 1973.

[161] P. W. Yu, D. Downing, and Y. Park, "Electrical properties of $CuGaS_2$ single crystals," *Journal of Applied Physics,* vol. 45, pp. 5283-5288, 1974.

[162] N. Abdullaev, K. V. Aliguliyeva, L. Aliyeva, I. Qasimoglu, and T. Kerimova, "Low-temperature conductivity in $CuGaS_2$ single crystals," *Semiconductors,* vol. 49, pp. 428-431, 2015.

[163] N. F. Mott and E. A. Davis, "Electronic Processes in Non-Crystalline Materials, Clarendon," ed: Oxford, 1979.

[164] B. I. Shklovskii and A. L. Efros, *Electronic Properties of Doped Semiconductors* vol. 45: Springer Science & Business Media, 2013.

[165] E. Lähderanta, M. Guc, M. Shakhov, E. Arushanov, and K. Lisunov, "Influence of scattering and interference effects on the low-temperature magnetotransport of Cu_2ZnSnS_4 single crystals," *Journal of Applied Physics,* vol. 120, p. 035704, 2016.

[166] E. Hajdeu-Chicarosh, M. Guc, K. Neldner, G. Gurieva, S. Schorr, E. Arushanov*, et al.*, "Mechanisms of conductivity and energy spectrum of near-edge holes in Cu_2ZnSnS_4 powder samples," *Journal of Alloys and Compounds,* vol. 703, pp. 315-320, 2017.

[167] M. Guc, E. Lähderanta, E. Hajdeu-Chicarosh, S. Levcenko, M. A. Shakhov, I. Zakharchuk*, et al.*, "Mechanisms of charge transfer and electronic properties of Cu_2ZnGeS_4 from investigations of the high-field magnetotransport," *Scientific Reports,* vol. 7, p. 10685, 2017.

[168] M. Guc, K. Lisunov, E. Hajdeu, S. Levcenko, V. Ursaki, and E. Arushanov, "Variable-range hopping conductivity in $Cu_2ZnGeSe_4$ single crystals," *Solar Energy Materials and Solar Cells,* vol. 127, pp. 87-91, 2014.

[169] K. Lisunov, M. Guc, S. Levcenko, D. Dumcenco, Y. Huang, G. Gurieva*, et al.*, "Energy spectrum of near-edge holes and conduction mechanisms in $Cu_2ZnSiSe_4$ single crystals," *Journal of Alloys and Compounds,* vol. 580, pp. 481-486, 2013.

[170] E. Lähderanta, K. Lisunov, M. Shakhov, M. Guc, E. Hajdeu-Chicarosh, S. Levcenko*, et al.*, "High-field hopping magnetotransport in kesterites," *Journal of Magnetism and Magnetic Materials,* 2017.

List of figures

Figure 1 - Maximum power conversation efficiency for solar cell operating at ambient conditions illuminated with the AM 1.5G spectral irradiance (ASTM 173-03; AM1.5: 1.5 atmosphere thickness) as function of the band gap energy, adapted from the data of Rühle [13]. Arrows indicate the variability of the band gap due to chemical changes. 2

Figure 2 - Schematic progress in structural evolution from the diamond to chalcopyrite type structure adapted from Schorr [17]. Roman numbers indicate the valence state of the cations and anions. The anion are big spheres (brown-carbon, yellow-sulfur) and the cations are represented as small spheres (grey-zinc, blue-gallium and red-copper). The size of the spheres refers to their crystal radius in the structure taken from Shannon [18]. 3

Figure 3 - Correlation between the mean radii of the cation sites 4a (R4a) and 4b (R4b) ratio and the anion parameter x as function of the bandgap energy. The anion parameter x was calculated by the formalism of Jaffe and Zunger [19]. The band gap energies of the chalcopyrite type compound semiconductors were taken from literature [12, 20, 21]. The solid lines indicate the solid solution of $Cu(In,Ga)S_2$ and $Cu(In,Ga)Se_2$ chalcopyrite type compound semiconductor. 4

Figure 4 - Band structure of $CuGaS_2$ using scCOHSEX + G_0W_0 taken from Aguilera et. al [22]. 4

Figure 5 - Band diagram showing the transitions corresponding to absorption thresholds and bounds (left). Absorption bands associated with the electronic band structure of the IB semiconductor (right). Dashed lines represent qualitatively the real absorption coefficients. Squared shapes represent the simplified absorption coefficients [30]. 6

Figure 6 - Limiting efficiency at one sun of a solar cell with the bandgap of CuGaS2. The transition metals that could lead to the intermediate band located at the indicated position are shown as hollow dots [33]. 6

Figure 7 - Evolution of the Cu/Ga ratio (left) and the Cu/(Ga+TM) ratio (right) resulting from its specific substitution as function of the transition metal (TM) content. The black arrow refers to a coupled substitution, whereas the blue and red refer to a unilateral substitution of the transition metal with copper (red) or gallium (blue). 8

Figure 8 - Evolution of the M/S ratio resulting from its specific substitution as function of the transition metal (TM) content with respect to the charge of the transition metal (divalent- left; trivalent-right). The black arrow refers to a coupled substitution, whereas the blue and red refer to a unilateral substitution of the transition metal with copper (red) or gallium (blue). 9

Figure 9 - Schematic illustration of locations of the ternary isopleths examined by DTA and Guinier diffraction in the ternary phase field surrounding copper gallium sulfide (left). Ternary phase fields around copper gallium sulfide as determined in this investigation at room temperature by Guinier x-ray diffraction (right). Chalcopyrite phase denoted by cross-hatched area [39]. 11

Figure 10 - Binary phase diagram of copper and sulfur with the phases Dg-Digenite, Ch-Chalcocite, An-Anilite, Cv-Covellite (left) [44]. Detail view into the copper - sulfur binary phase diagram within the sulfur range of 32-37at% (right) [44]. 12
Figure 11 - Binary phase diagram of gallium and sulfur(left) [57]. Binary phase diagram of copper and gallium (right) [58]. 13
Figure 12 - Binary phase diagram of chromium and sulfur (left) [65]. Binary phase diagram of chromium and copper (right) [66]. 14
Figure 13 - Calculated binary phase diagram of chromium and gallium from Gröbner et al. [74] based on experimental data from Bornand and Feschotte [68]. 15
Figure 14 - Binary phase diagram of iron and sulfur (left) [80]. Detail view into the iron - sulfur binary phase diagram within the sulfur range of 0-0.25at% (right) [80]. 16
Figure 15 - Binary phase diagram of iron and copper (left) [81]. Binary phase diagram of iron and gallium (right) [82]. 17
Figure 16 - Binary phase diagram of manganese and sulfur (left) [89]. Detail view into the manganese - sulfur binary phase diagram within the sulfur range of 0-8at% (right) [89]. 18
Figure 17 - Binary phase diagram of manganese and copper (left) [94]. Binary phase diagram of manganese and gallium (right) [95]. 19
Figure 18 - Binary phase diagram of nickel and sulfur [102]. 20
Figure 19 - Binary phase diagram of nickel and copper (left) [103]. Binary phase diagram of nickel and gallium (right) [104]. 21
Figure 20 - Schematic temperature profiles of the first synthesis step (a) and the homogenization step (b). The different color code does not represent specific sample series, it is only a matter of visualization. 26
Figure 21 - Photographs of a sample from the iron series during preparation, a) weighted elements before first reaction, b) after first reaction, c) after first homogenization and d) final pellet before grinding. 27
Figure 22 - Neutron scattering length b of relevant elements as function of atomic number after [111]. 30
Figure 23 - Schematic drawing of E9 [112]. 30
Figure 24 - Schematic representation of the excitation and relaxation processes of photoluminescence. 34
Figure 25 - Superconducting quantum interference device instruments and applications [123]. 35
Figure 26 - The actual (left) and the schematic (right) experimental assembly of the temperature dependent resistivity measurements. 37
Figure 27 - Origin of quadrupole splitting (Q. S.) (left), the magnitude is given by ΔEq as well as the source of magnetic splitting (I. S. isomer shift) (right); modified from Herber [131]. 38

Figure 28 - BSE micrograph of chromium doped chalcopyrite sample, dark gray grains: Cr-spinel, medium gray: chalcopyrite, light gray: γ CuGa phase. 39
Figure 29 - Initial vs. measured chromium mole fraction within the chalcopyrite type phase (left), zoomed-in area (right). 40
Figure 30 - Copper to gallium ratio (a), copper to trivalent cations ratio (b), cation to anion ratio (c) and gallium to chromium ratio (d) as a function of the chromium molar fraction within the chalcopyrite type phase. 41
Figure 31 - Volume fraction of the phases and the corresponding chromium content of the chalcopyrite type phase. On the left-hand side, low temperature and on the right-hand side, high temperature synthesis. 42
Figure 32 - Lattice parameter a and c/2 of the chalcopyrite type phase as function of the chromium molar fraction and color coded according their copper to gallium ratio (left). Tetragonal deformation and distortion of the chalcopyrite type phase as function of the chromium molar fraction and color coded according their copper to gallium ratio (right). 43
Figure 33 - Comparison of the measured and calculated average neutron scattering length (ANSL) (left). Red line marks the NSL of copper, the blue line of gallium. Resulting cationic distribution and corresponding chromium molar fraction (right); x_m refers to the chromium molar fraction within the chalcopyrite type phase. 44
Figure 34 - Defect concentration calculated from cation distribution of the chalcopyrite type phase regarding the measured chromium content (x_m). 44
Figure 35 - PL spectra of chromium containing chalcopyrite type phases, with 0.0014(10)mol% CrS (left) and 0.0028(10)mol% CrS (right) in $Cu_{0.5}Ga_{0.5}S$. 45
Figure 36 - BSE micrograph of chromium doped chalcopyrite sample, dark gray grains: Nickeline, medium gray: chalcopyrite, light gray: α´ Ni-Ga phase. 47
Figure 37 - Initial vs. measured nickel mole fraction within the chalcopyrite type phase (left), zoomed-in area (right). 48
Figure 38 - Copper to gallium ratio (a), copper to trivalent cations ratio (b), cation to anion ratio (c) and gallium to nickel ratio (d) as a function of the nickel molar fraction within the chalcopyrite type phase. 49
Figure 39 - Volume fraction of the phases and the corresponding nickel content of the chalcopyrite type phase. 50
Figure 40 - Simulated X-ray diffraction pattern of the $CuGaS_2$ chalcopyrite type phase and Heazlewoodite (Ni_3S_2). 50
Figure 41 - Lattice parameter a and c/2 of the chalcopyrite type phase as function of the nickel molar fraction and color coded according their copper to gallium ratio (left). Tetragonal deformation and distortion of the chalcopyrite type phase as function of the nickel molar fraction and color coded according their copper to gallium ratio (right). 51

Figure 42 - 550nm PL spectra of nickel containing chalcopyrite type phases as function of NiS mole fraction (x_m) in $Cu_{0.5}Ga_{0.5}S$. 52
Figure 43 - BSE micrograph of iron alloyed chalcopyrite samples, gray grains: chalcopyrite type phase, white grains: intermetallic compounds (left); bright grains: low iron content, dark grains: high iron content (right). 54
Figure 44 - Initial vs. measured iron mole fraction within the chalcopyrite type phase. 55
Figure 45 - Copper to gallium ratio (a), copper to trivalent cations ratio (b), cation to anion ratio (c) and gallium to iron ratio (d) as a function of the iron molar fraction within the chalcopyrite type phase. 56
Figure 46 - Lattice parameter a and c/2 as a function of the measured iron content of the chalcopyrite type phase and Cu/(Ga+Fe) ratio. The dotted lines refer to the evolution of the lattice parameters regarding Vegard´s law. 58
Figure 47 - Tetragonal deformation (left) and tetragonal distortion (right) as a function of the measured iron content of the chalcopyrite type phase and Cu/(Ga+Fe) ratio. 58
Figure 48 – Anion parameter x as function of the measured iron content of the chalcopyrite type phase, color-coded regarding the Cu/(Ga+Fe) ratio. 59
Figure 49 - BSE micrograph of manganese alloyed chalcopyrite samples, light gray grains: chalcopyrite type phase, dark gray grains: manganese sulfide, white grains: intermetallic compounds (left); light gray grains chalcopyrite type phase, dark grains: 3-3-4 Cu-Ga-Mn-sulfide phase (right). 63
Figure 50 - Initial vs. measured manganese mole fraction within the chalcopyrite type phase (left) and zoomed-in area with manganese mole fraction below the miscibility gap (right). 63
Figure 51 - Copper to gallium ratio (a), copper to gallium plus manganese cations ratio (b), cation to anion ratio (c) and gallium to manganese ratio (d) as a function of the manganese molar fraction within the chalcopyrite type phase. 64
Figure 52 - Lattice parameter of chalcopyrite type phase as function of the containing MnS mole fraction, color-coded regarding their copper to gallium ratio (left) and their cation to anion ration (right). 65
Figure 53 - Tetragonal deformation η of chalcopyrite type phase as function of the containing MnS mole fraction, color-coded regarding their copper to gallium ratio (left) and their cation to anion ration (right). 66
Figure 54 - Tetragonal distortion u of chalcopyrite type phase as function of the containing MnS mole fraction, color-coded regarding their copper to gallium ratio (left) and their cation to anion ration (right). 67
Figure 55 - Structural parameters obtained by XRD, color-coded regarding the measured copper to gallium ratio, compared to the structural evolution considering Vegard´s law as a function of the

MnS molar fraction (lines); lattice parameter a (a); lattice parameter c (b); tetragonal deformation η (c); tetragonal distortion u (d). 68
Figure 56 - Average neutron scattering length (left) and corresponding cation distribution (right) of chalcopyrite type phases from unilateral substitution; x_m refers to the manganese molar fraction within the chalcopyrite type phase. 70
Figure 57 - Average neutron scattering length (left) and corresponding cation distribution (right) of chalcopyrite type phases from coupled substitution; x_m refers to the manganese molar fraction within the chalcopyrite type phase. 70
Figure 58 - Defect concentration calculated from cation distribution, x_m refers to the manganese molar fraction within the chalcopyrite type phase. (*) marks samples which show one PL band, (#) marks samples with two PL band. 71
Figure 59 - Effect of synthesis temperature on the Cu/Ga ratio (left), the Cu/(Ga+Mn) ratio (middle) and the M/S ratio (right) of chalcopyrite type phases from unilateral substitution series. 72
Figure 60 - Temperature dependency of the Cu/Ga ratio (left), the Cu/(Ga+Mn) ratio (middle) and the M/S ratio (right) of chalcopyrite type phases from coupled substitution series. 73
Figure 61 - Effect of synthesis temperature on tetragonal deformation η (left) and tetragonal distortion u (right) of chalcopyrite type phases from unilateral substitution series. 73
Figure 62 - Temperature dependency of tetragonal deformation η (left) and tetragonal distortion u (right) of chalcopyrite type phases from coupled substitution series. 74
Figure 63 - BSE micrograph of the expected 3-3-4 phase. 75
Figure 64 - Measured atomic ratio of both 3-3-4 samples, left - I, right - II. 75
Figure 65 - Obtained XRD pattern of the 3-3-4(I) sample and simulated XRD pattern of chalcopyrite type $CuGaS_2$ and MnS 76
Figure 66 - TEM bright field image with corresponding electron diffraction pattern taken from Herkelrath [106]. 77
Figure 67 - TEM bright field image with corresponding EDX analysis of the marked phases taken from Herkelrath [106]. 77
Figure 68 - Detailed view on a $Cu_{0.5}Ga_{0.5}S$ tetrahedron from the chalcopyrite type structure with the bond length of the cation site 4a and 4b to the sulfur anion, as well as the 4a-S-4a and 4b-S-4b bond angles with respect to the anion parameter x. 79
Figure 69 - Variation of band energies at high-symmetry points of $CuInSe_2$ (left) and $CuAlS_2$ (right) with anion parameter x after Jaffe and Zunger [19]. Shaded areas denote the direct band gap; arrows mark the calculated [19] (red) and experimental [146] (blue) values. 80
Figure 70 - Chalcopyrite type structure around a copper vacancy with an anion position of x=0.2 (left), x=0.25 (middle) and x=0.3 (right) parallel to the c-axis. 82
Figure 71 - Observed cation site radii (4a-left, 4b-right) as function of the manganese molar fraction, color-coded regarding the calculated vacancy concentration from chemical composition. As

comparison with the simulated evolution due to the incorporation of manganese on 4a or 4b color-coded regarding the calculated vacancy concentration. The two extrema of 0% and 7.5% copper vacancies are displayed in thicker lines. 83
Figure 72 - Observed tetragonal distortion as function of the manganese mole fraction, color-coded regarding the calculated vacancy concentration from chemical composition. As comparison with the simulated evolution due to the incorporation of manganese on 4a or 4b color-coded regarding the calculated vacancy concentration. The two extrema of 0% and 7.5% copper vacancies are displayed in thicker lines. 84
Figure 73 - Observed lattice constants a (left) and c (right) as function of the manganese molar fraction, color-coded regarding the calculated vacancy concentration from chemical composition. As comparison with the simulated evolution due to the incorporation of manganese on 4a or 4b color-coded regarding the calculated vacancy concentration. The two extrema of 0% and 7.5% copper vacancies are displayed in thicker lines. 85
Figure 74 - Tetragonal deformation as function of the manganese molar fraction, color-coded regarding the calculated vacancy concentration from chemical composition. As comparison with the simulated evolution due to the incorporation of manganese on 4a or 4b color-coded regarding the calculated vacancy concentration. The two extrema of 0% and 7.5% copper vacancies are displayed in thicker lines. 85
Figure 75 - $CuGaS_2$ chalcopyrite type structure with one copper vacancy (0.5, 0.5, 0.5). The anion are big spheres (yellow-sulfur) and the cations are represented as small spheres, (red-copper, and blue-gallium). The size of the spheres refers to their crystal radius in the structure taken from Shannon [18]. 86
Figure 76 - Comparison of observed and calculated average cation radii of the 4a (left) and 4b (right) site. The lines refer to the trends following Vegard´s law of manganese occupying exclusively the 4a (solid) or 4b (dashed) site, without consideration of copper vacancies. 87
Figure 77 - Comparison of observed and calculated tetragonal distortion u. The lines refer to the trends following Vegard´s law of manganese occupying exclusively the 4a (solid) or 4b (dashed) site, without consideration of copper vacancies. 87
Figure 78 - Comparison of PL spectra of $CuGaS_2$ and two Mn containing $CuGaS_2$ phases from the two different groups (* and #). 89
Figure 79 - PL spectra of the chalcopyrite type phases which show only on PL band (left), PL spectra of the chalcopyrite type phases which show two PL bands (right). 89
Figure 80 - Schematic drawing of the band diagram with defect levels resulting from the incorporation of manganese adapted from Zhao and Zunger [6]. The bandgap energy of 2.43eV was taken from Tell [12]. 91
Figure 81 - Magnetization of manganese containing $CuGaS_2$ (x_m=0.021 (left), x_m=0.041 (right)) as a function of the magnetic field cycled between +60 kOe and -60 kOe at different temperatures. 92

Figure 82 - Inverse magnetic susceptibility as a function of temperature, with zero field cooling (ZFC) (left) and with field cooling (FC) (right). The red lines are linear fit of the data denoting the region of the Curie-Weiss law. 93
Figure 83 - Temperature dependence of resistivity of pure manganese doped chalcopyrite type phases (left). The plots of $\ln(\rho T^{-1/4})$ vs. $T^{-1/4}$ for the investigated samples (right). The red lines are linear fit of the data denoting the region with Mott VRH conductivity. 94

List of Tables

Table I - Defect formation energies, ΔG_D, for intrinsic defects in $CuGaS_2$, from Bailey et al. [34]. 7
Table II - Sulfide Crystal Radii from Shannon [36]; LS-low spin; HS-high spin. 9
Table III - Overview of all possible phases according to the relevant binary phase diagrams and the Cu-Ga-S ternary phase diagram discussed in this chapter. 23
Table IV - Overview of studied systems and their corresponding pseudo-binary section. Y indicates the area of variation or as a first approximation the transition metal content within the pseudo-binary section. 24
Table V - Detailed overview of experimental series and their synthesis temperature profile. 26
Table VI - Overview of the observed secondary phases within the Cr:$CuGaS_2$ experiments as well as their commonness; the max. volume fraction of the phases was determined by Rietveld refinement of XRD data. 46
Table VII - Overview of the observed secondary phases within the Ni:$CuGaS_2$ experiments as well as their commonness; the max. volume fraction of the phases was determined by Rietveld refinement of XRD data. 53
Table VIII - Overview of the observed secondary phases from iron alloyed $CuGaS_2$ as well as their commonness; the max. volume fraction of the phases was determined by Rietveld refinement of XRD data. 61
Table IX - Calculated structural parameters of the endmembers using the routine from Jaffe and Zunger [19], (-) is marking actually negative values. 67
Table X - Compilation of experimentally obtained anion parameter x and tetragonal distortion u. 81
Table XI - Overview of all parameters obtained from temperature dependent resistivity measurements of the two manganese containing chalcopyrite type phases $(Cu_{0.5}Ga_{0.5}S)_{1-x}MnS_x$ 95
Table XII - Overview of the observed secondary phases from manganese alloyed $CuGaS_2$; the max. volume fraction of the phases was determined by Rietveld refinement of XRD data. 96

Acknowledgment

I would like to thank the people who made the completion of this dissertation possible and supported me at any stage of the research.

- Prof. Dr. Susan Schorr Head of the Department "Structure and Dynamic of Energy Materials" for the opportunity to do research in this interesting field, as well as the supervision of the research with numerous comments, hints and commitment, but also for giving me the possibility of attending several conferences to present my research.
- Prof. Dr. Christiane Stephan-Scherb for trusting me with this interesting subject and the support.
- Dr. Galina Gurieva for any support in the chemical lab and in the furnace lab, as well as for kind explanation regarding physics.
- Dr. Alexandra Franz for support and guidance in the neutron diffraction experiments, as well as the deployment of the data.
- Dr. Ralf Milke for support with the electron beam microprobe.
- Christiane Behr for preparing the powder samples for the electron beam microprobe.
- Dr. Konrad Siemensmeyer for the measurements with the SQUID and the support with evaluation of the data.
- Dr. Maxim Guc for measuring the temperature dependent resistivity as well as the evaluation of the data.
- Prof. Dr. Georg Amthauer for ^{57}Fe Mössbauer spectroscopy measurements.
- Dr. Sergiu Levcenco for support and guidance of the PL spectroscopy as well as the deployment and evaluation of the data and for the long fruitful discussions of the results.
- René Gunder, who always has an open ear for questions and problems. As well as the support in every respect, be it when working in the laboratory or in the evaluating of results.
- Frederike Lehmann for proofreading and having a different point of view on my results, but also for traveling with me to different conferences and having an open ear.
- All other people that supported me on my way for the Department of "Structure and Dynamic of Energy Materials" and the Mineralogy Group of the Freie Universität Berlin, for fruitful discussions and spending some time with me.
- Many thanks to Josi for your endless patience.

Appendix

C-I-I 0.02

$Cu_{0.501}Ga_{0.509}Cr_{0.0007}S$

a: 5.355 Å c: 10.485 Å x: 0.2571(13)

94% Chp; 6% γ Cu-Ga; <1% Cr-spinel

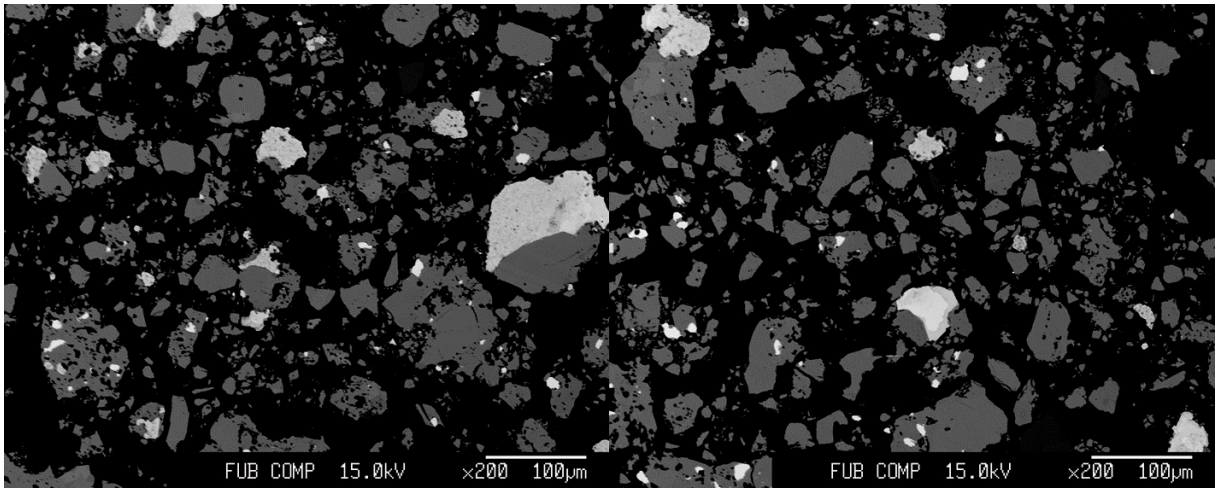

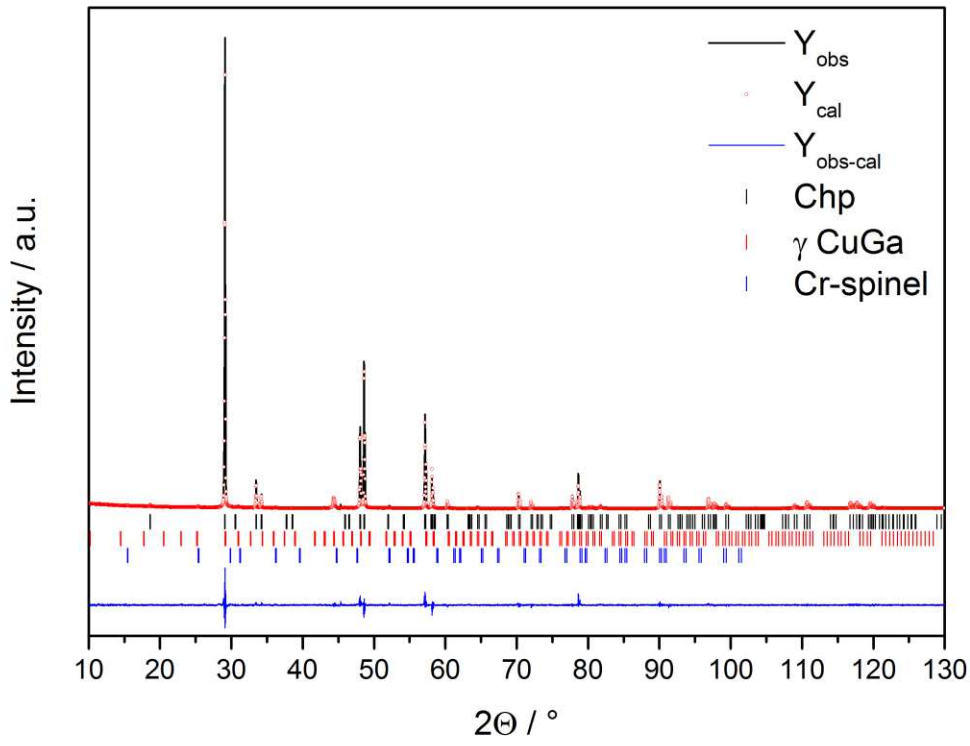

XRD: Chi^2: 5.79 Bragg R-factor: 1.92

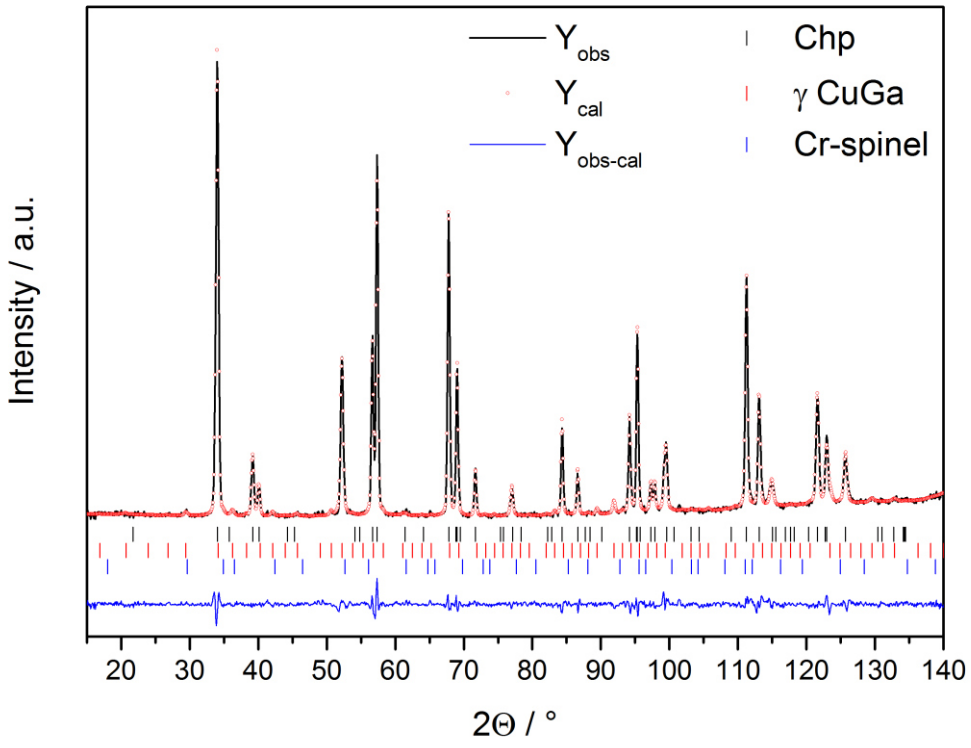

ND: Chi^2: 2.0 Bragg R-factor: 1.73

C-I-I 0.06

$Cu_{0.492}Ga_{0.508}Cr_{0.0008}S$

a: 5.356 Å c: 10.487 Å x: 0.2626(10)

95% Chp; 3% γ Cu-Ga; >1% Cr-spinel

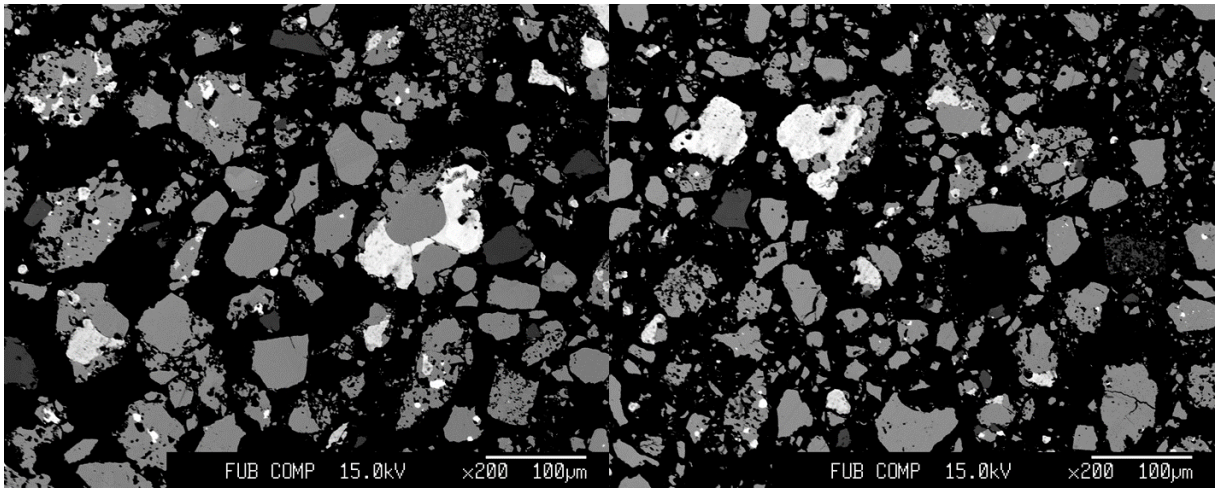

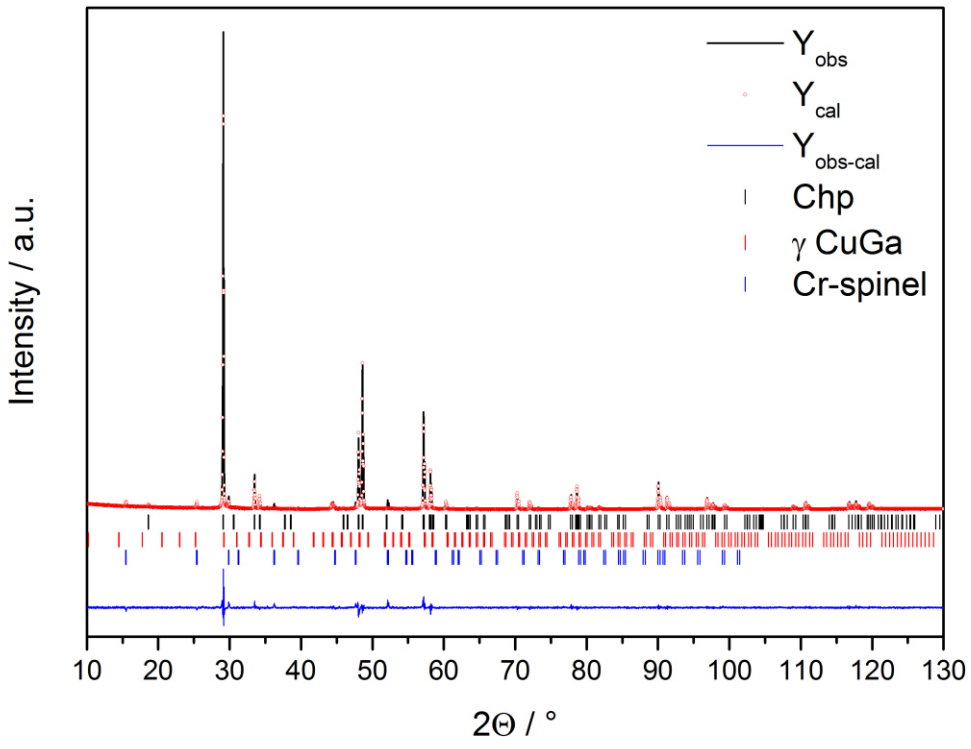

XRD: Chi^2: 1.84 Bragg R-factor: 4.68

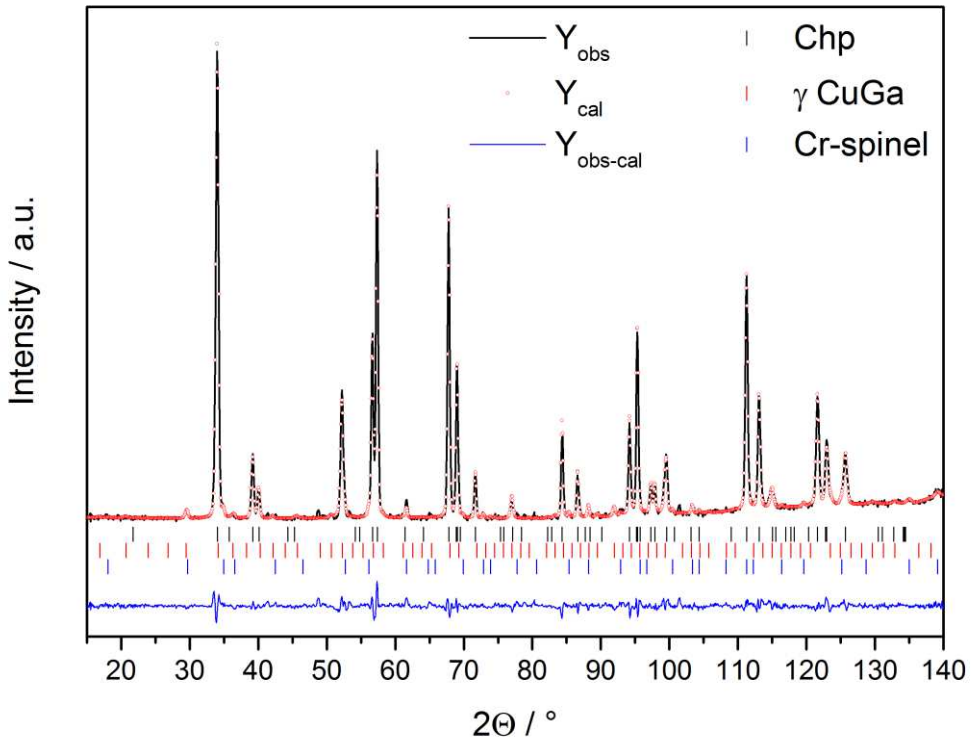

ND: Chi^2: 2.37 Bragg R-factor: 2.30

C-I-I 0.08

$Cu_{0.500}Ga_{0.510}Cr_{0.0013}S$

a: 5.356 Å c: 10.486 Å x: 0.2590(13)

98% Chp; 1% γ Cu-Ga; 1 % Cr-spinel

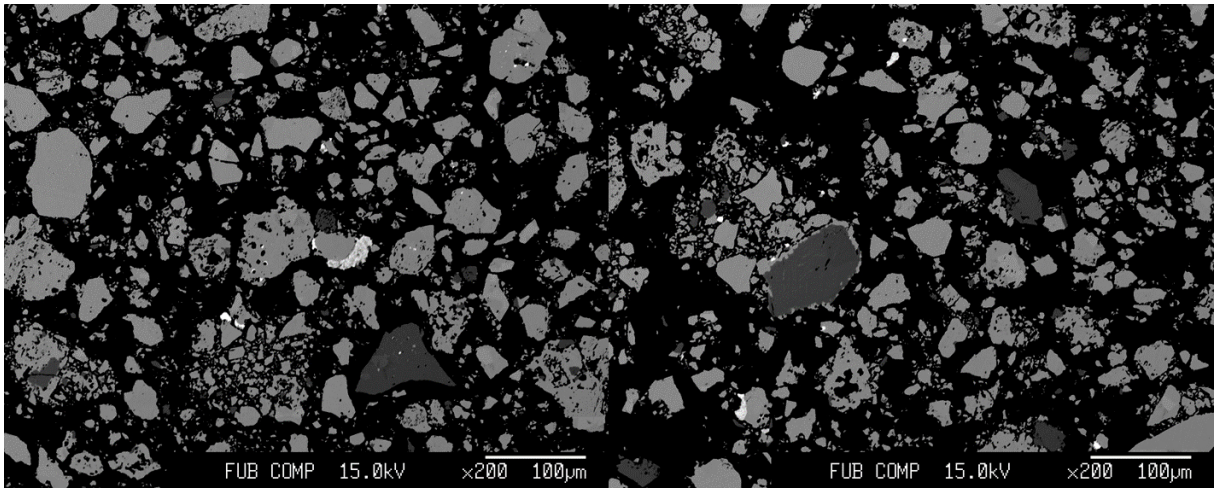

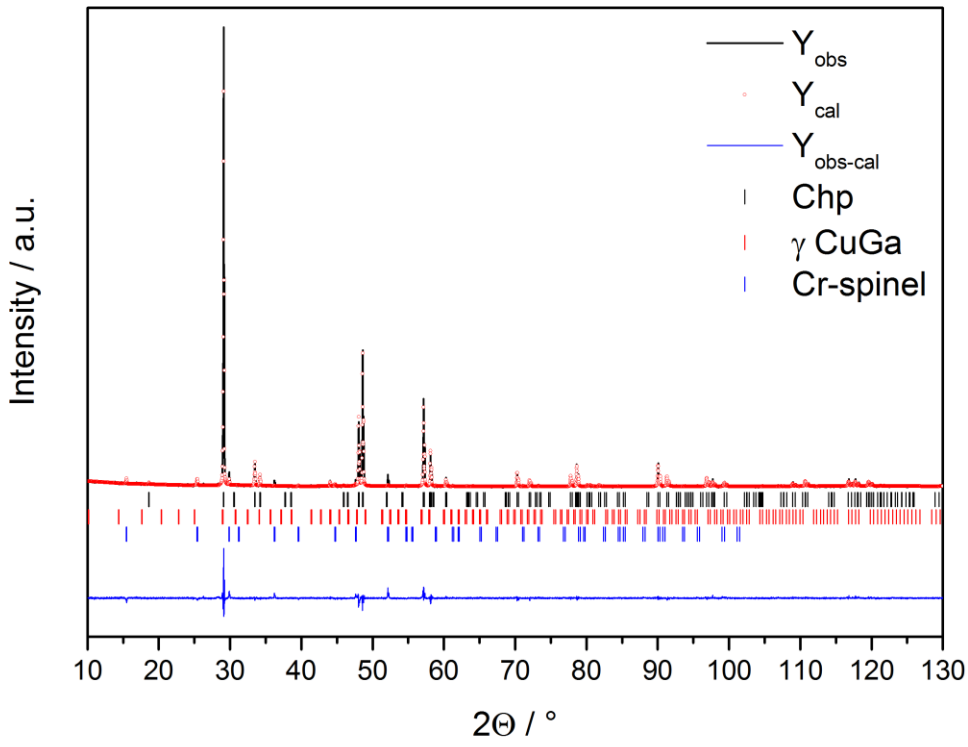

XRD: Chi^2: 2.29 Bragg R-factor: 4.94

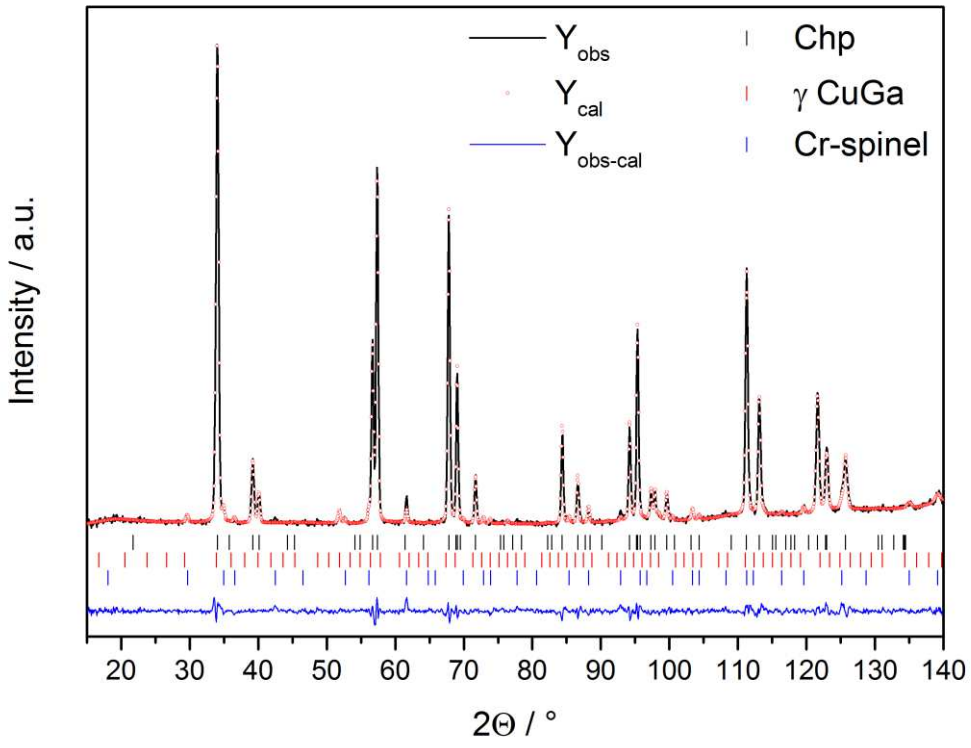

ND: Chi^2: 1.82 Bragg R-factor: 1.89

C-I-I 0.1

$Cu_{0.494}Ga_{0.494}Cr_{0.0014}S$

a: 5.356 Å c: 10.486 Å x: 0.2599(14)

98% Chp; 2 % Cr-spinel

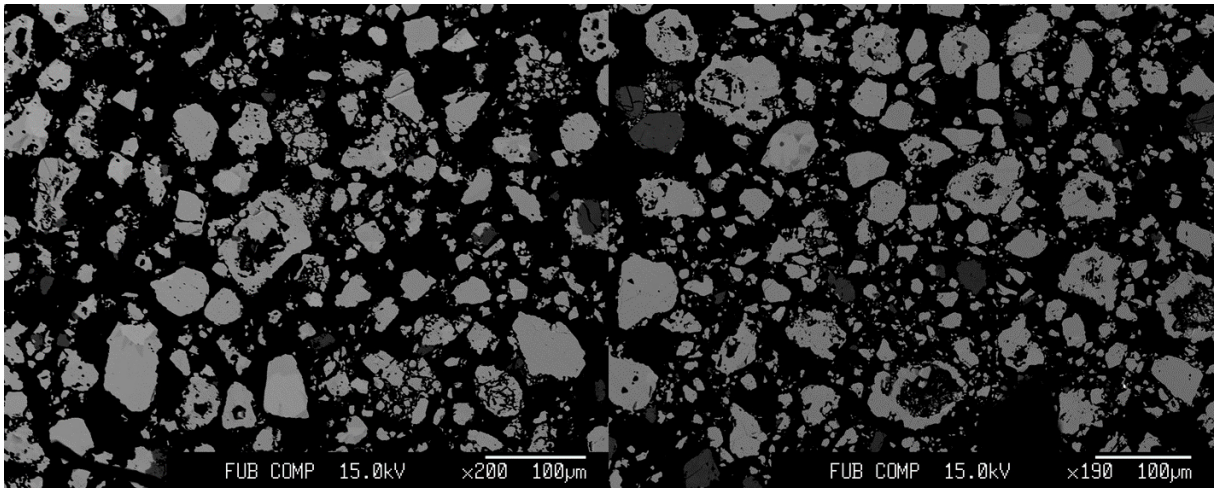

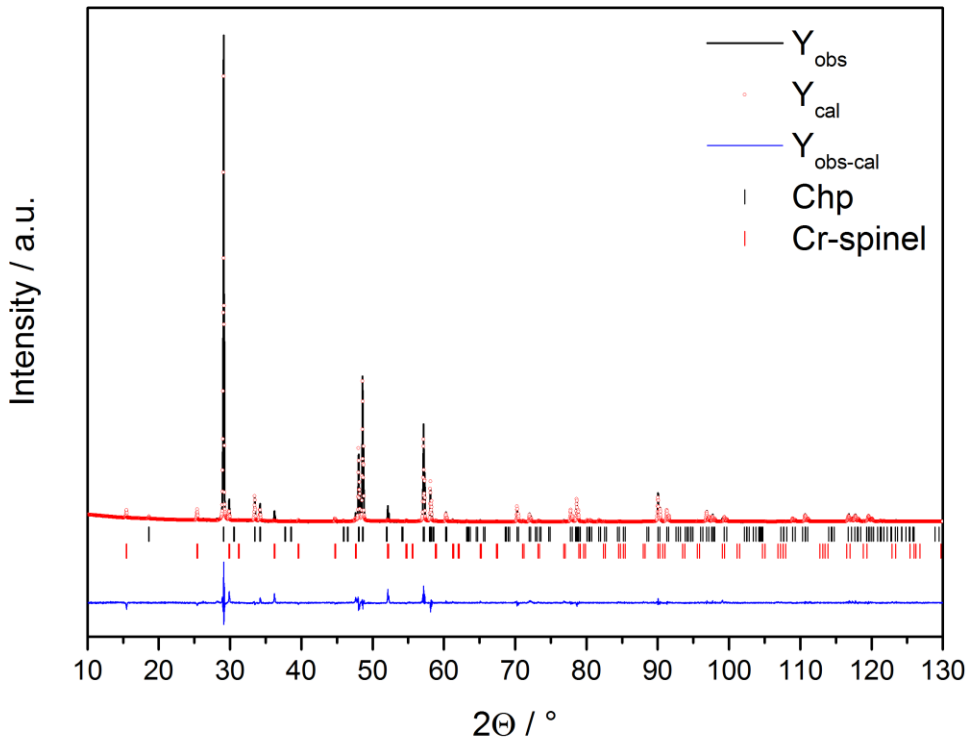

XRD: Chi^2: 4.11 Bragg R-factor: 5.12

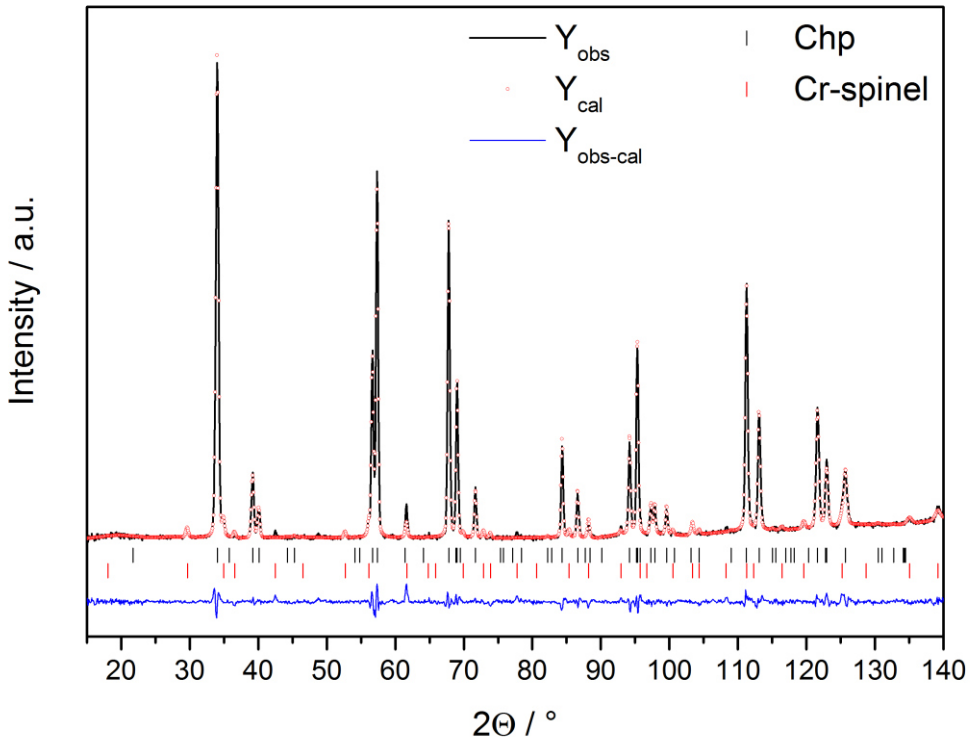

ND: Chi^2: 2.15 Bragg R-factor: 1.64

C-I-I 0.2

$Cu_{0.494}Ga_{0.499}Cr_{0.0028}S$

a: 5.356 Å c: 10.485 Å x: 0.2574(23)

95% Chp; 5 % Cr-spinel

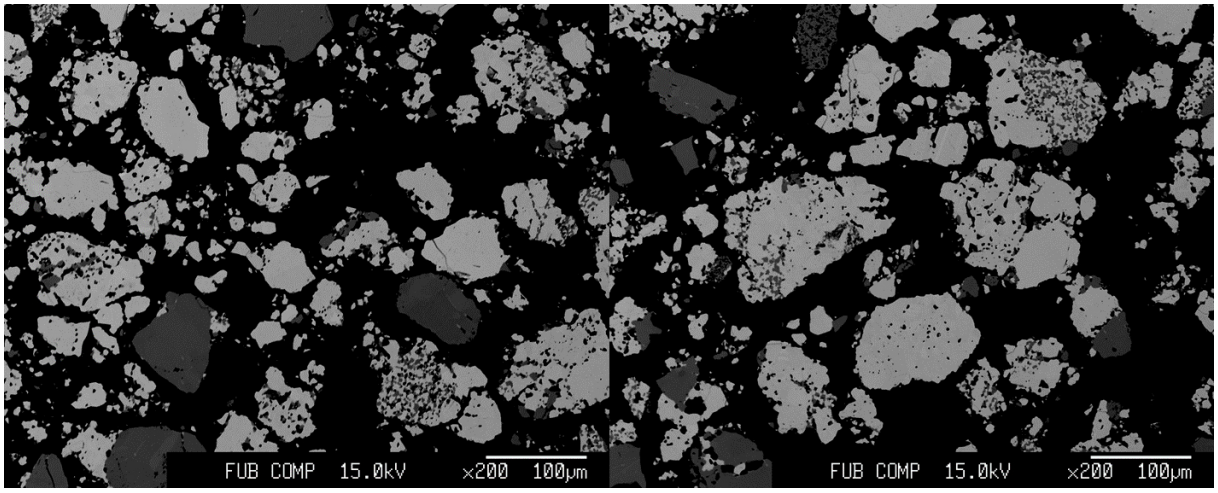

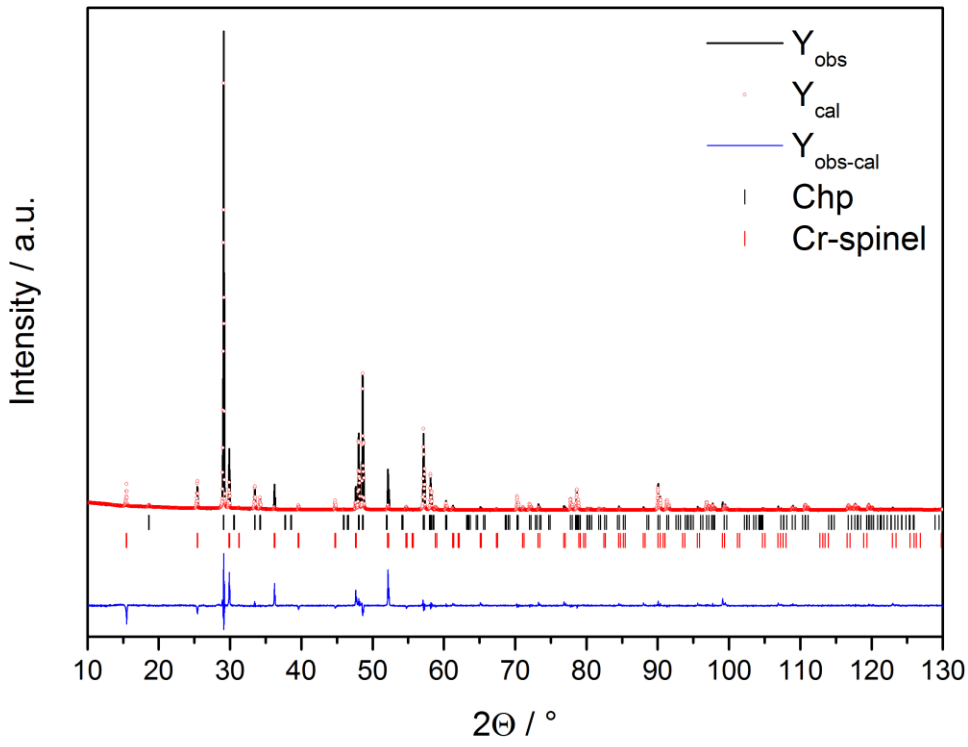

XRD: Chi^2: 7.16 Bragg R-factor: 5.42

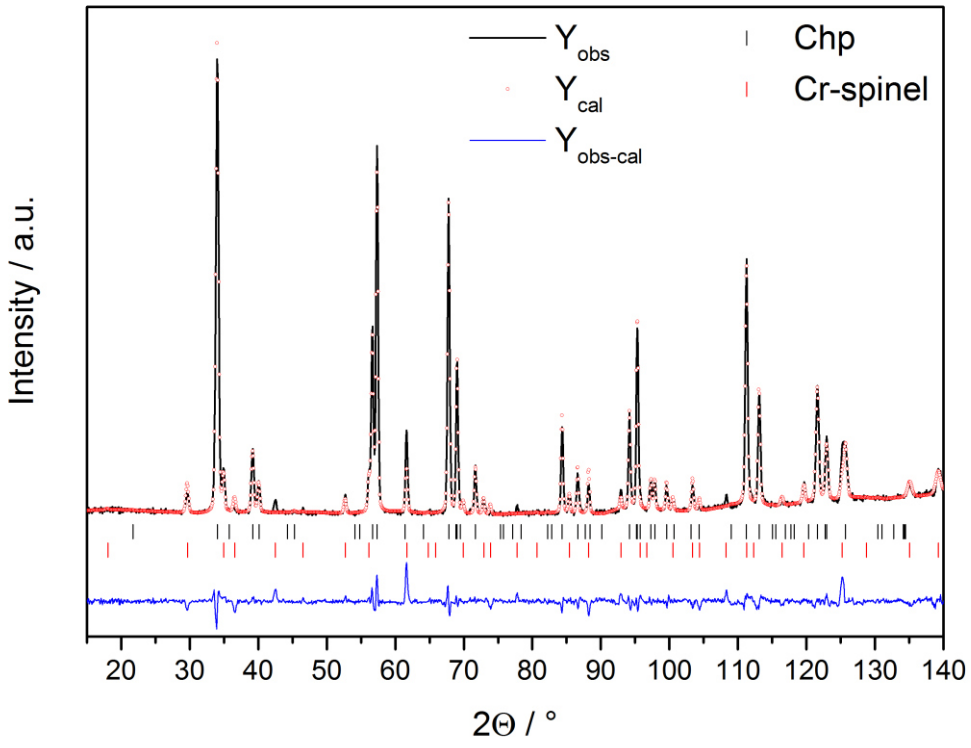

ND: Chi^2: 3.61 Bragg R-factor: 2.15

C-I-II 0.02

$Cu_{0.522}Ga_{0.503}Cr_{0.0008}S$

a: 5.355 Å c: 10.486 Å x: 0.2622(12)

79% Chp; 16% γ Cu-Ga; 5 % υ Cu-Ga

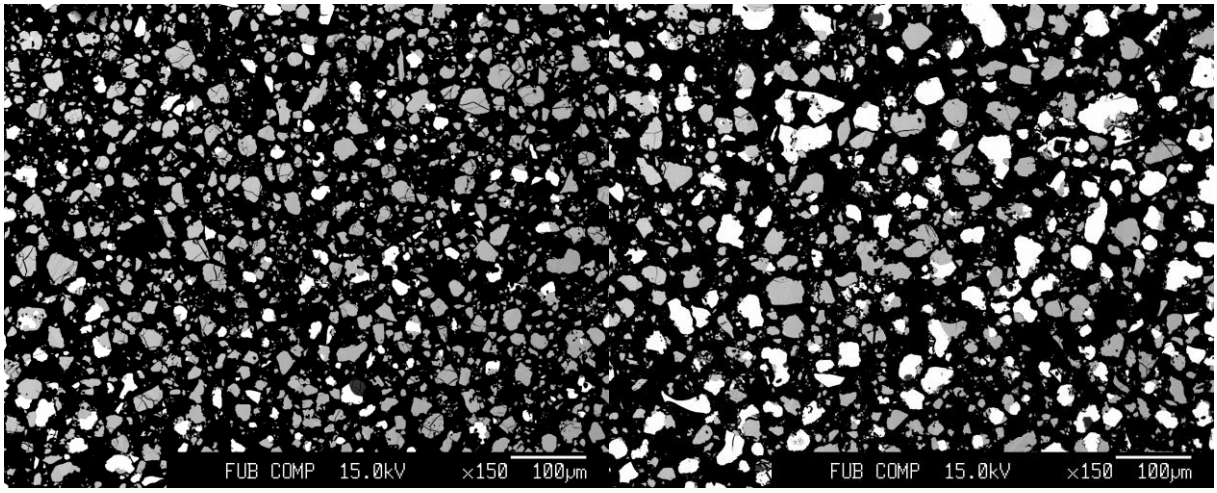

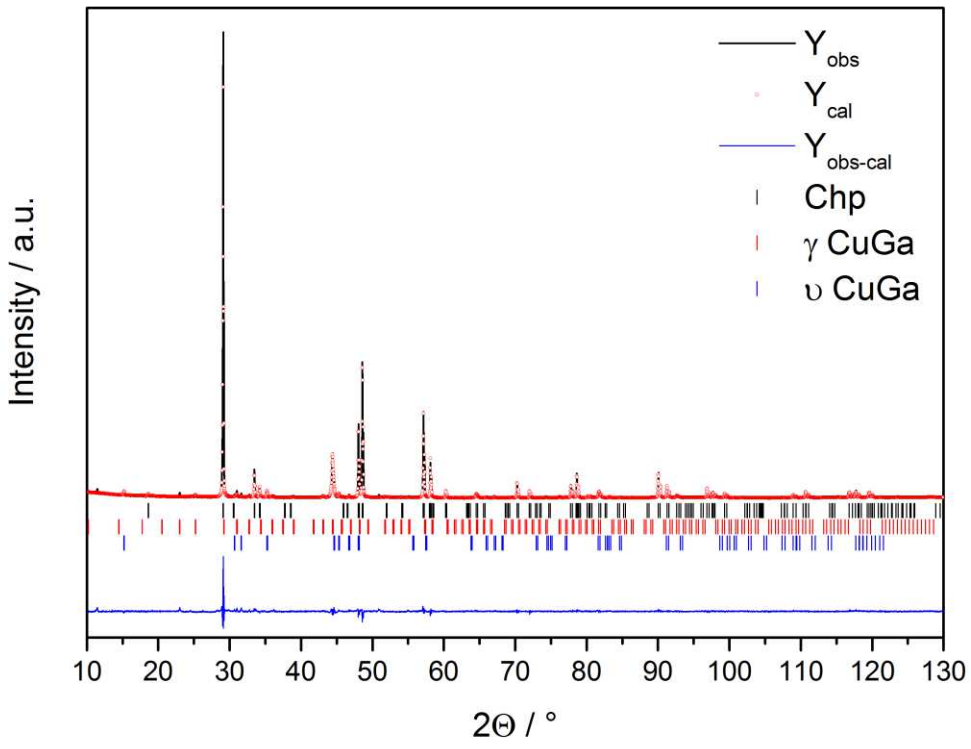

XRD: Chi^2: 3.60 Bragg R-factor: 5.49

C-I-II 0.03

$Cu_{0.512}Ga_{0.495}Cr_{0.0008}S$

a: 5.356 Å c: 10.487 Å x: 0.2604(14)

79% Chp; 17% γ Cu-Ga; 4 % υ Cu-Ga; <1 % Cr-spinel

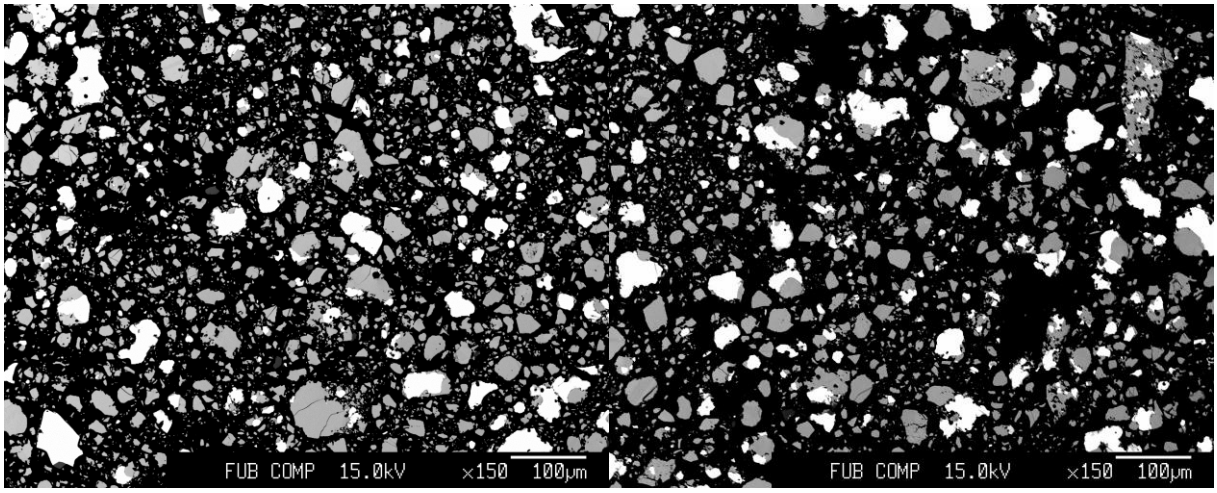

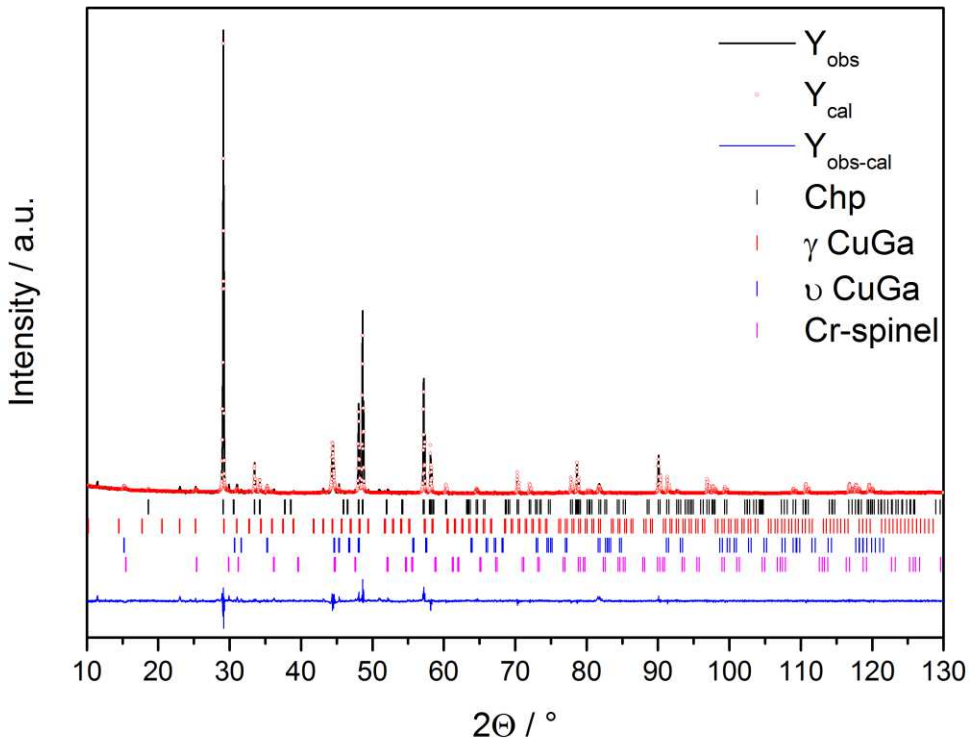

XRD: Chi^2: 3.31 Bragg R-factor: 5.91

C-I-II 0.04

$Cu_{0.520}Ga_{0.509}Cr_{0.0010}S$

a: 5.355 Å c: 10.487 Å x: 0.2617(9)

92% Chp; 7% γ Cu-Ga; <1 % Cr-spinel

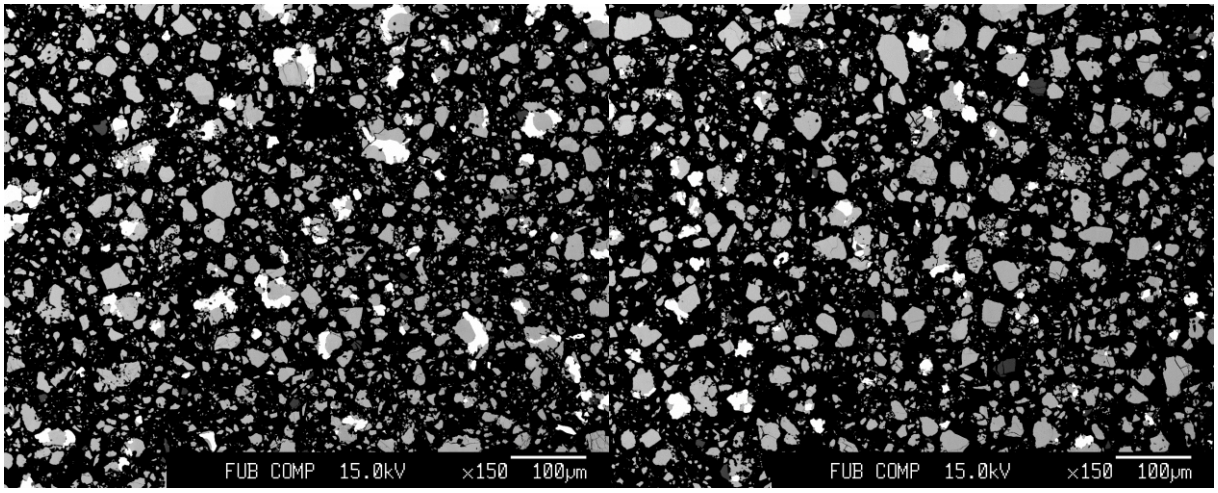

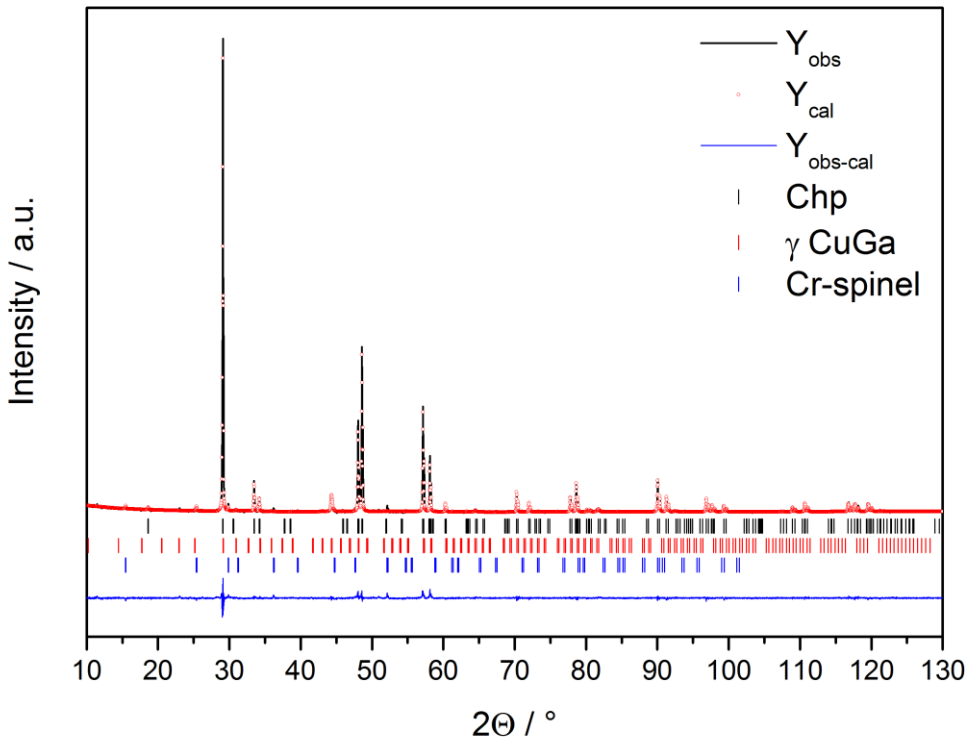

XRD: Chi^2: 2.18 Bragg R-factor: 4.87

C-I-II 0.05

$Cu_{0.515}Ga_{0.502}Cr_{0.0012}S$

a: 5.355 Å c: 10.486 Å x: 0.2601(10)

93% Chp; 7% γ Cu-Ga; <1 % Cr-spinel

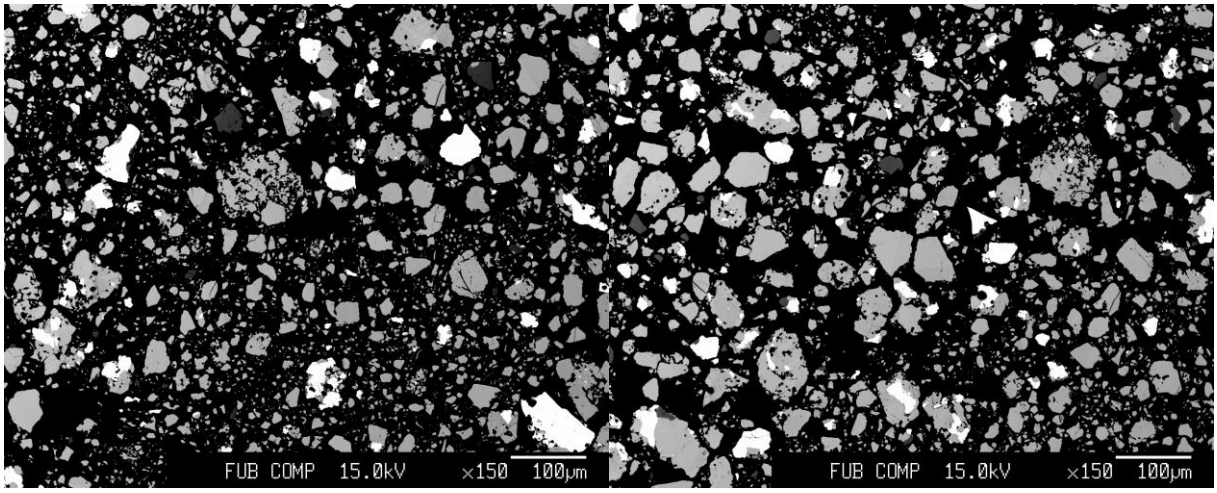

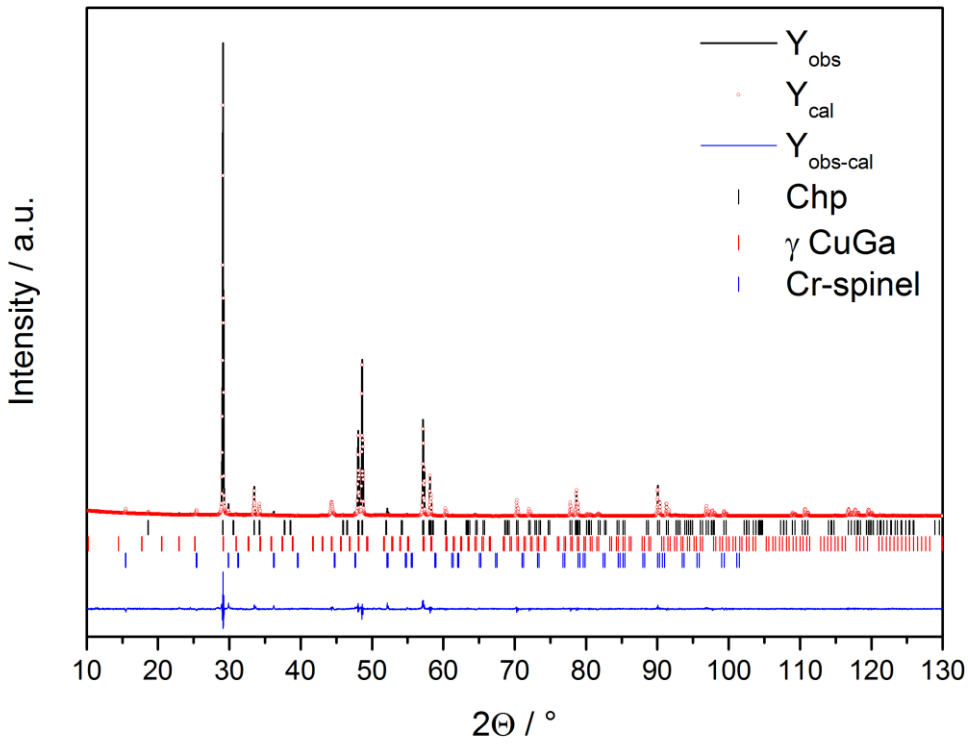

XRD: Chi^2: 2.61 Bragg R-factor: 4.28

Mn-I-I 0.02

$Cu_{0.477}Ga_{0.475}Mn_{0.021}S$

a: 5.360 Å c: 10.502 Å x: 0.2605(12)

100% Chp

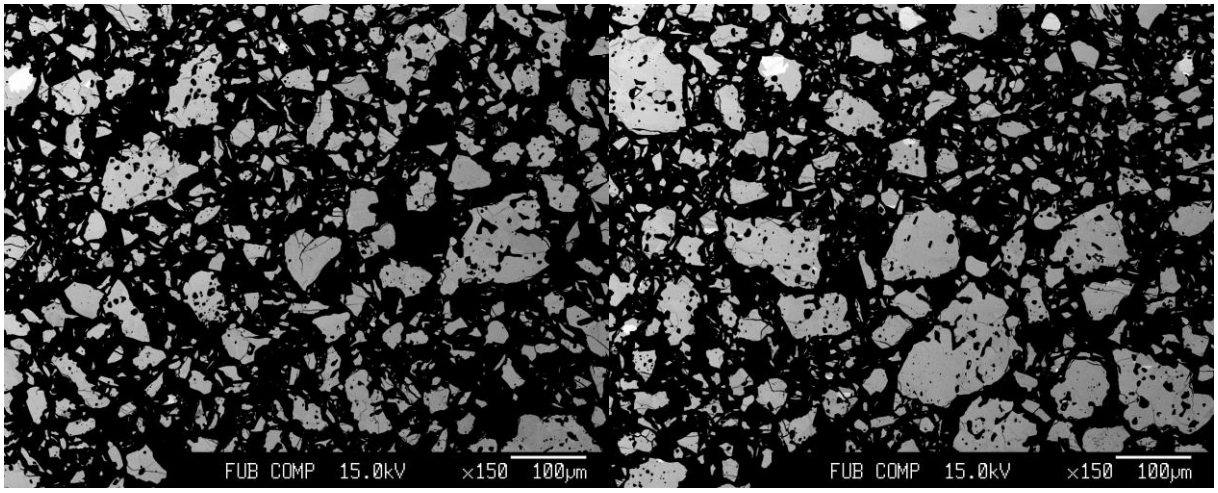

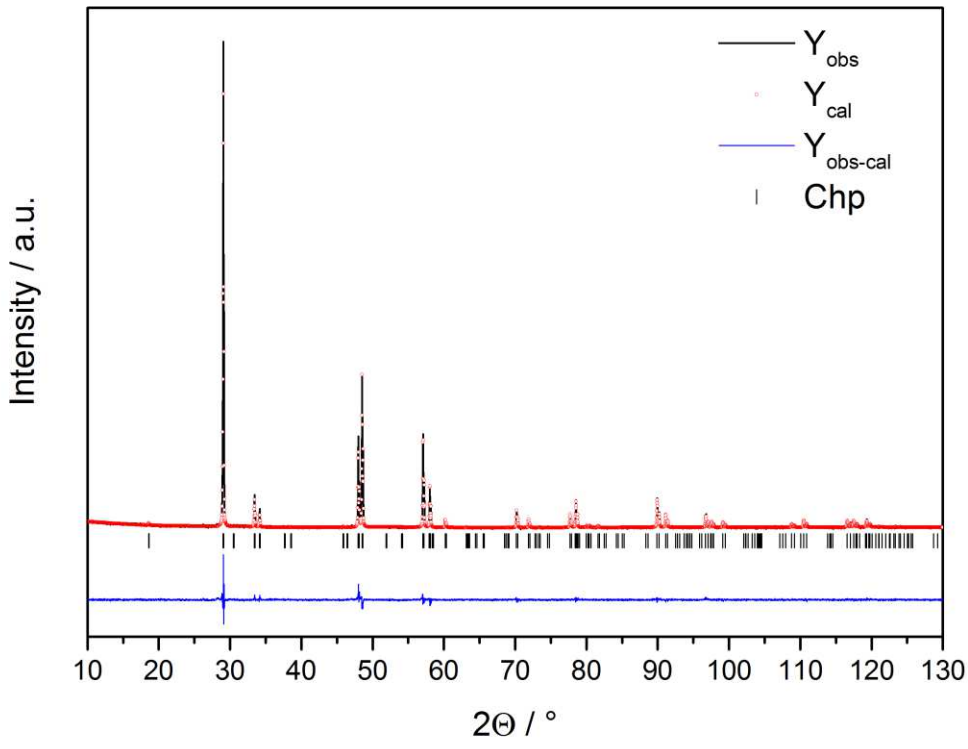

XRD: Chi^2: 2.08 Bragg R-factor: 5.12

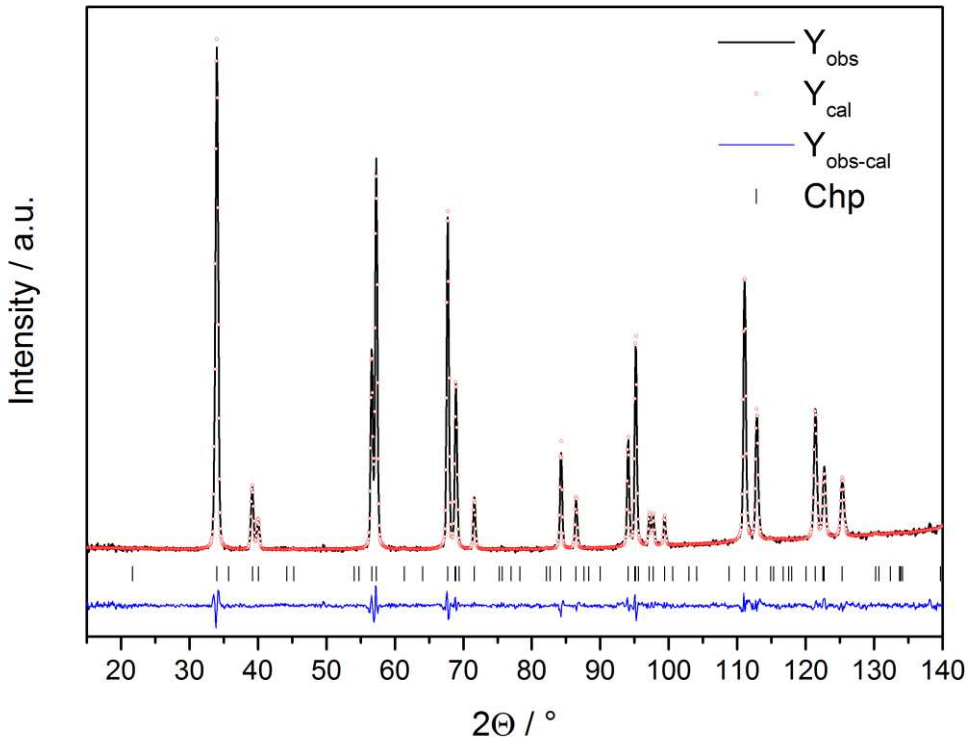

ND: Chi^2: 1.52 Bragg R-factor: 1.44

Mn-I-I 0.04

$Cu_{0.467}Ga_{0.465}Mn_{0.041}S$

a: 5.365 Å c: 10.517 Å x: 0.2609(13)

100% Chp

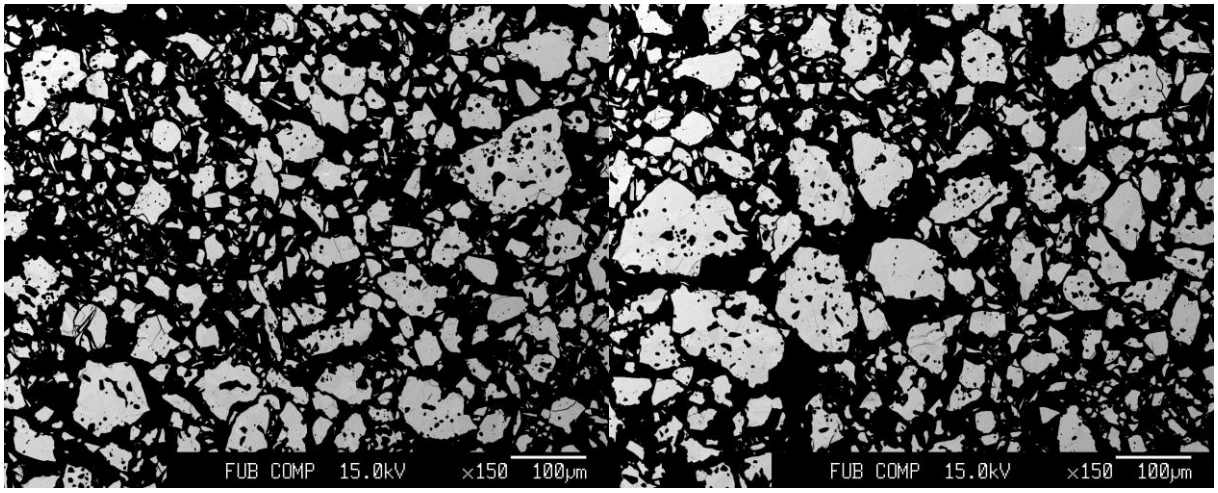

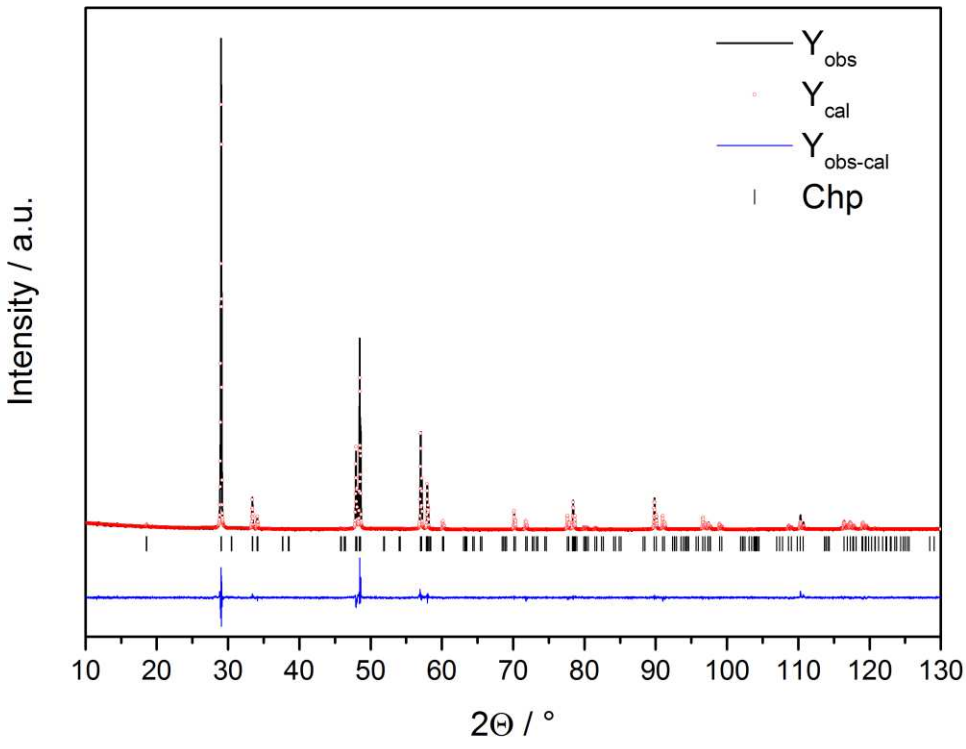

XRD: Chi^2: 2.26 Bragg R-factor: 6.68

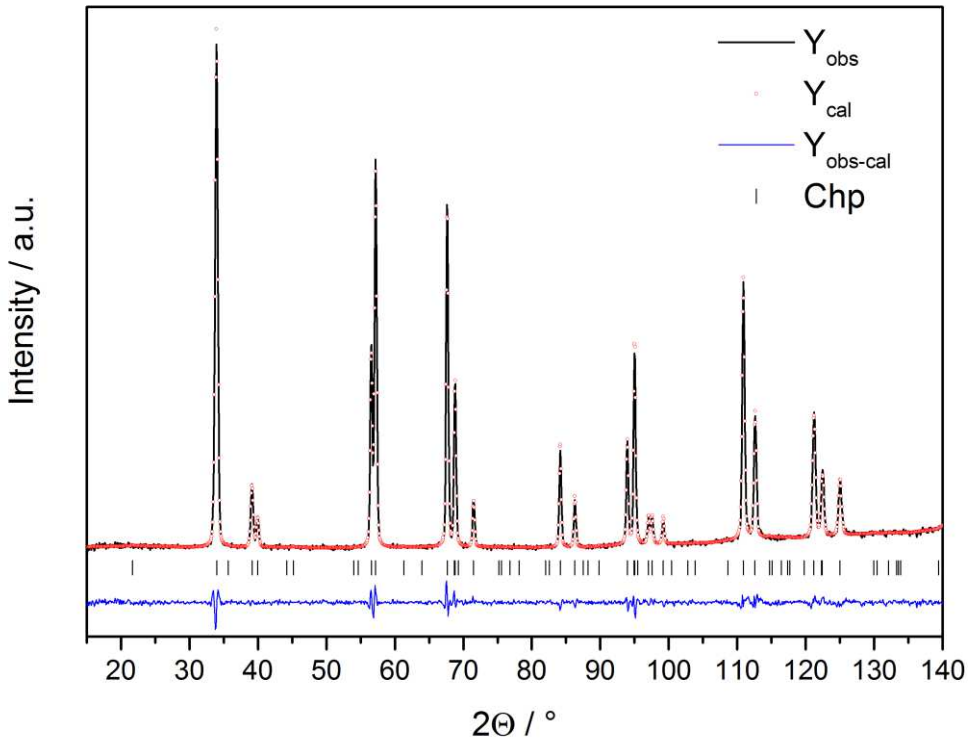

ND: Chi^2: 1.44 Bragg R-factor: 1.76

Mn-I-I 0.08

$Cu_{0.421}Ga_{0.463}Mn_{0.082}S$

a: 5.370 Å c: 10.493 Å x: 0.2660(10)

95% Chp; 4% γ Cu-Ga; 1% MnS

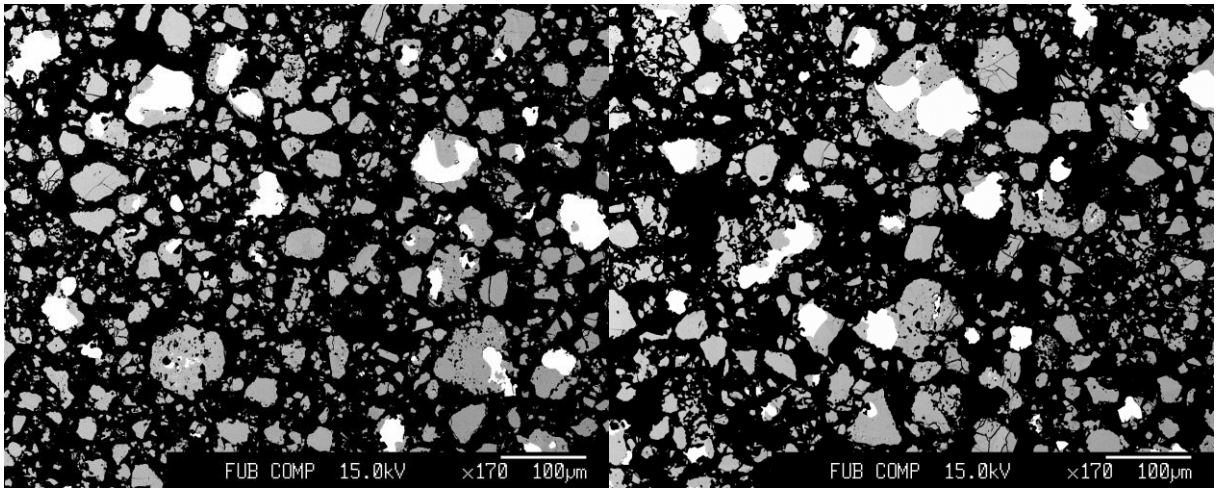

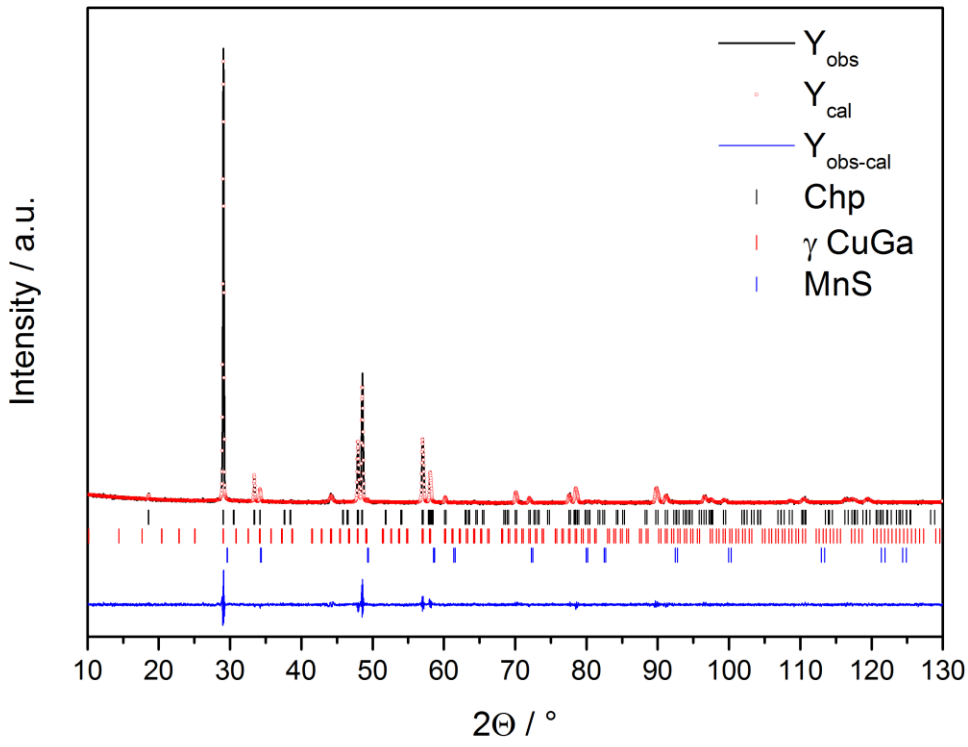

XRD: Chi^2: 1.66 Bragg R-factor: 4.32

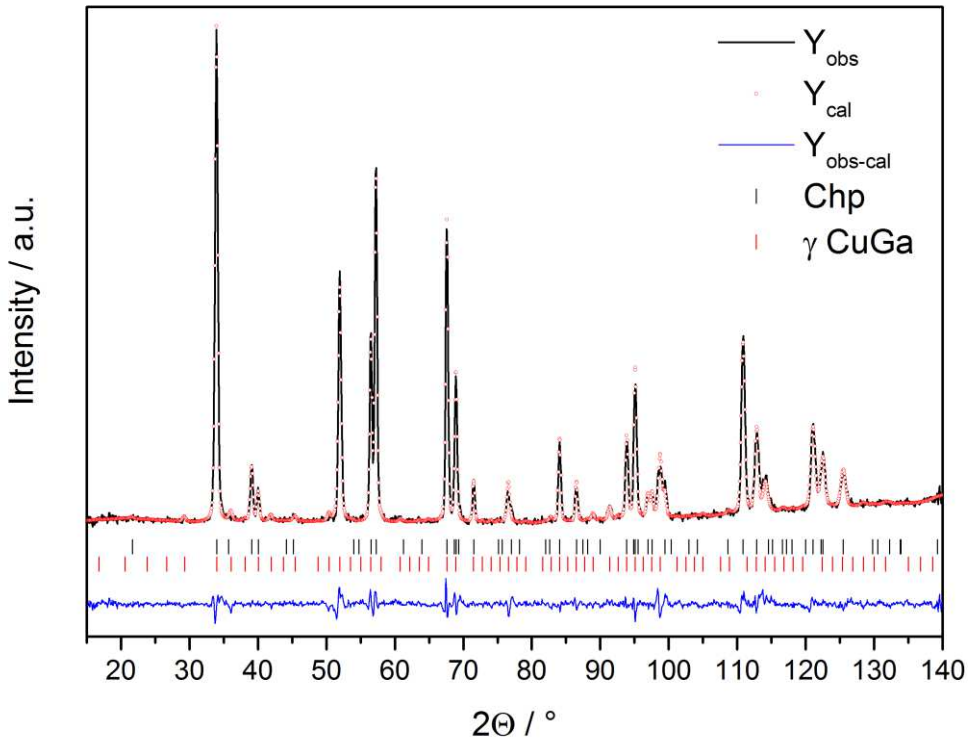

ND: Chi^2: 2.26 Bragg R-factor: 2.44

Mn-I-I 0.1

$Cu_{0.432}Ga_{0.447}Mn_{0.092}S$

a: 5.368 Å c: 10.507 Å x: 0.2611(12)

94% Chp; 1% γ Cu-Ga; 5% MnS

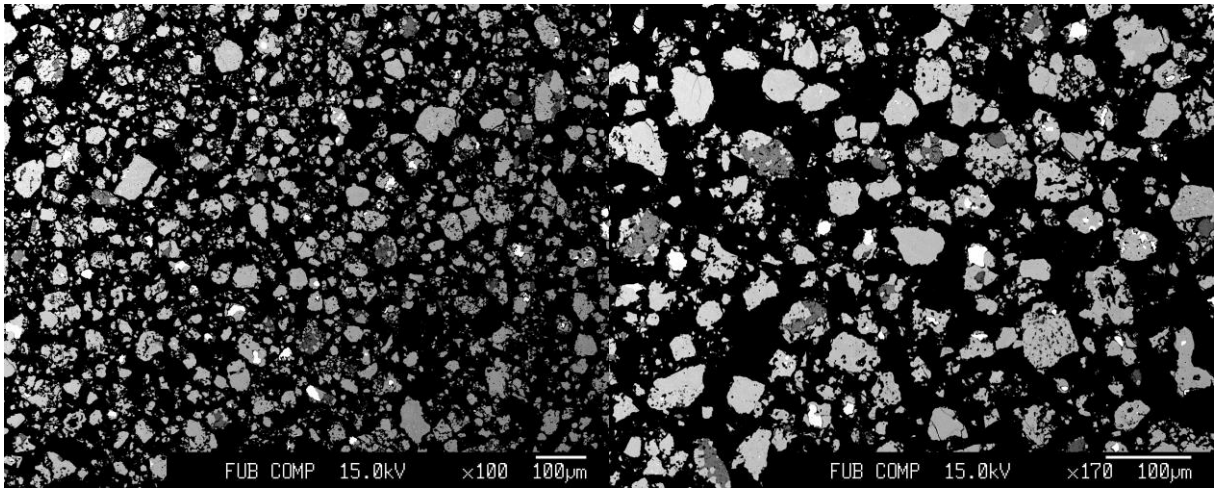

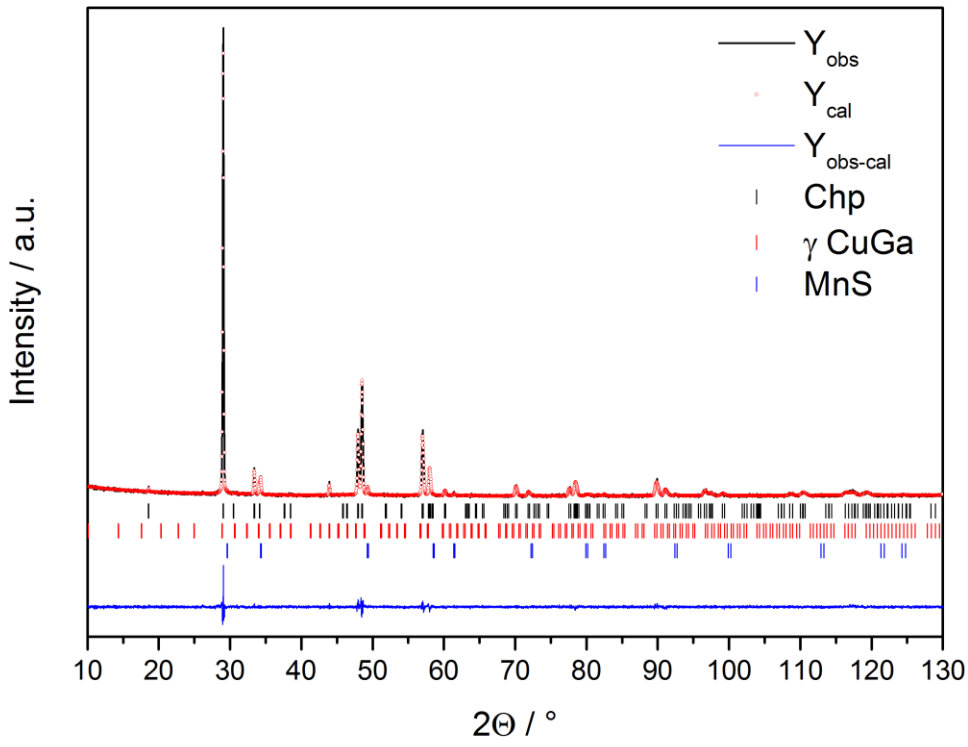

XRD: Chi^2: 1.52 Bragg R-factor: 3.17

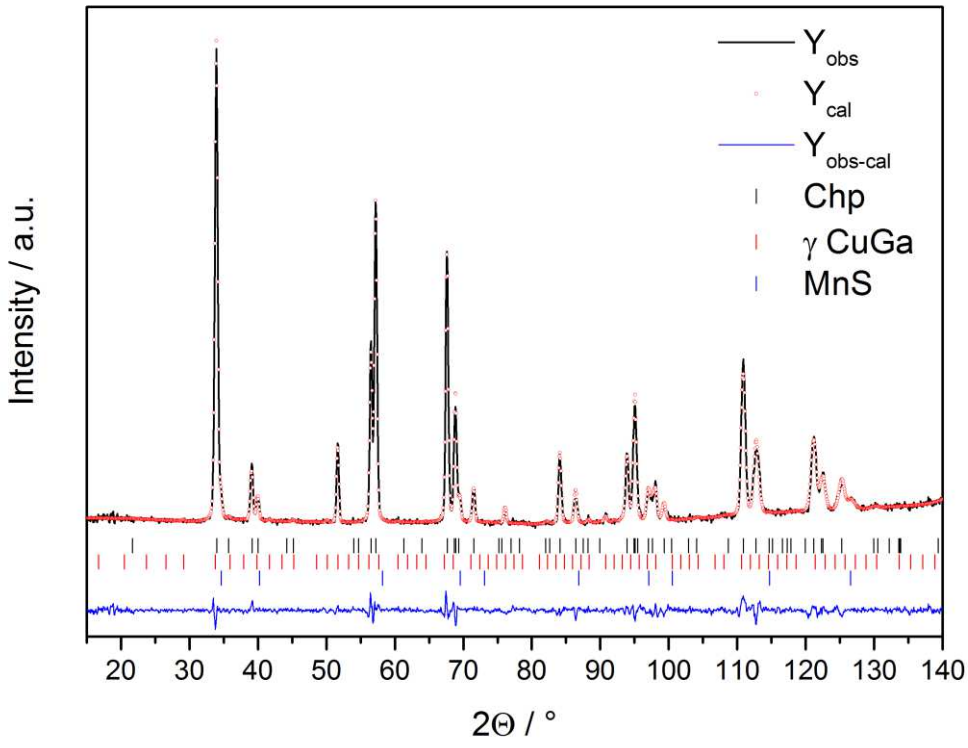

Chi^2: 1.52 Bragg R-factor: 2.29

Mn-I-II 0.01

$Cu_{0.465}Ga_{0.487}Mn_{0.014}S$

a: 5.359 Å c: 10.480 Å x: 0.2628(8)

96% Chp; 4% γ Cu-Ga

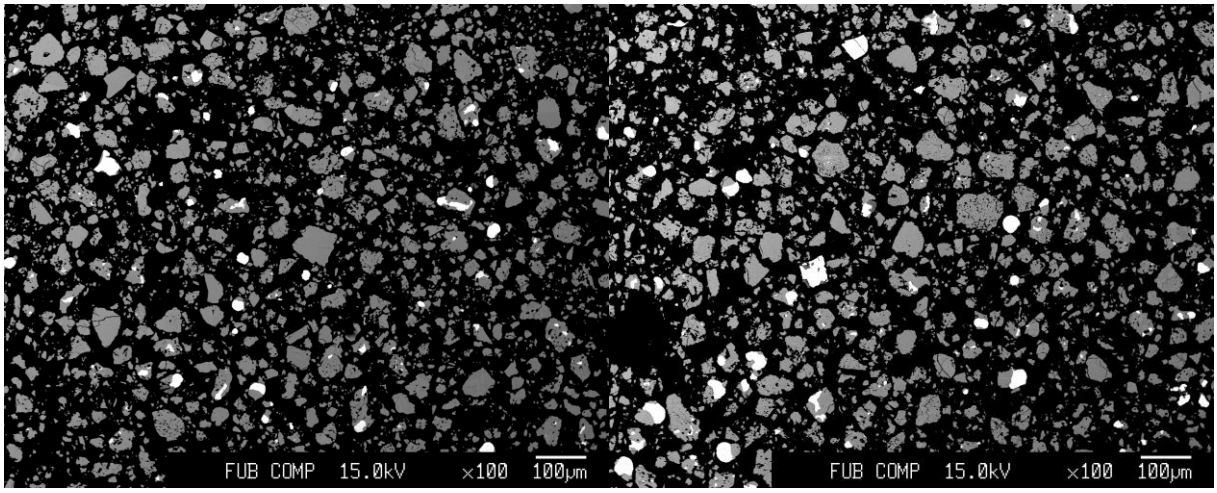

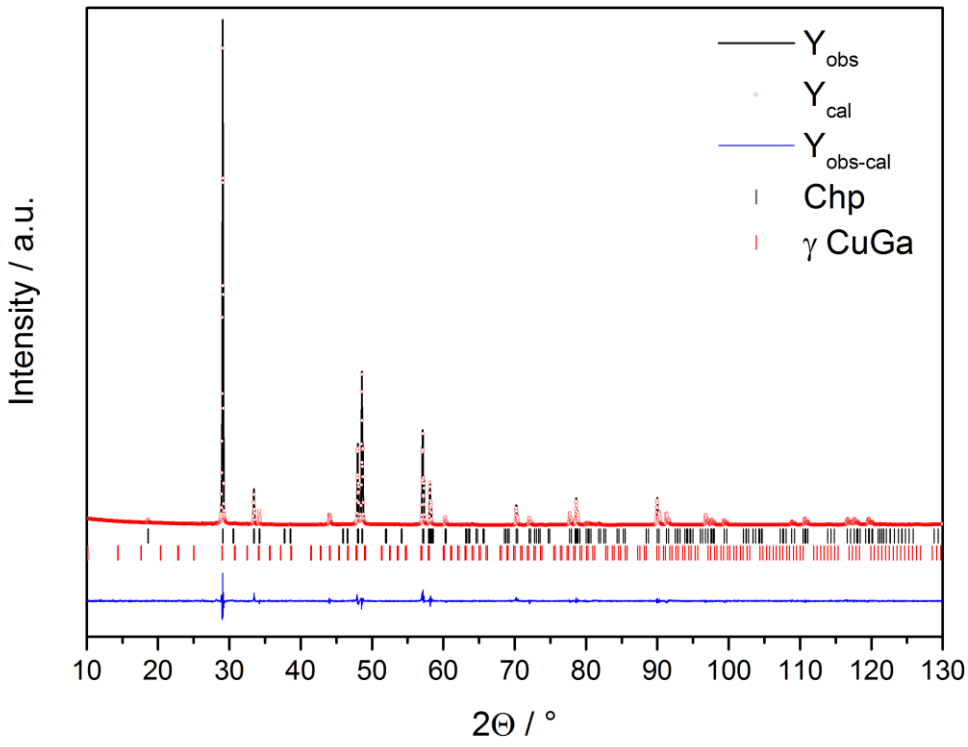

XRD: Chi^2: 2.03 Bragg R-factor: 4.52

Mn-I-II 0.03

$Cu_{0.444}Ga_{0.479}Mn_{0.041}S$

a: 5.367 Å c: 10.488 Å x: 0.2638(8)

93% Chp; 7% γ Cu-Ga

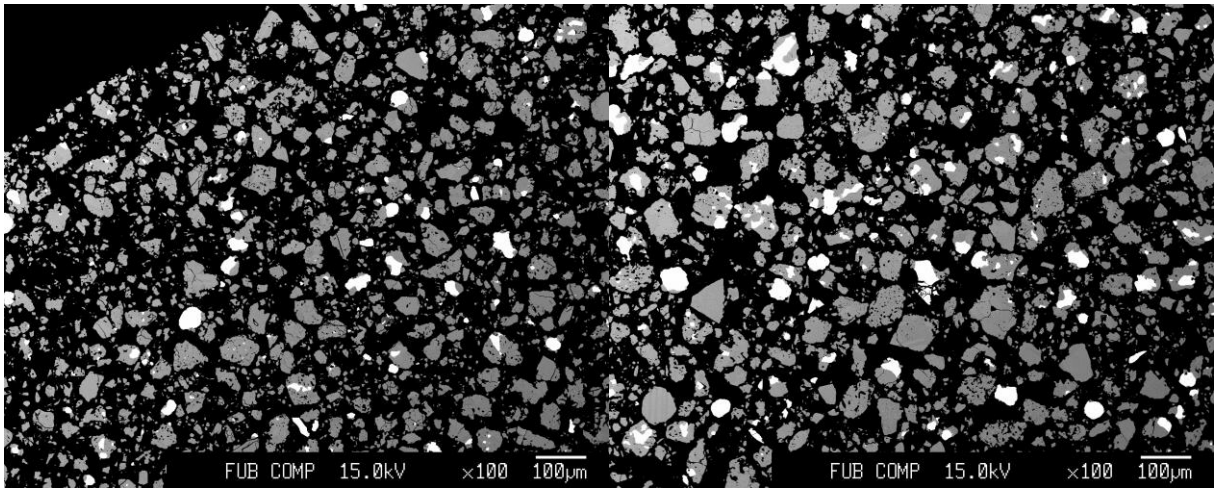

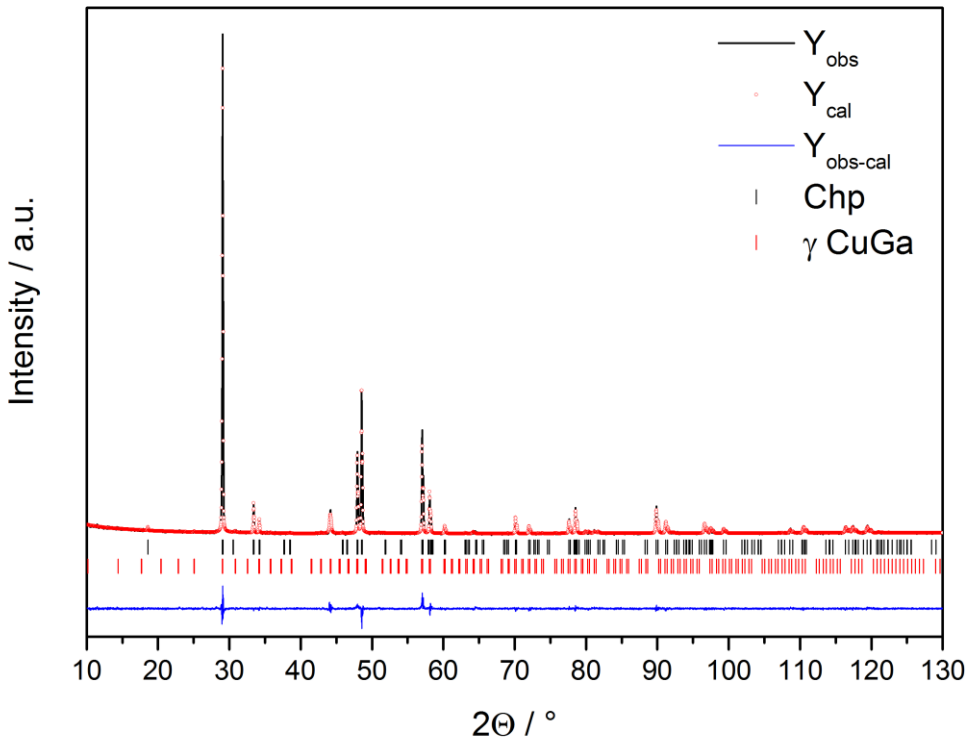

XRD: Chi^2: 1.83 Bragg R-factor: 4.65

Mn-I-II 0.05

$Cu_{0.433}Ga_{0.469}Mn_{0.063}S$

a: 5.369 Å c: 10.491 Å x: 0.2646(8)

94% Chp; 6% γ Cu-Ga

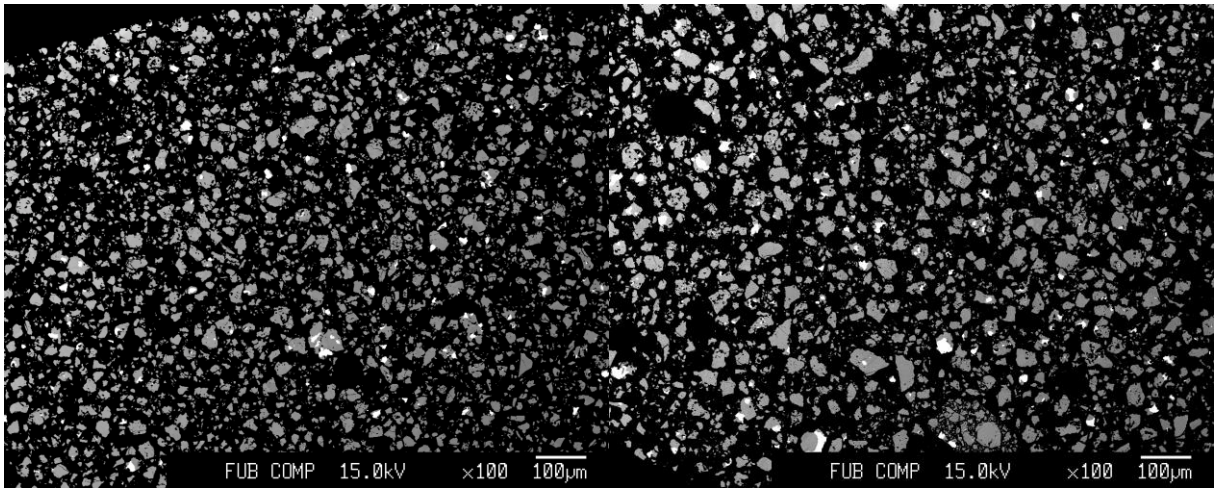

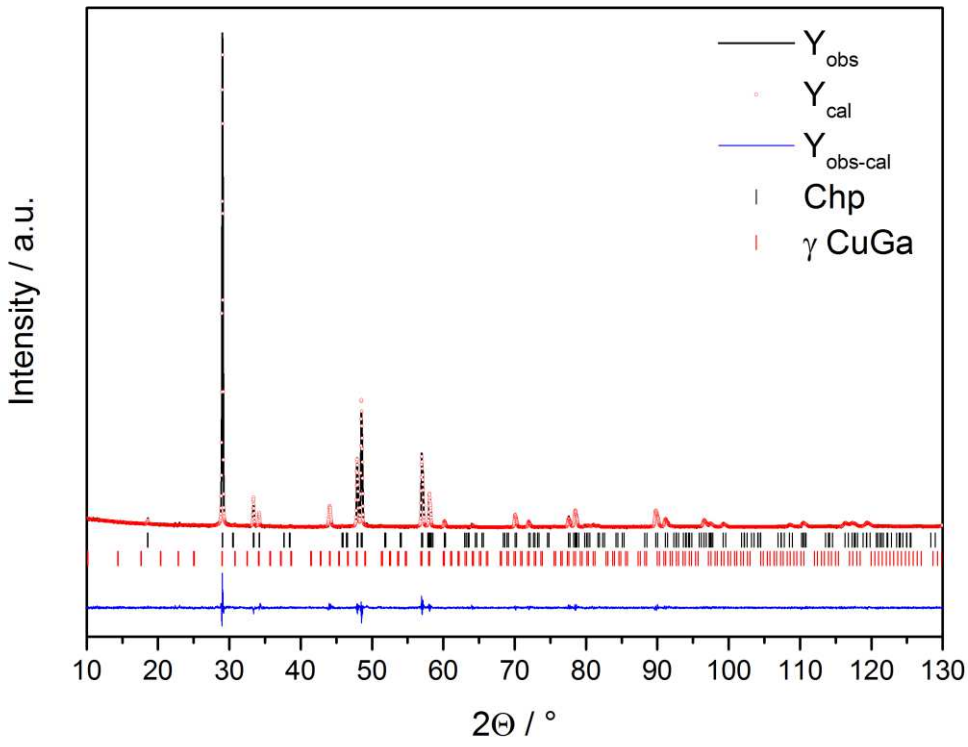

XRD: Chi^2: 1.69 Bragg R-factor: 4.14

Mn-I-II 0.07

$Cu_{0.465}Ga_{0.456}Mn_{0.069}S$

a: 5.368 Å c: 10.523 Å x: 0.2528(28)

98% Chp; 2% MnS

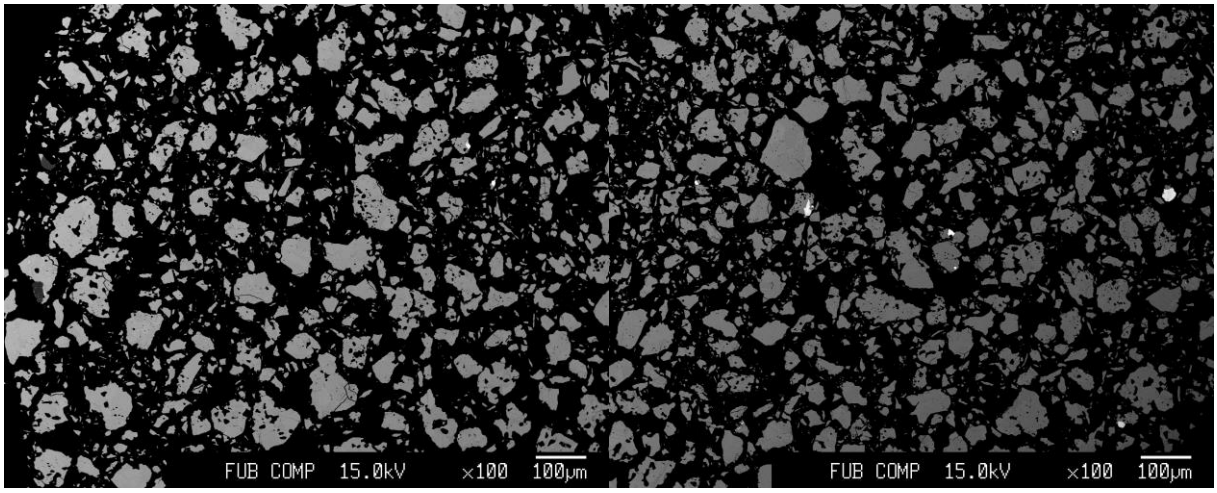

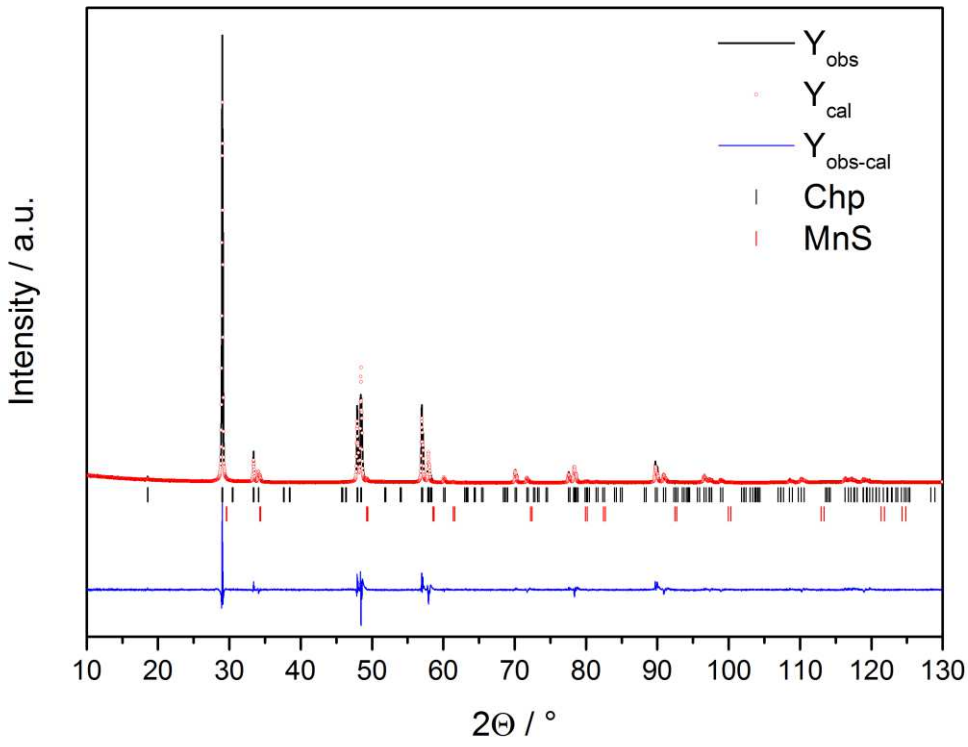

XRD: Chi^2: 5.56 Bragg R-factor: 8.31

Mn-I-III 0.00

$Cu_{0.495}Ga_{0.493}S$

a: 5.355 Å c: 10.487 Å x: 0.2612(13)

95% Chp; 5% γ Cu-Ga

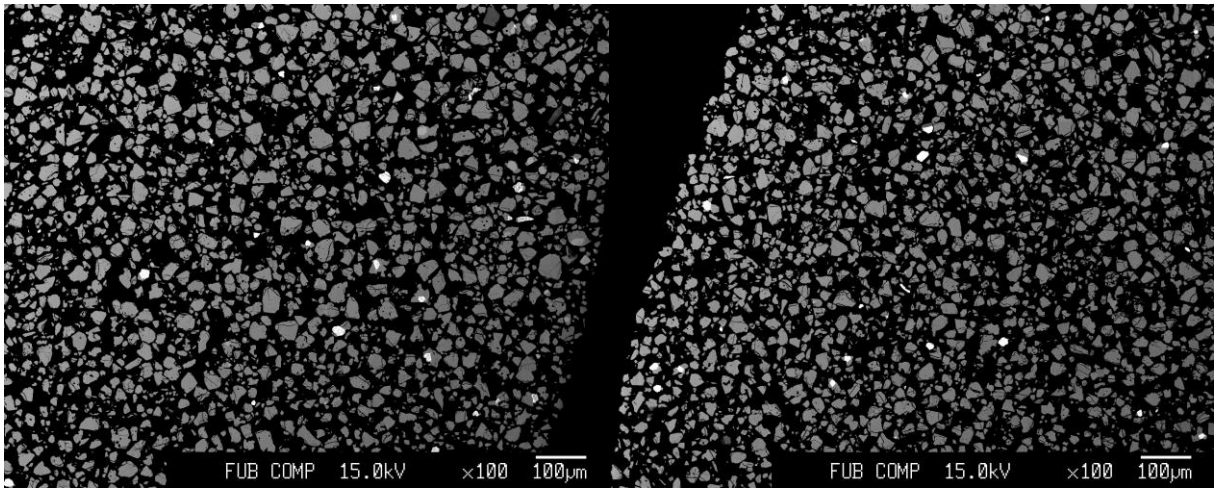

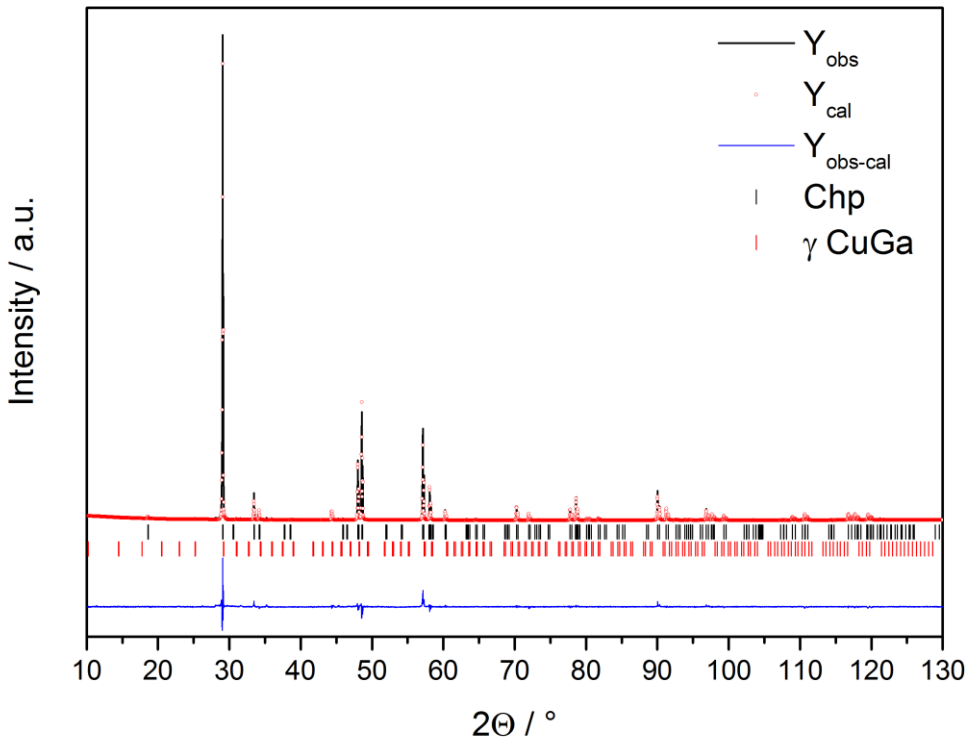

XRD: Chi^2: 4.34 Bragg R-factor: 7.28

Mn-I-III 0.05

$Cu_{0.446}Ga_{0.469}Mn_{0.063}S$

a: 5.371 Å c: 10.508 Å x: 0.2521(15)

99% Chp; >1% γ Cu-Ga

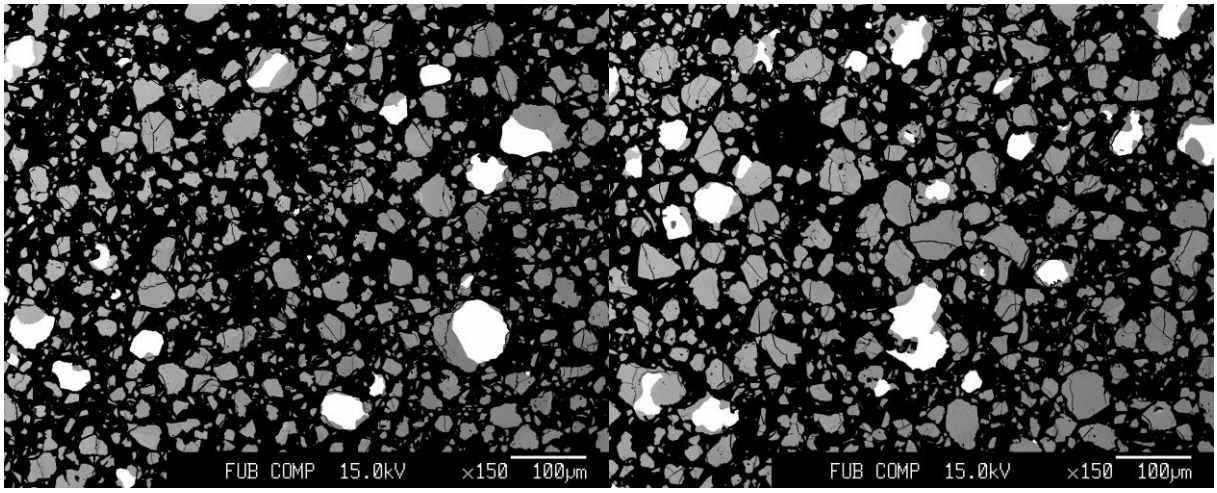

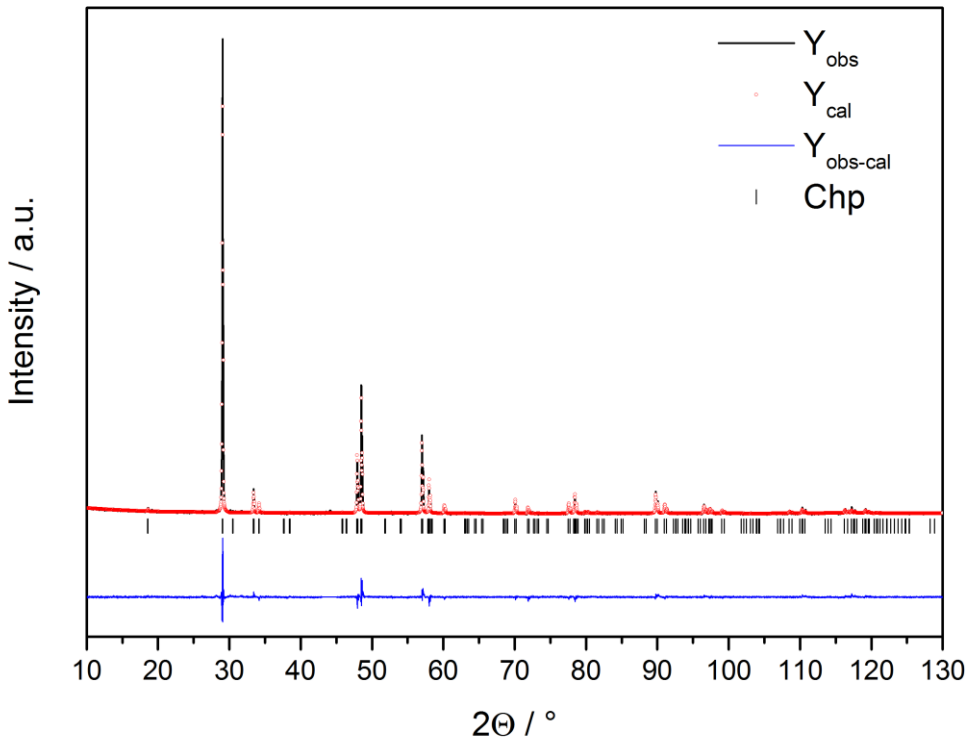

XRD: Chi^2: 2.64 Bragg R-factor: 8.36

Mn-I-III 0.15

$Cu_{0.413}Ga_{0.454}Mn_{0.098}S$

a: 5.370 Å c: 10.490 Å x: 0.2596(21)

77% Chp; 9% γ Cu-Ga; 14% MnS *second Chp

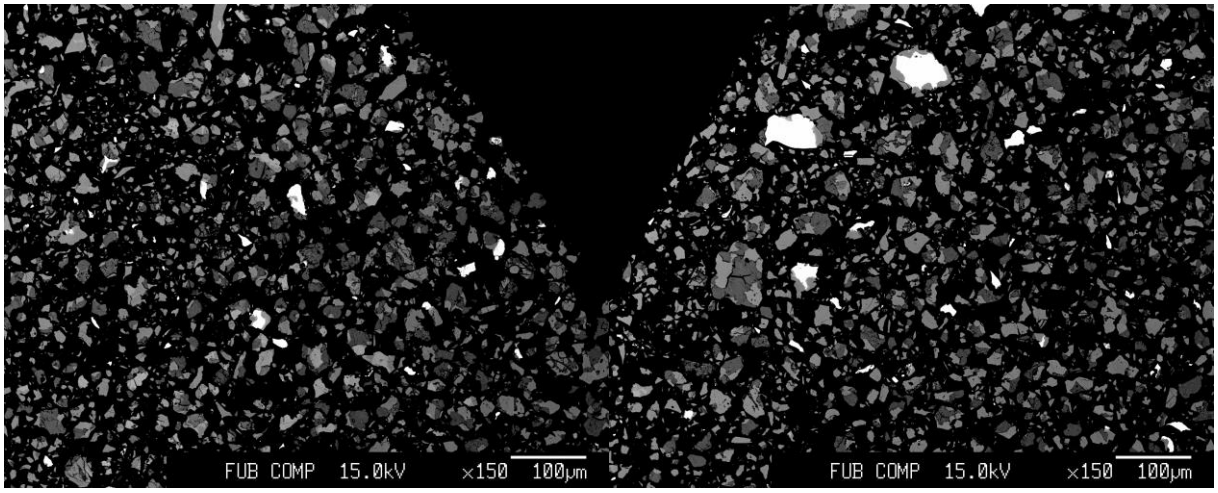

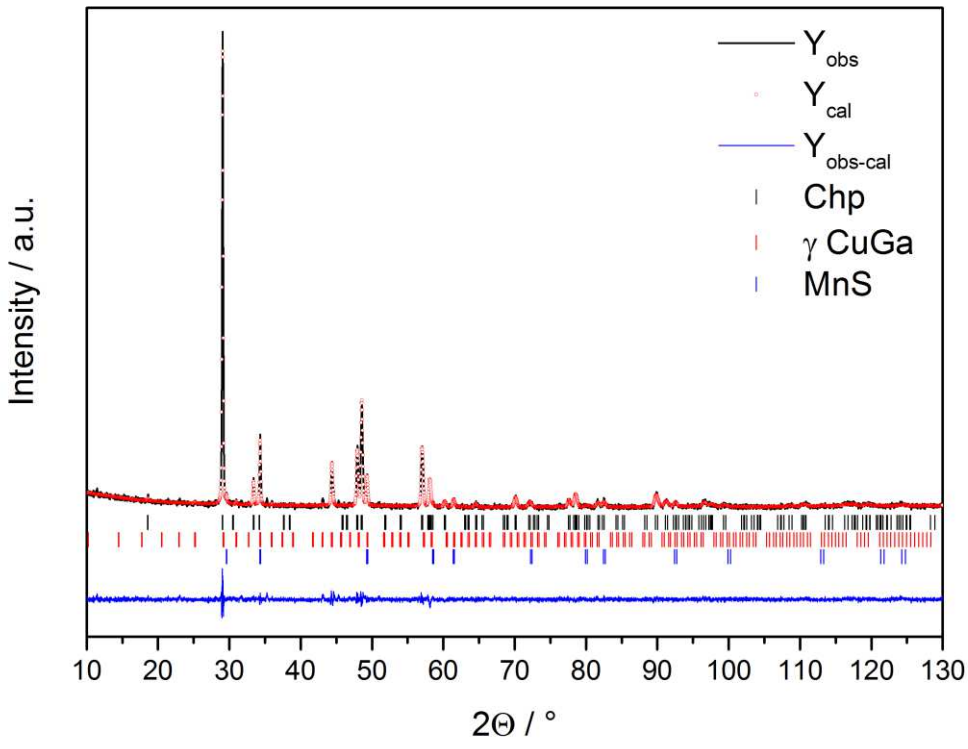

XRD: Chi^2: 1.38 Bragg R-factor: 4.59

Mn-I-III 0.2

$Cu_{0.451}Ga_{0.452}Mn_{0.087}S$

a: 5.375 Å c: 10.550 Å x: 0.2524(47)

87% Chp; 13% MnS *second Chp

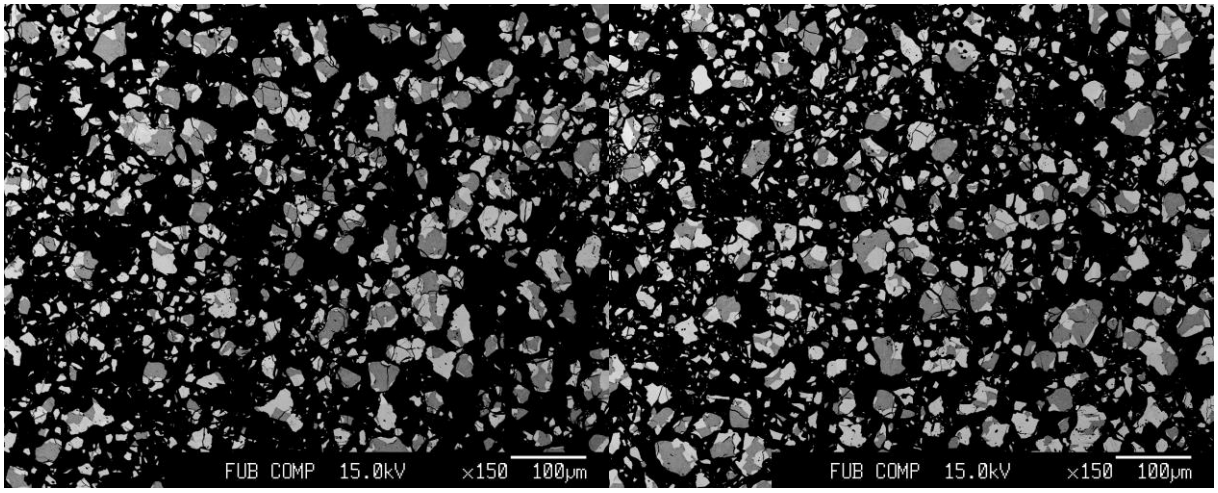

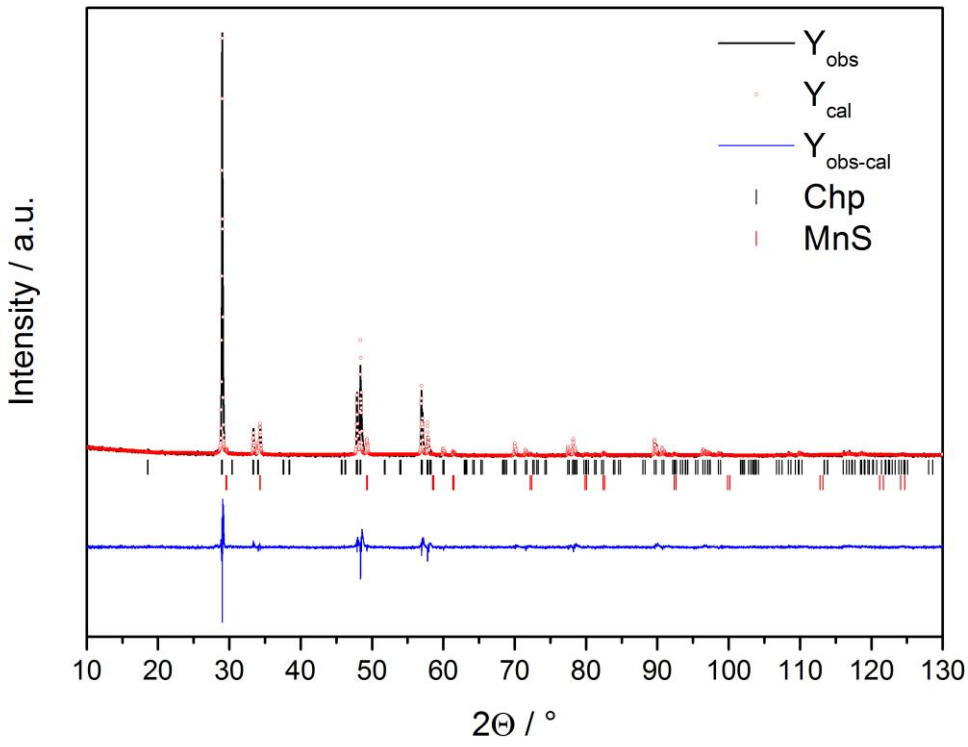

XRD: Chi^2: 4.24 Bragg R-factor: 13.3

Mn-I-III 0.25

$Cu_{0.449}Ga_{0.449}Mn_{0.089}S$

a: 5.375 Å c: 10.550 Å x: 0.2554(56)

81% Chp; 19% MnS *second Chp

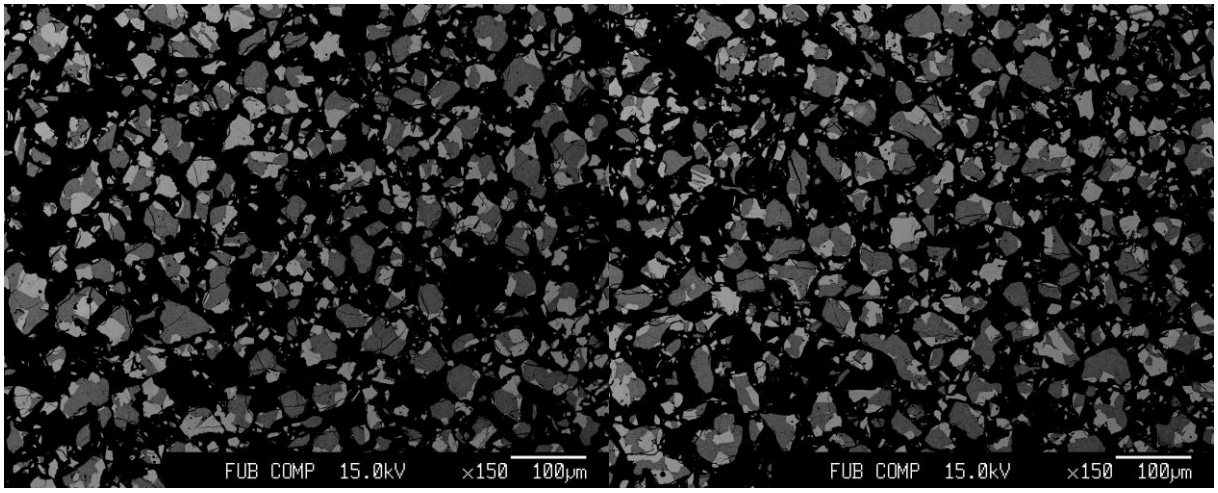

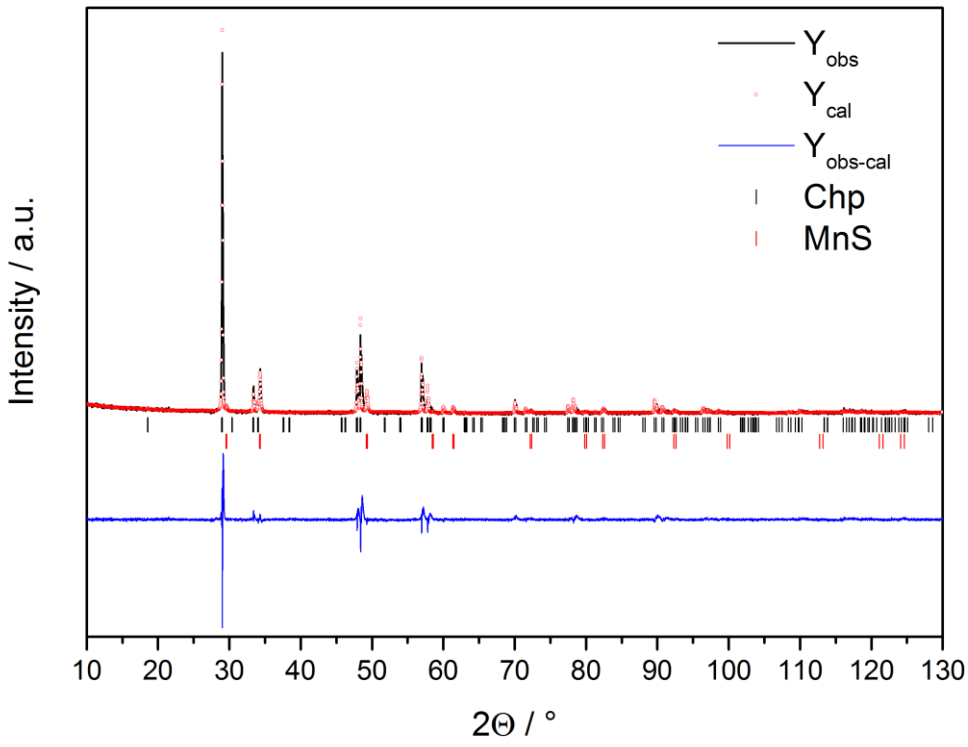

XRD: Chi^2: 5.68 Bragg R-factor: 18.1

Mn-334-I

$Cu_{0.299}Ga_{0.290}Mn_{0.410}S$

a: 5.359 Å c: 10.475 Å x: 0.2567(40)

63% Chp; 37% MnS

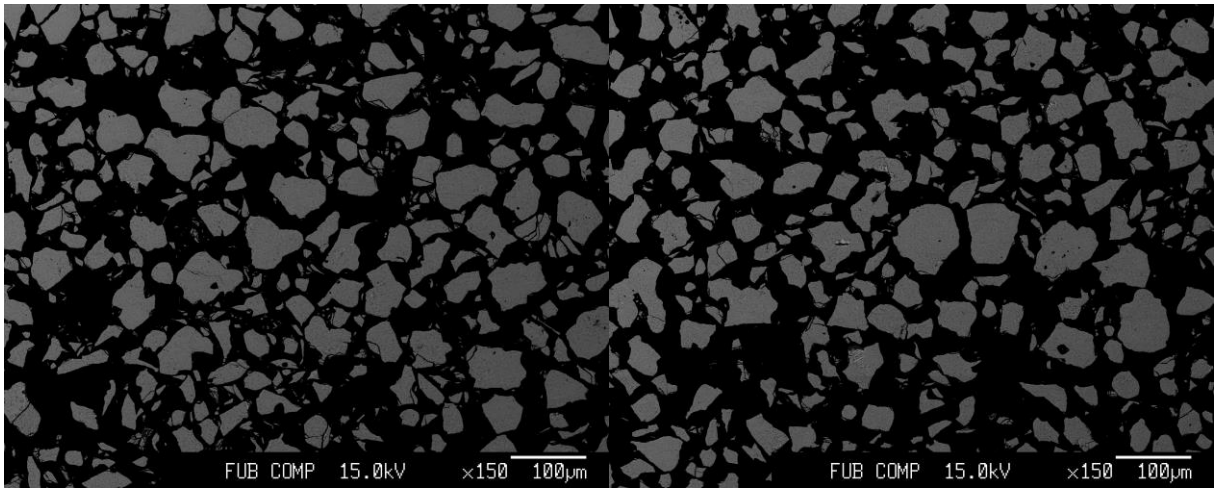

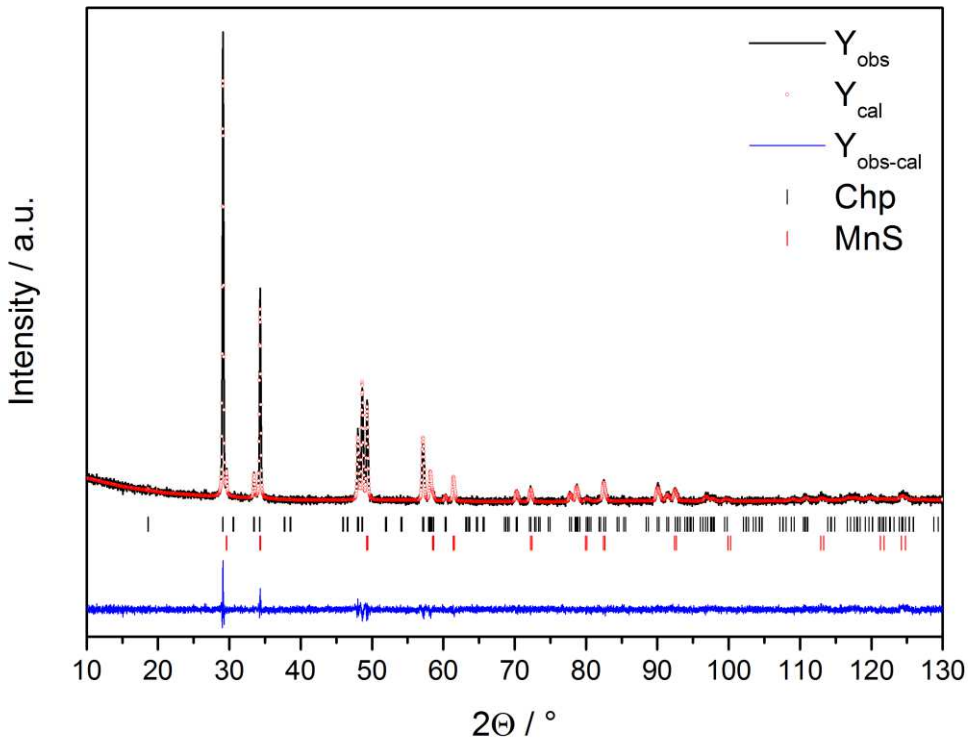

XRD: Chi^2: 1.39 Bragg R-factor: 8.47

Mn-334-II

$Cu_{0.299}Ga_{0.289}Mn_{0.410}S$

a: 5.360 Å c: 10.477 Å x: 0.2583(36)

63% Chp; 37% MnS

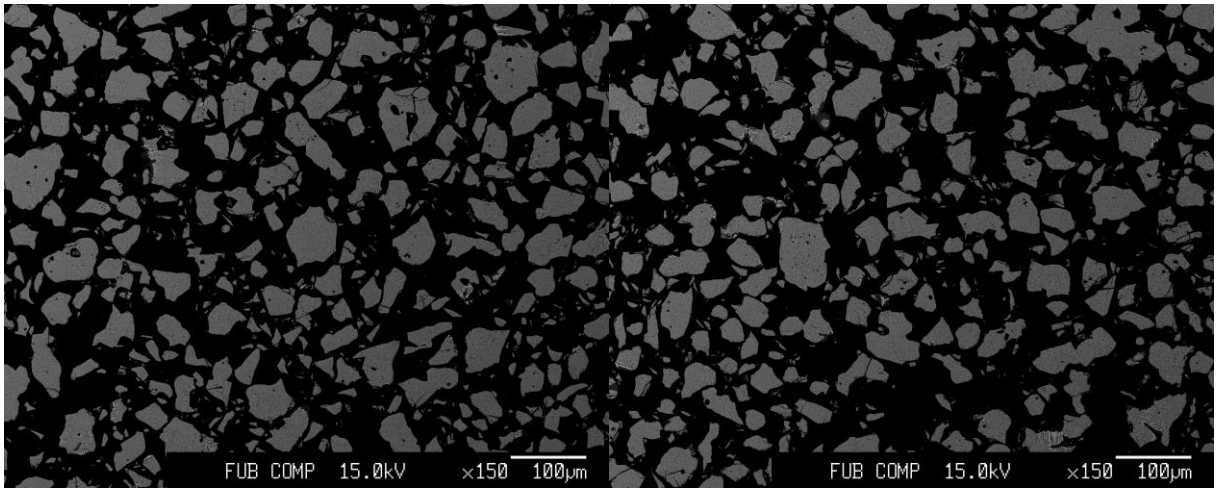

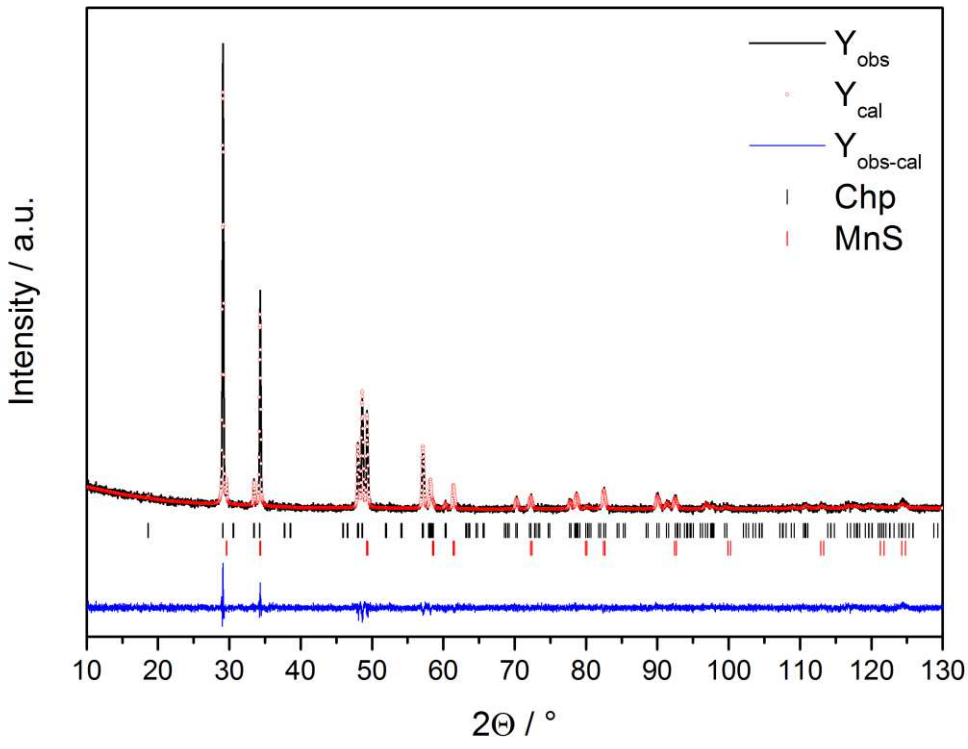

XRD: Chi^2: 1.55 Bragg R-factor: 5.26

Ni 0.05

$Cu_{0.488}Ga_{0.487}Ni_{0.0063}S$

a: 5.355 Å c: 10.488 Å x: 0.2596(13)

94% Chp; 5% Nickeline; 1% Heazlewoodite (Hzl)

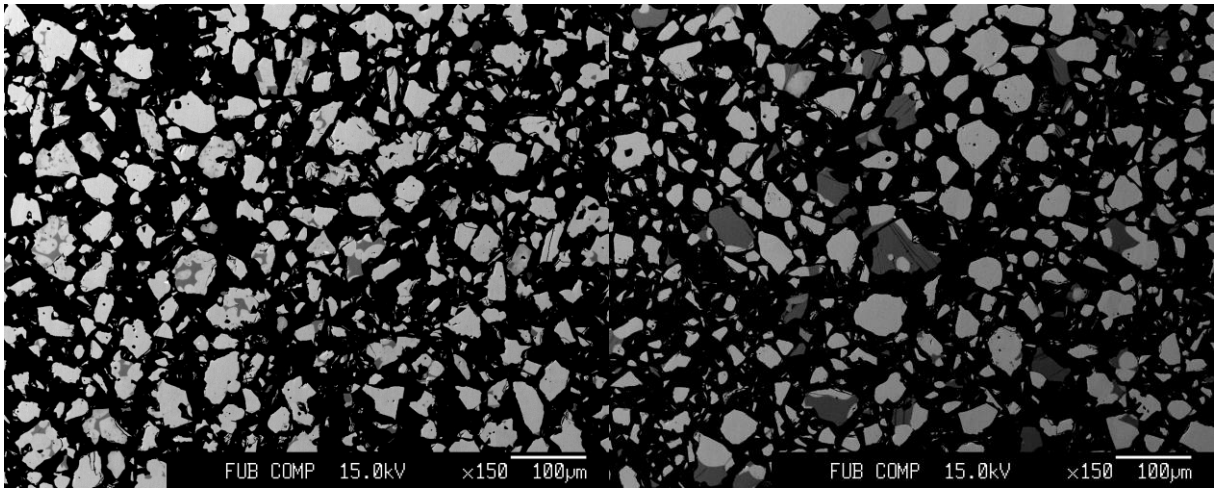

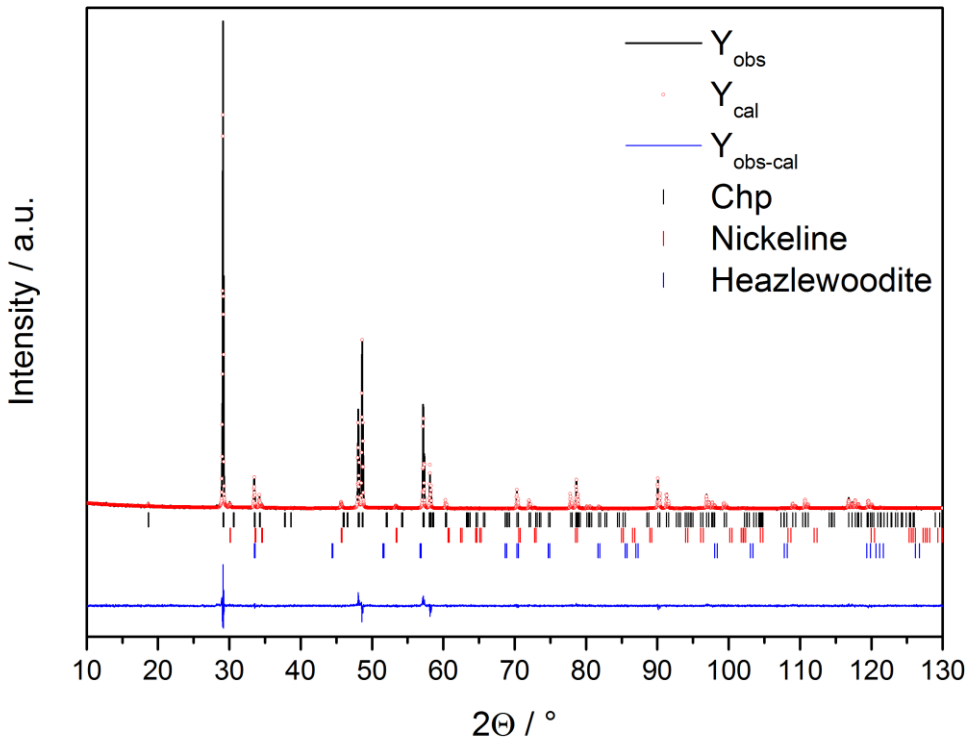

XRD: Chi^2: 2.08 Bragg R-factor: 6.49

Ni 0.1

$Cu_{0.494}Ga_{0.484}Ni_{0.0022}S$

a: 5.355 Å c: 10.488 Å x: 0.2561(22)

91% Chp; 7% α´ Ni-Ga; 2% Heazlewoodite

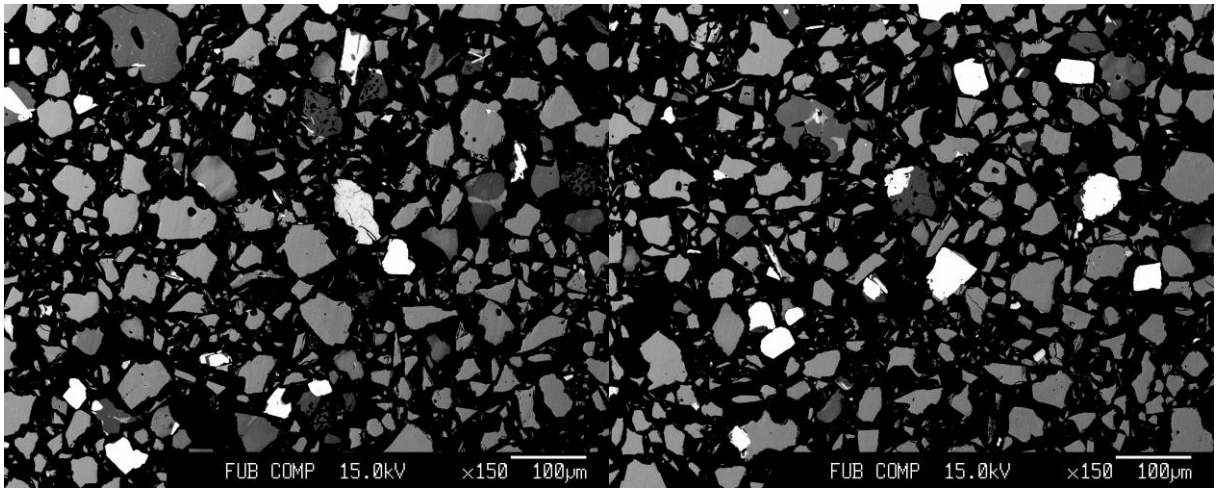

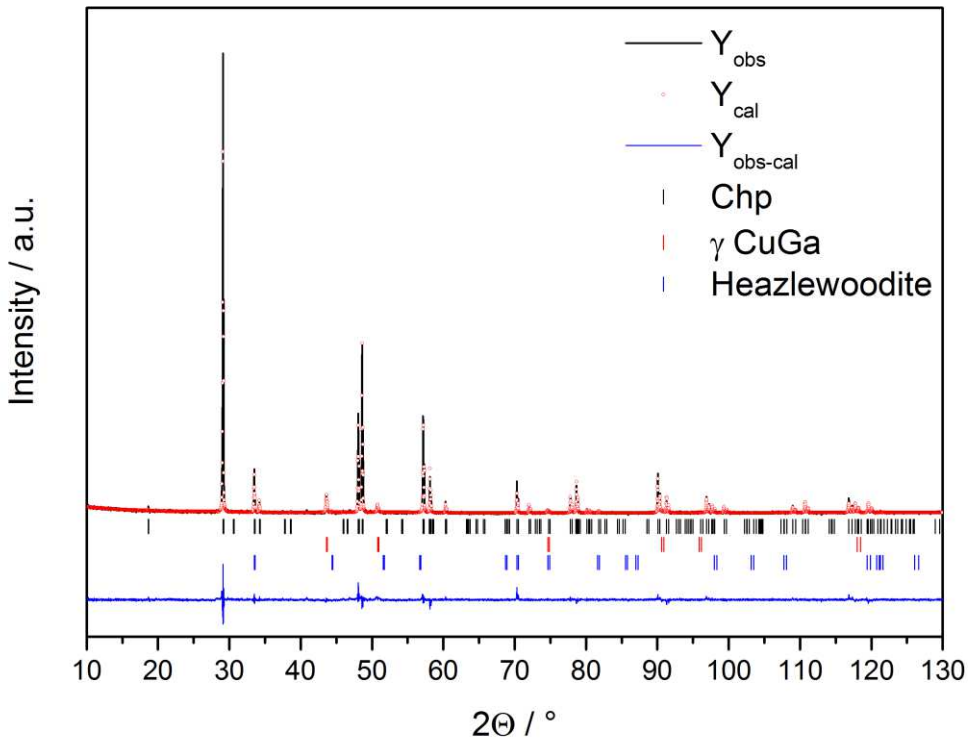

XRD: Chi^2: 2.42 Bragg R-factor: 9.19

Ni 0.15

$Cu_{0.488}Ga_{0.488}Ni_{0.0063}S$

a: 5.355 Å c: 10.488 Å x: 0.2560(27)

99% Chp; 1% Heazlewoodite

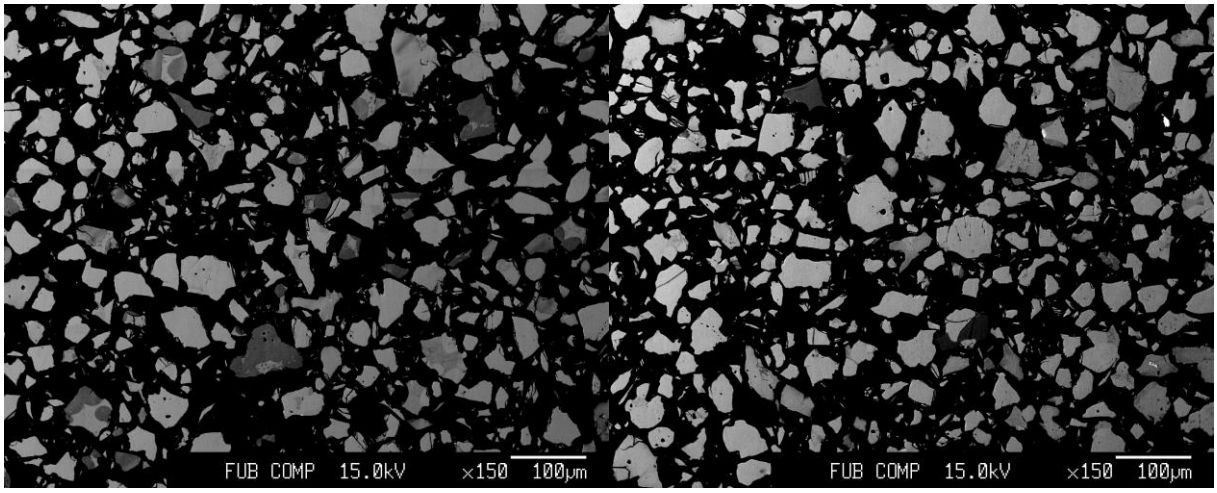

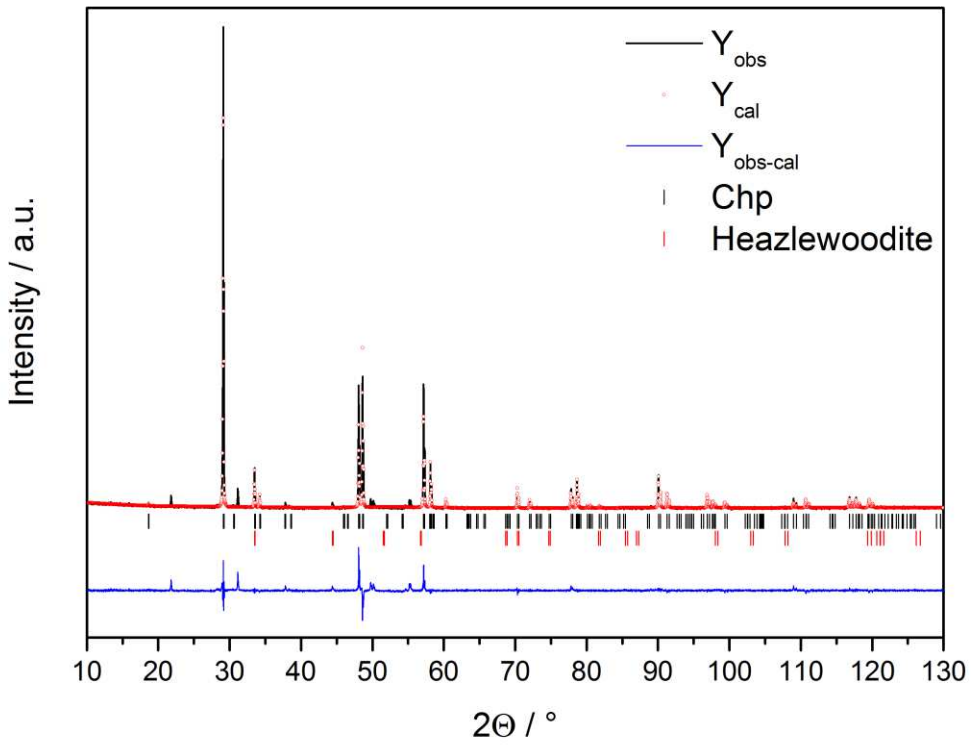

XRD: Chi^2: 4.33 Bragg R-factor: 11.8

Ni 0.2

$Cu_{0.483}Ga_{0.490}Ni_{0.0085}S$

a: 5.355 Å c: 10.487 Å x: 0.2624(16)

81% Chp; 18% Nickeline; 1% Heazlewoodite

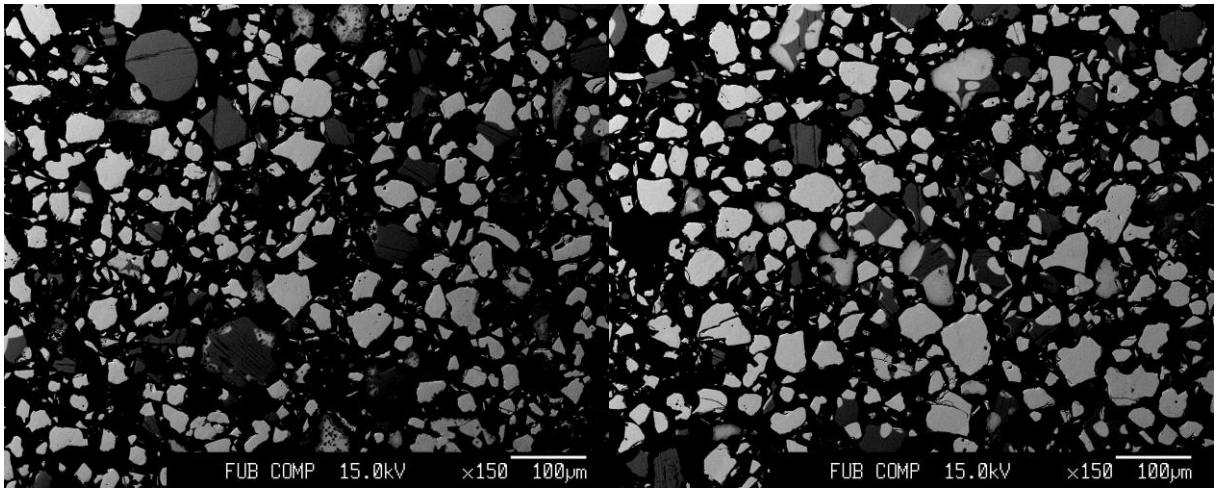

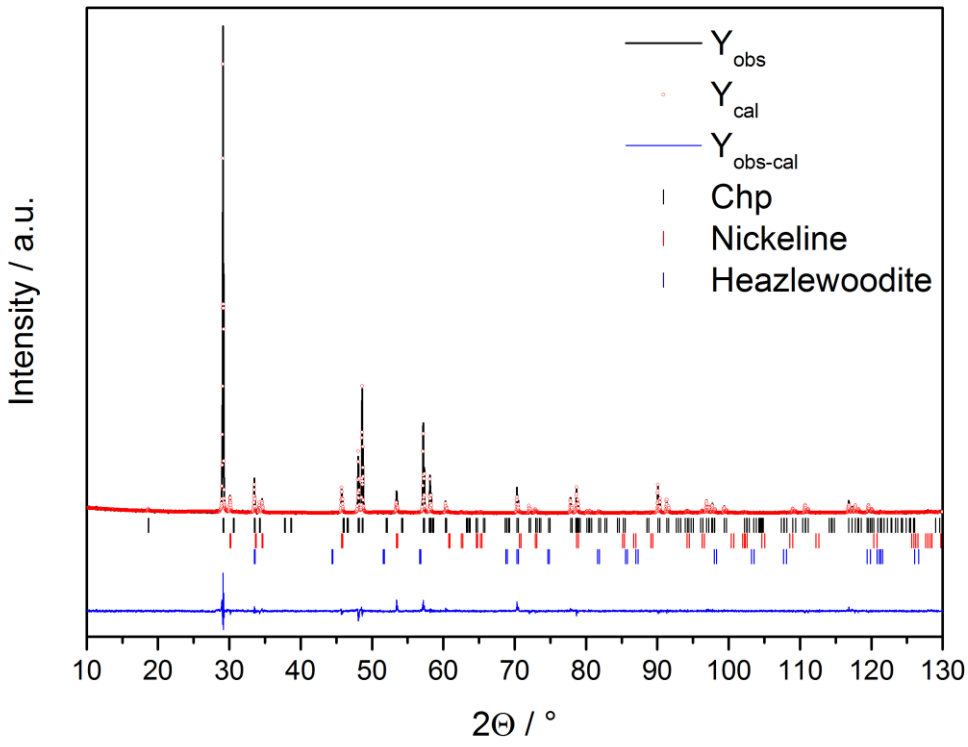

XRD: Chi^2: 2.37 Bragg R-factor: 6.76

Mn-X-I 0.01

$Cu_{0.486}Ga_{0.491}Mn_{0.012}S$

a: 5.362 Å c: 10.501 Å x: 0.2612(8)

96% Chp; 2% γ Cu-Ga; 2% υ Cu-Ga

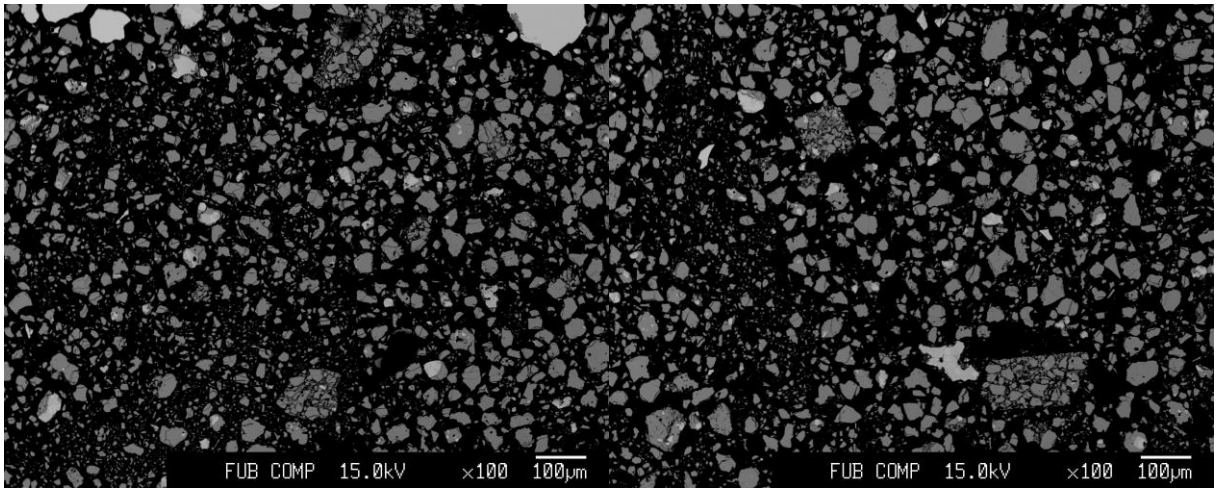

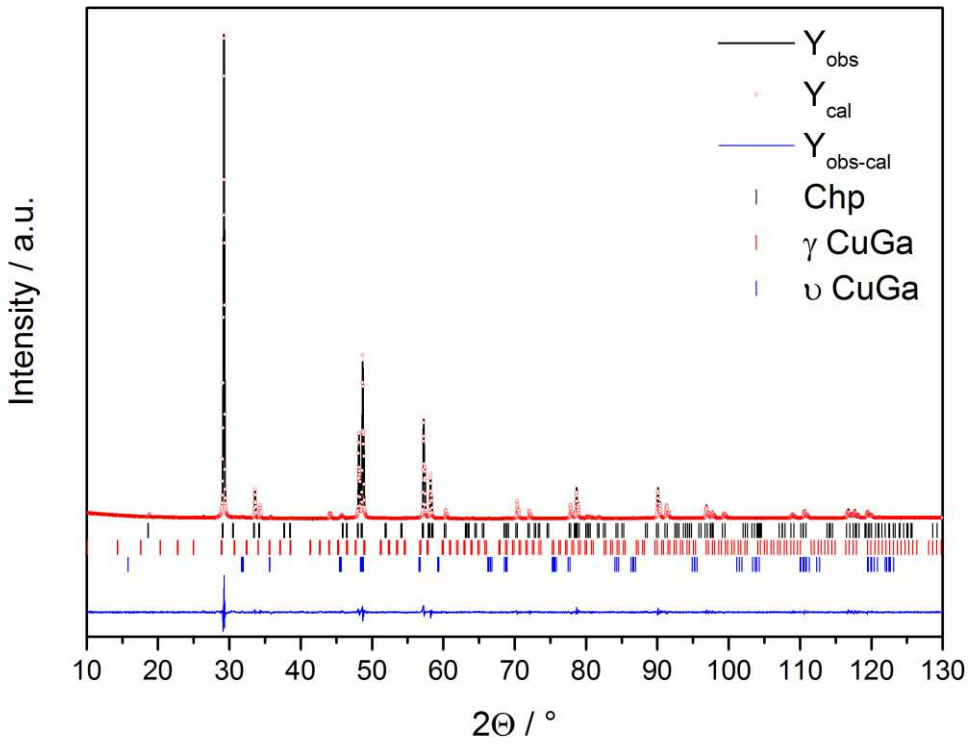

XRD: Chi^2: 1.98 Bragg R-factor: 2.62

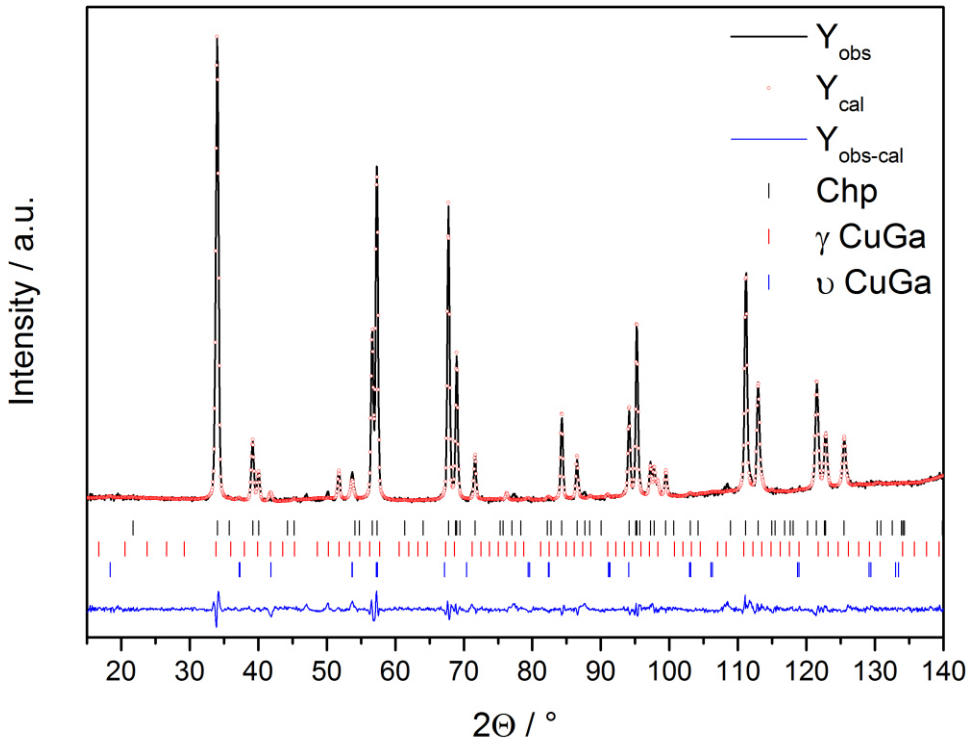

ND: Chi^2: 1.96 Bragg R-factor: 2.34

Mn-X-I 0.02

$Cu_{0.443}Ga_{0.476}Mn_{0.063}S$

a: 5.374 Å c: 10.512 Å x: 0.2606(18)

64% Chp; 34% γ Cu-Ga; 2% υ Cu-Ga

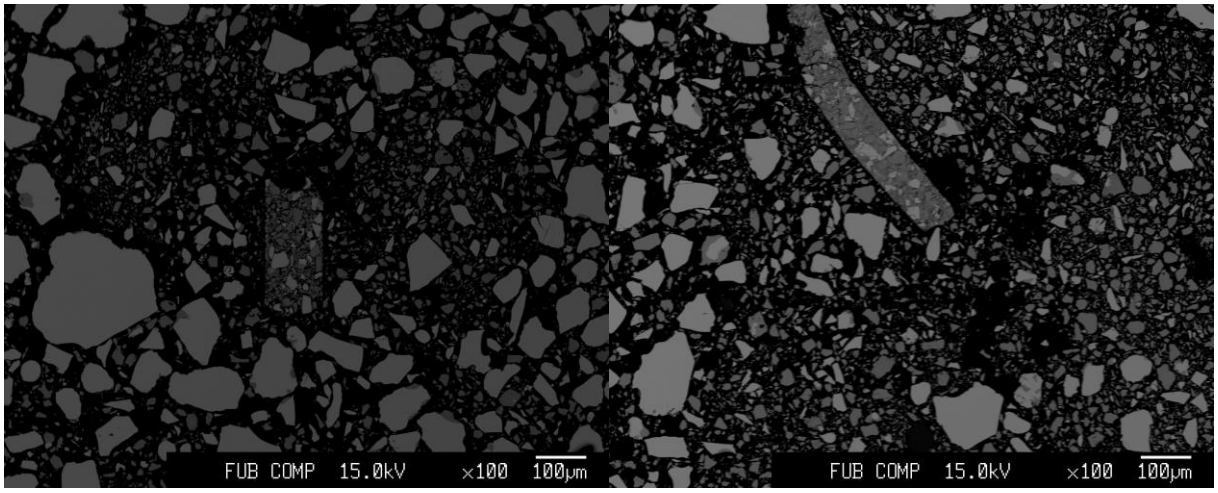

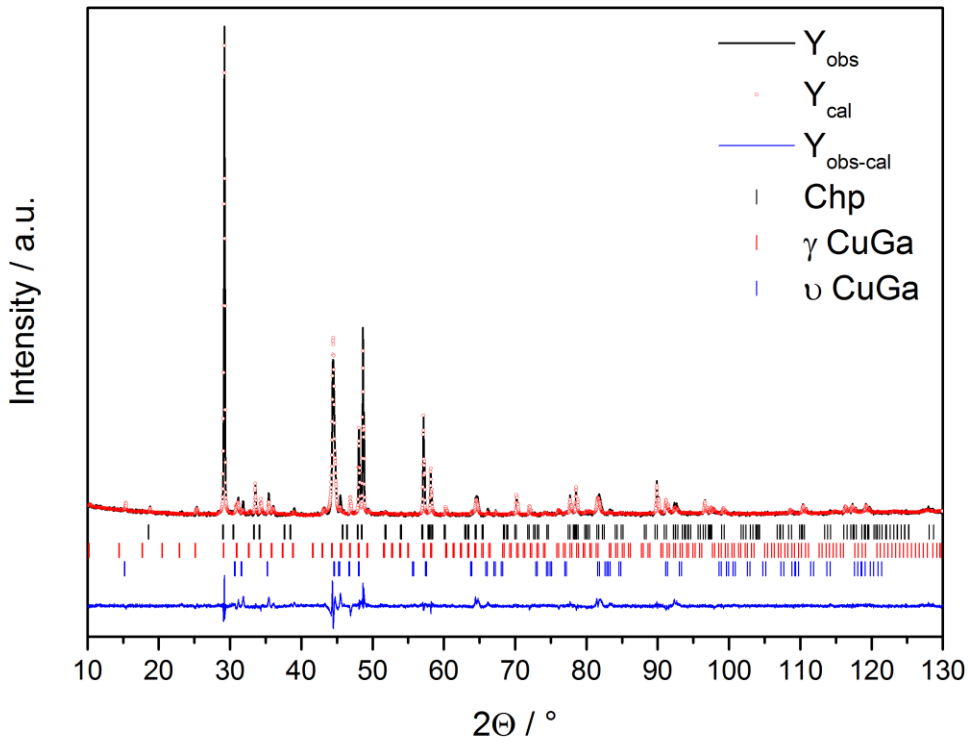

XRD: Chi^2: 3.26 Bragg R-factor: 6.13

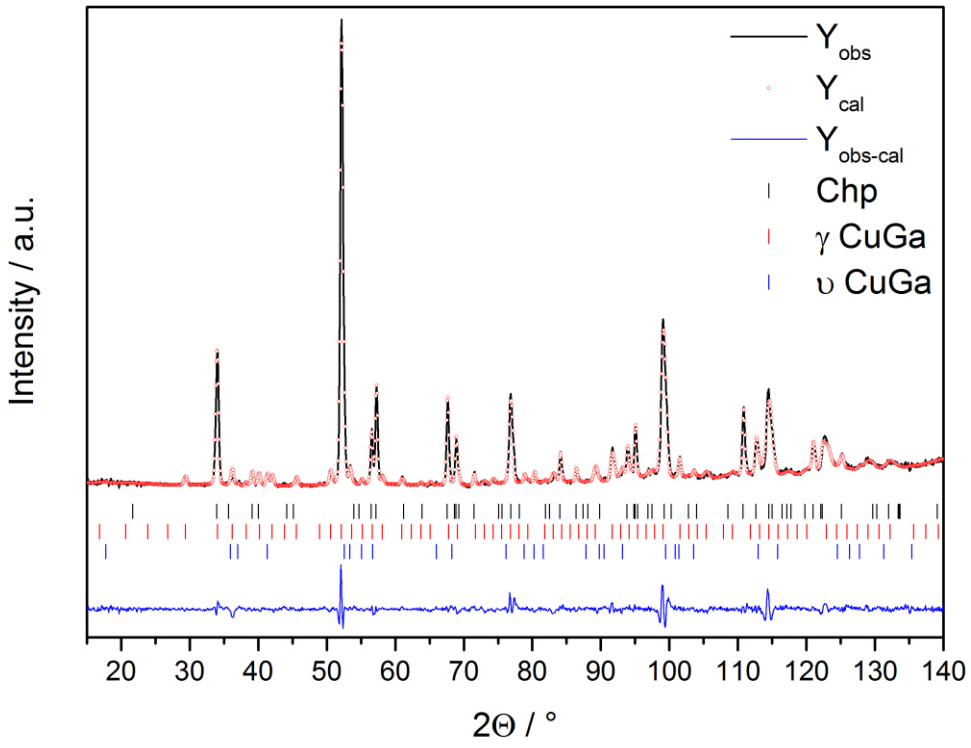

ND: Chi^2: 5.16 Bragg R-factor: 4.01

Mn-X-I 0.04

$Cu_{0.434}Ga_{0.469}Mn_{0.079}S$

a: 5.379 Å c: 10.524 Å x: 0.2581(14)

74% Chp; 23% γ Cu-Ga; 3% υ Cu-Ga

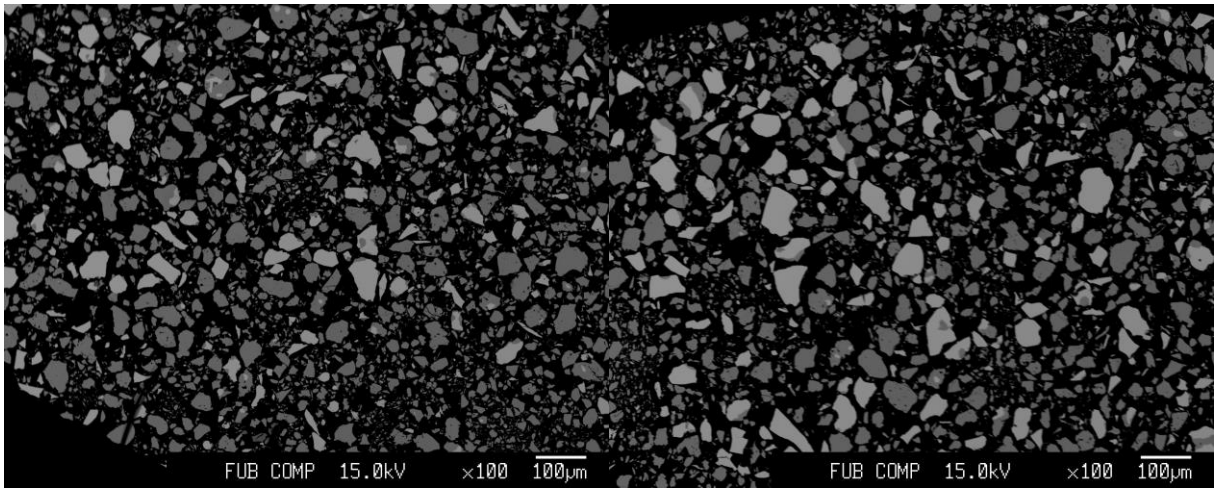

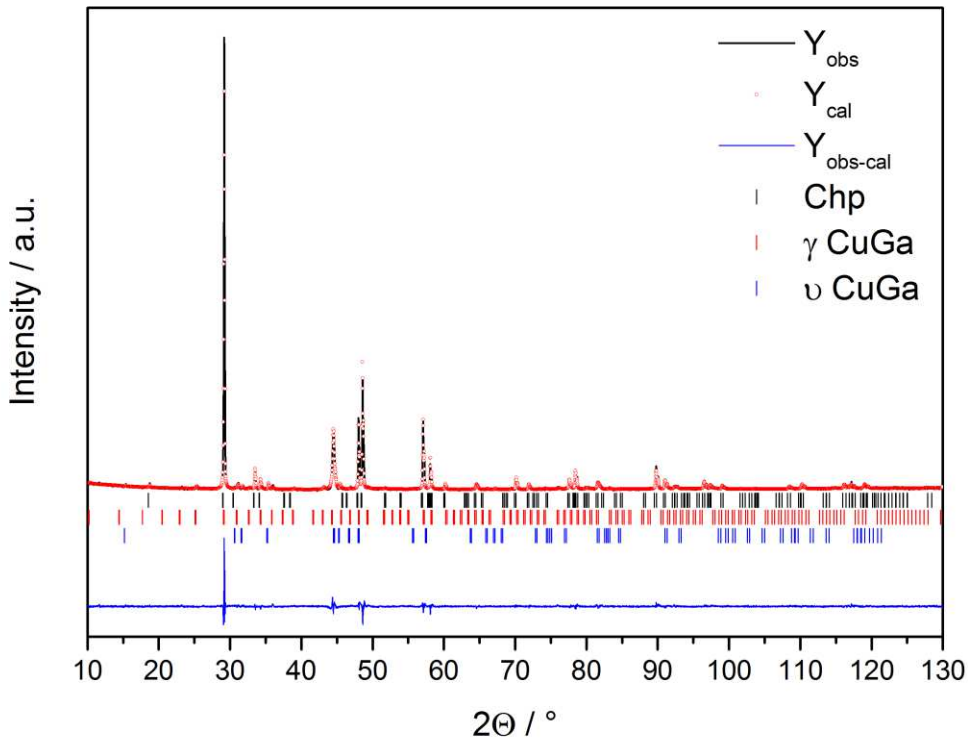

XRD: Chi^2: 2.35 Bragg R-factor: 5.88

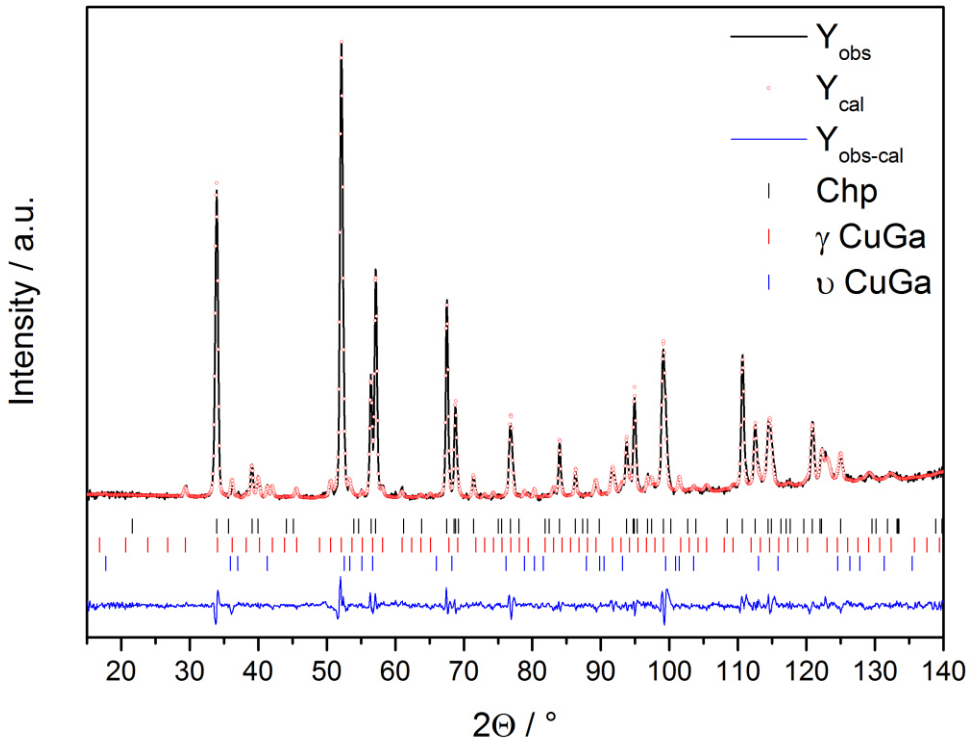

ND: Chi^2: 3.13 Bragg R-factor: 2.31

Mn-X-I 0.05

$Cu_{0.431}Ga_{0.470}Mn_{0.084}S$

a: 5.380 Å c: 10.532 Å x: 0.2647(12)

66% Chp; 30% γ Cu-Ga; 4% υ Cu-Ga

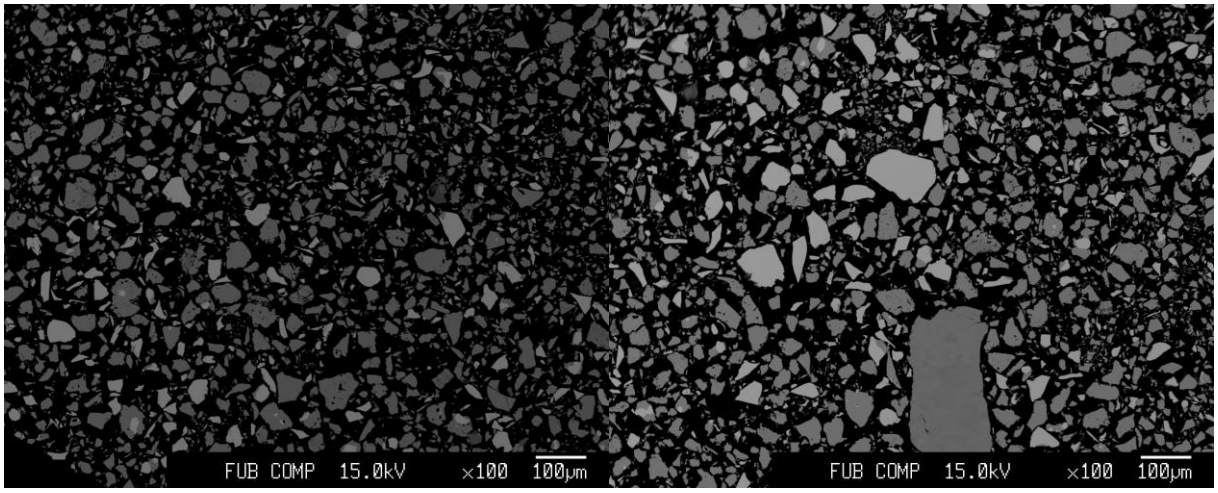

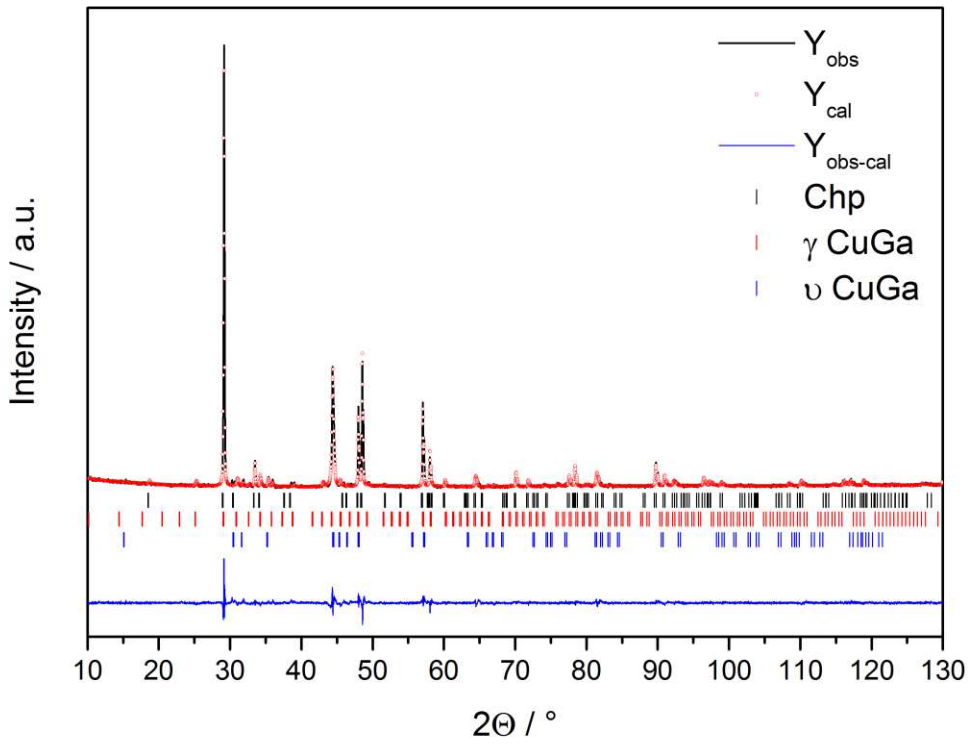

XRD: Chi^2: 2.45 Bragg R-factor: 5.99

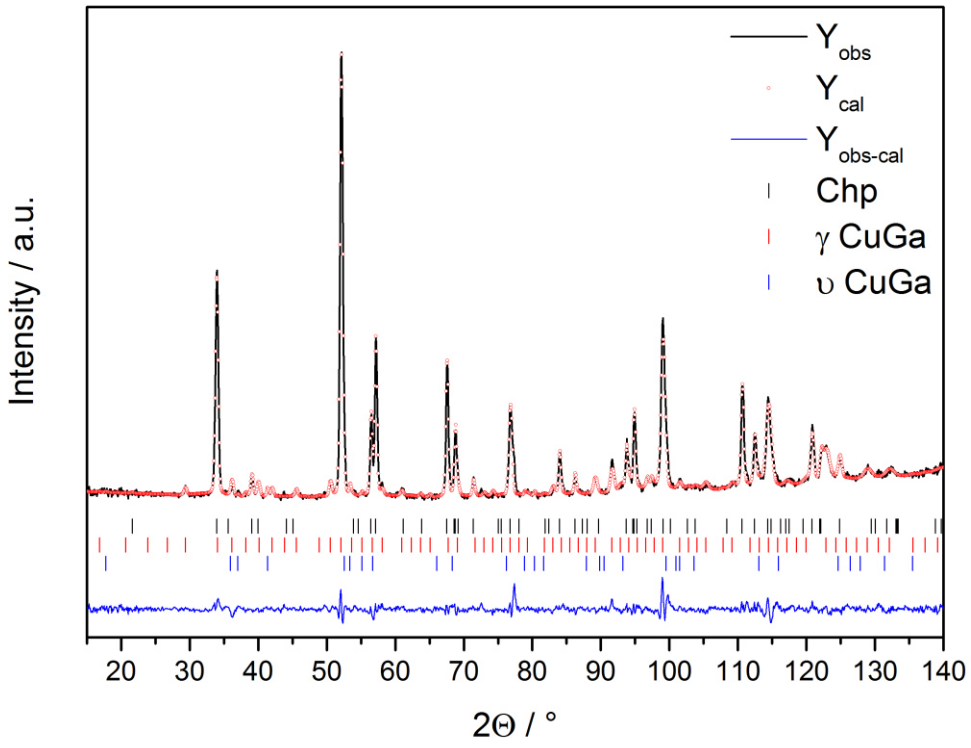

ND: Chi^2: 3.24 Bragg R-factor: 3.06

Mn-X-II 0.025

$Cu_{0.470}Ga_{0.483}Mn_{0.040}S$

a: 5.364 Å c: 10.492 Å x: 0.2604(12)

90% Chp; 10% γ Cu-Ga

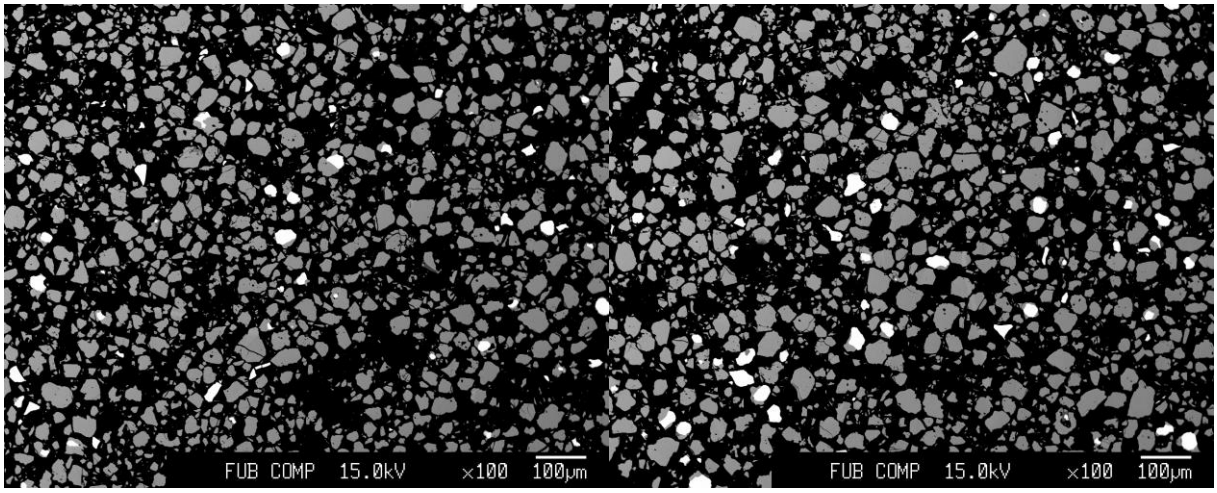

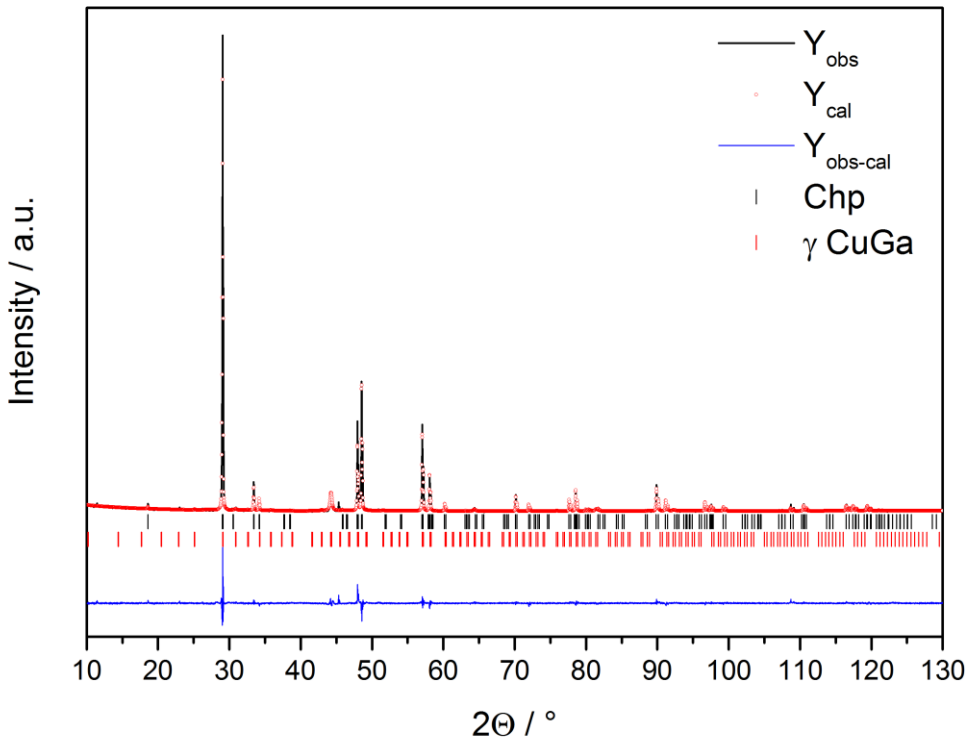

Chi^2: 2.57 Bragg R-factor: 5.79

Mn-X-II 0.05

$Cu_{0.457}Ga_{0.470}Mn_{0.081}S$

a: 5.374 Å c: 10.518 Å x: 0.2632(16)

92% Chp; 8% γ Cu-Ga

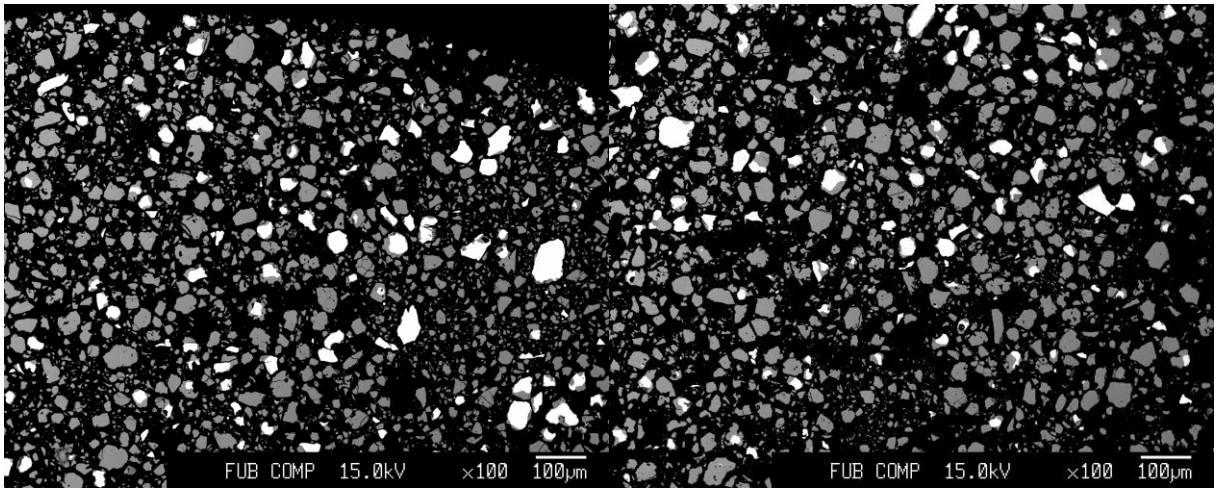

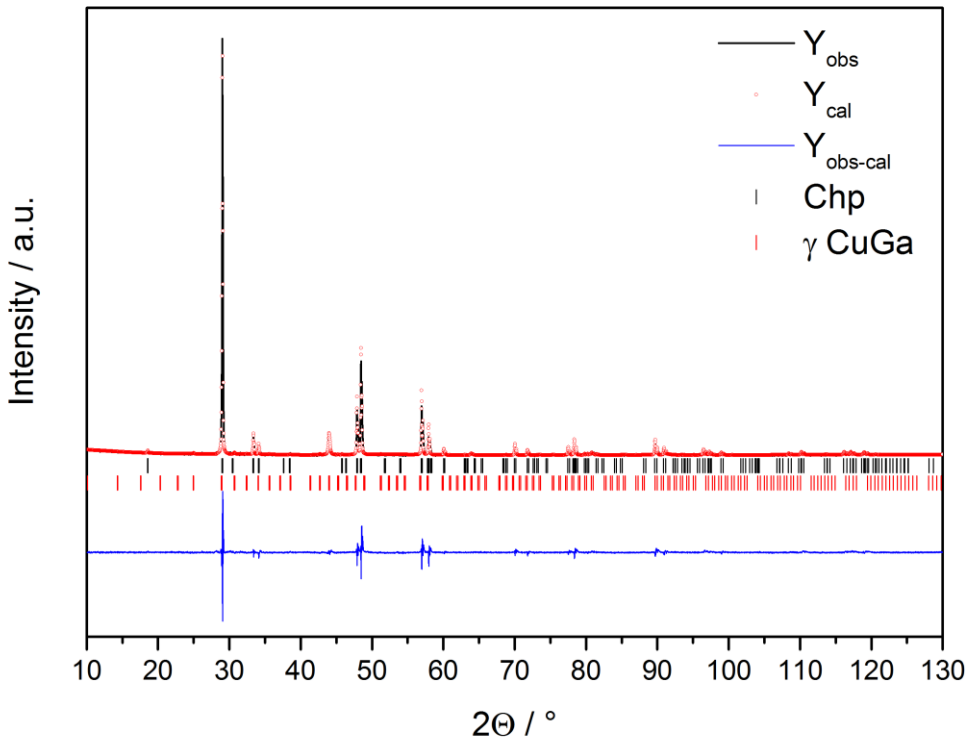

Chi^2: 5.53 Bragg R-factor: 10.7

Mn-X-II 0.1

$Cu_{0.462}Ga_{0.460}Mn_{0.071}S$

a: 5.372 Å c: 10.541 Å x: 0.2540(26)

92% Chp; 5% MnS; 3% Cu

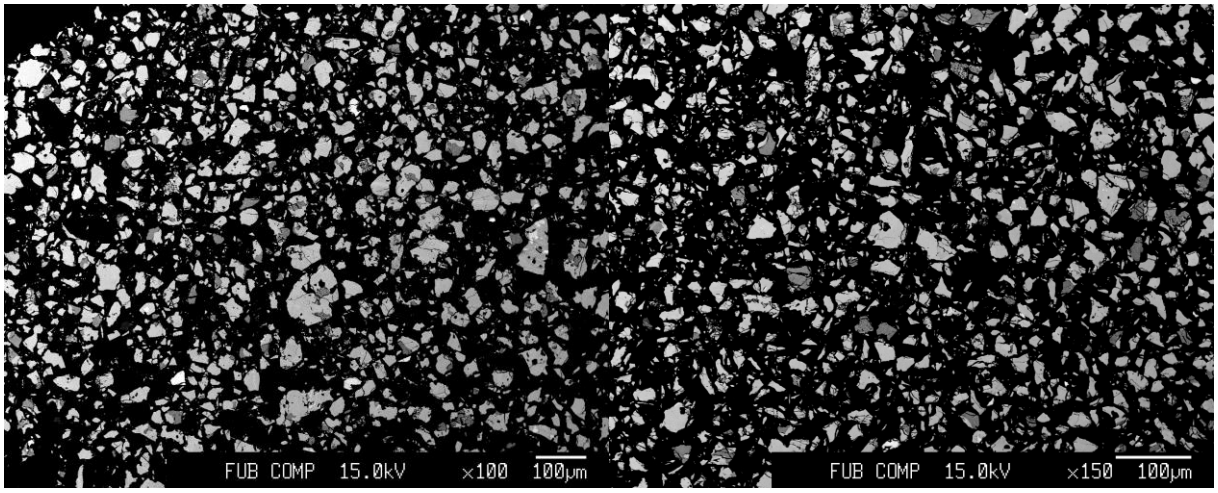

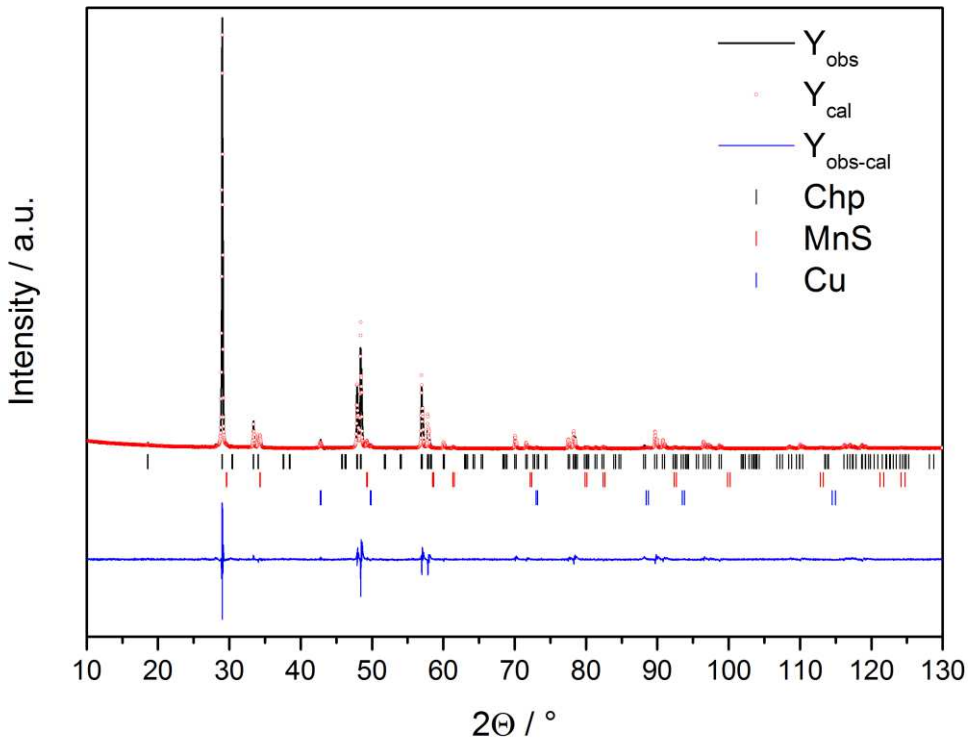

Chi^2: 4.95 Bragg R-factor: 9.40

Mn-X-II 0.175

$Cu_{0.474}Ga_{0.460}Mn_{0.061}S$

a: 5.364 Å c: 10.510 Å x: 0.2558(23)

86% Chp; 13% MnS; 1% Digenite

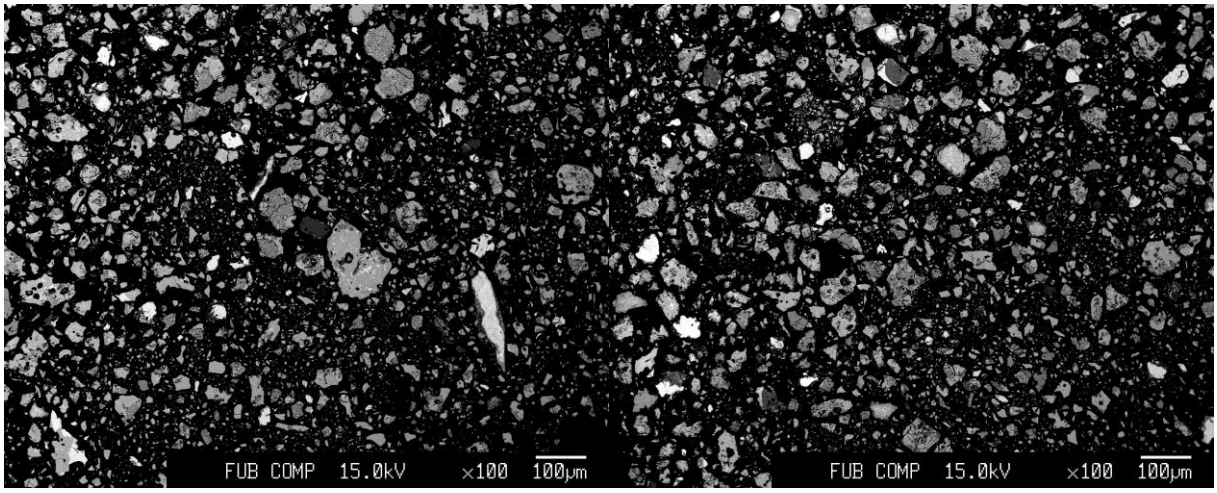

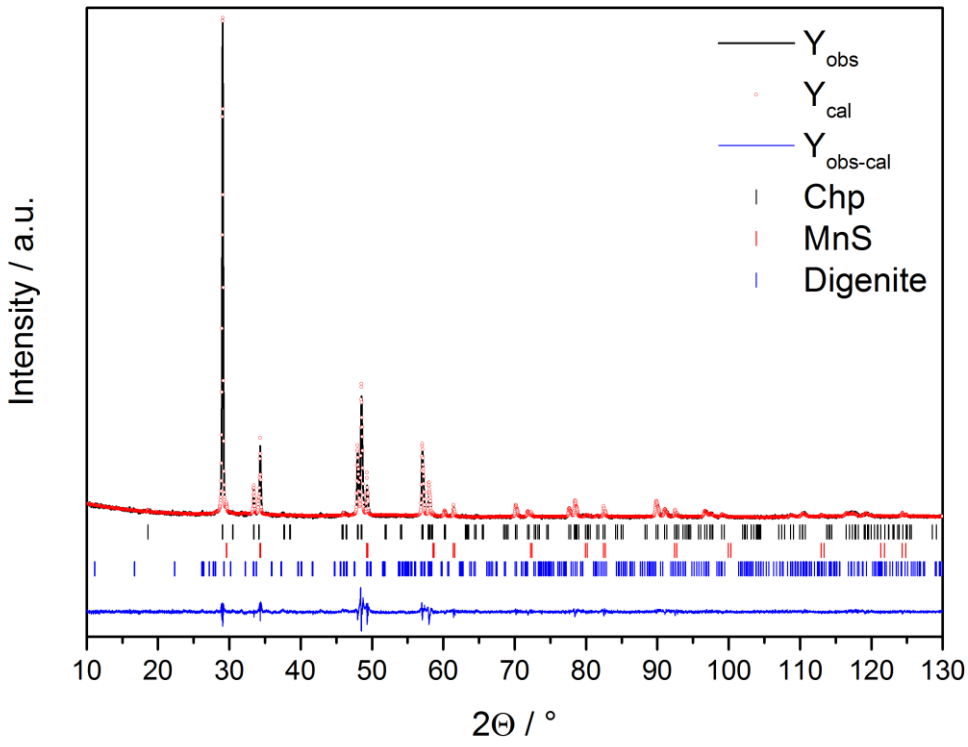

Chi^2: 2.74 Bragg R-factor: 6.19

Fe 0.025

$Cu_{0.505}Ga_{0.493}Fe_{0.018}S$

a: 5.355 Å c: 10.490 Å x: 0.2571(13)

95% Chp; 5% γ Cu-Ga

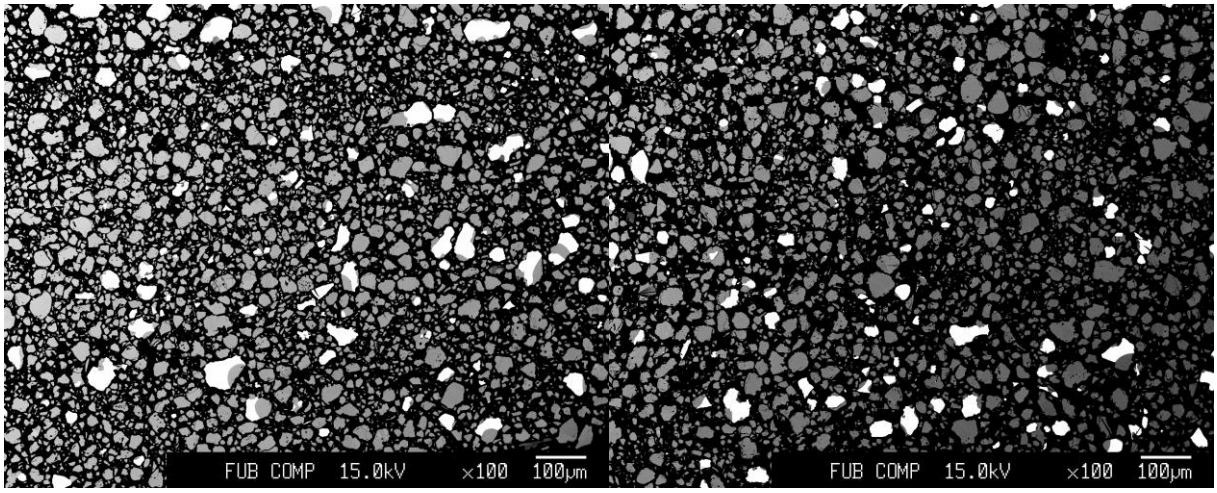

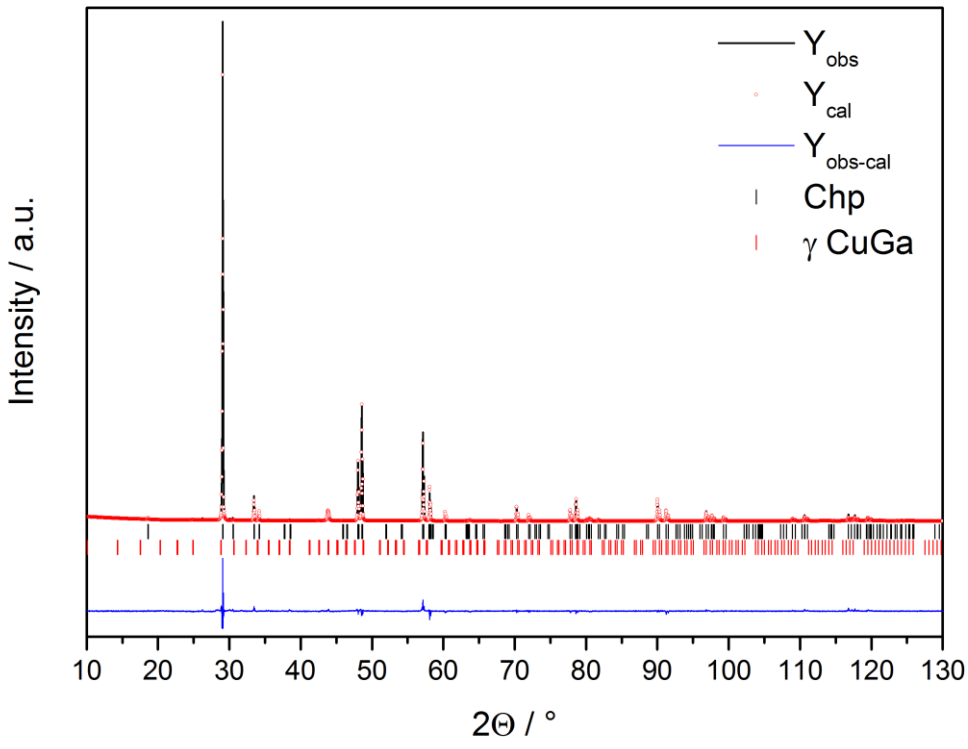

XRD: Chi^2: 3.15 Bragg R-factor: 6.20

Fe 0.05

$Cu_{0.489}Ga_{0.474}Fe_{0.054}S$

a: 5.357 Å c: 10.514 Å x: 0.2512(14)

100% Chp *secondary phases <1%

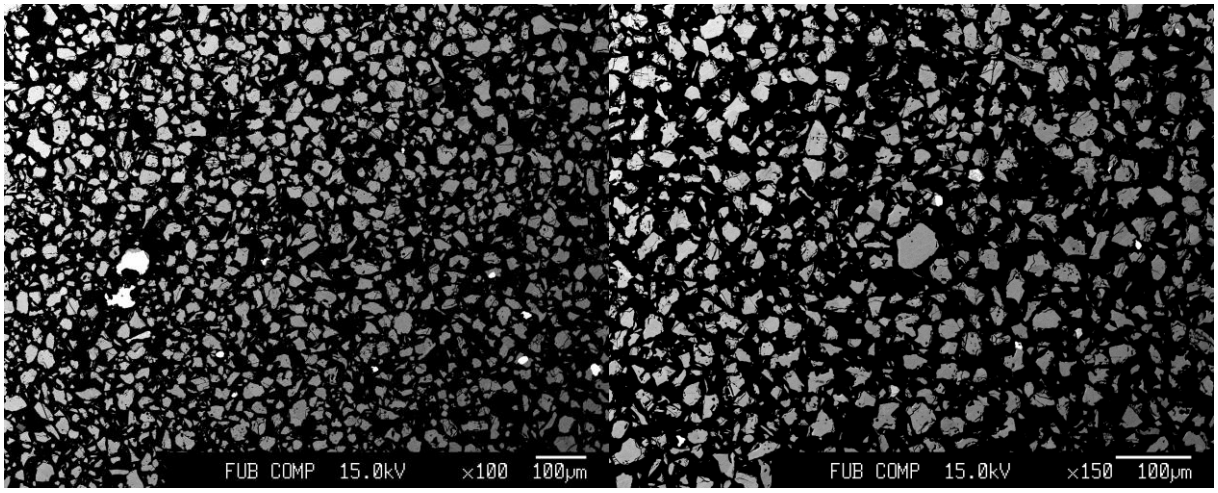

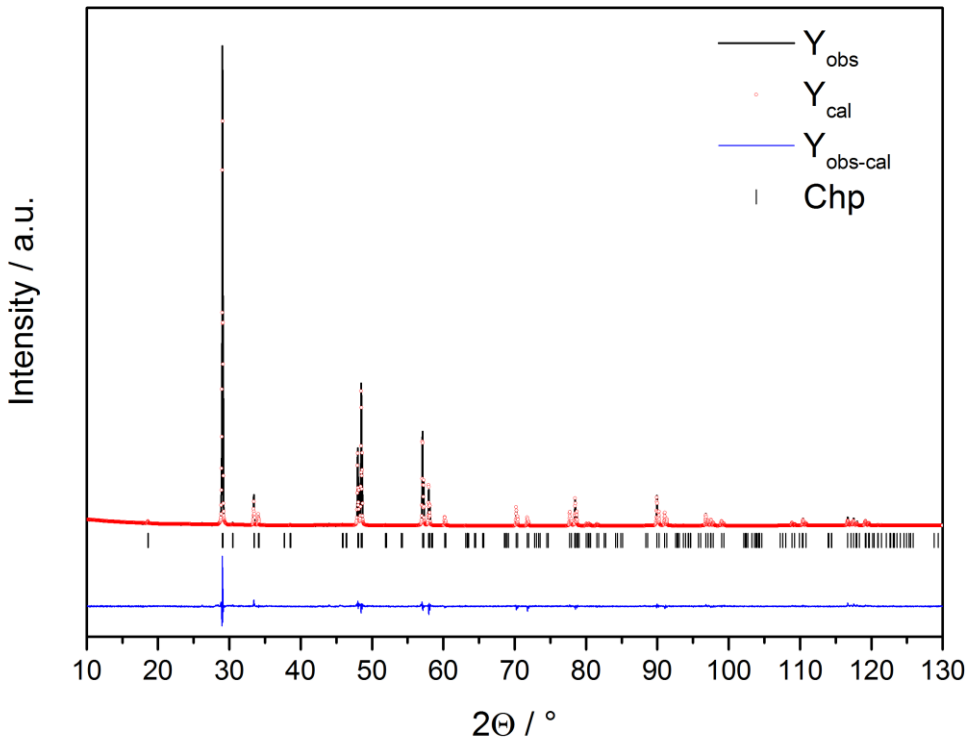

XRD: Chi^2: 3.15 Bragg R-factor: 5.96

Fe 0.075

$Cu_{0.483}Ga_{0.458}Fe_{0.080}S$

a: 5.358 Å c: 10.526 Å x: 0.2482(12)

100% Chp *secondary phases <1%

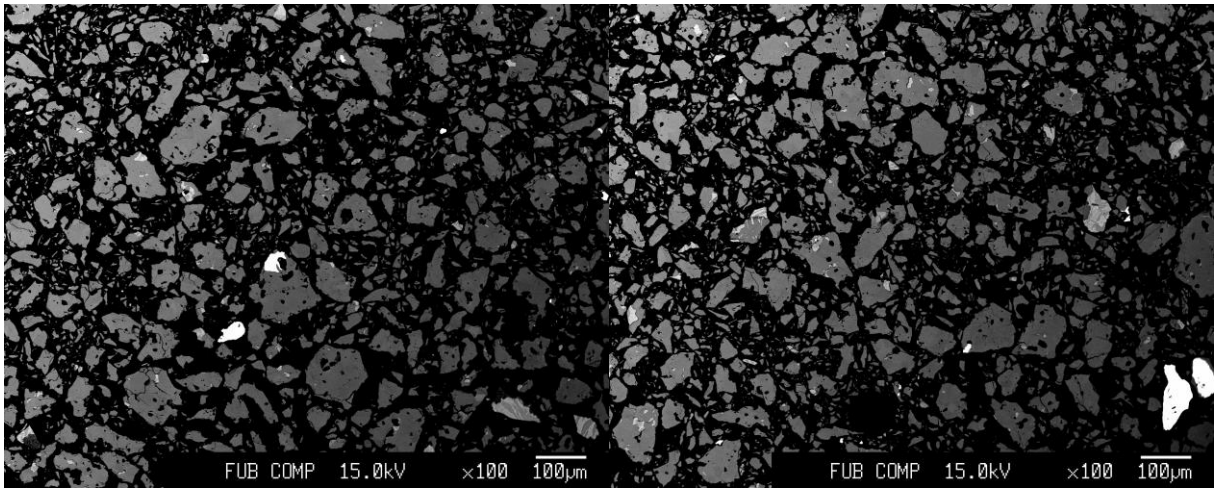

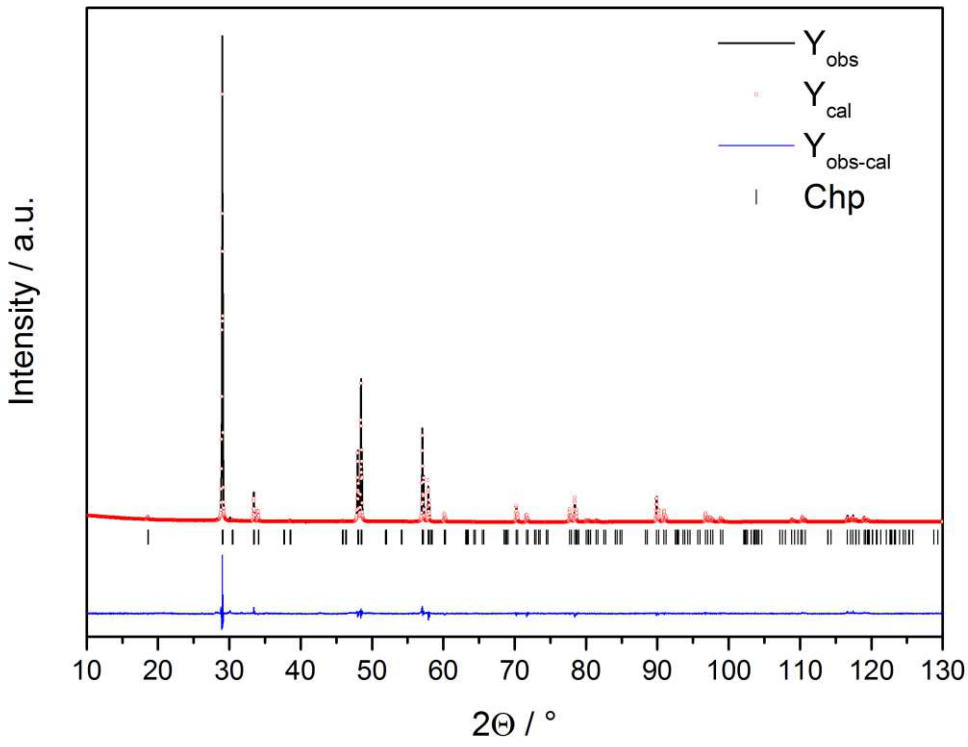

XRD: Chi^2: 3.11 Bragg R-factor: 6.30

Fe 0.1

$Cu_{0.471}Ga_{0.454}Fe_{0.105}S$

a: 5.359 Å c: 10.536 Å x: 0.2448(11)

100% Chp *secondary phases <1%

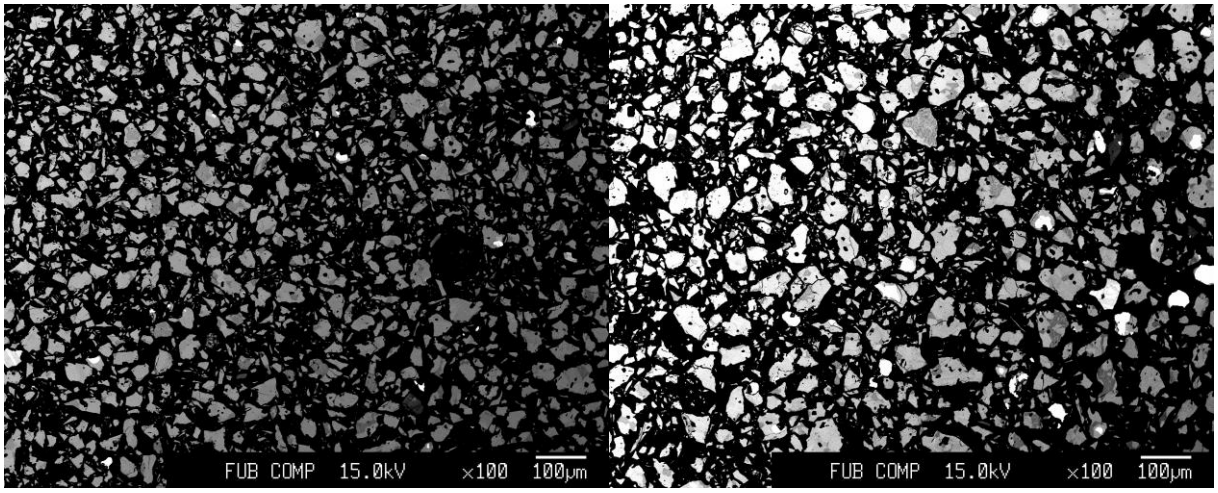

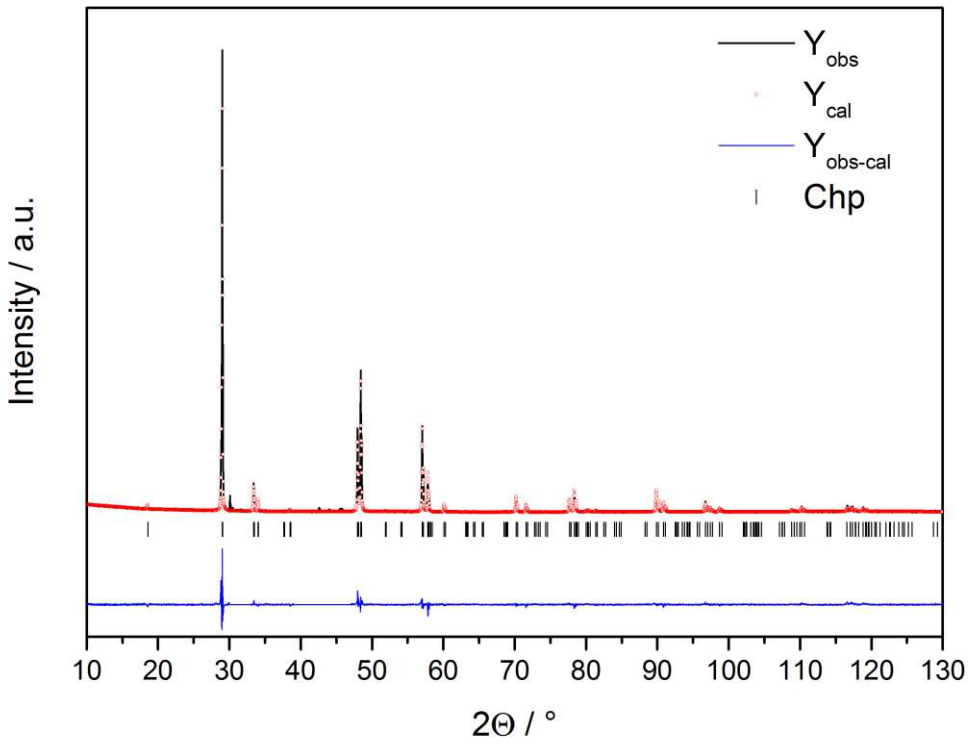

XRD: Chi^2: 3.61 Bragg R-factor: 6.97

Fe 0.125

$Cu_{0.497}Ga_{0.432}Fe_{0.065}S$

a: 5.347 Å c: 10.498 Å x: 0.2499(47)

73% Chp (low iron); 27% Chp ($Cu_{0.506}Ga_{0.131}Fe_{0.360}S$)

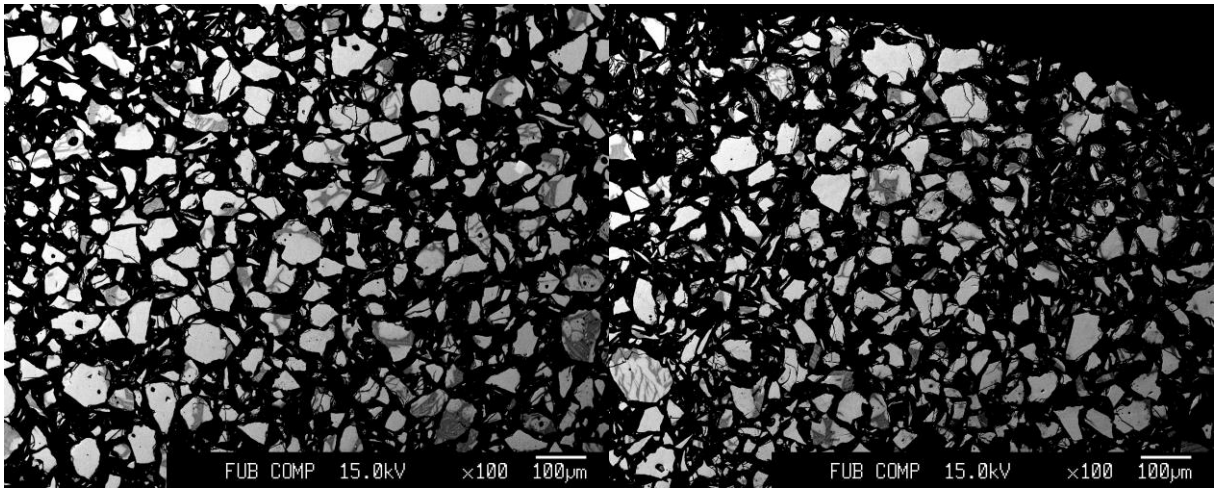

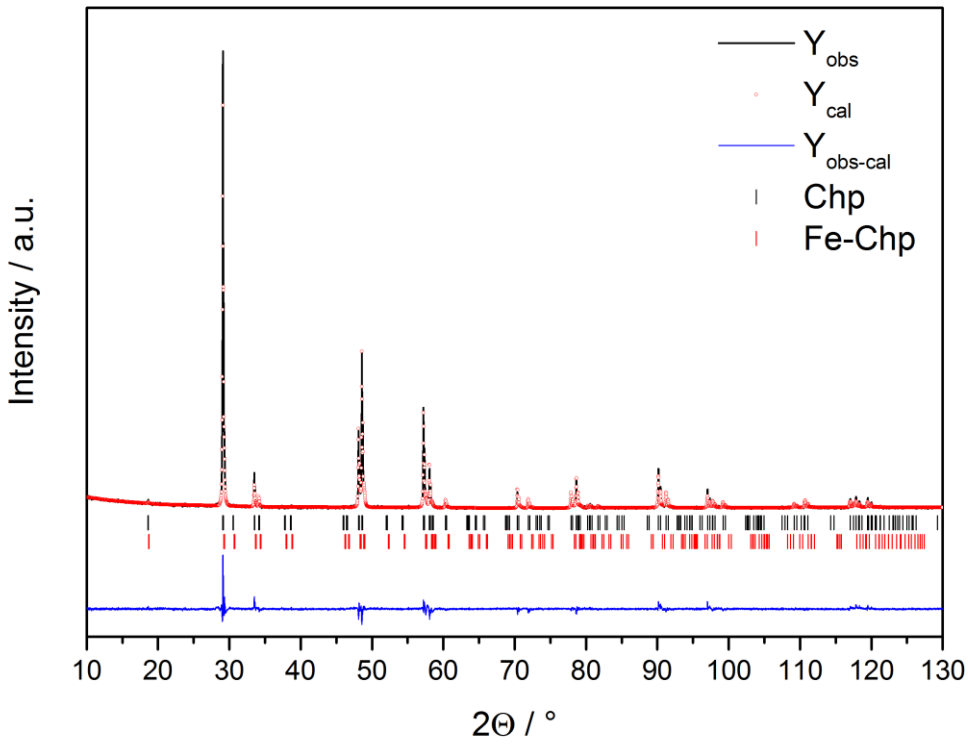

XRD: Chi^2: 3.46 Bragg R-factor: 10.6

Fe 0.15

$Cu_{0.496}Ga_{0.426}Fe_{0.070}S$

a: 5.346 Å c: 10.499 Å x: 0.2579(23)

81% Chp (low iron); 19% Chp ($Cu_{0.502}Ga_{0.120}Fe_{0.374}S$)

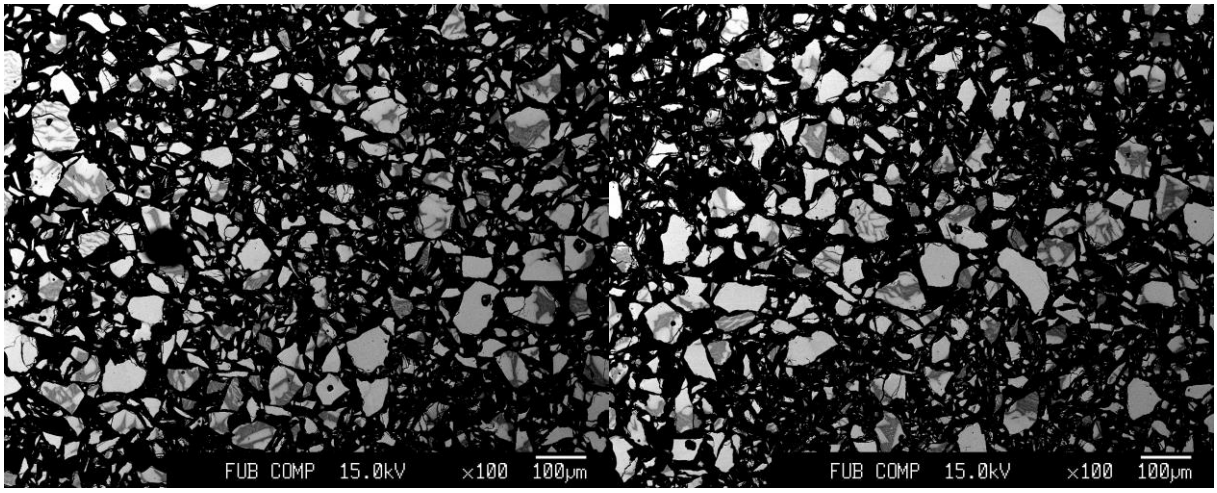

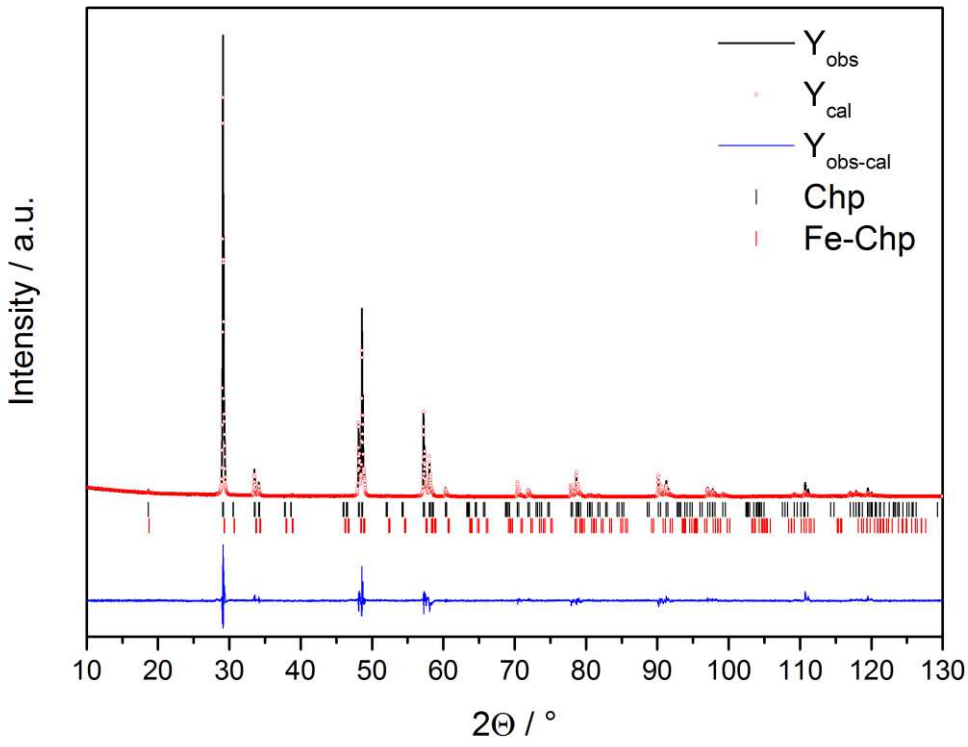

XRD: Chi^2: 4.20 Bragg R-factor: 8.05

Fe 0.175

$Cu_{0.497}Ga_{0.425}Fe_{0.070}S$

a: 5.345 Å c: 10.500 Å x: 0.2556(33)

73% Chp (low iron); 27% Chp ($Cu_{0.506}Ga_{0.138}Fe_{0.361}S$)

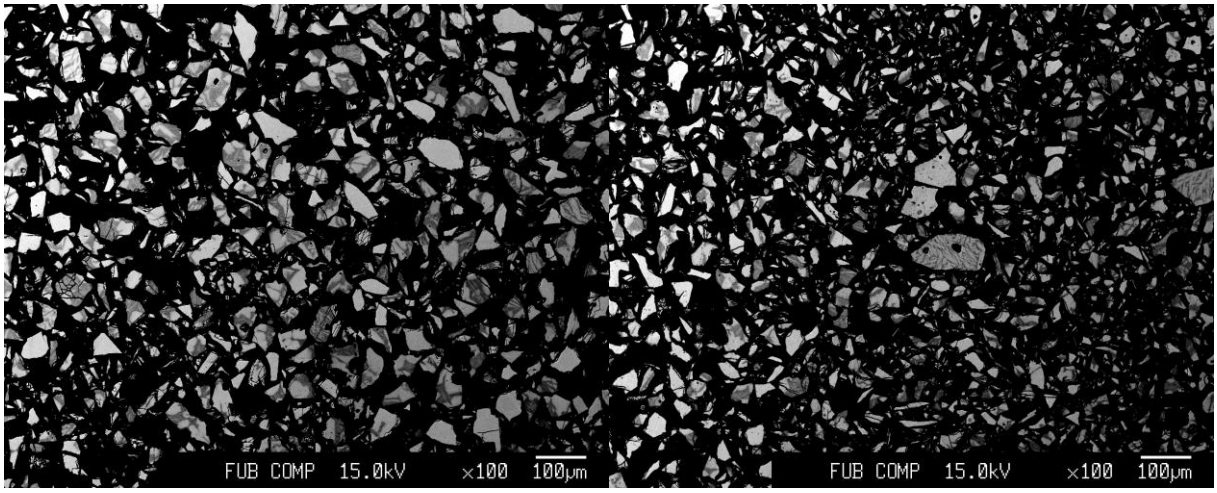

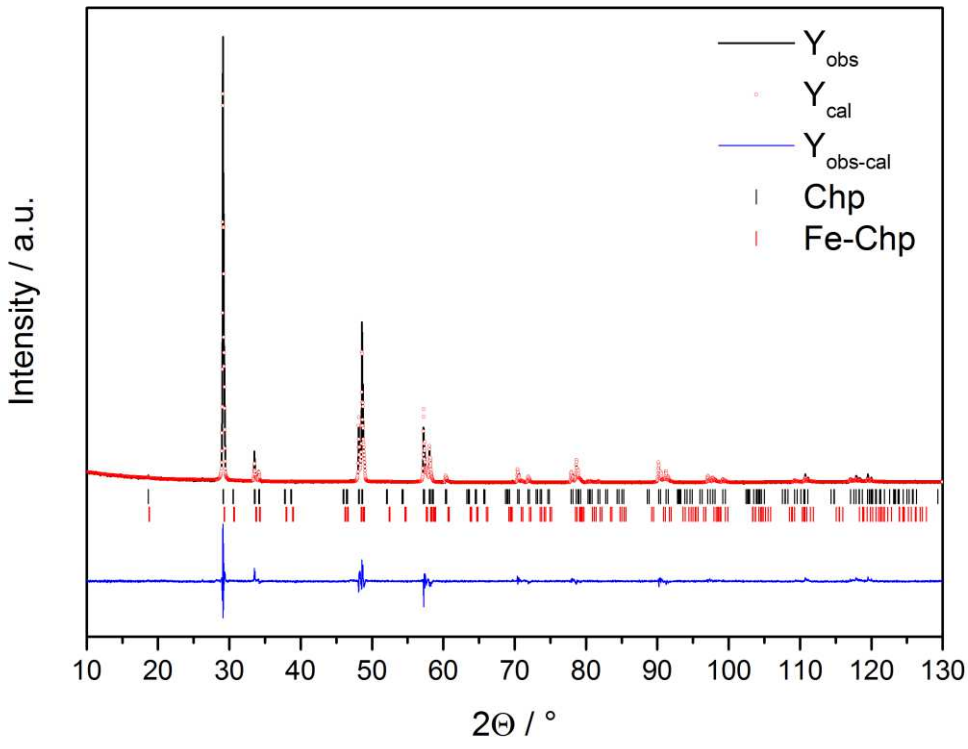

XRD: Chi^2: 3.69 Bragg R-factor: 9.03

Fe 0.2

$Cu_{0.496}Ga_{0.408}Fe_{0.090}S$

a: 5.343 Å c: 10.502 Å x: 0.2539(47)

70% Chp (low iron); 30% Chp ($Cu_{0.517}Ga_{0.130}Fe_{0.379}S$)

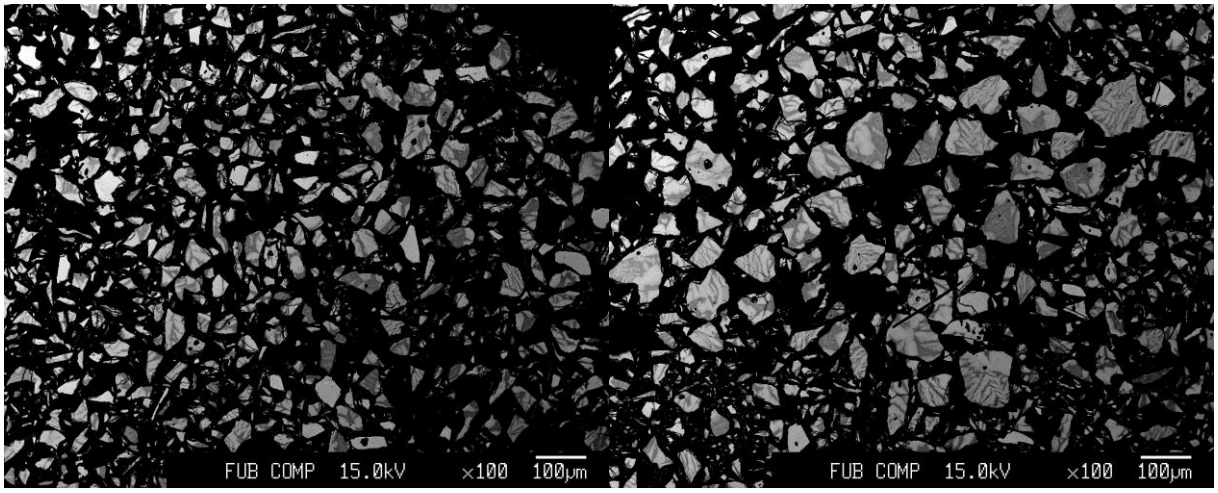

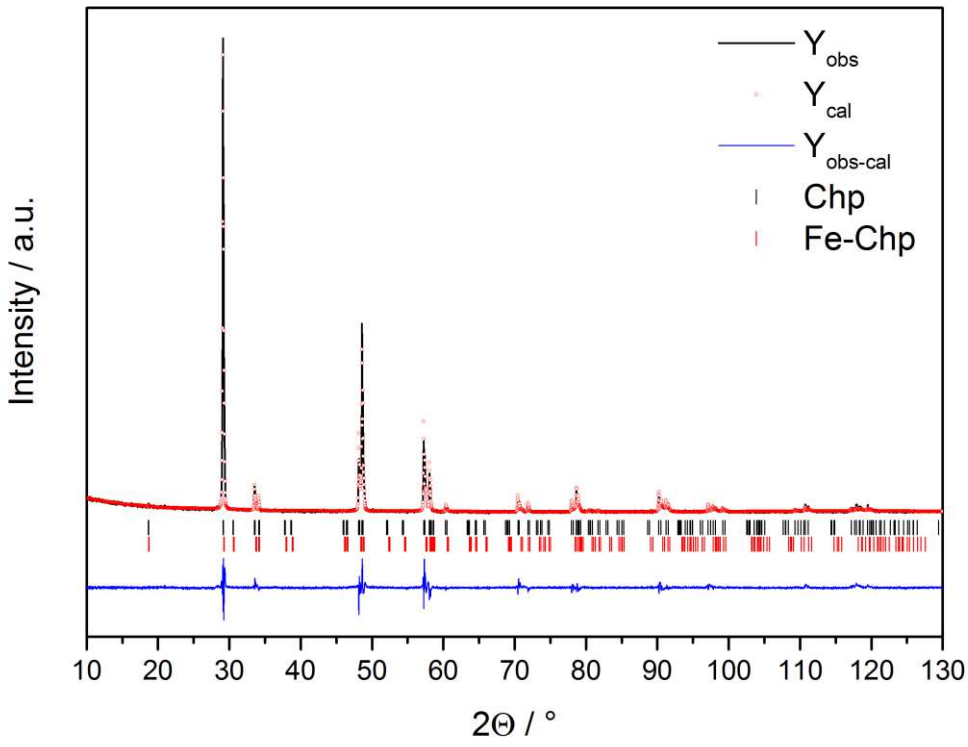

XRD: Chi^2: 4.39 Bragg R-factor: 10.3

Fe 0.225

$Cu_{0.500}Ga_{0.373}Fe_{0.125}S$

a: 5.339 Å c: 10.507 Å x: 0.2503(87)

73% Chp (low iron); 27% Chp ($Cu_{0.521}Ga_{0.115}Fe_{0.400}S$)

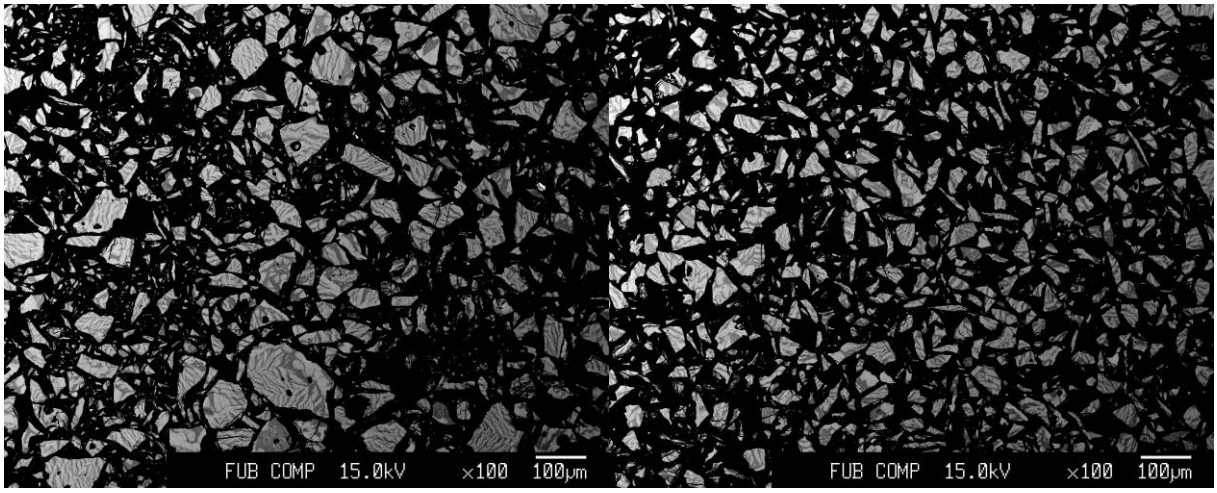

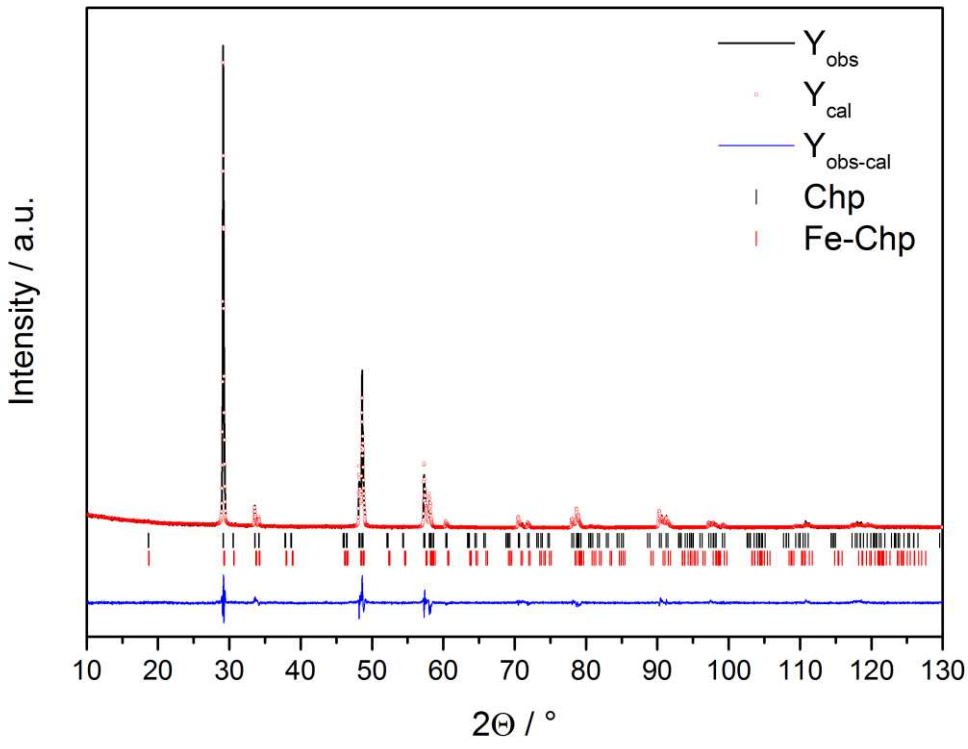

XRD: Chi^2: 3.25 Bragg R-factor: 9.02

Appendix II : chemical composition and phase content

Cr-I-I	Sample name	Formula $_{initial}$	Formula $_{measured}$	Cr [at.-%]	Cu/Ga	Cu/(Ga+Cr)	M/S	Phase content (XRD) [%]		comment
0.02	CCGS-002	$Cu_{0.49}Ga_{0.49}Cr_{0.013}S$	$Cu_{0.501}Ga_{0.509}Cr_{0.001}S$	0.03	0.98(2)	0.98(2)	1.01(2)	Chp	93.77(31)	
								γ Cu-Ga	5.95(11)	a = 8.662(3)
								Cr-Spinel	0.29(3)	a = 9.923(5)
0.04	CCGS-004	$Cu_{0.48}Ga_{0.48}Cr_{0.027}S$								oxidized
0.06	CCGS-006	$Cu_{0.47}Ga_{0.47}Cr_{0.040}S$	$Cu_{0.492}Ga_{0.508}Cr_{0.001}S$	0.04	0.97(2)	0.97(2)	1.00(2)	Chp	95.44(47)	
								γ Cu-Ga	3.41(11)	a = 8.656(3)
								Cr-Spinel	1.15(3)	a = 9.924(5)
0.08	CCGS-008	$Cu_{0.46}Ga_{0.46}Cr_{0.053}S$	$Cu_{0.500}Ga_{0.510}Cr_{0.001}S$	0.07	0.98(2)	0.98(2)	1.01(2)	Chp	97.73(52)	
								γ Cu-Ga	0.91(6)	a = 8.723(3)
								Cr-Spinel	1.36(1)	a = 9.924(5)
0.1	CCGS-01	$Cu_{0.45}Ga_{0.45}Cr_{0.067}S$	$Cu_{0.494}Ga_{0.494}Cr_{0.001}S$	0.07	1.00(2)	1.00(2)	0.99(2)	Chp	97.89(73)	
								Cr-Spinel	2.11(2)	a = 9.922(5)
0.2	CCGS-02	$Cu_{0.40}Ga_{0.40}Cr_{0.133}S$	$Cu_{0.494}Ga_{0.499}Cr_{0.003}S$	0.14	0.99(2)	0.98(2)	1.00(2)	Chp	94.91(81)	
								Cr-Spinel	5.09(7)	a = 9.921(5)

Cr-I-II	Sample name	Formula $_{initial}$	Formula $_{measured}$	Cr [at.-%]	Cu/Ga	Cu/(Ga+Cr)	M/S	Phase content (XRD) [%]		comment
0.02	CCGS-C-E-002	$Cu_{0.49}Ga_{0.49}Cr_{0.013}S$	$Cu_{0.522}Ga_{0.503}Cr_{0.001}S$	0.04	1.04(2)	1.04(2)	1.03(2)	Chp	78.87(47)	
								γ Cu-Ga	16.32(15)	a = 8.656(3)
								υ Cu-Ga	4.81(10)	a = 2.831(3)
										c = 5.833(5)
0.03	CCGS-C-E-003	$Cu_{0.485}Ga_{0.485}Cr_{0.020}S$	$Cu_{0.512}Ga_{0.495}Cr_{0.001}S$	0.04	1.03(2)	1.03(2)	1.01(2)	Chp	78.65(41)	
								γ Cu-Ga	16.81(16)	a = 8.660(3)
								υ Cu-Ga	3.91(4)	a = 2.831(3)
										c = 5.834(5)
								Cr-Spinel	0.64(4)	a = 9.926(5)

Cr-I-II	Sample name	Formula $_{initial}$	Formula $_{measured}$	Cr [at.-%]	Cu/Ga	Cu/(Ga+Cr)	M/S	Phase content (XRD) [%]		comment
0.04	CCGS-C-E-004	$Cu_{0.48}Ga_{0.48}Cr_{0.027}S$	$Cu_{0.520}Ga_{0.509}Cr_{0.001}S$	0.06	1.02(2)	1.02(2)	1.03(2)	Chp	92.45(36)	
								γ Cu-Ga	6.90(9)	a = 8.669(3)
								Cr-Spinel	0.64(2)	a = 9.924(5)
0.05	CCGS-C-E-005	$Cu_{0.475}Ga_{0.475}Cr_{0.033}S$	$Cu_{0.515}Ga_{0.502}Cr_{0.001}S$	0.05	1.03(2)	1.02(2)	1.02(2)	Chp	92.55(42)	
								γ Cu-Ga	6.64(10)	a = 8.670(3)
								Cr-Spinel	0.82(2)	a = 9.923(5)

Mn-I-I	Sample name	Formula $_{initial}$	Formula $_{measured}$	Mn [at.-%]	Cu/Ga	Cu/(Ga+Mn)	M/S	Phase content (XRD) [%]		comment
0.02	CMGS-B-E-002	$Cu_{0.49}Ga_{0.49}Mn_{0.02}S$	$Cu_{0.477}Ga_{0.475}Mn_{0.021}S$	1.04	1.00(2)	0.96(2)	0.97(2)	Chp	100.00(66)	
0.04	CMGS-B-E-004	$Cu_{0.48}Ga_{0.48}Mn_{0.04}S$	$Cu_{0.467}Ga_{0.466}Mn_{0.041}S$	2.07	1.00(2)	0.92(2)	0.97(2)	Chp	100.00(55)	
0.06	CMGS-B-E-006	$Cu_{0.47}Ga_{0.47}Mn_{0.06}S$								oxidized
0.08	CMGS-B-E-008	$Cu_{0.46}Ga_{0.46}Mn_{0.08}S$	$Cu_{0.421}Ga_{0.463}Mn_{0.082}S$	4.09	0.91(2)	0.77(2)	0.97(2)	Chp	94.78(67)	
								γ Cu-Ga	4.01(2)	a = 8.704(3)
								MnS	1.21(10)	a = 5.226(5)
0.1	CMGS-B-E-01	$Cu_{0.45}Ga_{0.45}Mn_{0.1}S$	$Cu_{0.432}Ga_{0.447}Mn_{0.091}S$	4.56	0.97(2)	0.80(2)	0.97(2)	Chp	93.68(53)	
								γ Cu-Ga	1.59(5)	a = 8.748(5)
								MnS	4.73(17)	a = 5.228(3)
0.2	CMGS-B-E-02	$Cu_{0.4}Ga_{0.4}Mn_{0.2}S$								heterogeneous

Mn-I-II	Sample name	Formula $_{initial}$	Formula $_{measured}$	Mn [at.-%]	Cu/Ga	Cu/(Ga+Mn)	M/S	Phase content (XRD) [%]		comment
0.01	CMGS-D-E-001	$Cu_{0.495}Ga_{0.495}Mn_{0.01}S$	$Cu_{0.465}Ga_{0.487}Mn_{0.014}S$	0.72	0.95(2)	0.93(2)	0.97(2)	Chp	96.20(36)	
								γ Cu-Ga	3.80(9)	a = 8.719(3)
0.03	CMGS-D-E-003	$Cu_{0.485}Ga_{0.485}Mn_{0.03}S$	$Cu_{0.444}Ga_{0.479}Mn_{0.041}S$	2.07	0.93(2)	0.85(2)	0.96(2)	Chp	93.07 (41)	
								γ Cu-Ga	6.93 (22)	a = 8.703(3)
0.05	CMGS-D-E-005	$Cu_{0.475}Ga_{0.475}Mn_{0.05}S$	$Cu_{0.433}Ga_{0.469}Mn_{0.063}S$	3.13	0.92(2)	0.81(2)	0.96(2)	Chp	93.70(38)	
								γ Cu-Ga	6.30(17)	a = 8.715(3)

Mn-I-II	Sample name	Formula $_{initial}$	Formula $_{measured}$	Mn [at.-%]	Cu/Ga	Cu/(Ga+Mn)	M/S	Phase content (XRD) [%]		comment
0.07	CMGS-D-E-007	$Cu_{0.465}Ga_{0.465}Mn_{0.07}S$	$Cu_{0.465}Ga_{0.456}Mn_{0.069}S$	3.46	1.02(2)	0.89(2)	0.99(2)	Chp	97.79(82)	
								MnS	2.21(24)	a = 5.227(5)

Mn-I-III	Sample name	Formula $_{initial}$	Formula $_{measured}$	Mn [at.-%]	Cu/Ga	Cu/(Ga+Mn)	M/S	Phase content (XRD) [%]		comment
0.00	CMGS-F-E	$Cu_{0.5}Ga_{0.5}S$	$Cu_{0.495}Ga_{0.493}S$		1.00(2)		0.99(2)	Chp	95.20(81)	
								γ Cu-Ga	4.80(11)	a = 8.655(3)
0.05	CMGS-F-E-005	$Cu_{0.475}Ga_{0.475}Mn_{0.05}S$	$Cu_{0.446}Ga_{0.469}Mn_{0.063}S$	3.16	0.95(2)	0.84(2)	0.98(2)	Chp	100.0(8)	+alloy
0.10	CMGS-F-E-010	$Cu_{0.45}Ga_{0.45}Mn_{0.1}S$								heterogeneous
0.15	CMGS-F-E-015	$Cu_{0.425}Ga_{0.425}Mn_{0.15}S$	$Cu_{0.413}Ga_{0.454}Mn_{0.098}S$	4.90	0.91(2)	0.75(2)	0.96(2)	Chp	77.03(82)	(334)
								γ Cu-Ga	8.63(29)	a = 8.665(3)
								MnS	14.34(28)	a = 5.228(3)
0.20	CMGS-F-E-020	$Cu_{0.4}Ga_{0.4}Mn_{0.2}S$	$Cu_{0.451}Ga_{0.452}Mn_{0.087}S$	4.36	1.00(2)	0.84(2)	0.99(2)	Chp	86.88(133)	(334)
								MnS	13.12(55)	a = 5.232(3)
0.25	CMGS-F-E-025	$Cu_{0.375}Ga_{0.375}Mn_{0.25}S$	$Cu_{0.449}Ga_{0.449}Mn_{0.089}S$	4.43	1.00(2)	0.83(2)	0.99(2)	Chp	81.29(145)	(334)
								MnS	18.71(62)	a = 5.233(3)
0.30	CMGS-F-E-030	$Cu_{0.35}Ga_{0.35}Mn_{0.3}S$								
0.35	CMGS-F-E-035	$Cu_{0.325}Ga_{0.325}Mn_{0.35}S$								
0.40	CMGS-F-E-040	$Cu_{0.3}Ga_{0.3}Mn_{0.4}S$								
0.45	CMGS-F-E-045	$Cu_{0.275}Ga_{0.275}Mn_{0.45}S$								
0.50	CMGS-F-E-050	$Cu_{0.25}Ga_{0.25}Mn_{0.5}S$								
0.60	CMGS-F-E-060	$Cu_{0.2}Ga_{0.2}Mn_{0.6}S$								
0.70	CMGS-F-E-070	$Cu_{0.15}Ga_{0.15}Mn_{0.7}S$								

heterogeneous

Mn-334	Sample name	Formula $_{initial}$	Formula $_{measured}$	Mn [at.-%]	Cu/Ga	Cu/(Ga+Mn)	M/S	Phase content (XRD) [%]		comment
I	334-I	$Cu_{0.3}Ga_{0.3}Mn_{0.4}S$	$Cu_{0.299}Ga_{0.290}Mn_{0.410}S$	20.51	1.03(2)	0.43(2)	1.00(2)	Chp	62.91(67)	(334)
								MnS	37.09(50)	a = 5.229(3)
II	334-II	$Cu_{0.3}Ga_{0.3}Mn_{0.4}S$	$Cu_{0.299}Ga_{0.289}Mn_{0.410}S$	20.49	1.03(2)	0.43(2)	1.00(2)	Chp	62.95(66)	(334)
								MnS	37.05(49)	a = 5.229(3)

Ni	Sample name	Formula $_{initial}$	Formula $_{measured}$	Ni [at.-%]	Cu/Ga	Cu/(Ga+Ni)	M/S	Phase content (XRD) [%]		comment
0.05	CNGS-005	$Cu_{0.475}Ga_{0.475}Ni_{0.05}S$	$Cu_{0.488}Ga_{0.487}Ni_{0.006}S$	0.32	1.00(2)	0.99(2)	0.98(2)	Chp	94.43(70)	
								NiS	4.92(18)	a = 3.435(3)
										c = 5.339(5)
								Hzl	0.65(8)	a = 4.08(1)
										c = 4.10(1)
0.1	CNGS-010	$Cu_{0.45}Ga_{0.45}Ni_{0.1}S$	$Cu_{0.494}Ga_{0.484}Ni_{0.002}S$	0.11	1.02(2)	1.02(2)	0.98(2)	Chp	91.06(58)	
								α´ Ni-Ga	6.91(15)	a = 3.596(3)
								Hzl	2.03(9)	a = 4.085(5)
										c = 4.097(5)
0.15	CNGS-015	$Cu_{0.425}Ga_{0.425}Ni_{0.15}S$	$Cu_{0.488}Ga_{0.488}Ni_{0.006}S$	0.31	1.00(2)	0.99(2)	0.98(2)	Chp	98.81(112)	
								Hzl	1.19 (12)	a = 4.08(1)
										c = 4.10(1)
0.20	CNGS-020	$Cu_{0.4}Ga_{0.4}Ni_{0.2}S$	$Cu_{0.483}Ga_{0.490}Ni_{0.008}S$	0.42	0.99(2)	0.97(2)	0.98(2)	Chp	80.68(81)	
								NiS	17.97(46)	a = 3.430(3)
										c = 5.330(5)
								Hzl	1.35(8)	a = 4.09(1)
										c = 4.10(1)

Mn-X-I	Sample name	Formula $_{initial}$	Formula $_{measured}$	Mn [at.-%]	Cu/Ga	Cu/(Ga+Mn)	M/S	Phase content (XRD) [%]		comment
0.01	CMGS-002	$Cu_{0.5}Ga_{0.49}Mn_{0.01}S$	$Cu_{0.486}Ga_{0.491}Mn_{0.012}S$	0.59	0.99(2)	0.97(2)	0.99(2)	Chp	97.13(42)	
								γ Cu-Ga	1.45(6)	a = 8.739(5)
								υ Cu-Ga	1.42(17)	a = 2.821(5)
										c = 5.612(10)
0.02	CMGS-004	$Cu_{0.5}Ga_{0.48}Mn_{0.02}S$	$Cu_{0.443}Ga_{0.476}Mn_{0.063}S$	3.17	0.93(2)	0.82(2)	0.98(2)	Chp	64.10(38)	
								γ Cu-Ga	33.94(22)	a = 8.683(3)
								υ Cu-Ga	1.96(7)	a = 2.833(5)
										c = 5.835(10)
0.03	CMGS-002	$Cu_{0.5}Ga_{0.47}Mn_{0.03}S$								oxidized
0.04		$Cu_{0.5}Ga_{0.46}Mn_{0.04}S$	$Cu_{0.434}Ga_{0.469}Mn_{0.079}S$	3.97	0.93(2)	0.79(2)	0.98(2)	Chp	74.44(37)	
								γ Cu-Ga	22.60(11)	a = 8.680(3)
								υ Cu-Ga	2.96(16)	a = 2.833(3)
										c = 5.839(5)
0.05		$Cu_{0.5}Ga_{0.45}Mn_{0.05}S$	$Cu_{0.431}Ga_{0.470}Mn_{0.085}S$	4.27	0.92(2)	0.78(2)	0.99(2)	Chp	66.35(31)	
								γ Cu-Ga	29.87(16)	a = 8.693(3)
								υ Cu-Ga	3.78(62)	a = 2.831(3)
										c = 5.872(5)

Mn-X-II	Sample name	Formula $_{initial}$	Formula $_{measured}$	Mn [at.-%]	Cu/Ga	Cu/(Ga+Mn)	M/S	Phase content (XRD) [%]		comment
0.025	CMGS-E-E-005	$Cu_{0.5}Ga_{0.475}Mn_{0.025}S$	$Cu_{0.470}Ga_{0.483}Mn_{0.040}S$	2.01	0.97(2)	0.90(2)	0.99(2)	Chp	90.81(50)	
								γ Cu-Ga	9.19(24)	a = 8.685(3)
0.05	CMGS-E-E-010	$Cu_{0.5}Ga_{0.45}Mn_{0.05}S$	$Cu_{0.467}Ga_{0.470}Mn_{0.081}S$	4.05	0.97(2)	0.83(2)	1.01(2)	Chp	92.01(66)	
								γ Cu-Ga	7.99(15)	a = 8.739(3)
0.075	CMGS-E-E-015	$Cu_{0.5}Ga_{0.425}Mn_{0.075}S$								heterogeneous
0.1	CMGS-E-E-020	$Cu_{0.5}Ga_{0.4}Mn_{0.1}S$	$Cu_{0.462}Ga_{0.460}Mn_{0.071}S$	3.56	1.00(2)	0.87(2)	0.99(2)	Chp	92.45(76)	
								MnS	4.98(16)	a = 5.231(3)
								Cu	2.57(15)	a = 3.663(3)

Mn-X-II	Sample name	Formula $_{initial}$	Formula $_{measured}$	Mn [at.-%]	Cu/Ga	Cu/(Ga+Mn)	M/S	Phase content (XRD) [%]		comment
0.125	CMGS-E-E-025	$Cu_{0.5}Ga_{0.375}Mn_{0.125}S$								
0.15	CMGS-E-E-030	$Cu_{0.5}Ga_{0.35}Mn_{0.15}S$								heterogeneous
0.175	CMGS-E-E-035	$Cu_{0.5}Ga_{0.325}Mn_{0.175}S$	$Cu_{0.474}Ga_{0.460}Mn_{0.061}S$	3.13	1.03(2)	0.91(2)	1.00(2)	Chp	86.04(56)	
								MnS	12.93(13)	a = 5.227(3)
								Dg	1.03(12)	a = 3.943(5)
										c = 47.78(2)
0.2	CMGS-E-E-040	$Cu_{0.5}Ga_{0.3}Mn_{0.2}S$								
0.225	CMGS-E-E-045	$Cu_{0.5}Ga_{0.275}Mn_{0.225}S$								heterogeneous
0.25	CMGS-E-E-050	$Cu_{0.5}Ga_{0.25}Mn_{0.25}S$								

Fe	Sample name	Formula $_{initial}$	Formula $_{measured}$	Fe [at.-%]	Cu/Ga	Cu/(Ga+Fe)	M/S	Phase content (XRD) [%]		comment
0.025	CFGS-A-E-005	$Cu_{0.5}Ga_{0.475}Fe_{0.025}S$	$Cu_{0.505}Ga_{0.493}Fe_{0.018}S$	0.91	1.02(2)	0.99(2)	1.02(2)	Chp	95.69(57)	
								γ Cu-Ga	4.31(7)	a = 8.759(3)
0.05	CFGS-A-E-010	$Cu_{0.5}Ga_{0.45}Fe_{0.05}S$	$Cu_{0.489}Ga_{0.474}Fe_{0.054}S$	2.68	1.03(2)	0.93(2)	1.02(2)	Chp	100.00(56)	
0.075	CFGS-A-E-015	$Cu_{0.5}Ga_{0.425}Fe_{0.075}S$	$Cu_{0.483}Ga_{0.458}Fe_{0.080}S$	4.01	1.05(2)	0.90(2)	1.02(2)	Chp	100.00(59)	
0.1	CFGS-A-E-020	$Cu_{0.5}Ga_{0.4}Fe_{0.1}S$	$Cu_{0.471}Ga_{0.454}Fe_{0.105}S$	5.25	1.04(2)	0.84(2)	1.03(2)	Chp	100.00(56)	
								+ one unidentified		
0.125	CFGS-A-E-025	$Cu_{0.5}Ga_{0.375}Fe_{0.125}S$	$Cu_{0.497}Ga_{0.432}Fe_{0.065}S$	3.25	1.05(2)	1.00(2)	0.99(2)	Chp	72.62(67)	
			$Cu_{0.506}Ga_{0.131}Fe_{0.360}S$	18.01	3.87(8)	1.03(2)	1.00(2)	Fe-Chp	27.38(46)	a = 5.321(5)
										c = 10.43(1)
0.15	CFGS-A-E-030	$Cu_{0.5}Ga_{0.35}Fe_{0.15}S$	$Cu_{0.496}Ga_{0.426}Fe_{0.070}S$	3.50	1.06(2)	1.00(2)	0.99(2)	Chp	80.61(61)	
			$Cu_{0.502}Ga_{0.120}Fe_{0.374}S$	18.71	4.19(8)	1.02(2)	1.00(2)	Fe-Chp	19.39(24)	a = 5.315(5)
										c = 10.45(1)
0.175	CFGS-A-E-035	$Cu_{0.5}Ga_{0.325}Fe_{0.175}S$	$Cu_{0.497}Ga_{0.425}Fe_{0.070}S$	3.52	1.07(2)	1.00(2)	0.99(2)	Chp	72.83(69)	
			$Cu_{0.506}Ga_{0.138}Fe_{0.361}S$	18.05	3.67(7)	1.01(2)	1.00(2)	Fe-Chp	27.17(28)	a = 5.310(5)
										c = 10.47(1)

Fe	Sample name	Formula $_{initial}$	Formula $_{measured}$	Fe [at.-%]	Cu/Ga	Cu/(Ga+Fe)	M/S	Phase content (XRD) [%]		comment
0.2	CFGS-A-E-040	$Cu_{0.5}Ga_{0.3}Fe_{0.2}S$	$Cu_{0.496}Ga_{0.408}Fe_{0.090}S$	4.48	1.22(2)	1.00(2)	0.99(2)	Chp	70.44(69)	
			$Cu_{0.517}Ga_{0.130}Fe_{0.379}S$	18.95	3.98(8)	1.02(2)	1.03(2)	Fe-Chp	29.56(28)	a = 5.314(5)
										c = 10.50(1)
0.225	CFGS-A-E-045	$Cu_{0.5}Ga_{0.375}Fe_{0.225}S$	$Cu_{0.500}Ga_{0.373}Fe_{0.125}S$	6.27	1.34(2)	1.00(2)	1.00(2)	Chp	73.33(42)	
			$Cu_{0.521}Ga_{0.115}Fe_{0.400}S$	19.98	4.53(9)	1.01(2)	1.04(2)	Fe-Chp	26.67(27)	a = 5.313(5)
										c = 10.49(1)
0.25	CFGS-A-E-050	$Cu_{0.5}Ga_{0.35}Fe_{0.25}S$								
0.3	CFGS-A-E-060	$Cu_{0.5}Ga_{0.2}Fe_{0.3}S$								heterogeneous
0.35	CFGS-A-E-070	$Cu_{0.5}Ga_{0.15}Fe_{0.35}S$								

Appendix III : Rietveld refinement results

				X-ray powder diffraction					Neutron powder diffraction			
Cr-I-I	**a [Å]**	**c [Å]**	**η**	**u**	**4a-S [Å]**	**4b-S [Å]**	**R-Bragg**	**Chi²**	**OCC-4a**	**OCC-4b**	**R-Bragg**	**Chi²**
0.02	5.355(1)	10.485(2)	0.0211(6)	0.0071(13)	2.325(4)	2.281(4)	5.79	1.92	0.974(30)	1.013(33)	1.73	2.00
0.06	5.356(1)	10.487(2)	0.0210(6)	0.0126(10)	2.343(4)	2.264(3)	4.68	1.84	0.962(26)	0.986(25)	2.30	2.37
0.08	5.356(1)	10.486(2)	0.0211(6)	0.0090(13)	2.331(4)	2.275(4)	4.94	2.29	1.011(28)	1.009(23)	1.89	1.82
0.1	5.356(1)	10.486(2)	0.0211(6)	0.0099(14)	2.334(4)	2.273(4)	5.12	4.11	1.010(22)	0.998(19)	1.64	2.15
0.2	5.356(1)	10.485(2)	0.0212(6)	0.0074(23)	2.325(6)	2.281(6)	5.42	7.16	1.018(31)	0.972(24)	2.15	3.61
Cr-I-II	**a [Å]**	**c [Å]**	**η**	**u**	**4a-S [Å]**	**4b-S [Å]**	**R-Bragg**	**Chi²**	**OCC-4a**	**OCC-4b**	**R-Bragg**	**Chi²**
0.02	5.355(1)	10.487(2)	0.0209(6)	0.0122(12)	2.331(4)	2.275(4)	5.49	3.60				
0.03	5.356(1)	10.487(2)	0.0209(6)	0.0104(14)	2.326(5)	2.281(5)	5.91	3.31				
0.04	5.355(1)	10.487(2)	0.0209(6)	0.0118(9)	2.339(3)	2.268(3)	4.87	2.18				
0.05	5.355(1)	10.486(2)	0.0209(6)	0.0101(10)	2.336(3)	2.271(3)	4.28	2.61				
Mn-I-I	**a [Å]**	**c [Å]**	**η**	**u**	**4a-S [Å]**	**4b-S [Å]**	**R-Bragg**	**Chi²**	**OCC-4a**	**OCC-4b**	**R-Bragg**	**Chi²**
0.02	5.360(1)	10.502(2)	0.0204(6)	0.0105(12)	2.339(4)	2.273(4)	5.12	2.08	0.927(30)	0.976(31)	1.44	1.52
0.04	5.365(1)	10.502(2)	0.0199(6)	0.0109(13)	2.342(4)	2.274(4)	6.68	2.26	0.937(18)	0.920(19)	1.76	1.44
0.08	5.370(1)	10.493(2)	0.0230(6)	0.0160(10)	2.359(3)	2.259(3)	4.32	1.66	0.889(22)	0.846(22)	2.44	2.26
0.1	5.368(1)	10.501(2)	0.0214(6)	0.0111(12)	2.343(4)	2.274(4)	3.17	1.52	0.835(14)	0.853(15)	2.29	1.52
Mn-I-II	**a [Å]**	**c [Å]**	**η**	**u**	**4a-S [Å]**	**4b-S [Å]**	**R-Bragg**	**Chi²**	**OCC-4a**	**OCC-4b**	**R-Bragg**	**Chi²**
0.01	5.358(1)	10.480(2)	0.0222(6)	0.0128(8)	2.344(3)	2.264(2)	4.52	2.03				
0.03	5.367(1)	10.488(2)	0.0228(6)	0.0137(8)	2.350(3)	2.264(2)	4.65	1.83				
0.05	5.369(1)	10.491(2)	0.0229(6)	0.0146(8)	2.354(3)	2.262(2)	4.14	1.69				
0.07	5.369(1)	10.523(2)	0.0199(6)	0.0028(28)	2.319(9)	2.300(9)	8.31	5.56				

Mn-I-III	a [Å]	c [Å]	η	u	4a-S [Å]	4b-S [Å]	R-Bragg	Chi²	OCC-4a	OCC-4b	R-Bragg	Chi²
0.00	5.355(1)	10.487(2)	0.0208(6)	0.0112(13)	2.338(4)	2.269(4)	7.28	4.34				
0.05	5.371(1)	10.508(2)	0.0217(6)	0.0121(15)	2.351(5)	2.268(4)	8.36	2.64				
0.15	5.370(1)	10.490(2)	0.0233(6)	0.0096(21)	2.339(6)	2.277(6)	4.59	1.38				
0.20	5.375(1)	10.550(2)	0.0186(6)	0.0024(47)	2.322(16)	2.304(15)	13.3	4.24				
0.25	5.375(1)	10.550(2)	0.0186(6)	0.0054(56)	2.329(16)	2.298(15)	18.1	5.68				

Mn-334	a [Å]	c [Å]	η	u	4a-S [Å]	4b-S [Å]	R-Bragg	Chi²	OCC-4a	OCC-4b	R-Bragg	Chi²
I	5.360(1)	10.475(2)	0.0227(6)	0.0067(40)	2.325(13)	2.282(12)	8.47	1.56				
II	5.360(1)	10.477(2)	0.0226(6)	0.0083(36)	2.329(13)	2.279(12)	5.26	1.55				

Ni	a [Å]	c [Å]	η	u	4a-S [Å]	4b-S [Å]	R-Bragg	Chi²	OCC-4a	OCC-4b	R-Bragg	Chi²
0.05	5.355(1)	10.488(2)	0.0208(6)	0.0096(13)	2.333(4)	2.273(4)	6.49	2.08				
0.1	5.355(1)	10.488(2)	0.0208(6)	0.0061(22)	2.322(6)	2.284(6)	9.19	2.42				
0.15	5.355(1)	10.488(2)	0.0208(6)	0.0060(27)	2.322(9)	2.284(9)	11.8	4.33				
0.2	5.355(1)	10.487(2)	0.0208(6)	0.0124(16)	2.342(5)	2.265(5)	6.76	2.37				

Mn-X-I	a [Å]	c [Å]	η	u	4a-S [Å]	4b-S [Å]	R-Bragg	Chi²	OCC-4a	OCC-4b	R-Bragg	Chi²
0.01	5.362(1)	10.501(2)	0.0208(6)	0.0112(8)	2.341(3)	2.271(3)	2.62	1.98	0.958(30)	1.029(31)	2.34	1.96
0.02	5.374(1)	10.512(2)	0.0219(6)	0.0106(18)	2.344(6)	2.278(5)	6.13	3.26	0.833(47)	0.986(45)	4.01	5.16
0.04	5.379(1)	10.524(2)	0.0217(6)	0.0081(14)	2.338(4)	2.287(4)	5.88	2.35	0.829(39)	0.890(41)	2.31	3.13
0.05	5.380(1)	10.532(2)	0.0212(6)	0.0147(12)	2.360(4)	2.268(4)	5.99	2.45	0.902(36)	0.806(30)	3.06	3.24

Mn-X-II	a [Å]	c [Å]	η	u	4a-S [Å]	4b-S [Å]	R-Bragg	Chi²	OCC-4a	OCC-4b	R-Bragg	Chi²
0.025	5.364(1)	10.492(2)	0.0221(6)	0.0104(12)	2.341(4)	2.272(4)	5.79	2.57				
0.05	5.374(1)	10.518(2)	0.0214(6)	0.0132(16)	2.356(5)	2.266(4)	10.7	5.53				
0.1	5.372(1)	10.541(2)	0.0189(6)	0.0040(26)	2.327(6)	2.296(6)	9.40	4.95				
0.175	5.364(1)	10.510(2)	0.0203(6)	0.0058(23)	2.322(6)	2.282(6)	6.19	2.74				

Fe	a [Å]	c [Å]	η	u	4a-S [Å]	4b-S [Å]	R-Bragg	Chi^2	OCC-4a	OCC-4b	R-Bragg	Chi^2
0.025	5.355(1)	10.490(2)	0.0206(6)	0.0071(13)	2.326(4)	2.281(4)	6.20	3.15				
0.05	5.357(1)	10.514(2)	0.0187(6)	0.0016(14)	2.307(4)	2.304(4)	5.96	3.15				
0.075	5.358(1)	10.526(2)	0.0178(6)	0.0018(12)	2.298(4)	2.315(4)	6.30	3.11				
0.1	5.359(1)	10.536(2)	0.0170(6)	0.0052(11)	2.290(3)	2.325(3)	6.97	3.61				
0.125	5.347(3)	10.498(6)	0.0183(17)	0.0001(47)	2.301(16)	2.301(16)	10.6	3.46				
0.15	5.346(3)	10.499(6)	0.0181(17)	0.0079(23)	2.326(6)	2.277(6)	8.05	4.20				
0.175	5.345(3)	10.500(6)	0.0178(17)	0.0056(33)	2.320(9)	2.282(9)	9.03	3.69				
0.2	5.343(3)	10.502(6)	0.0172(17)	0.0038(47)	2.313(16)	2.288(15)	10.3	4.39				
0.225	5.339(3)	10.507(6)	0.0160(17)	0.0003(87)	2.300(30)	2.300(30)	9.02	3.25				